

UNCLASSIFIED

AD 270 217

*Reproduced
by the*

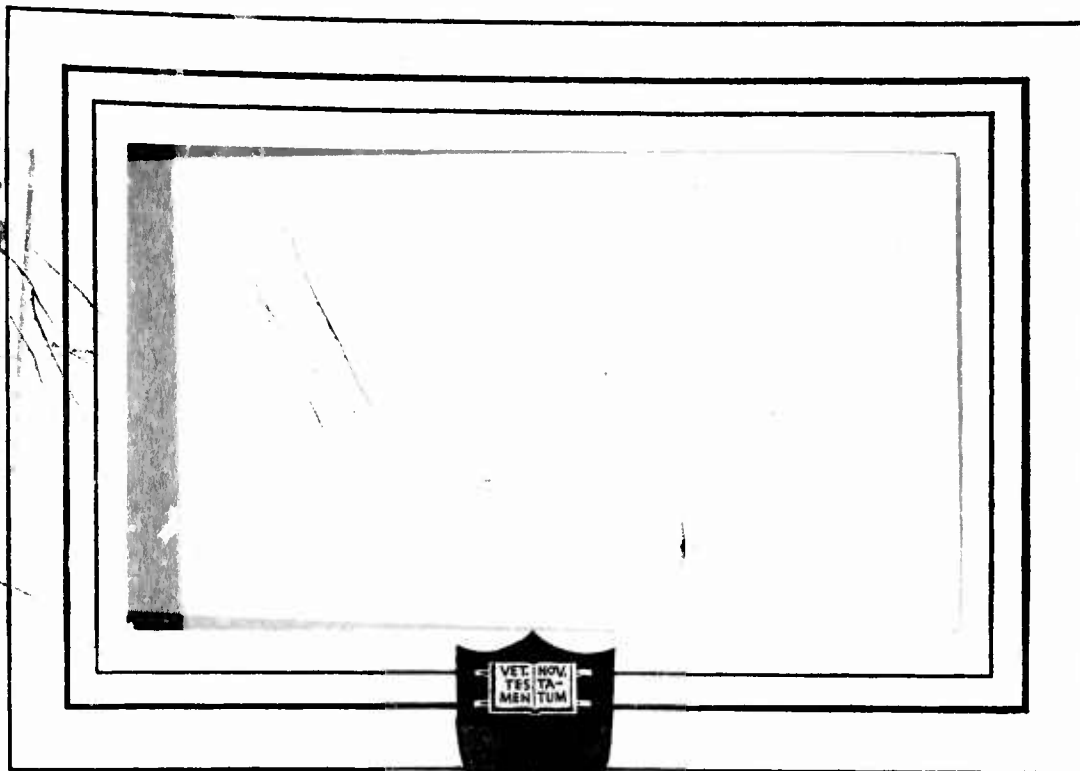
**ARMED SERVICES TECHNICAL INFORMATION AGENCY
ARLINGTON HALL STATION
ARLINGTON 12, VIRGINIA**



UNCLASSIFIED

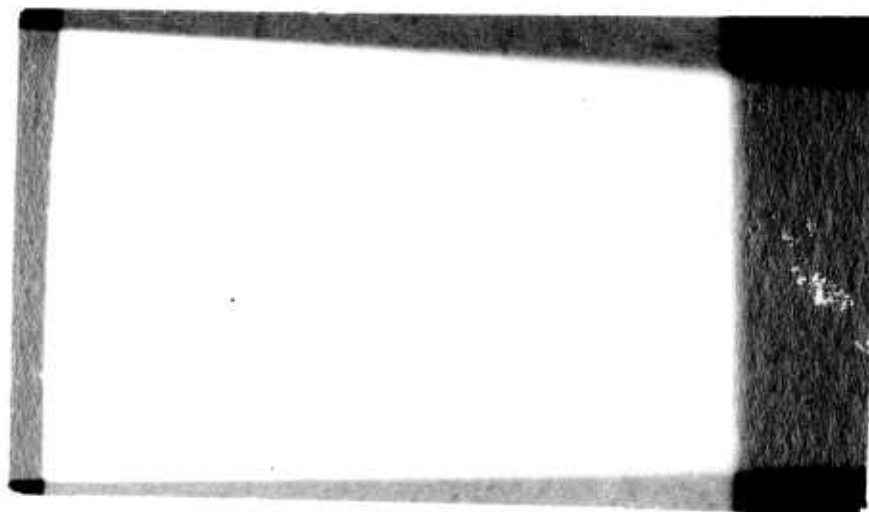
NOTICE: When government or other drawings, specifications or other data are used for any purpose other than in connection with a definitely related government procurement operation, the U. S. Government thereby incurs no responsibility, nor any obligation whatsoever; and the fact that the Government may have formulated, furnished, or in any way supplied the said drawings, specifications, or other data is not to be regarded by implication or otherwise as in any manner licensing the holder or any other person or corporation, or conveying any rights or permission to manufacture, use or sell any patented invention that may in any way be related thereto.

6.12-2-1
NOX



PRINCETON UNIVERSITY

DEPARTMENT OF AERONAUTICAL ENGINEERING



Reproduction, translation, publication, use and disposal in whole or in part by or for the United States Government is permitted.

The views contained in this report are those of the contractor and do not necessarily reflect those of the Department of the Army.

The information contained herein will not be used for advertising purposes.

Agencies within the Department of Defense and their contractors may obtain copies of this report on a loan basis from:

Armed Services Technical
Information Agency
Arlington Hall Station
Arlington 12, Virginia

Others may obtain copies from:

Office of Technical Services
Acquisition Section
Department of Commerce
Washington 25, D.C.

U. S. Army Transportation Research Command
Fort Eustis, Virginia

Project Number: 9-38-01-000, TK902
Contract Number: DA 44-177-TC-524

RESULTS OF EXPERIMENTS ON A
TILT-WING VTOL AIRCRAFT USING
THE PRINCETON UNIVERSITY
FORWARD FLIGHT FACILITY

by

William F. Putman

Aeronautical Engineering Department

Report No. 542
May 1961

William F. Putman
William F. Putman

Approved by:

A. A. Nikolsky
A. A. Nikolsky
Project Leader

ACKNOWLEDGEMENT

Grateful acknowledgement is made of the capable assistance and full cooperation of the entire staff of the Princeton University Forward Flight Facility. In particular the guidance and counsel of Mr. Howard C. Curtiss, Jr. and Professor A. A. Nikolsky in the formulation and execution of all facets of this endeavor were of inestimable value.

FOREWORD

The research in this report was conducted by the Department of Aeronautical Engineering of Princeton University under the sponsorship of the United States Army Transportation Research Command, as Phase 1 of work under the ALART Program. The development of the apparatus and a part of the experiments reported herein were conducted under the Office of Naval Research Contract Nonr-1858(11).

The work was performed under the supervision of Professor A. A. Nikolsky, Department of Aeronautical Engineering, Princeton University.

Mr. Esteban Martinez was responsible for the design and development of the apparatus. Mr. Theodor Dukes developed the electronic circuitry.

TABLE OF CONTENTS

	Page
List of Figures	v — vii
Summary	1
Introduction	2 - 7
List of Symbols	8 - 11
Part I — Experimental Test Equipment	12 - 53
Discussion:	13 - 29
1) Model	13 - 18
2) Carriage	18 - 21
3) Instrumentation	21 - 26
4) Data Link	26 - 29
Conclusions	50 - 53
Part II — Experimental Techniques and Procedures	54 - 62
Discussion:	55 - 59
1) Static Tests	55 - 57
2) One Degree of Freedom Tests	57 - 59
Conclusions	59 - 62
Part III — Experimental and Theoretical Presentation and Analysis	63 - 186
Discussion:	64 - 164
a. Test Conditions and Accuracies	64 - 68
b. Theoretical Static Stability and Trim Analysis	90 - 138
1) Assumptions and Limitations	90 - 92
2) Momentum Considerations	93 - 98
3) Rotor Operating Conditions	99 - 100
4) Rotor Contributions	101 - 102
5) Wing Operating Conditions	104 - 105
6) Wing Contributions	110 - 113
7) Slipstream Rotation Considerations	126 - 131
c. Predicted Longitudinal Dynamics	139 - 164
1) Equations of Motion	139 - 140
2) Characteristic Equation	140 - 142
3) Root Locus Developments	142 - 146
4) Theoretical Tail Effects	152 - 156

	Page
Results:	165 - 184
a. Experimental Data	165
1) Comparison to 1/4 Scale Wind Tunnel Model Results	165 - 167
2) Comparison to Full Scale Results	167 - 168
b. Predicted Longitudinal Trim	174 - 175
1) Comparison of Assumed Wings	176 - 177
2) Effect of Slipstream Rotation	178 - 179
c. Predicted Longitudinal Dynamics	180 - 182
Conclusions:	185 - 186
Bibliography	187 - 188
Appendices:	
Appendix A — Development of Analytical Expressions	189 - 212
Appendix B — Development of Inflow Derivative Charts	213 - 219
Appendix C — Discussion of Scaling Techniques	220 - 223

LIST OF FIGURES

Figure		Page
1.	Interior of track	30
2.	Model for 1-D/F tests	31
3.	1/5.2 Scale model	32
4.	Rotor blade construction	34
5.	Detail of wing construction	35
6.	Detail of collective pitch actuator	36
7.	Tail pitch fan and spoiler	37
8.	Schematic of c.g. motion	38
9.	Linkages for pitching restraint	39
10.	Magnetic clutch carriage with static test model	40
11.	Loop diagram for magnetic clutch carriage constant velocity servomechanism	41
12.	Hydraulic carriage	42
13a.	Hydraulic carriage velocity servo schematic	43
13b.	Hydraulic carriage position servo schematic	44
13c.	Hydraulic carriage position servo transfer function	45
14.	Schematic of horizontal error link and 1-D/F instrumentation	46
15.	Schematic of static test instrumentation	47
16.	Schematic of 1-D/F vertical force	48
17.	Data receiving and recording equipment	49
18.	Axis system	69
19.	Hovering experimental data	70
20.-27.	Static test experimental data	71-78
28.-33.	One degree of freedom test experimental data	79-84
34.-38.	Trim cross plots	85-89

Figure		Page
39.	Normal and total mass flow comparison	98
40.	Vector diagram of wing dependent variables	103
41.	Reference 4 wing characteristics	106
42. a,b,c.	Reference 7 experimental wing characteristics	107-109
43. 44.	Comparison of assumed wing characteristics to requirements for horizontal and vertical trim	114-115
45. 46.	Experimental static derivatives (Acc. & Trim)	116-117
47.- 54.	Theoretical derivative build-up	118-125
55.	Hovering induced velocity	132
56.- 58.	Vector diagrams of local rotational effects	133-135
59.	Effect of rotation on wing lift characteristics	136
60.	Effect of rotation on wing drag characteristics	137
61.	General trends of rotation effects	138
62.- 64.	Loci of tail off roots	149-151
65.	Pitching contributions to tail variables	159
66.	Theoretical rotor, wing and tail M_0 contributions	160
67.- 70.	Loci of roots of tail-on airplane	161-164
71.- 73.	Comparison of experimental data to 1/4 scale wind tunnel data	169-171
74.	Comparison of model to full scale trim speeds	172
75.	Full scale transition	173
76.- 77.	Theoretical and experimental trim conditions	176-177
78.- 79.	Effect of rotation on longitudinal trim	178-179
80.	Period of short-period oscillatory mode	183
81.	Real part of oscillatory roots	184

Figure		Page
82.	Pitching rate influence on rotor and wing variables	212
83.- 87.	Inflow derivatives	212-219
88.	Relationships of activated forces	222
Table I.	Physical characteristics of model and full scale machine	33
Table II	Experimental and theoretical trim conditions	157
Table III	Experimental static derivatives and predicted tail contributions	158
Table IV	Dynamical similitude scale factors	223

SUMMARY

This report presents the results of a series of experiments conducted on a $\frac{1}{5.2}$ scale dynamically similar model of a tilt-wing VTOL aircraft. The static longitudinal forces and moment and the character of horizontally-free partial transitions were examined through the use of the Princeton University Forward Flight Facility.

Included are discussions of the equipment and testing techniques employed in these tests as well as a development and evaluation of various analytical approaches to the prediction of the static and dynamic stability characteristics of a wing-rotor system.

Results demonstrate that additional experimental information is necessary in order to predict accurately the forces and moments developed by the wing and rotor.

A preliminary analysis indicates significant contributions to stability and control from the effects of slipstream rotation on wing local flow conditions.

The presentation is divided into Parts I, II and III, concerned respectively with the experimental test equipment, procedures and analysis techniques. Each Part is semi-autonomous and includes its own Figures, results and conclusions.

INTRODUCTION

It is the purpose of this report to present the results of tests conducted on a tilt-wing VTOL aircraft model on the Princeton University Forward Flight Facility. Included are discussions of the experimental equipment and techniques employed in these tests, as well as the actual test results. In general, an attempt has been made to assess the feasibility, limitations and potential of the equipment and techniques and to determine the validity of the results by comparison with experimental data from other sources, when possible, and with theoretical predictions developed herein. There follows immediately in this section a brief background and description of the Facility, and an explanation of the purposes of the tests.

Due to increasing interest in the past decade in helicopters and vertical take-off and land (VTOL) type aircraft, it was thought desirable at Princeton University to design, develop and construct an apparatus with which it would be possible to investigate the characteristics of such aircraft, and which would be specifically tailored to meet the requirements of experimental investigation in the very low speed flight regime. In particular, such an apparatus should permit the direct measurement of the dynamic behavior of these aircraft, by the use of relatively inexpensive scale models, tested in a controlled environment, i.e. independently of outside weather conditions. In addition, there should exist the capability of performing steady-state, or static, experiments to determine static stability derivatives which would facilitate the development of theoretical methods of predicting the dynamic

characteristics of these aircraft.

Provisions should be made to allow precise and direct measurement and control of all aircraft flight variables, such as attitudes, velocities and accelerations, as well as to restrain the model in such a way as to permit isolation of particular degrees of freedom or modes of motion for detailed study, and to prevent destruction of the model in the event of excessive or uncontrollable motions sometimes characteristic of the type of aircraft under consideration.

Various possibilities presented themselves in the selection of the type of apparatus satisfying the above requirements. Should the model be moved through the air under its own power similar to the manner of operation of the full scale aircraft, or should the air be moved past the model as is done in wind tunnel testing, or might a compromise be reached somewhere between these two extremes? The resolution of these questions lay in the consideration of particular problems associated with the apparatus in question and in a careful appraisal of the cost, utility and performance of the facility resulting from each solution.

To allow the testing of models whose maximum dimension would be of the order of 8 feet (rotor diameter or wing span) in zero flight speed conditions and free from wall and ground effects, minimum Y-Z plane enclosure dimensions of 30 feet x 30 feet were deemed necessary. The model size assumed would permit the necessary scaling of rotor and hub geometry to produce dynamic similarity while at the same time keeping model weight and power requirements within attainable limits. The requirements for measurement and control of variables, conditions, and restraints necessitate providing a known reference with the model at

all times. In the case of the wind tunnel this reference would be the stationary pylon upon which the model was mounted. However, with the model scales implied characteristic periods of oscillation could be as low as two seconds, with velocity excursions of the order of ± 10 feet/second, and with the model held stationary the power requirements to provide the resulting accelerations to the masses of air involved would indeed be prodigious. Compromising by allowing the model to oscillate about some steady-state trim velocity provided by the wind tunnel would mean providing a reference moving with the model and slaved to it through some sort of automatic positioning device. This scheme, however, would require accelerating the air in the tunnel corresponding to a VTOL transition of 10-15 seconds duration from zero velocity through a stall speed of some 60-70 feet/second while maintaining turbulence levels and velocity fluctuations at some reasonably low value. Such a scheme, if possible, would be expensive due to the size and power requirements of the wind tunnel necessary.

After consideration of the problems associated with the above schemes the best solution seemed to be to eliminate the necessity for moving large quantities of air simply by allowing the above-mentioned moving reference to follow even the steady-state component of the model's motion allowing sufficient space to perform any of the indicated maneuvers such as VTOL transition. This, in essence, is the Princeton University Forward Flight Facility. In fact, it is a building 30 feet x 30 feet x 750 feet long, providing shelter from the elements and housing a mono-rail track running its length. A photograph of the interior of this building is presented on page 30 showing the general arrangement of the track.

Dynamically-similar powered scale models are "free" flown in the building, their motion being followed and monitored by a powered carriage running on the track. The carriage serves only to provide a known reference traveling with the model, to restrain the degrees of freedom not under study, and to limit the model excursions if excessive and/or hazardous. A positioning servomechanism senses the relative position error between the model and the carriage and drives the carriage to minimize this error. Pertinent variables are measured directly and the data transmitted back and recorded on the ground. In addition, the model may be restrained by the carriage through force-measuring devices such as strain gages, so that by driving the carriage along the track at a steady pre-set velocity, static force and moment measurements may be made.

It is the purpose of this report to discuss tests made on the above-described Facility, using a $\frac{1}{5.2}$ scale dynamically similar model of the Vertol V-76 tilt-wing VTOL aircraft. These tests were conducted during the periods of 9-17-58 to 11-26-58 and 11-10-58 to 1-7-60 for the following purposes:

- 1) To obtain useful longitudinal stability and trim information on a tilt-wing type VTOL aircraft;
- 2) To provide an initial evaluation of the Facility, equipment and techniques; and
- 3) To establish a basis for the extrapolation of the future potential, requirements and limitations of such a Facility.

The first group of tests were of a steady-state nature as described above. The model was restrained in the longitudinal degrees of freedom

(that is, horizontal and vertical translation of the c.g. and pitching about the c.g.) by strain gages attached to the carriage and supporting the model. Constant velocity runs were made at various fuselage attitudes and wing tilt angles, and rotor collective pitch was adjusted to provide thrust levels corresponding to the desired conditions of trimmed lift and drag forces. Constant velocity was provided by presetting the carriage to the desired velocity and then allowing the carriage to accelerate itself and the model to V_0 and drive it at this velocity, while a feedback mechanism insured that the preset velocity was maintained by comparing the carriage's velocity at all times to the preset value. A separate run was made and steady-state data recorded for each change in the variables - velocity, wing tilt, fuselage altitude, and rotor collective pitch. In all, a total of 174 runs were made, 126 of them providing useful static stability and trim information.

The second series of tests differed in method from the first in that, rather than drive the model with the carriage, the model was allowed a single longitudinal degree of freedom - horizontal translation - and the carriage was arranged to follow the model in its horizontal velocity excursions while vertical force and pitching moment were measured with strain gages between the carriage and the model. Runs were made in this testing configuration by adjusting tilt angle and rotor collective pitch to trim the model in a hovering attitude at zero fuselage pitch angle and then allowing the wing to tilt downward at a constant rate with collective pitch and fuselage attitude held constant. As the wing tilted downward the model would accelerate until such time as the wing stopped tilting, whereupon the model velocity

would decay to that value required for horizontal trim. Repeated runs were made, stopping the wing tilt at various angles, and in several cases reversing the direction of wing tilting at various angles and allowing the run to proceed until the model was again in a hovering attitude at end of the run trim. This series of tests involved 35 runs, of which 32 produced useful data concerning the model and carriage behavior.

For simplicity and clarity the two series of tests described above will be referred to in the remainder of this report as "static" and "1 D/F" (abbreviation for One degree of freedom) respectively.

LIST OF SYMBOLS

a	Lift curve slope of blade, per radian
a_1	Rotor longitudinal flapping
a.c.	Aerodynamic center of wing - assumed at .25 m.a.c.
$A \dots E$	Coefficients of C.E. in descending order
$A_\alpha \dots E_\alpha$	Coefficients of denominator for M_α root locus
$A_\theta \dots E_\theta$	Coefficients of denominator for M_θ root locus
$A_v \dots E_v$	Coefficients of denominator for M_v root locus
$a_\alpha, b_\alpha \dots$	Coefficients of numerator for M_α root locus
$a_\theta, b_\theta \dots$	Coefficients of numerator for M_θ root locus
$a_v, b_v \dots$	Coefficients of numerator for M_v root locus
b	Number of blades
B	Blade tip loss factor
c	Chord of blade
c_w	Chord of wing
c.g.	Center of gravity
C_L	Lift coefficient
C_D	Drag coefficient
$C_{L\alpha}$	Wing lift curve slope
$C_{D\alpha}$	Wing drag curve slope
$C_{L\alpha_s}$	Horizontal stabilizer lift curve slope
$C_{m.a.c.}$	Wing pitching moment coefficient about a.c.
C_T	Rotor thrust coefficient
C_H	Rotor H-force
C.F.	Centrifugal force per blade
D	Drag force

e	Rotor blade flapping hinge offset
f.r.l.	Fuselage reference line - defined as upper longeron
h_R	Distance of rotor hub from c.g.
h_W	Distance of wing a.c. from c.g.
H	Rotor force perpendicular to shaft
i_s	Horizontal stabilizer incidence
i_w	Wing incidence measured from f.r.l.
I	Airplane moment of inertia about pitch axis
I_1	Blade moment of inertia about flapping hinge
l_t	Tail length
L	Lift force
m	Mass flow
M	Pitching moment
M_h	Rotor moment at hub
M_α	Rate of change of pitching moment with angle of attack
$M_\dot{\theta}$	Rate of change of pitching moment with pitching rate
M_v	Rate of change of pitching moment with velocity
N	Number of rotors
r	Radial distance along rotor blade
R	Rotor radius
S	Wing area per semi-span
T	Rotor thrust
u	Body axis system longitudinal velocity
\bar{u}	Rotor axial induced velocity at disk
V	Freestream velocity along flight path
V_0	Carriage or model steady trim speed
V_R	Resultant velocity at wing - vector sum

w	Body axis system vertical velocity
W	Aircraft gross weight
x	Radial station along blade $\equiv \frac{r}{R}$
x_w	Longitudinal distance of wing a.c. from c.g.
x_R	Longitudinal distance of rotor hub from c.g.
X	Longitudinal force
X_α	Rate of change of longitudinal force with angle of attack
X_θ	Rate of change of longitudinal force with pitch attitude
$X_{\dot{\theta}}$	Rate of change of longitudinal force with pitch rate
X_v	Rate of change of longitudinal force with velocity
z_1	Roots of numerators in root loci
z_w	Normal distance of wing a.c. from c.g.
z_R	Normal distance of rotor hub from c.g.
α	Rotor angle of attack
α'	Wing angle of attack
γ	Locke's Number $= \frac{ac}{I_1}$
δ	Blade sectional profile drag coefficient
$\Delta\alpha'$	Change in α' due to slipstream rotation
θ	Aircraft pitch attitude
θ_{eff}	Effective blade pitch at $0.75R$
$\theta_{.75R}$	Blade collective pitch at $0.75R$
λ	Root of characteristic equation, also model scale factor
λ_o	$\lambda_o \equiv - C_T/2$
μ	Advance ratio $\equiv \frac{V \cos \alpha}{\Omega R}$
μ_x	Horizontal advance ratio $\equiv \frac{V}{\Omega R}$
ρ	Density of air

σ	Blade solidity factor $\equiv \frac{bc}{\pi R}$
ψ	Blade azimuth position
ω	Slipstream angular velocity, radians per second
Ω	Rotor rotational velocity, radians per second

SUBSCRIPTS

$()_{\alpha}$	Derivative with respect to angle of attack at constant velocity
$()_v$	Derivative with respect to velocity at constant angle of attack
$()_{\dot{\theta}}$	Derivative with respect to pitch rate at constant velocity and angle of attack
$()_h$	Hover, also hub
$()_w$	Wing
$()_R$	Rotor
$()_f$	Fuselage
$()_t$	Tail
$()_T$	Total
$()_{f.s.}$	Full scale
$()_{TF}$	Tail pitch fan
$()_s$	Horizontal stabilizer
$()_{ROT}$	Slipstream rotation
$()_{NON-ROT}$	Non-rotating
$()_{exp}$	Experimental

ABBREVIATIONS AND OTHER NOTATION

$()^*$	Change in variable due to pitching rate
$()^{\circ}$	Derivative with respect to time
1-D/F	One degree of freedom
$()^{-}$	Quantity divided by λ_0

PART I

EXPERIMENTAL TEST EQUIPMENT

DISCUSSION: TEST EQUIPMENT

The equipment used in the tests under consideration consisted in general of a powered scale model, a servo-controlled carriage, model and carriage monitoring and measuring instrumentation, and a radio-telemetry data-link with magnetic tape recorder. Each component of the system described above will be discussed separately and an evaluation given of its performance in conducting the tests discussed herein. The time period between the two sets of tests considered was one of transition when almost every component was changed to some extent in attempts to improve the performance of the entire system. As a result, the discussion of each item will be divided into parts associated with the equipment used in each of the tests.

MODEL

A photograph of the 1/5.2 scale dynamically-similar powered model of the Vertol V-76 used in the static tests appears on page 31. The dimensions of this model are as presented in the three view drawings on page 32, and the physical characteristics are given in a Table on page 33 along with a comparison with those of the full scale airplane. A development and discussion of the scaling used to achieve dynamic similarity appears in Appendix C. In general, no attempt was made to scale the elastic properties of the aircraft as a whole. However, rotor blade mass, mass distribution, and bending and torsional properties were preserved as closely as possible to those values simulating the full scale rotor blade. In design and construction of the model particular attention was given to avoiding natural frequencies

close to the one per revolution and three per revolution rotor forcing frequencies. Obvious success in this endeavor was demonstrated in the complete absence of any vibration problems throughout both test programs.

The model main drive system consists of a single 1.5 horsepower, three phase, 400 cycle electric motor driving the two three-bladed rotors through a geared-down transmission and a timing belt and sprocket arrangement. The timing belts transmit the power from the fuselage-located transmission, out the wing, to the rotor shafts, and are centered about the wing tilt hinge to allow the wing to tilt through the required limits. Such a drive system proved quite light and trouble-free under all power and wing-tilt conditions. The one drawback of this arrangement is a result of the sizeable belt tensions encountered in transmitting the power through reasonably-sized sprockets. Loads of the magnitude calculated (Tension \cong 50 pounds) make it very difficult to develop a system to measure rotor forces separately from the wing forces without resorting to the complications of direct shaft instrumentation. Separation of the wing and rotor forces would be a very significant contribution to the ability to assimilate information in both static and dynamic testing.

The model rotors are semi-articulated with full flapping but no lag freedom, and the hub geometry and blade static moment are exactly scaled to the full scale aircraft's values. Blade construction techniques used are quite similar to those discussed in References 1 and 2 using a steel insert imbedded in a foamed plastic shape. Some difficulty was experienced in attempting to apply the required twist to the

blade after molding and during the root-insert gluing operation. This difficulty was very easily overcome by modifying the fabrication procedure to allow the insert to be molded into the blade in an already-twisted mold. The twisted mold required was inexpensive and simple to fabricate, since the twist necessary was linear and easily generated as a regular surface. The master for the untwisted blade was originally parted at the chord line and made of flexible plastic. The procedure employed was to attach the master blade half to the twisted surface, build a dam around the periphery, and pour an aluminum-filled epoxy resin into the recess. The photograph on page 34 shows a blade mold, insert, completed blade, and assembled rotor.

A photograph on page 35 presents the essential details of the wing construction. The primary structural member is a thin-walled aluminum tube to which are attached the wing hinge points, rotor shaft housings and welded magnesium ribs. The aerodynamic surface is formed of .010 inch aluminum sheet to which is bonded 1/32 inch balsa sheet for stiffening. The covering is bonded and screwed to the wing with a resulting surface that is quite free of wrinkles, waves and other irregularities. The wing described above is the one used in the one degree of freedom tests, while the wing used in the static tests was of a similar construction but had a vacuum-formed plastic covering. The plastic covering was completely satisfactory as far as the resulting form and surface it provided, but excessive weight for dynamic tests, as well as fastening difficulties with the polystyrene plastic dictated a need for the more suitable covering.

The demand for light-weight construction for dynamic similitude

also required changes in the fuselage and nose bubble between the static and 1-D/F tests. The static test fuselage was cut from 1/8 inch aluminum sheet to simulate the full scale tubular stringer construction, and the nose bubble was of resin-impregnated fiberglass cloth. These two items were profitably replaced in the 1-D/F tests by a welded thin-wall aluminum tubing fuselage and a thin vacuum-formed polystyrene plastic bubble.

Although a tail assembly is shown in the photograph of the static test model on page 40 , no tail was used during the actual tests as discussed in Part III . A tail, complete with pitch fan, was in place for the 1-D/F tests, but the pitch fan was not operated since part of the test information desired was the tail load required to trim the aircraft. A photograph of this tail showing in some detail the flow-spoiling trimming device above the four-bladed pitch fan appears on page 37 . The power for the tail fan is taken from the main rotor drive system and transmitted along the fuselage and up through the vertical fin by means of a flexible cable drive. The horizontal stabilizer may be set at any desired incidence, but no rudder surface or yaw fan is provided as this model was originally intended for longitudinal testing only. It is anticipated that little development effort would be required to provide both of these additional items.

In the photograph of the wing construction on page 35 can be seen a small d.c. motor which drives the rotor collective pitch adjustment. A detail of the pitch adjustment assembly including the swash-plate and drive is presented on page 36 . Included in this photograph is the potentiometer used to measure model collective pitch

for telemetering to the ground. A similar d.c. motor drives a spring-loaded cable arrangement to rotate the spoiler plate above the tail pitch fan. This drive system is designed to have adequate response characteristics to apply a one second pulse input in model scale time for dynamic control response tests.

The wing tilting mechanism is driven by a 400 cycle synchronous motor through a high-reduction planetary gear box. Several combinations of motor speeds and gear ratios are available to allow different scaled time transitions to be accomplished. This same mechanism drives the links by which the model is supported and which allow the model supports to follow the c.g. travel of the aircraft during wing rotation. A schematic diagram of the geometric relationships involved in this c.g. motion is presented in Figure 8 on page 38. An examination of this Figure reveals the interesting effect that the airplane travels along a circular arc path with respect to the support point as the wing rotates through its transition travel. Motion of the aircraft with respect to the support presents a problem with regard to restraining the pitching freedom without producing a change in fuselage attitude during transition. It is possible to eliminate any fuselage attitude-wing tilt coupling by the use of a "passive" parallel linkage arrangement as depicted schematically in Figure 9 (a). Such a system was used in the 1-D/F tests, but limited the lower limits of wing tilting allowed when the angle i_w became sufficiently acute that the flexibility of supports allowed significant fuselage attitude deflection under load. The term "passive" is used to describe this linkage to differentiate it from an arrangement where the pitching restraint tie-in point is actually driven by a part

of the wing-tilt mechanism as shown schematically in Figure 9 (b). The advantage of the driven or "active" system is that it provides rigidity at all wing-tilt positions by applying torque as well as shearing restraint. A system similar to the one depicted in Figure 9 (b) is an absolute necessity for complete transition testing with this model when pitching freedom is to be restrained.

CARRIAGE

A general arrangement photograph of the carriage used in the static tests is shown on page 40 . This carriage had a drive system identical to the one described in Reference 2, with the exception that the magnetic clutches were not closed in a positioning servo loop. The 3 horsepower electric motor operated at maximum voltage at all times, and the carriage velocity was controlled by changing the voltage to the magnetic clutches. Excitation voltage on the clutches determined the torque transmitted and as a result the carriage acceleration and terminal velocity. Carriage velocity was sensed by a wheel driven tachometer, the output of which was fed back and compared to the applied voltage. A schematic of the resulting constant velocity servomechanism is presented in Figure 5. In practice this system maintained constant velocity within about 2 per cent, the carriage mass acting as a fairly effective filter to short-time track friction irregularities.

The major problem encountered in testing with this carriage was a general lack of prime motive power. Maximum steady velocities attainable were just over 26 feet/second , and as a result no data could be taken in the $i_w = 44$ degrees decelerated flight condition. At speeds above 26 feet/second track and wind resistance demanded more

power than the rather inefficient magnetic clutches would deliver with a 3 horsepower input. For tests run at velocities higher than 12-15 feet/second an auxiliary boost system was necessary in order to attain these speeds in a sufficiently short distance. Using the additional acceleration provided by the boost, steady state velocity of 26 feet/second could be maintained for as long as 8 to 10 seconds with ample space allowances for braking at the end of the run.

The problems encountered with the carriage described above were partially realized even before the static tests were undertaken, and work was underway in developing a completely different carriage, drive, and control system. Accordingly, the time period between the static tests and the 1-D/F tests saw the completion of an entirely new carriage system which was given its initial testing in the 1-D/F tests. A truly comprehensive discussion of this carriage is beyond the scope of this report, and for such a treatment the reader is referred to Reference 3. However, a brief description of the hydraulic drive and control system will be given herein to point out solutions to the problems encountered on the static carriage and the use of the new carriage in the 1-D/F tests.

A photograph of the hydraulic carriage system appearing on page 42 shows the vertical boom arrangement for accommodating vertical translational motion. The vertical positioning servo mechanism was not used in either of the tests discussed in this report and will not be discussed herein. A full treatment of this component can be found in Reference 3.

The hydraulic carriage is driven by a 30 horsepower 400 cycle

electric motor driving a 1000 psi variable-displacement hydraulic pump. Motive power is transmitted by a hydraulic motor driving a single knurled wheel through an adjustable-ratio gear box. Maximum attainable speeds with this system are above 80 feet/second, corresponding to about 175 feet/second on a full scale aircraft for scale factors of the order of 1/5. At the time of writing this report acceleration is limited only by drive wheel traction at about $0.7g$.¹

Carriage operation is controlled by a choice of two closed-loop servo mechanism arrangements, one for carriage velocity and the other for carriage position. Block diagrams for these two loops are presented in Figure 13 along with their respective transfer functions and magnitudes of the system parameters. Carriage velocity is set by adjusting V_0 to the trim speed desired and control is maintained by the inner loop controlling the displacement of the pump. In this condition the velocity is constant by virtue of the constant fluid displacement and hydraulic motor speed. Any irregularities in resistance to the motion are overcome by pressure build-up in the delivery lines, giving a response characterized by the approximately 10 cps natural frequency of

1. With the increased carriage performance capability it became feasible to increase the length of track available for testing. Accordingly, in the period from 11-26-58 to 11-10-59 the track and building were lengthened from the 450 feet used in the static tests to 750 feet. The additional length was not available for the 1-D/F tests, and indeed would not have been used if it had been, due to the exploratory nature of these tests with the new drive system. Subsequent test programs have made very profitable use of this extra length, and as many as 3 cycles of motions with seven second periods have been measured about trim speeds of 26 feet/second. A full explanation and discussion of the current problems and capabilities of this carriage-track system is to be found in Reference 3.

the hydraulic system under load. In tests made with this system no significant variations from steady state velocity can be detected in timed runs through four consecutive 25 feet intervals.

The positioning servo mechanism loop used in the 1-D/F tests is shown schematically in Figure 13. In this configuration the carriage drives itself to follow the horizontal position excursions of the model mounted on the error link. Descriptions of the error link system are given in Reference 2 and 3 and so will not be included here, but a schematic drawing of the horizontal error link appears on page 46 of this report. It is of interest to note that in the system as depicted in the block diagram of Figure 13 no provision is made to supply the carriage with a signal proportional to the steady state component of the model's velocity. Such a feature was omitted for the 1-D/F tests since the flight profile of transition tests is not one of steady velocity. Little difficulty was encountered in allowing a steady position error to accumulate as the model velocity changed during transition, a result attributable both to high error position gain and to negligible longitudinal perturbation of the model with only horizontal freedom.

INSTRUMENTATION

One of the major problem areas associated with conducting static tests on the Forward Flight Facility is concerned with model force and moment measuring instrumentation. The difficulties encountered arise primarily due to the peculiar nature of the testing facility, in that the forces to be measured are those acting on a moving model

rather than on one with the flow moving past it. The carriage velocity during a static run is held quite steady as far as effects aerodynamic are concerned. However, there is still considerable jostling and shaking of the model due to small track irregularities and carriage hydraulic drive response. Although no appreciable effect can be attributed to these disturbances when the model is free for dynamic tests,² a restrained model on the end of the six-foot horizontal boom sees these accelerations or vibrations as forcing inputs. The result is that if the model is suspended on conventional strain gage measuring devices, considerable noise will be superimposed on the steady state force signal. This section is concerned primarily with the attempts made to surmount the carriage-vibration noise problem in the two series of tests under consideration. The remaining test instrumentation involved only geared d.c. tachometers used to measure carriage velocity and rotor RPM and d.c. excited potentiometers for measuring wing tilt and horizontal error position. The sole difficulty experienced with any of these devices was brush noise in the tachometers - a problem easily solved by use of simple R-C filter networks.

The first approach to the problem of vibration noise in the strain gage system involved the use of very soft beams allowing sizeable deflections under load. The resulting finite motions were then damped

2. This statement is completely true to the extent that small perturbations in the carriage motion in no way effect the time history of the model's free motion. However, horizontal and vertical translational disturbances can impose rather severe positioning servo mechanism stability criteria as discussed in Reference 3.

by including oil-filled bellows arrangements in parallel with the spring of the strain gage beams. A schematic drawing of the system used to measure lift, drag and pitching moment is presented on page 47. Results using this scheme with battery-excited gages were compatible with the accuracies allowed by other parts of the data-gathering system, with noise in the lift and drag readings of the order of 6 to 8 per cent of full scale values. Pitching moment readings were particularly noise free, due mostly to the fine balancing of the model about its support points and the relative absence of carriage pitch-attitude forcing. Noise levels of the order of 2 per cent were easily achieved in the pitch gage with quite low damping ratios, whereas the unbalanced model inertial forces required large supercritical damping ratios in both lift and drag. In order to translate the per cent telemeter readings into model forces, the following calibrations were used:

$$L = 15.7 + (.125)(T) \text{ pounds}$$

$$D = (.192)(T) \text{ pounds}$$

$$M = (.070)(T) \text{ foot - pounds}$$

It should be noted that the systems described do nothing to alleviate or attenuate the force readings produced by low frequency vibrational accelerations of the model by the carriage, but only allow the relative motions produced by such forcing to be damped out. In general, such will always be the case as long as the suspension spring is the force measuring device, and it is important that such a scheme not be considered as being a noise filter or instrumentation shock mount. A true noise filter for the configuration under consideration would involve an inter-mediate shock-mounted platform between the

carriage and the model, relative to which the forces acting on the model would be measured. A scheme such as this would have the same limitation, as an electrical filtering network on the strain gage output, in that the noise spectrum includes too many sufficiently low frequencies to permit successful attenuation without limiting the data-sensing capabilities. A preferable and mechanically far less complicated scheme was attempted in the 1-D/F tests with results compromised more by execution than by conception.

One additional remark is in order before proceeding to the 1-D/F test instrumentation discussion. Elsewhere in this report reference is made to the soft beams used in the pitching moment strain gage and to the resultant moment-attitude coupling produced. This is not a serious consequence in its effect on the validity of the data, but it does permit small changes of model attitude to occur between supposedly constant α_F velocity-varying runs. The true angle of attack may be determined under any condition by applying the measured pitching moment to the beam spring rate for an attitude correction. This, however, complicates the data reduction procedure, and of particular annoyance is the loss of a truly constant α_F setting. Either of these was felt to be sufficient grounds for remedial action to be taken, and, accordingly, the static test arrangement was modified for the 1-D/F tests.

Instrumentation requirements in the 1-D/F tests were somewhat different from those of the static tests in that no horizontal restraint was desired and the wing was not fixed in position but allowed to tilt. On page 17 of this section mention is made of the complications involved in restraining the model in pitch during transition

and of the scheme used to accomplish this. Solutions to the problems associated with a soft pitching moment beam were made possible through the provision of additional instrumentation equipment - a.c. - excited strain gage carrier amplifiers. Use of an amplified S-G output signal allowed a vast increase in the stiffness of the pitch beam at the expense, however, of motions large enough to permit damping. It was found in the 1-D/F tests that with a sufficiently well-balanced model, it is not necessary to damp the pitching freedom, and these tests were conducted without benefit of any damping. The direct pitching moment data obtained in these tests exhibited no noise that could be directly attributed to carriage vibratory excitation of the model.

The only remaining longitudinal force to be measured during the transition runs is lift, or vertical force. This is probably the most difficult freedom to instrument, in that small variations in a rather large force are desired, and normal excitation of the model by track and carriage disturbances can be quite severe. The first of these problems was avoided in the static tests by engaging the lift beam only after the model was lifting its own weight less the equivalent of half of the full scale reading. This procedure allowed any desired sensitivity with 50 per cent output when the model was lifting gross weight. Carriage normal excitation is a severe problem and an attempt was made to eliminate these inputs by counter-balancing the model in such a way that normal accelerations of the end of the boom would produce no strain in the lift beam gages. The schematic presentation on page 48 depicts a system which gave significant alleviation

of the signal noise due to vibration, but whose performance was limited by its own failings. The use of gears for increasing mechanical advantage and of ball bearings for the large-load small-motion pivots resulted in large amounts of static friction in this system. Both of these components were used for expediency in these evaluation tests and performed sufficiently well to indicate that the technique has merit worthy of further examination and exploitation.

DATA LINK

In order to monitor and record the test information in a permanent and reproducible form the Forward Flight Facility is provided with a radio telemeter system with magnetic tape recorder. This arrangement circumvents the necessity of equipping the moving carriage with recording devices which might prove to be sensitive to the vibrations and accelerations encountered during running, or to the extremes of temperature and humidity experienced in year-round testing on the non-air-conditioned track. In addition, such a scheme permits quantitative monitoring of testing in progress while simultaneously recording the information on magnetic tape.

The ASCOP telemetering unit handles 45 channels of information, 43 of which are available for data, the remainder being used for synchronization purposes. In operation the various channels of d.c. information are applied to the poles of a rotating commutator switch, each of which is sampled 20 times per second. The d.c. value of each sample is then coded into a pulse duration which is transmitted to the ground by a pulse width modulation of the transmitter carrier frequency.

The incoming signal is recorded in this form on one channel of an AMPEX two-channel magnetic tape recorder, the other recorder channel is available for audio-information records. The signal is also simultaneously decoded and, with the help of the two synchronization channels, decommutated, whence it can be read as 43 channels of d.c. information. Visual monitoring of the incoming data is possible by means of an oscilloscope which presents the decommutated but still pulse-width coded information as 43 vertical lines, the height of which is proportional to the d.c. data voltage applied. A photograph on page 49 shows the tape recorder, telemeter ground station and a Sanborne recorder in operation. In this picture the three simultaneous monitoring and recording processes -- magnetic taping, scope presentation, and recorder graphing -- can be seen.

Another interesting and valuable feature of this telemetering system is an automatic calibration scheme which adjusts all data channels in proportion to a full scale reference. By supplying all strain gage and potentiometer excitation voltages from the same source as the full scale reference voltage, any change in the level of the power supply is compensated for automatically. With this system in operation, however, any independently supplied or absolute reading channels, such as a.c. excited gages or tachometers respectively, must be separately monitored by replaying the tape without automatic correction.

The airborne information coding device used in the static test program required a d.c. input signal of only ± 7.5 millivolts for full scale reading on the ground. This "low level" system allowed the

direct use of strain gage outputs without amplification, using battery-supplied excitation voltages of between 12 and 48 volts. With the battery power supply the automatic calibration feature proved to be quite valuable, and no difficulty was experienced in maintaining constant sensitivity. The two tachometers used to measure model Ω and carriage velocity, were intended only as monitoring devices and hence their effectiveness was not compromised by small changes in gain due to the compensation process. Absolute magnitude of model Ω was established by use of a strobotach and the carriage velocity was obtained by clocking each run over four measured intervals.

The low level system exhibited the very undesirable characteristic of large amounts of switching noise in the transmitted data. This proved to be a rather fundamental problem in that the switching noise level was essentially independent of signal level and seemed to be of the order of 0.5 to 1.5 millivolts. Magnitudes of this order resulted in from 3 to 10 per cent noise in the recorded signal, depending on the particular channel and the length of time the commutator had been running. The obvious solution to this problem was to increase the signal level since switching noise was apparently not a strong function of the applied voltage.

Accordingly, for the I-D/F tests the telemeter was modified to operate with signal levels of 0-5 volts applied at the commutator, and, as expected, switching noise was virtually undetectable. The "high level" telemetering system gave excellent results in these tests, but some additional complications resulted since amplifiers were now required on the strain gage outputs. As noted in another section, the

use of carrier amplifiers allowed the S/G beams to be made stiffer, and the resulting net benefits more than compensated for the complications involved.



Figure 1
INTERIOR OF TRACK

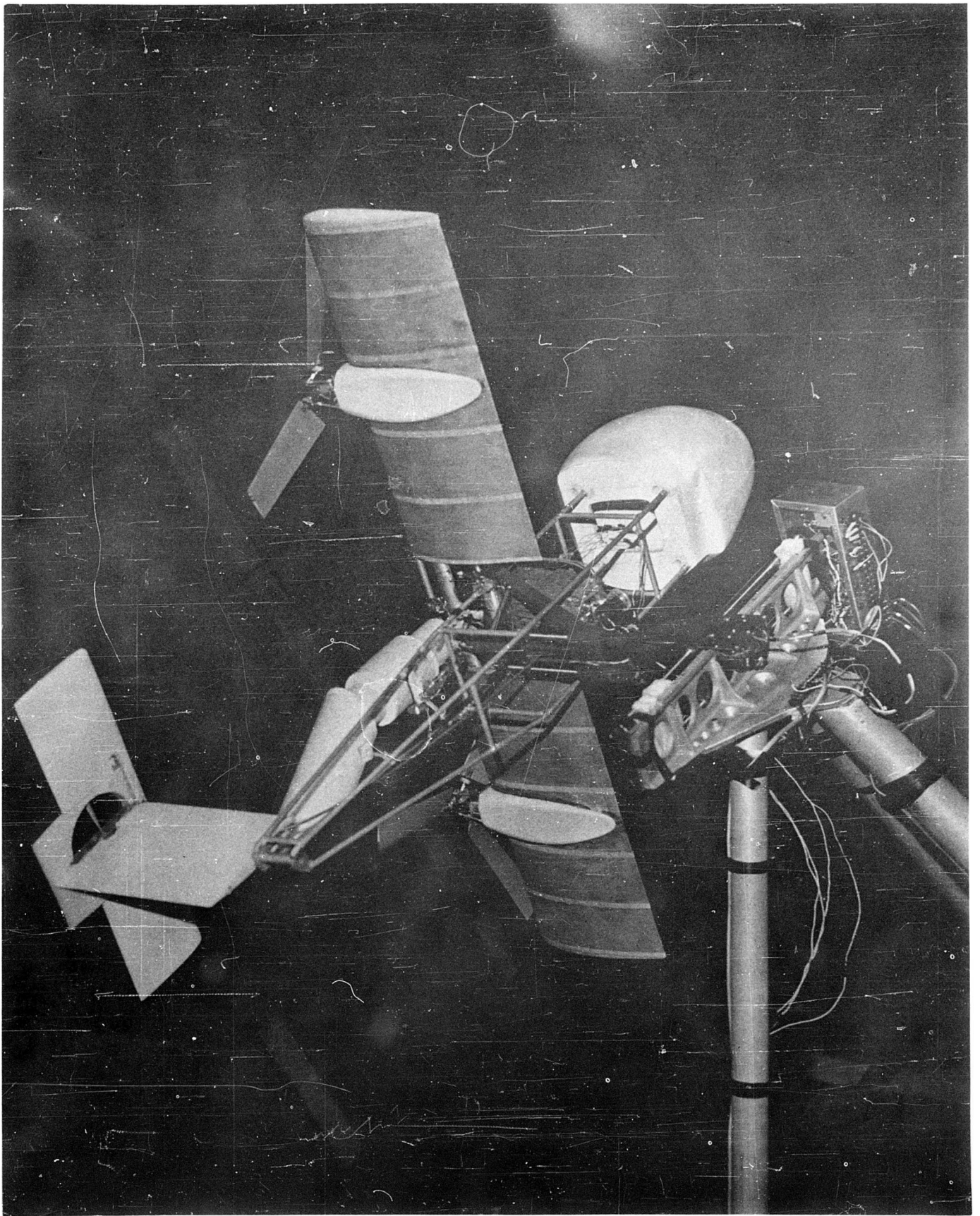
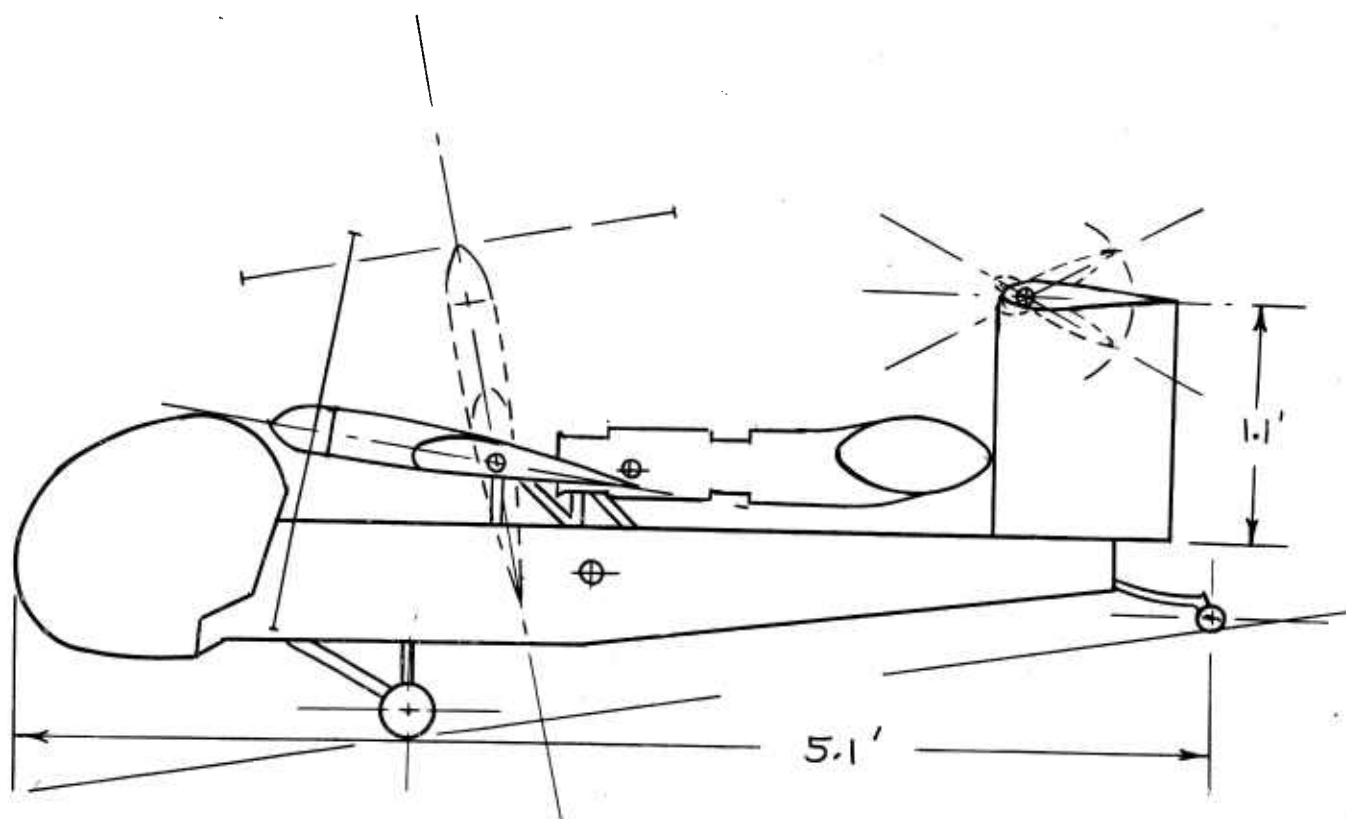
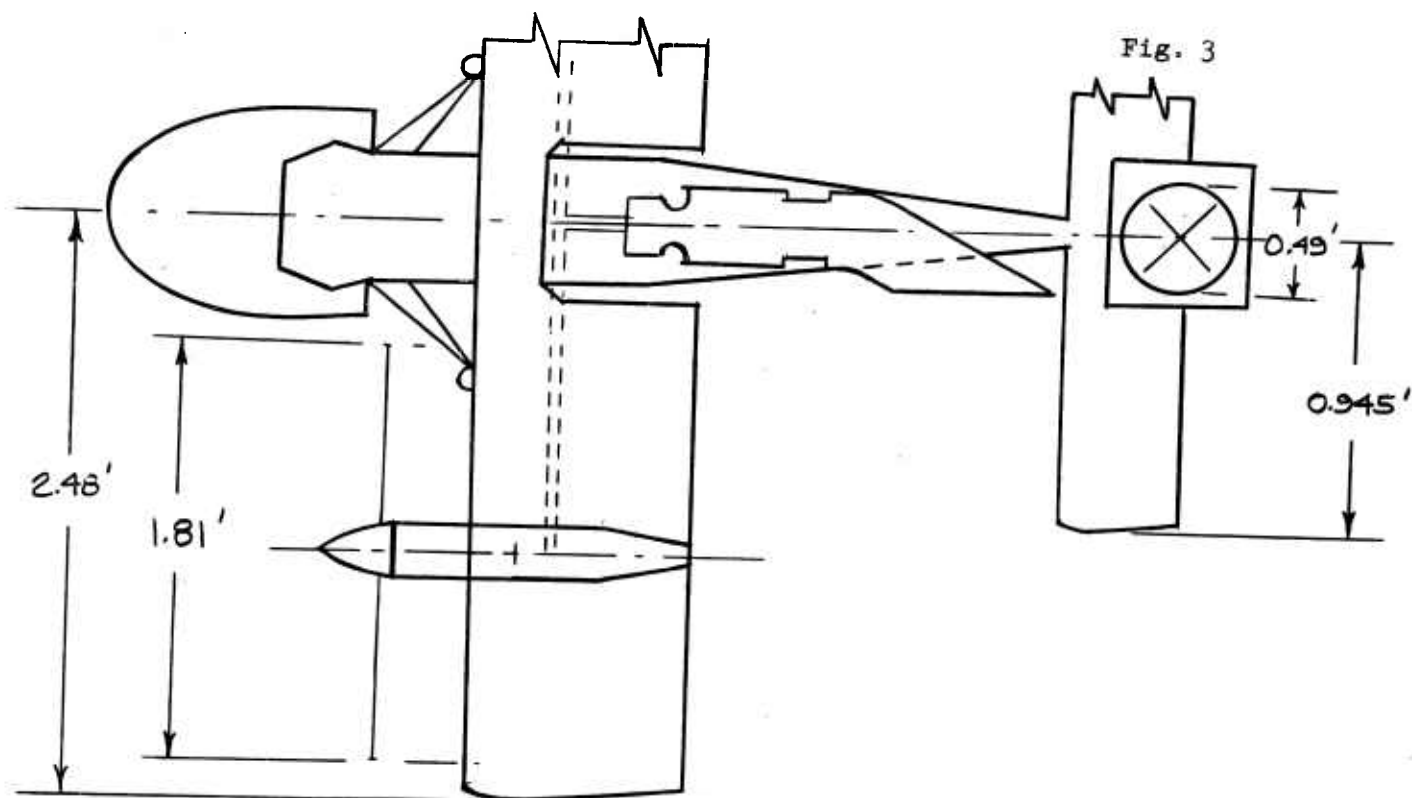


Figure 2
MODEL FOR ONE DEGREE OF FREEDOM TESTS



$\frac{1}{5.2}$ - SCALE MODEL

TABLE I
PHYSICAL CHARACTERISTICS OF MODEL
AND FULL SCALE AIRCRAFT

	$\frac{1}{5.2}$ Model (scaled up)	Full scale
Gross weight	3150 lb.	3150 - 3450 lb.
I_{yy}	2450 slug-ft. ²	2450 - 2680 slug-ft. ²
Ω	310 rad/sec.	\approx 310 rad/sec.
Center of	33.1% m.a.c.	33.7% m.a.c.
Gravity	11.2 inches below wing pivot	12.2 inches below wing pivot

General layout and model blade and hub characteristics are essentially identical to those of the full scale machine.

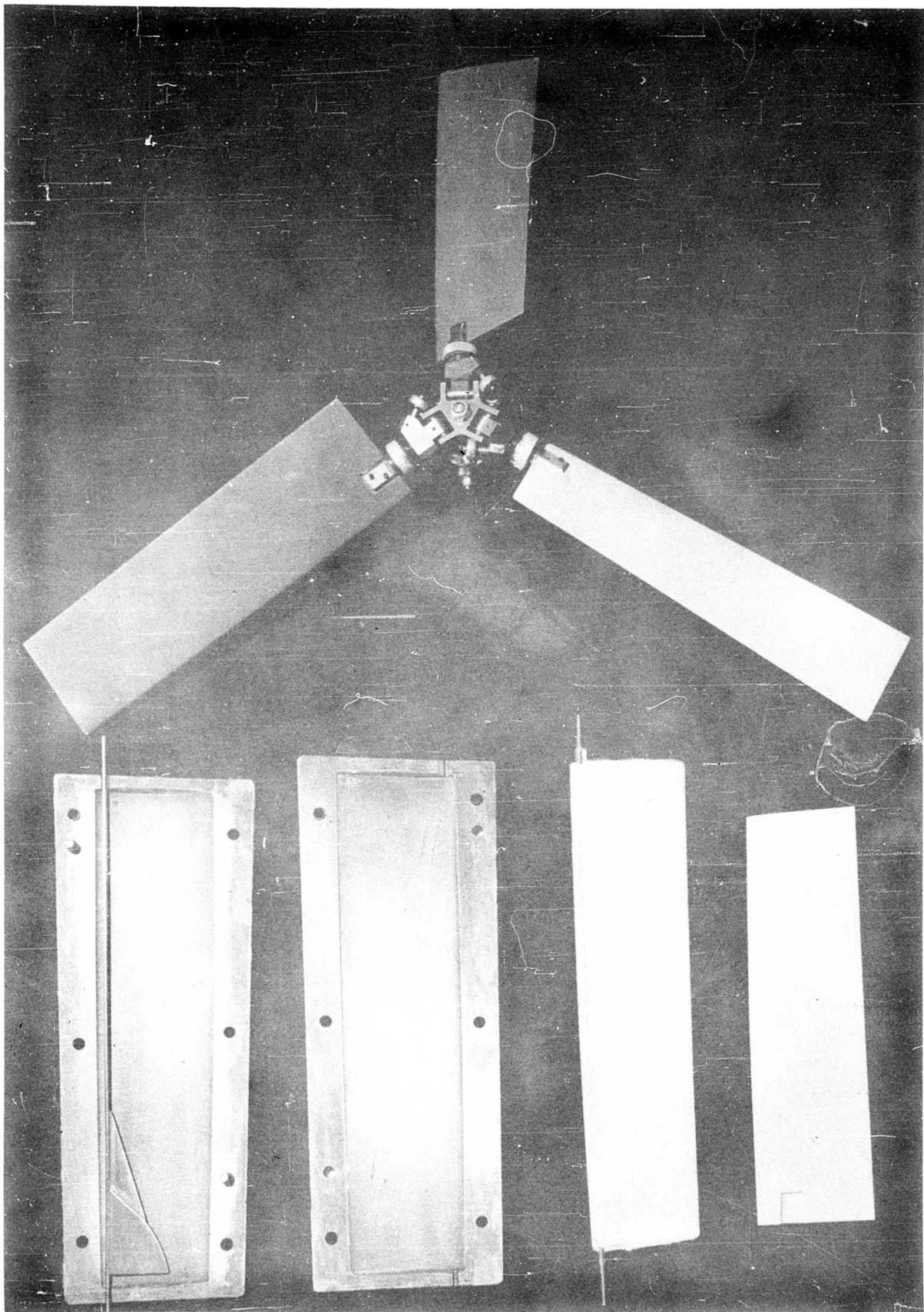


Figure 4
ROTOR BLADE CONSTRUCTION

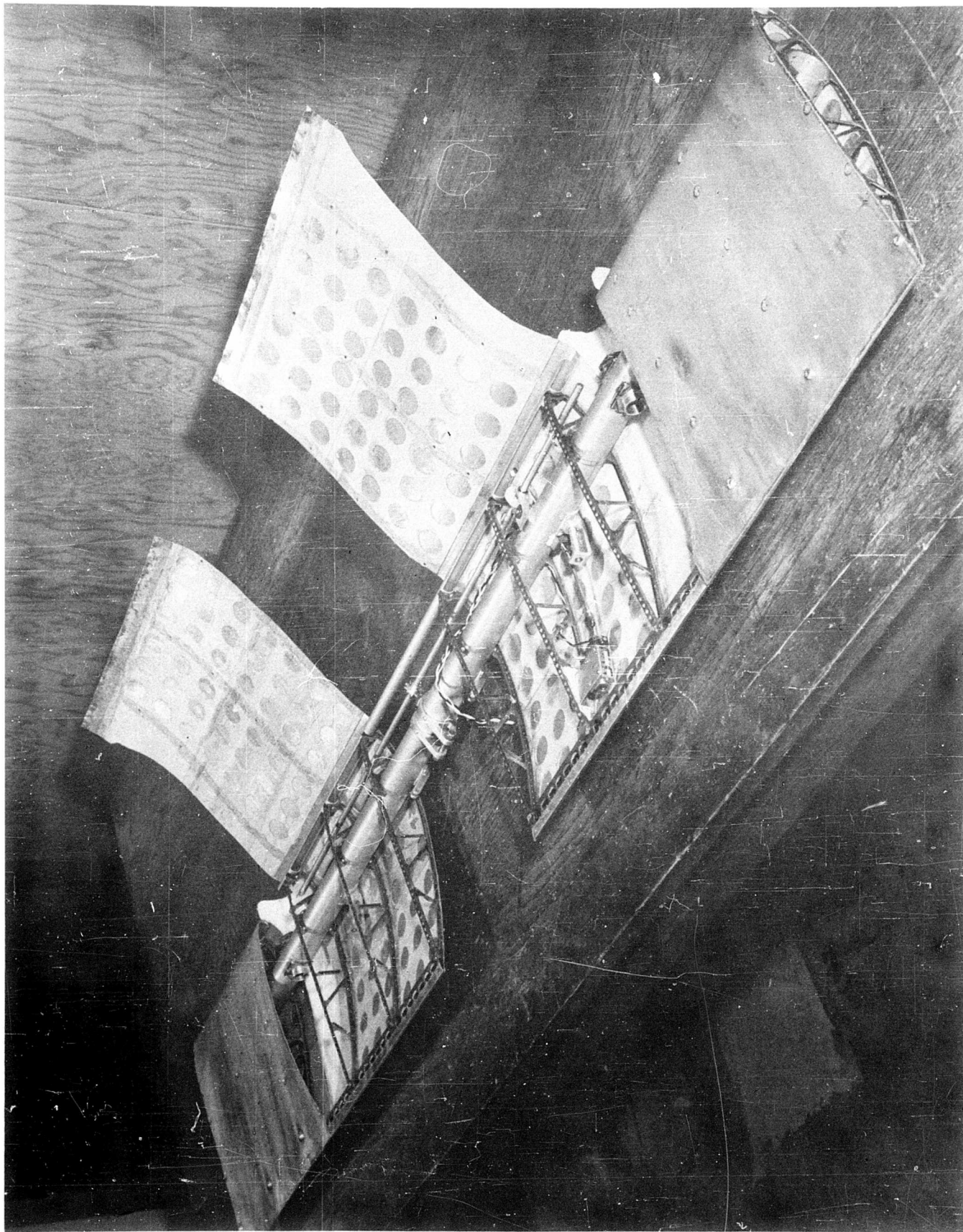


Figure 5
DETAIL OF WING CONSTRUCTION

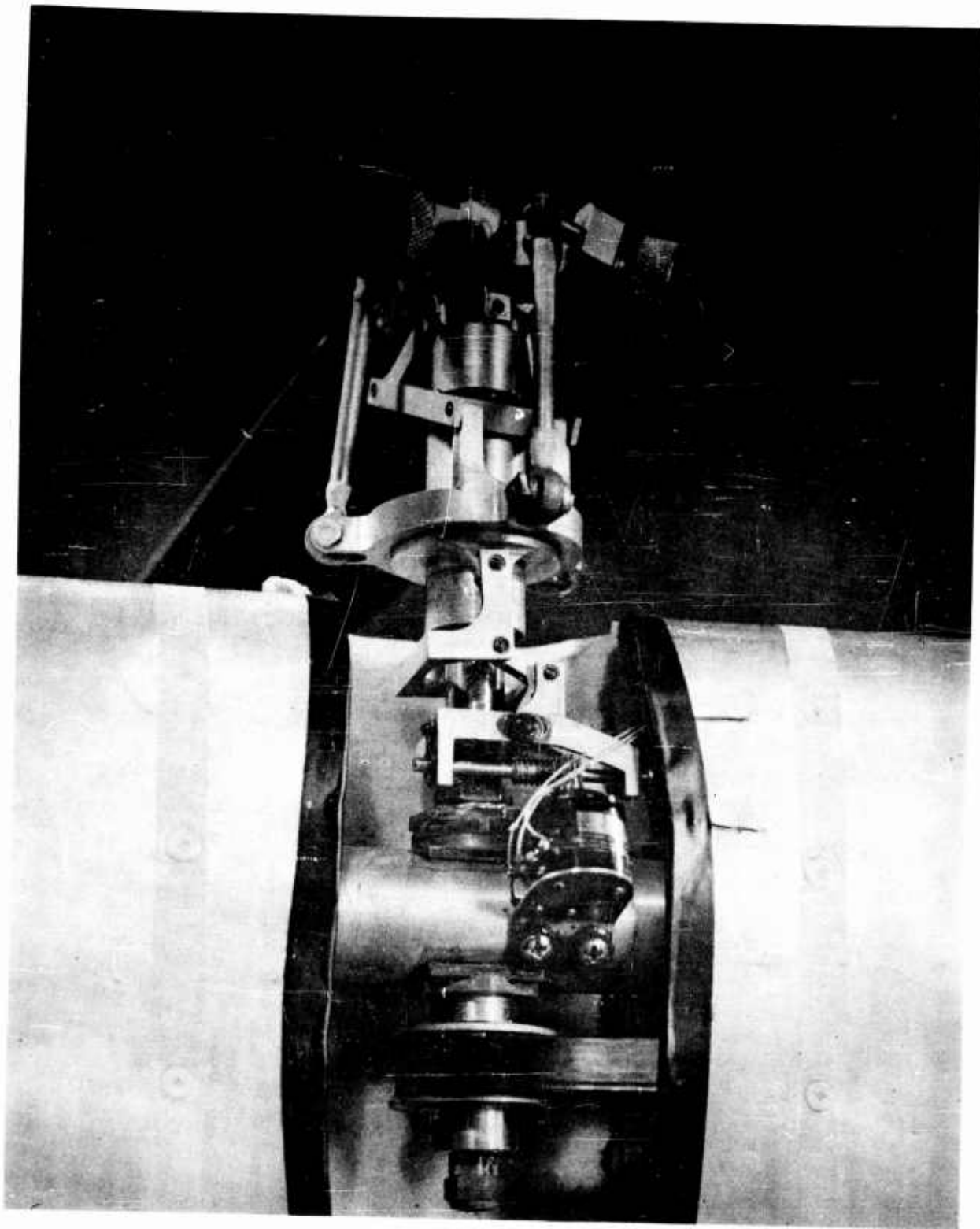
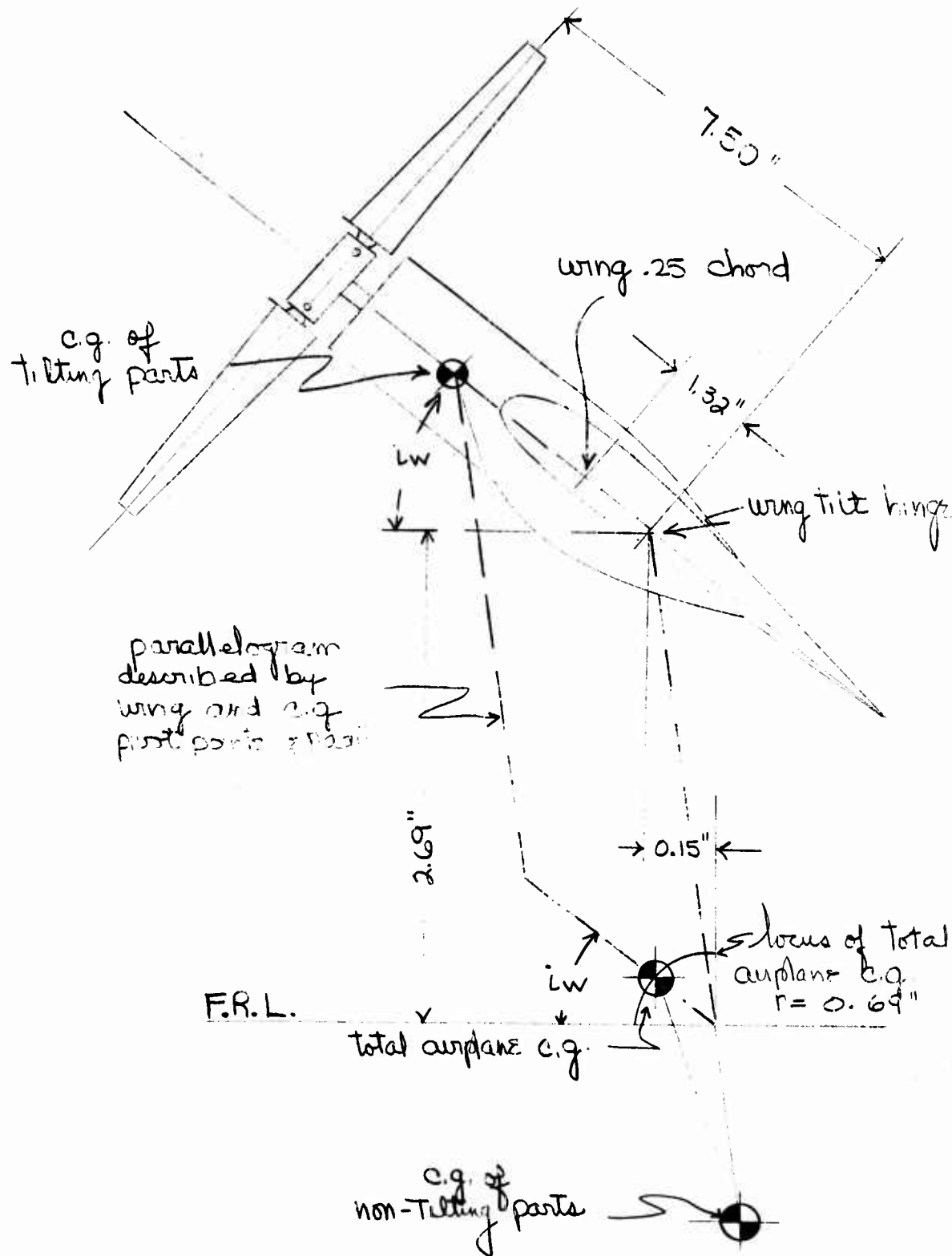


Figure 6
DETAIL OF COLLECTIVE PITCH ACTUATOR

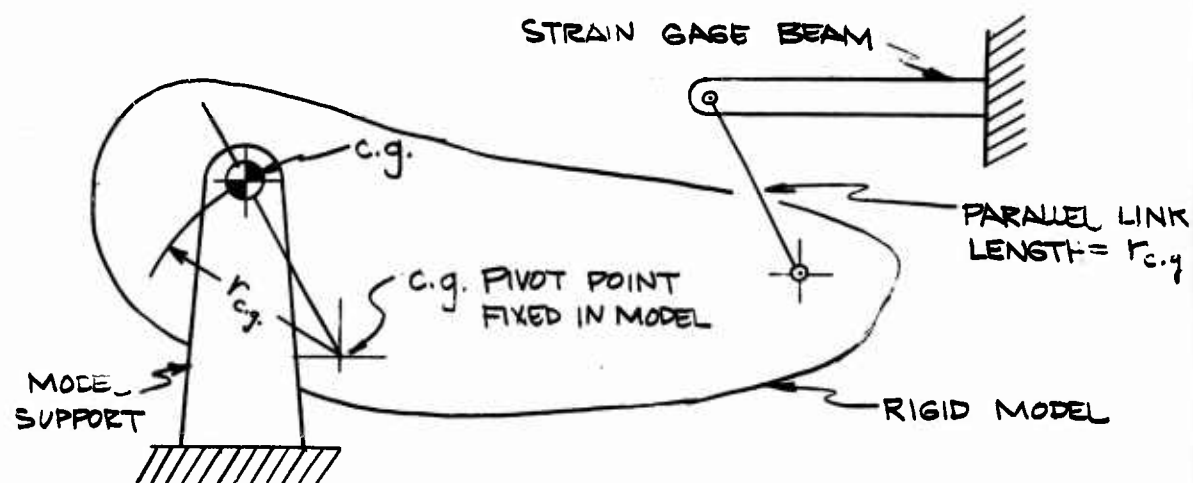


Figure 7
TAIL PITCH FAN AND SPOILER

Schematic of Center of Gravity Motion

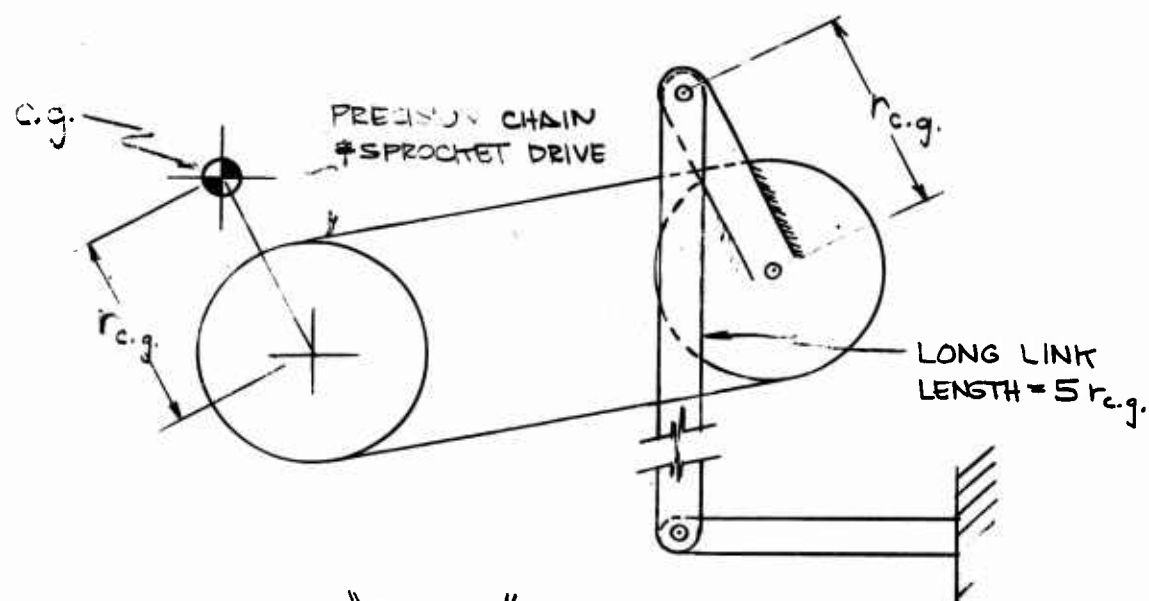


LINKAGES FOR PITCHING RESTRAINT



"PASSIVE" LINKAGE

FIGURE 9a



"ACTIVE" LINKAGE

FIGURE 9b

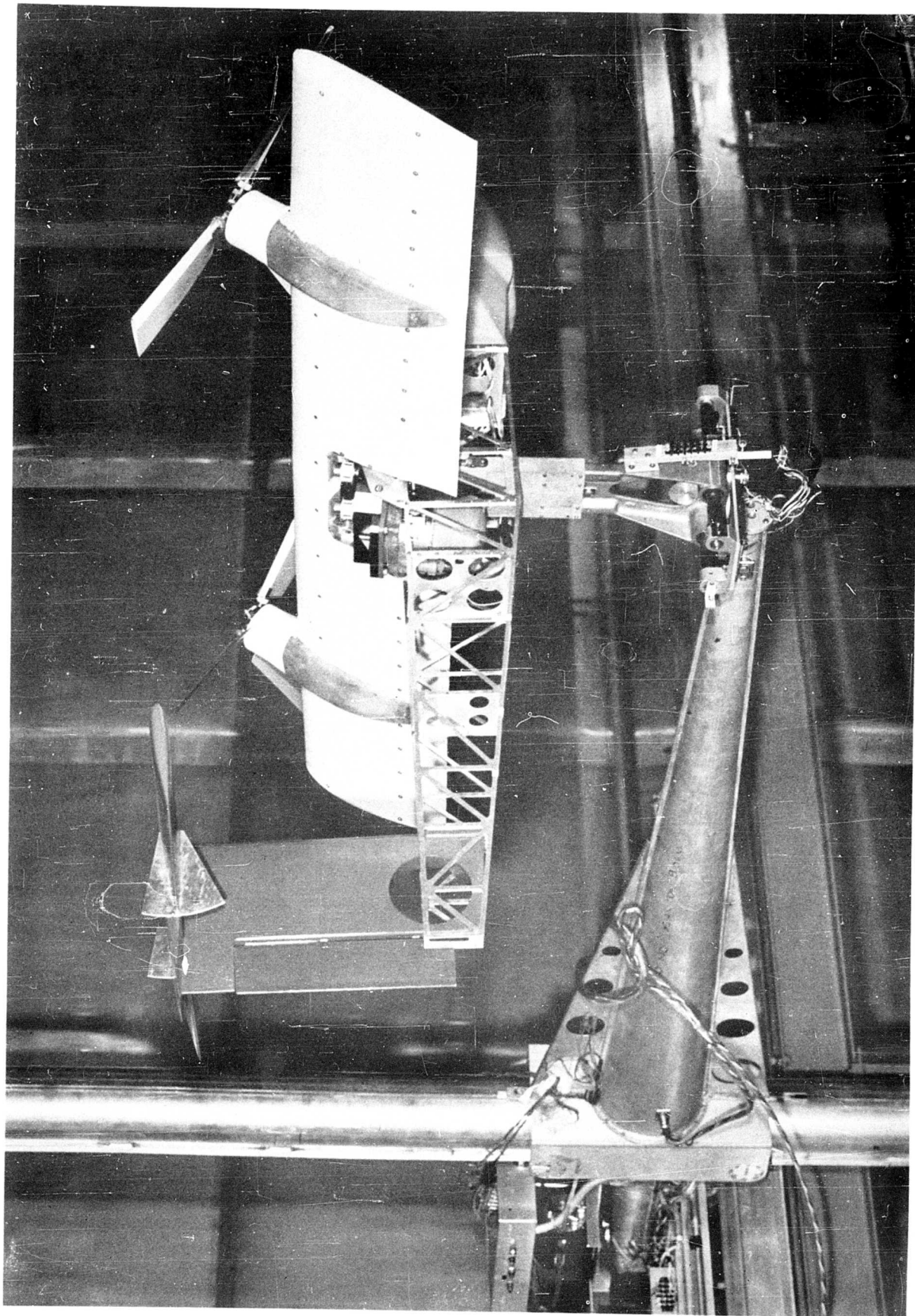
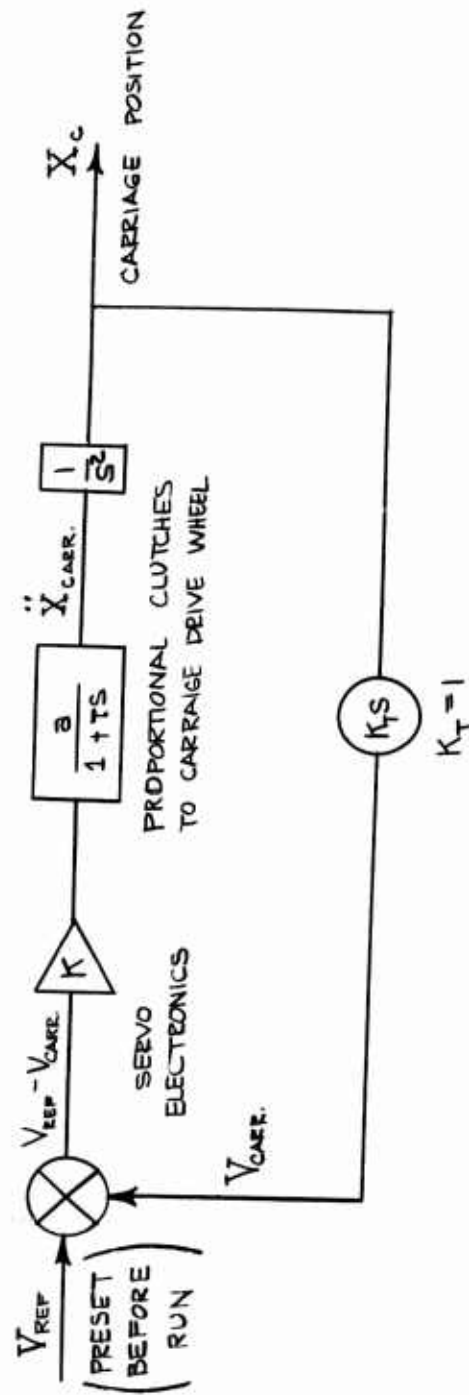


Figure 10
MAGNETIC CLUTCH CARRIAGE WITH STATIC TEST MODEL

MAGNETIC FLUID CLUTCH CARRIAGE



APPROXIMATE BLOCK DIAGRAM OF SERVOMECHANISM
FOR CONSTANT VELOCITY TESTS

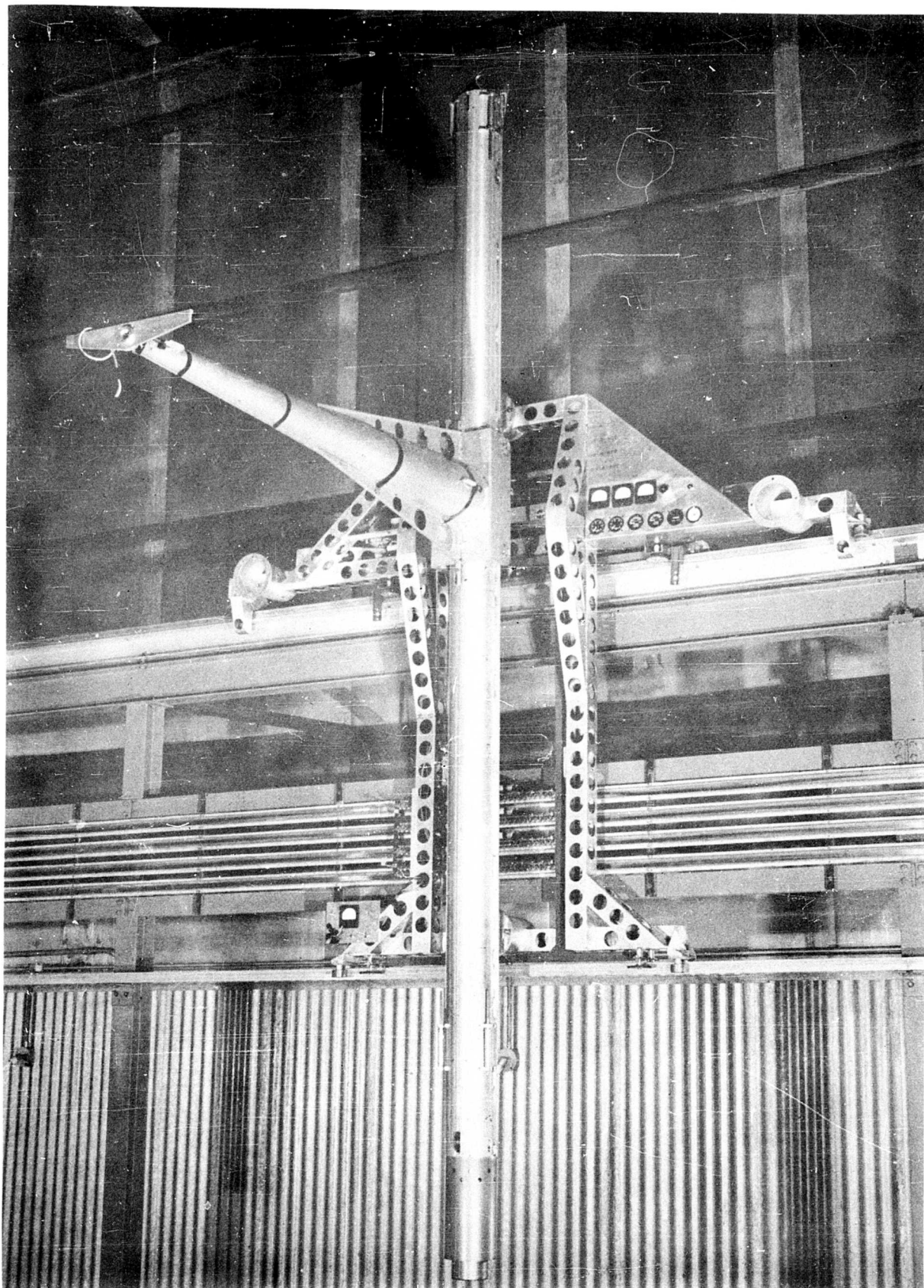
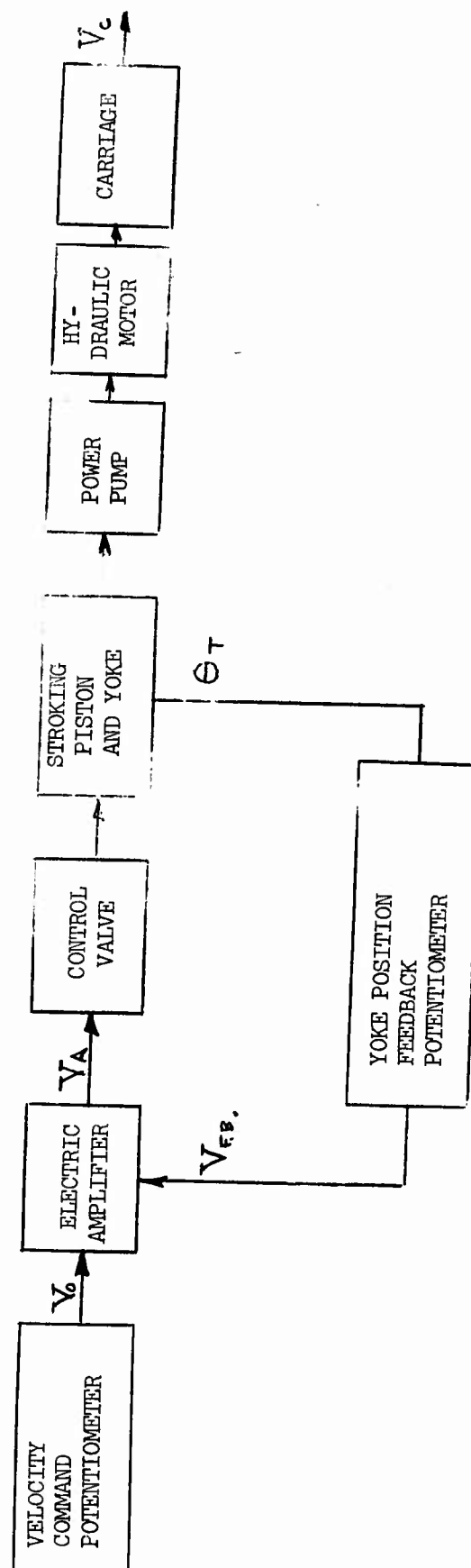


Figure 12
HYDRAULIC CARRIAGE



HYDRAULIC CARRIAGE VELOCITY SERVO SCHEMATIC

Fig. 13a

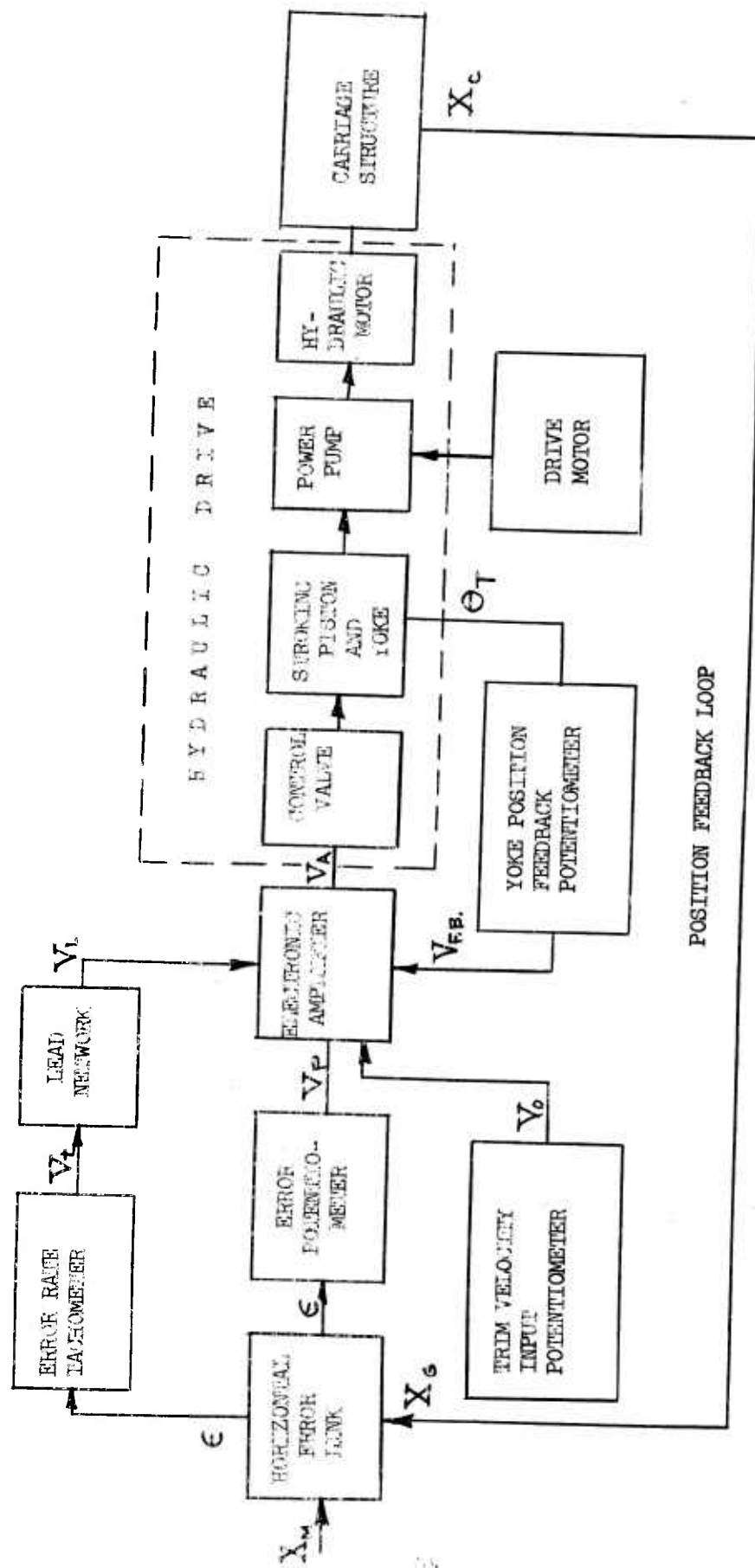


Fig. 13b

HYDRAULIC CARRIAGE HORIZONTAL POSITION SERVOMECHANISM SCHEMATIC

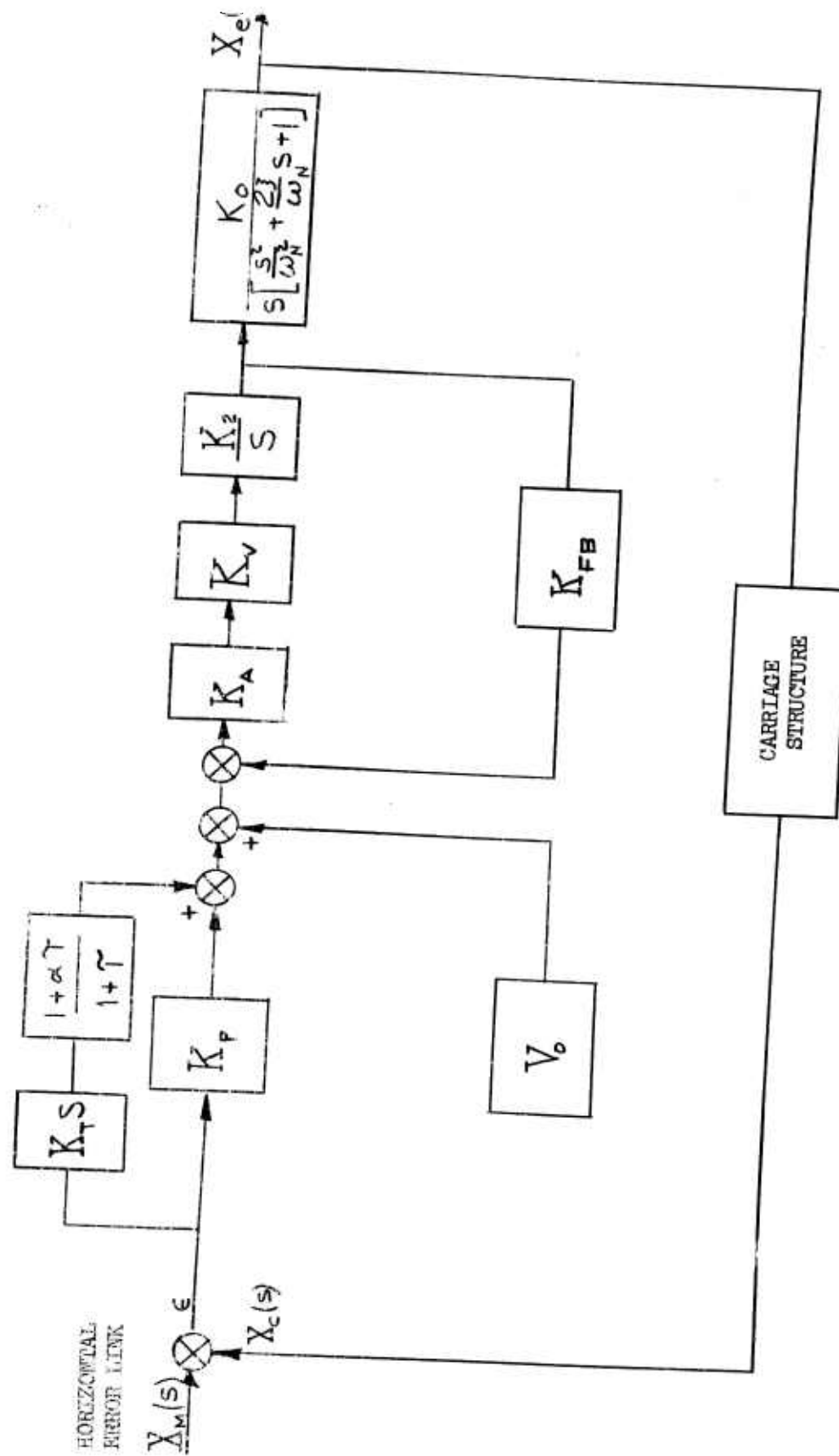
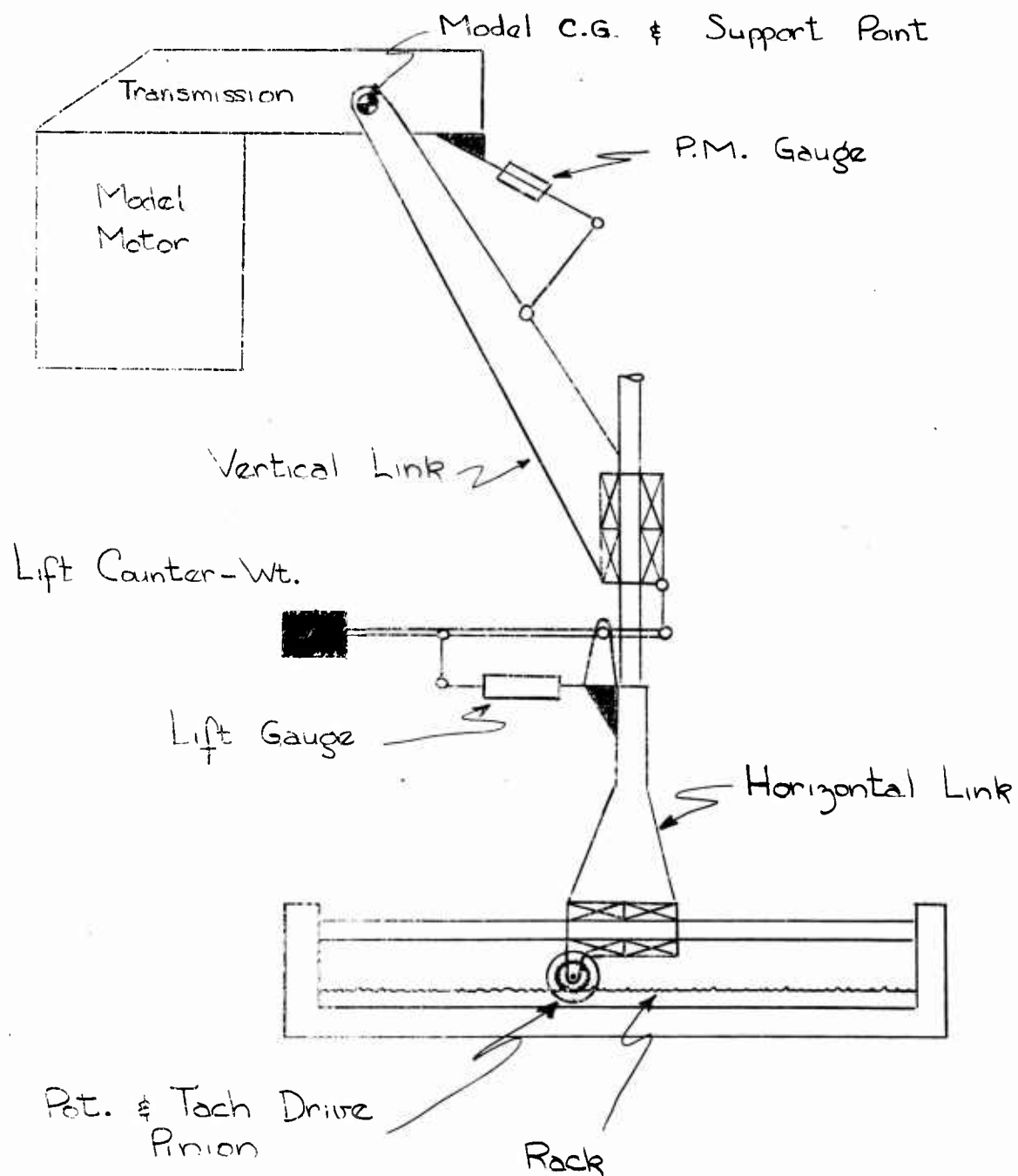


Fig. 13c

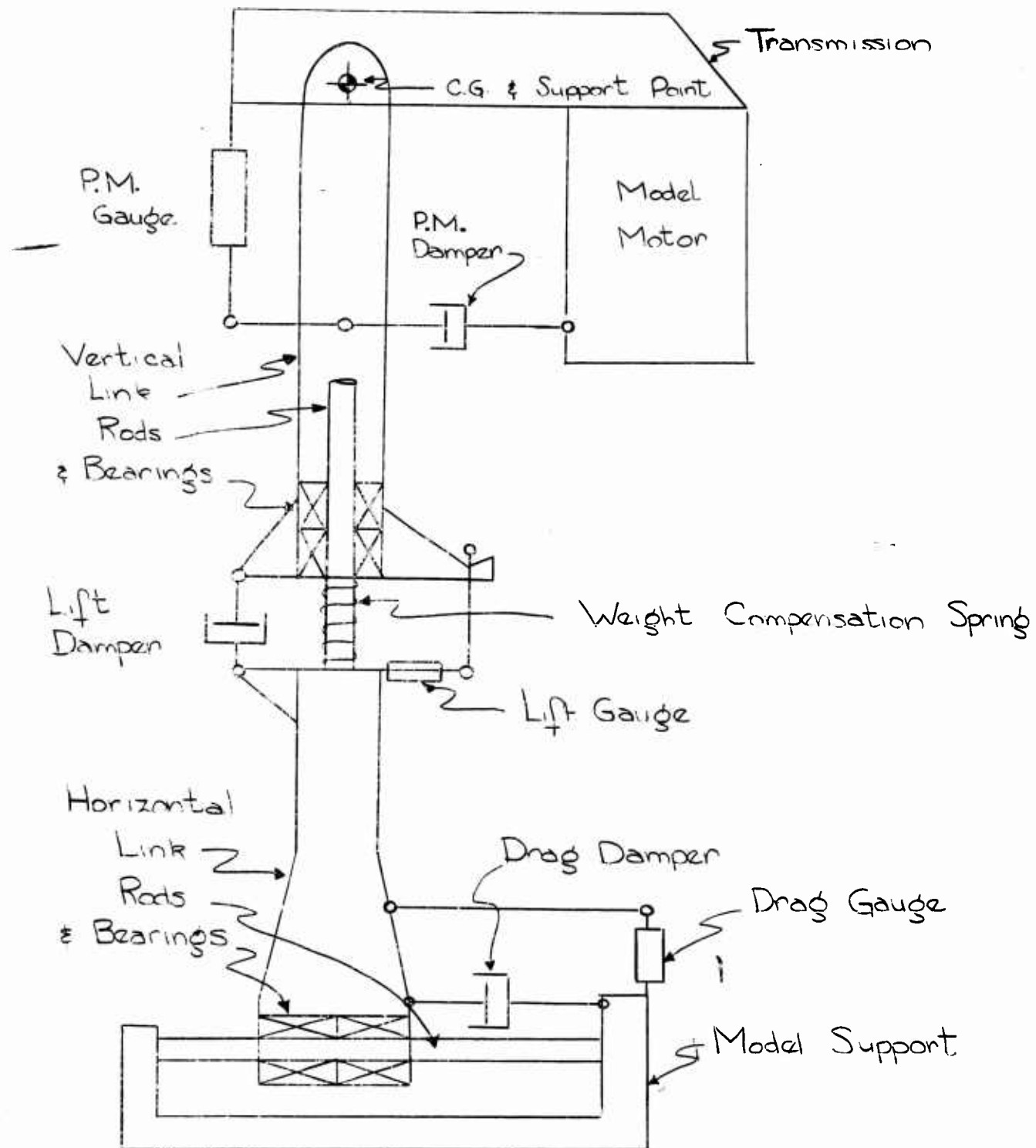
HORIZONTAL POSITION SERVO MECHANISM - TRANSFER FUNCTIONS OF THE VARIOUS COMPONENTS

Fig. 14

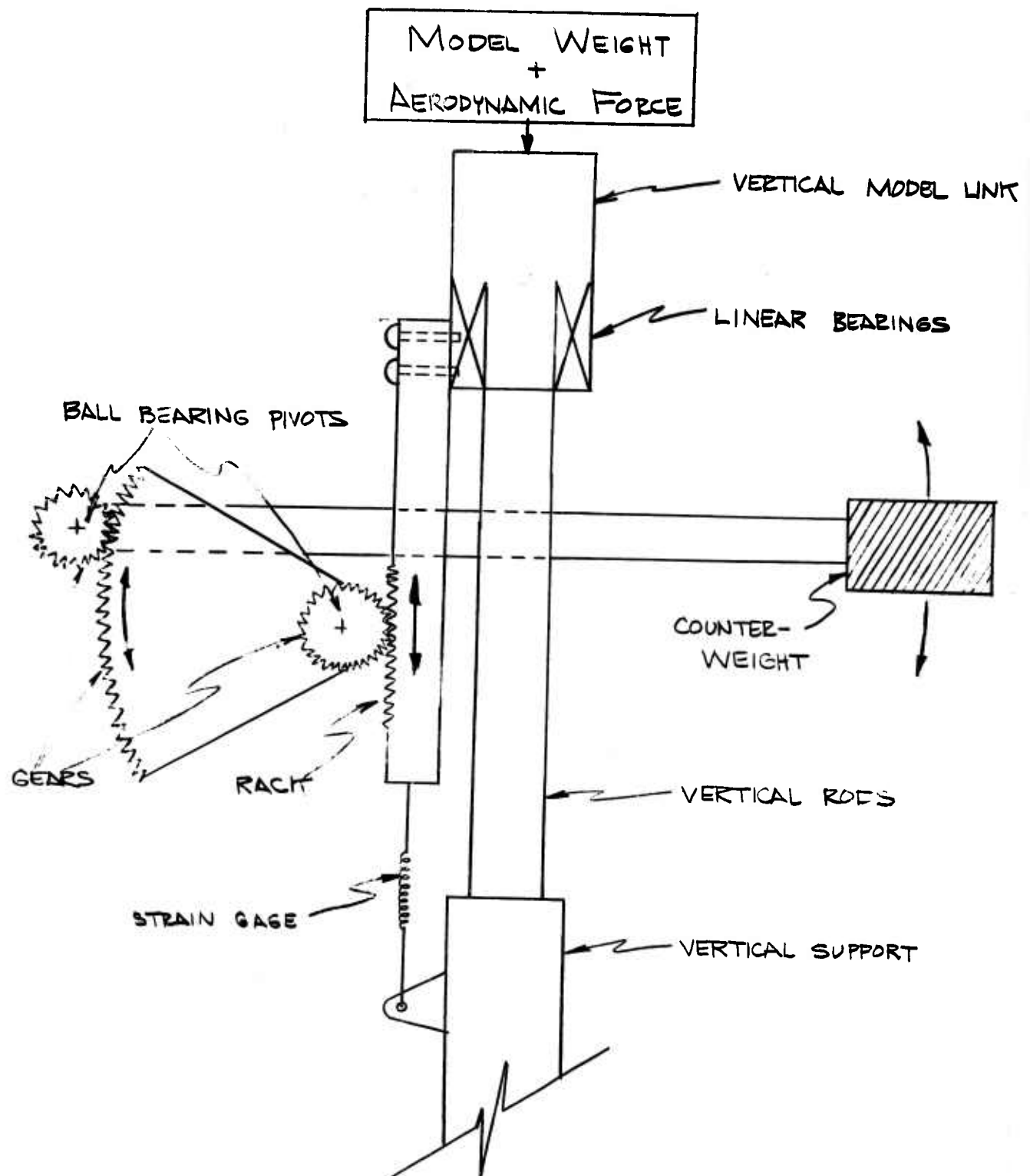


SCHEMATIC OF ONE DEGREE OF FREEDOM
TEST INSTRUMENTATION

Fig. 15



SCHEMATIC OF STATIC TEST INSTRUMENTATION



SCHEMATIC OF ONE-DEGREE-OF-FREEDOM

VERTICAL FORCE INSTRUMENTATION

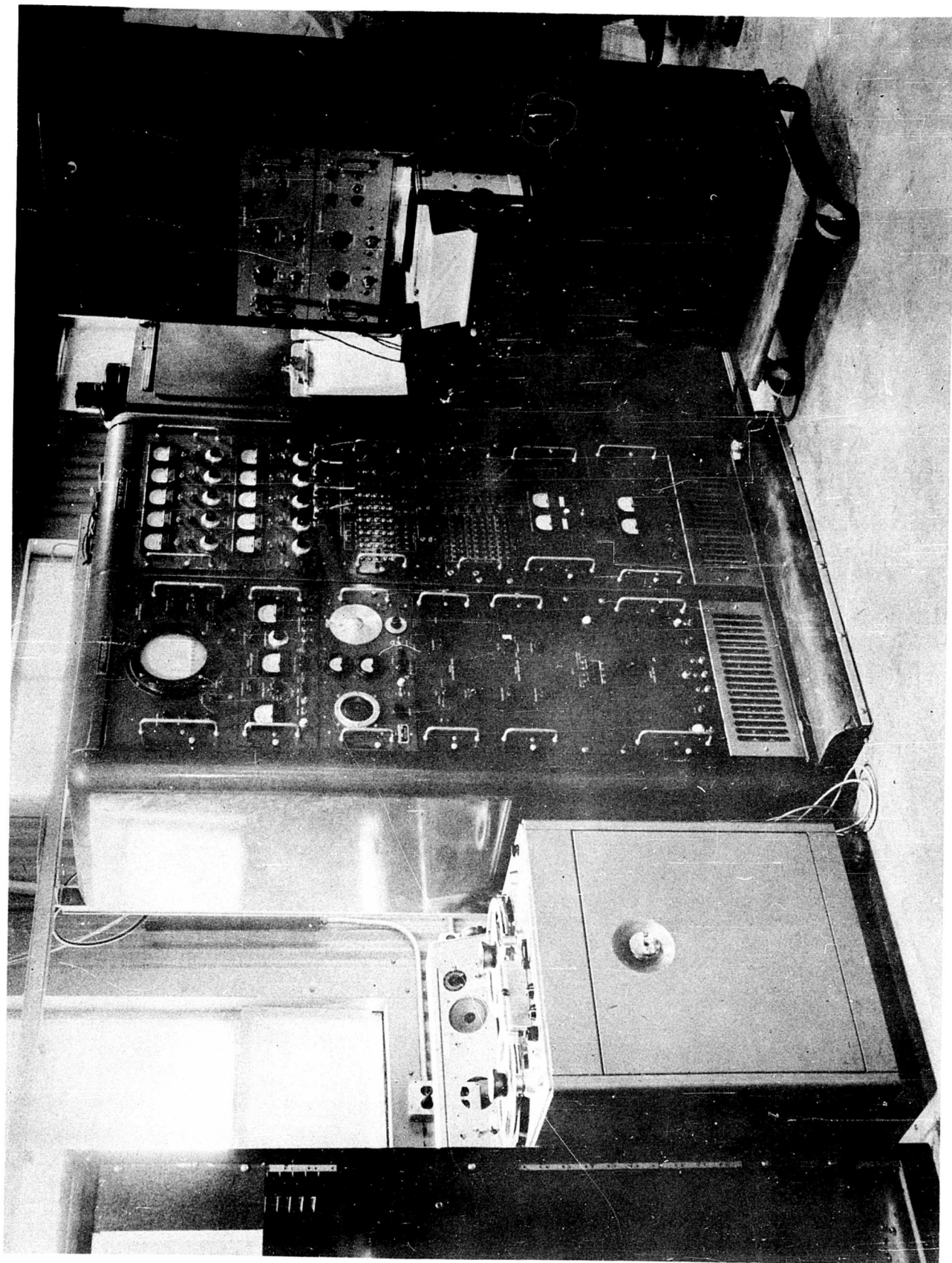


Figure 17
DATA RECEIVING AND RECORDING EQUIPMENT

CONCLUSIONS AND RECOMMENDATIONS

TEST EQUIPMENT

Considerable experience was accumulated in the static and 1-D/F tests concerning the operation of the equipment used. More important, however, is the information obtained about the suitability and adequacy of the existing equipment and the determination and possible solutions of particular problems associated with this equipment. In this respect the tests considered were unqualified successes.

In a novel and flexible Facility such as the Forward Flight Facility, it is always difficult to determine absolutely the suitability of the various components for the tasks that might be expected of them. However, the ability of the equipment to perform particular functions can be assayed and a fair evaluation determined. The following conclusions and recommendations are concerned with the performance of the test equipment in accomplishing static and 1-D/F longitudinal dynamic tests.

- 1) The hydraulic powered carriage used in the 1-D/F tests is completely adequate for all static and dynamic tests anticipated for the Forward Flight Facility.
 - a) All problems encountered with the magnetic clutch carriage used in the static tests were completely eliminated with the advent of the hydraulic carriage.
 - b) The capabilities of the hydraulic carriage in the performance of dynamic tests were demonstrated in the 1-D/F tests to be entirely sufficient.

- 2) The tilt-wing model used was an accurate simulation of the full scale aircraft and possessed all the necessary features required for dynamic similitude. No vibration problems were encountered in the drive or rotor system, and a minor change in rotor fabrication technique eliminated problems associated with providing blade twist.
- a) Of primary importance in the fabrication of models such as the one under consideration is obtaining a rigid light-weight structure. This was successfully accomplished in the modified model used in the 1-D/F tests.
 - b) Provision of powered model controls is an enormously time-saving feature, and should be incorporated wherever possible. It is an absolute necessity for the controls used to apply inputs in dynamic tests to be powered and to have very fast response.
 - c) The pitching moment restraint provided for the 1-D/F tests was adequate for the range of wing incidences tested, but was reaching its effective limits at the lower wing angles. A driven restraint similar to the one proposed in Figure 9 (b) is recommended for future testing in the complete transition envelope.
 - d) Serious consideration should be given to the problem of instrumenting the rotor shafts to measure rotor forces and moments independent of wing and fuselage contributions. Such instrumentation would provide valuable information in both static and dynamic testing programs.

- e) Little additional design or fabrication effort would be required to modify the present V-76 model to provide lateral and directional control. Addition of a yaw fan, rudder and differential collective pitch control should be considered to render the model suitable for 6 - degrees of freedom testing.
- 3) Several solutions to the problems of instrumenting the model with force measuring devices which would be insensitive to carriage-produced vibrational inputs were attempted in the two sets of tests. These attempts were met with varying degrees of success, but in both tests the strain gage instrumentation performance was adequate to allow all information to be read to within 4 per cent of the full scale value. Pitching moment readings were particularly noise-free due to model balancing and could easily be resolved within 2 per cent of the full scale telemeter.

It is felt that a complete solution to the problem of vibration noise could be achieved with a scheme very similar to that used on the vertical force gage in the 1-D/F tests. The undesirable static friction produced by the gears and bearings could be eliminated by the use of torsional spring pivots and lever arms. Any desired damping could be easily supplied at the geared up counter weight where the motions are sufficiently large and force requirements small. With such a system virtually any desired sensitivity and signal to noise ratio could probably be easily achieved in all force measurements.

- 4) The data link consisting of the ASCOP telemetering unit and Ampex magnetic tape recorder adequately accomplished the task of presenting and recording the test information. The flexibility of this system in recording and monitoring the test data as well as its automatic compensation feature proved to be valuable assets in conducting these tests. Use of the high-level coding system in the 1-D/F tests successfully eliminated the problems experienced in the static tests with excessive switching noise in the transmitted data.

PART II

TESTING TECHNIQUES AND PROCEDURES

TESTING TECHNIQUES AND PROCEDURES

Testing with a new and unique type of apparatus such as the Forward Flight Facility, requires development of new techniques, as well as new equipment. It is of primary importance that the testing techniques and procedures employed in conducting tests be compatible with the capabilities of the equipment used, and that improvements made in one area be complimented by advances in the other. Failure to accomplish contemporary development in techniques and equipment will inevitably result in inefficient if not ineffective operation. It is the purpose of this section to discuss the testing techniques and procedures used in the tests under consideration, and to indicate the difficulties and limitations encountered. More importantly, recommendations are made to the end of eliminating some of these shortcomings, not only for the types of tests considered herein, but also for future tests anticipated for the Facility.

The static tests discussed in this report were conducted by measuring the steady longitudinal forces and moment acting on a model moving at constant velocity and attitude through still air. The major variables considered in these tests were horizontal velocity and model pitching attitude, or since vertical velocity was not allowed, angle of attack. In conducting tests of this nature on a powered model of a full scale aircraft, it is desirable that the flight conditions considered be within the flight envelope of the actual aircraft. In particular, it is important that the variations made in the flight parameters in order to obtain static derivatives be referenced to an actual

scaled trim condition. Obtaining the trim condition involves scaling not only forces, moments and velocities, but also the rotor operating conditions. Accurate model design and scaling as discussed in Appendix C automatically achieve the necessary relations of rotor operating conditions provided the trim conditions are arrived at properly. The method used in the static tests was to assume that the rotor operated at essentially constant rotational speed and to accomplish trim changes by varying rotor collective pitch. Careful choice of gearing in the model rotor transmission allowed the above aim to be achieved without adjusting the excitation voltage on the model rotor.

A very laborious and time-consuming process was required to determine the actual trim condition for any given wing and fuselage attitude. The procedure followed was to set wing incidence for the particular condition to be examined, fix the fuselage attitude at $\alpha_f = 0$, and make repeated runs, adjusting rotor collective pitch and carriage velocity until vertical force equalled the desired model gross weight and net drag equalled zero. Since in-flight control of collective pitch was not provided, this iterative process proved to be quite inefficient and required from four to ten runs to establish a trim condition. Once the trim condition was established, repeated runs were made varying fuselage attitude at constant velocity, and varying velocity at $\alpha_f = 0$. Each individual run produced one set of values of L, D and M as plotted in Figures 21 through 27. A power-on zero-velocity point was taken at the beginning and end of each run, the resulting values being presented in Figure 20. After the trim condition had been established and examined, runs were made to determine an

accelerated "trim" condition. For these cases the wing incidence, fuselage attitude and $L = W$ were kept constant, but an unbalance in longitudinal force was allowed simulating the airplane in some phase of transition. This was accomplished by setting the carriage velocity above or below the zero drag trim value and adjusting collective pitch on successive runs until the vertical force condition was satisfied. The accelerated conditions sought were $D = \pm .25L$, but variations in the resulting values were allowed in view of the difficulties described above in the iterative process. In all cases, however, the resulting accelerated condition closely approximated an actual condition to be encountered in some phase of full scale transition. A procedure identical to that followed in the trim cases was employed to investigate the variations in model forces about the accelerated trim condition established.

Changes in air density due to atmospheric condition variations exerted little influence on the ability to maintain trim conditions once established. Obviously large changes in density would have caused rotor thrust variations sufficient to destroy the $L = W$ trim, however, effort was made to complete the testing of any trim condition quickly enough so that no significant variation in atmospheric conditions could occur. Day to day variation in pressure and temperature were recorded, and all data was corrected to standard conditions.

Execution of the 1-D/F tests involved far simpler procedures than those required for the static tests. The basic change of allowing the model to assume its own flight condition greatly reduced the testing complexities involved, as the only prerequisite to running was the

establishment of hovering trim. Addition of remotely controlled collective pitch and wing incidence adjustments allowed hover to be attained very quickly at the beginning of each run.

Once hover had been established, the carriage positioning servomechanism and the wing tilt drive motor were set into operation. As the wing was driven downward from the hovering condition at constant collective pitch, the model accelerated and the carriage followed. Model vertical force and pitching moment were measured by the restraining strain gage beams and recorded on the ground. Runs proceeded in this manner until the wing reached a lower limit switch which was preset to either stop or reverse the motion of the wing. Repeated runs were made in both conditions, the wing being set to stop or reverse in various positions during its travel. Following the cessation of wing motion, the model was allowed to decay to its natural horizontal trim speed, which, in the case of a wing-tilt reversed run, was the hovering condition previously determined and marked by an upper limit switch.

The only difficulty experienced in the actual testing procedures followed was associated with the rotor downwash recirculation in hover. Previous experience with this phenomenon had been encountered in the tests discussed in Reference 2, and a similar solution was applied. A downwash deflector was provided to divert the rotor slipstream along the longitudinal axis of the building and so delay the inception of its effects. The primary effect noted with the VTOL model was a gradual decay in rotor thrust due to increased inflow. This effect was more pronounced on the VTOL model than on the helicopter model of Reference 2,

probably due to the higher induced velocities associated with the higher disk loading. Associated with the lower mass flow but higher velocity downwash of the more heavily loaded VTOL rotor was a slight decrease in the time required for the effects to become manifest along with a relative decrease in recirculation energy due to dissipation in the higher velocity flow. With the deflector in place, hovering times of the order of 20 seconds were permissible without noticeable recirculation effects.

CONCLUSIONS AND RECOMMENDATIONS

TESTING PROCEDURES

The testing techniques discussed proved to be satisfactory and adequate for the successful completion of the desired test objectives. Of notable significance is the demonstrated ability to conduct steady-state force and moment measuring investigations in the low speed flight regime. The important requirements of steady and undisturbed flow conditions necessary for such tests were easily satisfied by the technique of moving the model through still air.

Real scale-time transitions were conducted with little effort and no requirement for providing in-flight control of the model. This is a very important consideration, in that exact quantitative measurements of the aircraft behavior were made without the effects of extraneous control inputs. The difficulty encountered with hovering recirculation was satisfactorily dealt with, provided hovering times were kept sufficiently brief. It is important to note that this phenomenon was not a wall or ground proximity effect, but rather was associated with the availability of a finite supply of undisturbed air within the confines of the building.

Although the desired ends were attained with the testing procedures employed, considerable improvements and modifications can be recommended concerning the means by which the test objectives were achieved. The recommendations that follow should be considered to be applicable not only to the types of tests considered herein, but also to other types proposed for the future.

1. Worthy of primary consideration are improvements in the methods of determining model trim conditions. For this purpose it would be extremely advantageous to provide inflight control of the model collective pitch and possibly the moment trimming control. With these provisions, it would be possible to use the following capability of the carriage positioning servomechanism to allow the model to establish its own trim velocity, while the vertical trim is made through collective pitch adjustments. An interesting corollary to such a scheme would be to provide a constant-altitude autopilot operating on the collective pitch adjustment. Any combination of model vertical acceleration, velocity, or position could be readily sensed and used as a signal to a simple feedback network to control altitude, and little difficulty is anticipated in achieving stability so long as the model is restrained in its pitching freedom. With such a system in operation, complete longitudinal trim could be established in one run with the additional capability of ground monitoring and control of aircraft pitching moment. The trimming capability provided would be in operation only during preliminary runs and would greatly reduce the number of runs required to achieve trim for both static and dynamic testing.

2. Once model trim has been established, considerable time could be saved in the actual performance of static tests through the use of programmed runs. Using this method would involve providing a programmed control of carriage velocity so that the actual run would consist of a staircase velocity profile with as many as five different steady velocities examined. A simple stepping switch in the inner-loop control setting, V_0 , would cause the carriage to travel at velocities

which are specified increments above and below the previously determined trim velocity. In this manner one run would provide all the required information on the change of variables with velocity about the trim condition. Similar runs could be made at various fuselage attitude settings, thereby providing a complete investigation of the significant static derivatives about a trim condition in a minimum number of runs.

3. The problem of downwash recirculation is not of significant importance except perhaps in experiments requiring long and precise measurements of aircraft behavior in the hovering condition. Transient oscillations of models about the hovering condition are not seriously affected by this phenomenon, in that the rotor mass flow demands are distributed through a large volume of the building due to the translational excursions of the model. However, experiments intended to examine the actual free-air, but in ground proximity, behavior of an aircraft hovering for extended periods would require provisions for an unlimited supply of undisturbed air. Such a requirement could probably be easily satisfied by venting the upper portions of the track enclosure, and allowing an outside exhaust of the downwash at floor level on the sides of the building. In such a system consideration should be given to the possibilities of gust interference from outside wind conditions, and proper baffling would be a necessity.

PART III
EXPERIMENTAL AND THEORETICAL
PRESENTATION AND ANALYSIS

EXPERIMENTAL DATA REDUCTION

PRESENTATION AND ANALYSIS

The experimental data gathered in the tests under consideration are presented on pages 71 through 89 of this report. The first two sets are the direct results of the static and 1-D/F tests, while the last group is an extrapolated presentation of trim conditions obtained from cross-plotting the experimental data. Static tests were conducted in the tail-off configuration only in order to eliminate the unknown contribution of stabilizer and pitch fan from the analysis of the wing and rotor effects. The tail lift and drag forces from these omitted parts would not greatly affect the trim conditions acquired, but their moment contributions would make a component breakdown very difficult. Test conditions were established so as to correspond to actual flight conditions of a full scale aircraft in trim and various phases of transition. This means that the accelerated and decelerated flight conditions at the same i_w as an unaccelerated condition do not occur necessarily at the same velocity, but rather keep constant vertical force or gross weight. This makes it impossible to evaluate directly the effects of acceleration in a partial derivative sense, but gives instead the total characteristics of accelerated flight conditions. The importance of such tests lies in the determination of the conditions of accelerated flight as a prelude to dynamic tests at a later date and in giving directly the character of the full scale machine in transition.

The static test results are presented in Figures 20 through 27 about both a wind and a body axis system; all the forces, moments, and velocities indicated are in the model scale as measured. It should

be noted that all forces and moments are resolved about an axis system with origin at the full scale aircraft's c.g., the position of which is a function of wing incidence. As depicted in Figure 8 the pivot point of the model is moved in such a fashion as to permit it to follow the c.g. shift as the wing rotates, thereby eliminating the necessity of an axis system transfer in the reduction of the data. This positioning, is not, of course, a necessity for static testing as axis transfers can be accomplished with little effort. However, dynamic testing requires that the model be suspended at its c.g. at all times and this model was designed for both types of tests.

The static data as presented has been corrected to standard conditions of atmospheric pressure and temperature, as well as for the angle of attack change due to finite deflection of the pitching moment strain gage.

Measured pitching moments in constant angle of attack runs where velocity is the variable, are somewhat in error depending upon the magnitude of M_{α} , the variation of the moment with angle of attack. These runs were made with constant angle of attack settings at $V = 0$ and no attempt was made to compensate for the spurious moment contributed by the α variation due to the 0.5°/feet - pound spring rate of the pitching moment beam, since M_{α} in most cases was of negligible magnitude. All static test data reduction and correction was carried out on an IBM 610 Digital Computer, following a standard program established for such data reduction. The L-D/F data reduction and correction was accomplished by transferring point by point readings from the recorder trace in per cent full scale to the desired plots with proportional

dividers. This proved to be a rather laborious procedure and one that could be profitably improved upon by processing the telemeter translator output in an analog computer .

A detailed discussion of the static data itself will be deferred until the theoretical developments have been discussed and some insight has been gained into the causes of the various effects. However, several points can be noted here pertinent to the interpretation of this data. The scales used in the presentation of Figures 20 through 27 are compatible with the accuracy of measurement of the various quantities. The apparent scatter in the α -varying points is due, in the most part, to mis-matching of velocity to the trim value. The curves are not faired, therefore, on the basis of average, mean, or r.m.s. value of the data points, but rather in such a manner as to show the variation of the quantity at the constant velocity indicated. Other scatter and difficulties in repeating points can be attributed to resolution of telemeter noise with the low-level telemetry system, carriage excitation of the unbalanced mass of the model, and in some instances, partial and intermittent wing stall. The first two effects are discussed in some detail on pages 28 and 22 of Part I, while the possibility of partial wing stall is considered along with the discussion of the theoretical development.

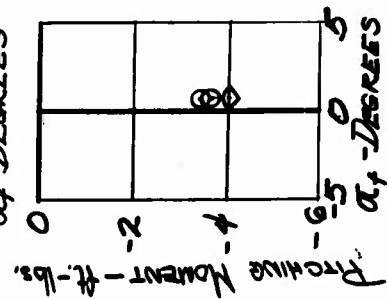
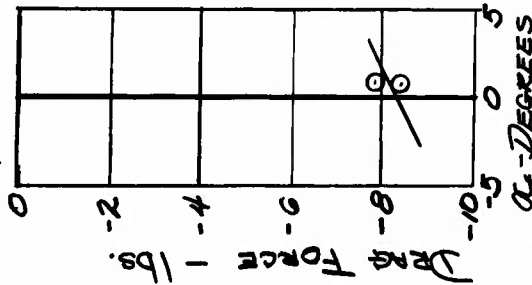
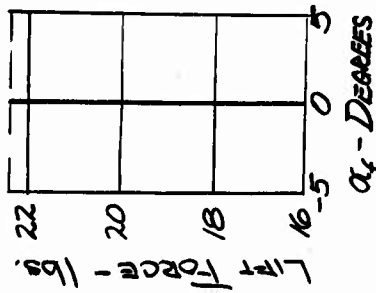
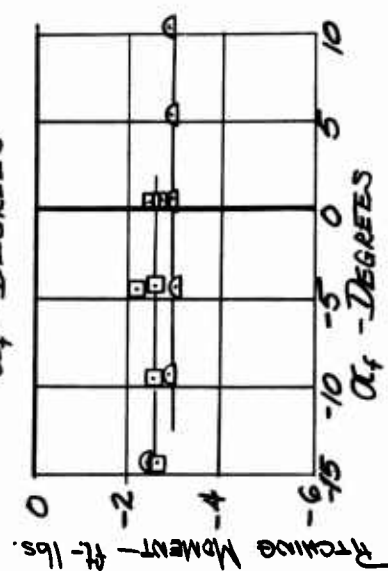
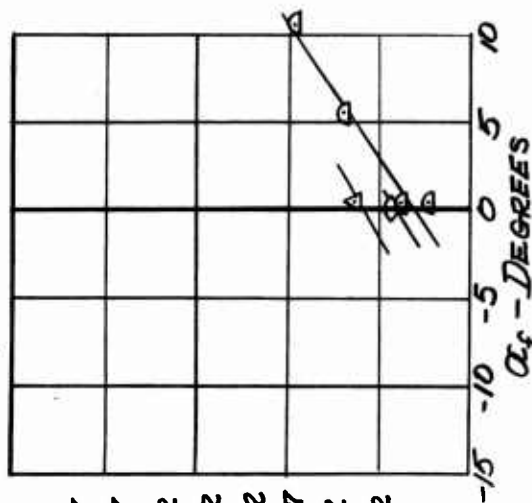
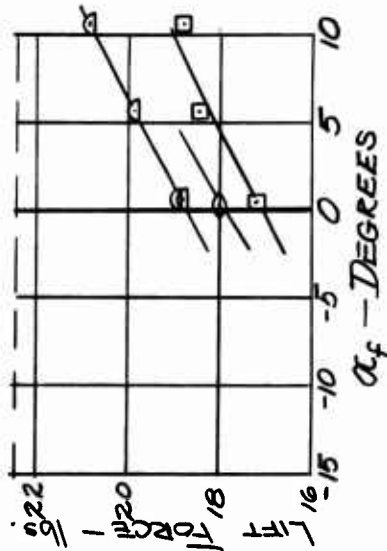
Some of the primary objectives in the 1-D/F tests were to evaluate new instrumentation, the hydraulic carriage, a high-level telemetering system, and the ability to conduct transition tests on the Facility. These various facets are discussed elsewhere in this report. Actually, the determination of particular information on this model

was considered secondary to checking out the above items and therefore only a few representative runs have been presented in Figures 28 through 33. In particular, it should be noted that the absolute magnitude of the lift values is somewhat in question due to the manner in which hovering lift was determined. In order to ascertain the gage reading when the model was lifting its own weight (hovering condition) a calibrated weight was hung on the counter-balance arm so the unloaded reading of the gage could be checked. Unfortunately, however, this resulted in quite large loadings on the support and pivot bearings in the counter-balance assembly, which would ordinarily not be present under operating conditions. The magnitude of static friction, even with shaking, in such a set-up was sufficient to produce as much as a one pound ambiguity in the "unloaded" reading. Another effect which caused errors in the hovering lift readings was the recirculation of the flow in the building which manifested itself in a gradual reduction of hovering lift with time. This effect was delayed by providing a slipstream deflection at floor level which deflected the slipstream along the major dimension of the building, rather than allowing it to recirculate around the sides. With the deflector in place hovering lift could be maintained for as long as 20 seconds before recirculation effects became apparent, but without the deflector maximum undisturbed hovering times were of the order of 10 seconds. Due to the exploratory nature of these experiments it was thought expedient to delay the tests until positive fixes of these phenomena could be achieved. Instead, they were written off as test results and as such are referred to at this point while their solutions are

discussed in other parts of this report. The general character and relative magnitude of the lift data retains its validity subject to the above-mentioned effects of local stalling and small effects of residual static friction in the counter-balance assembly.

Fig. 19

ZERO VELOCITY DATA

 $i_w = 44^\circ$  $i_w = 57^\circ$ 

0.75R
 ○ - 11.47
 △ - 11.97
 □ - 12.22
 ◇ - 13.22
 ○ - 13.72
 △ - 13.27
 ◇ - 14.72
 ○ - 15.22

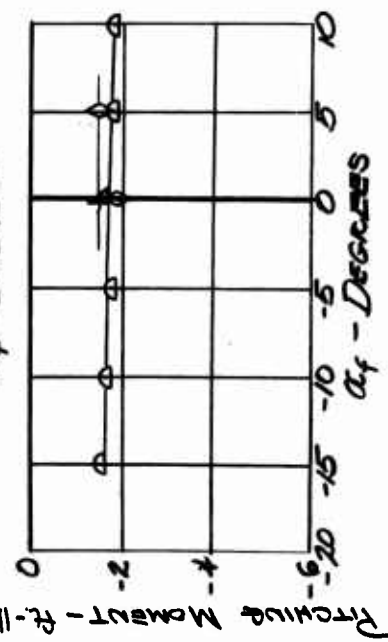
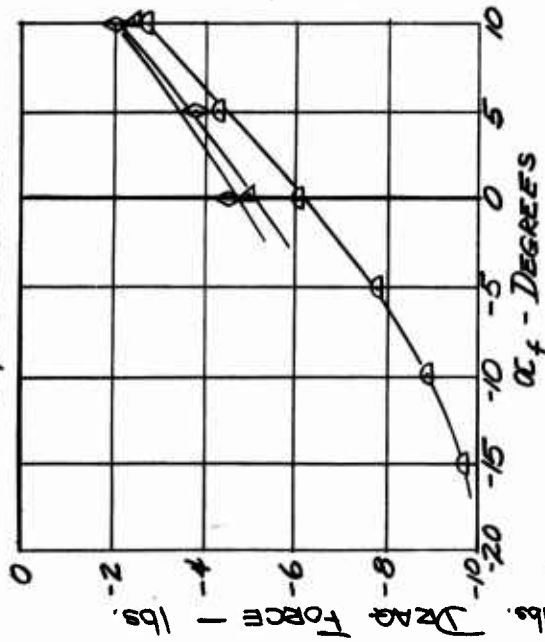
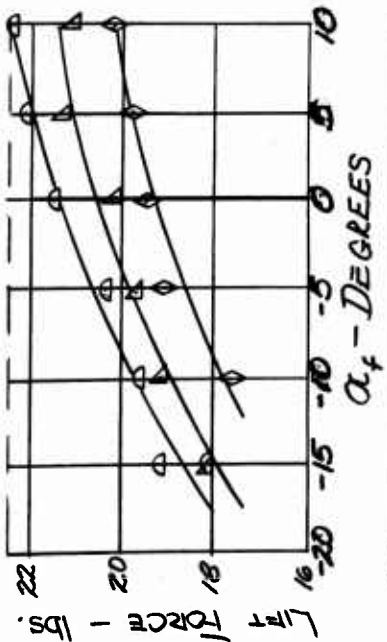
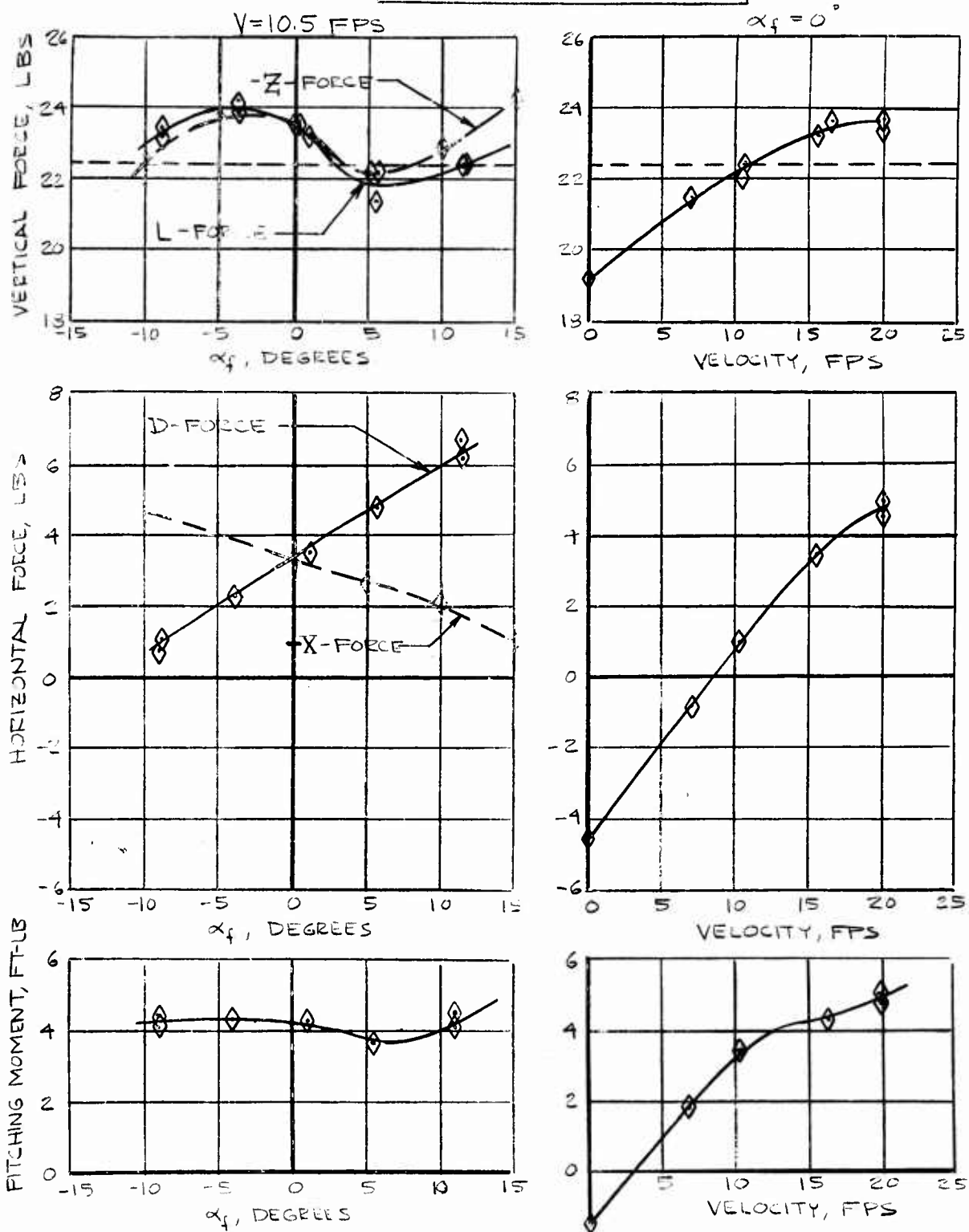
 $i_w = 70^\circ$ 

Fig. 20

$$\alpha_w = 70^\circ \quad \theta_{0.75R} = 13.22$$



Static Test Data

Fig. 21

Static Test Data

$$i_w = 70^\circ \quad \theta_{ATR} = 13.97^\circ$$

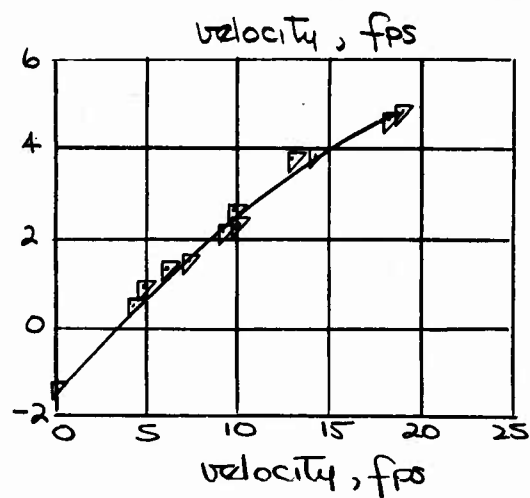
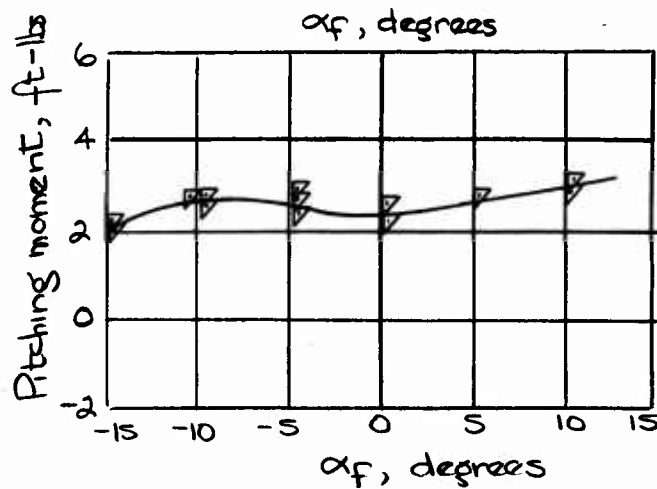
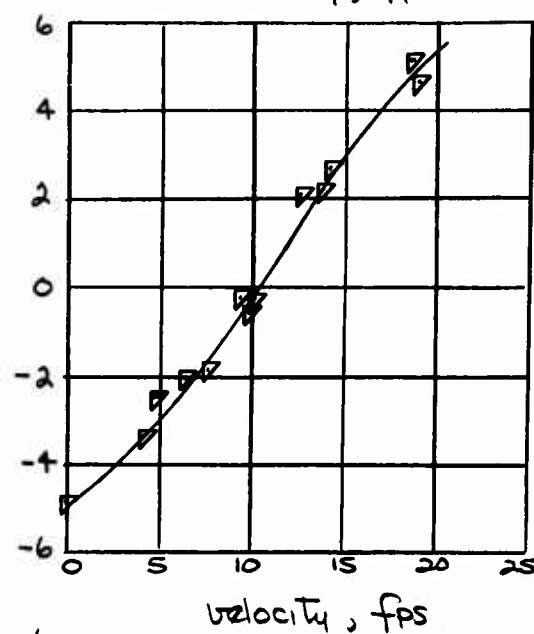
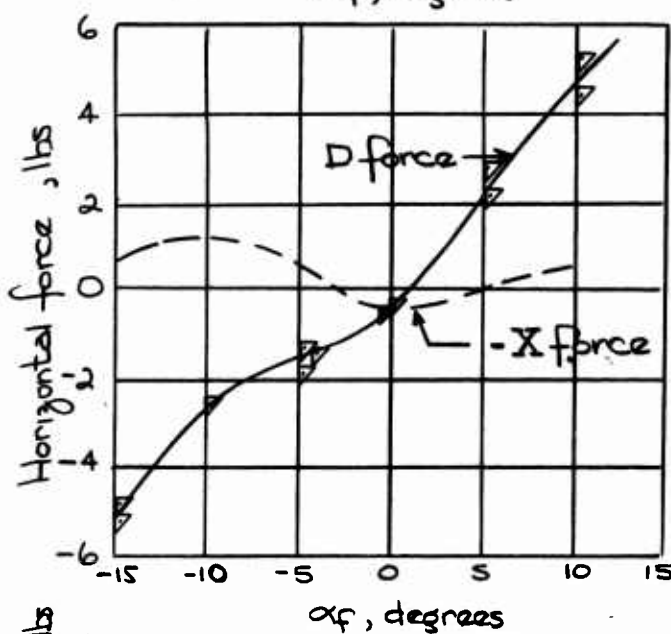
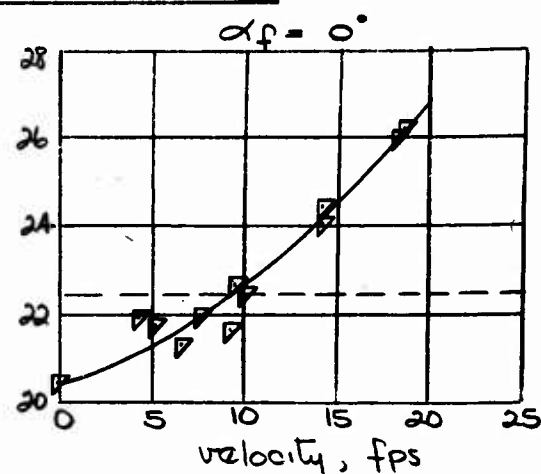
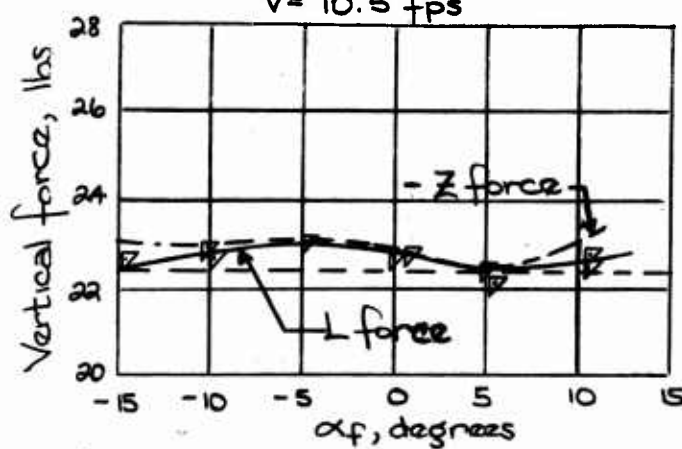
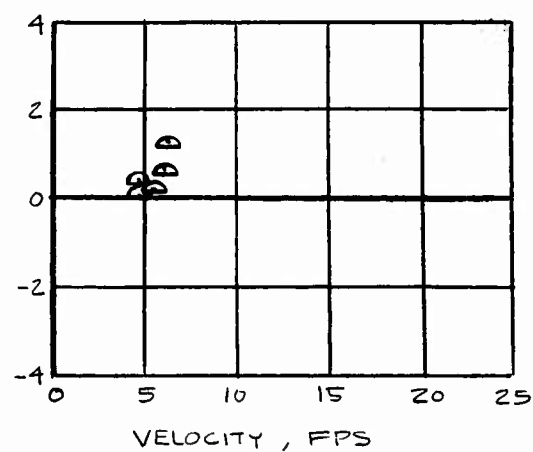
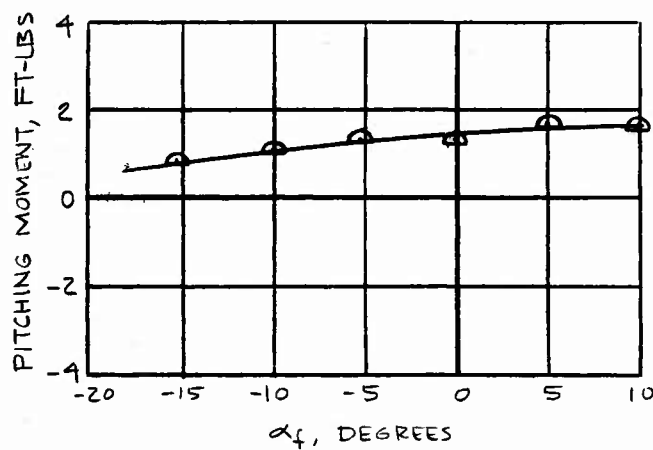
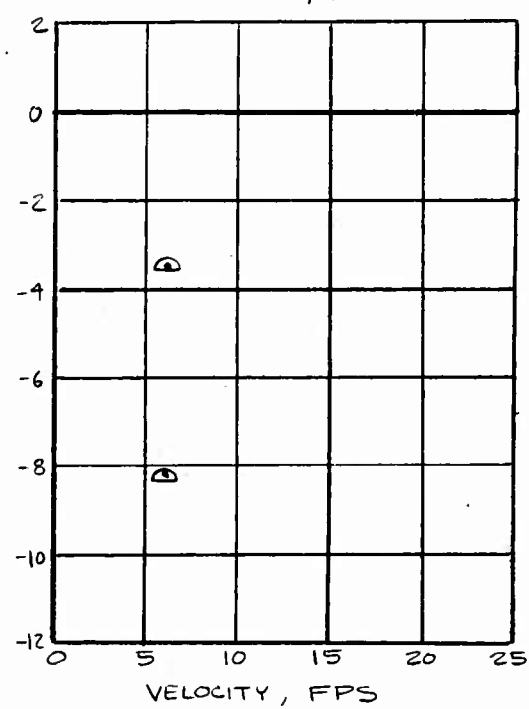
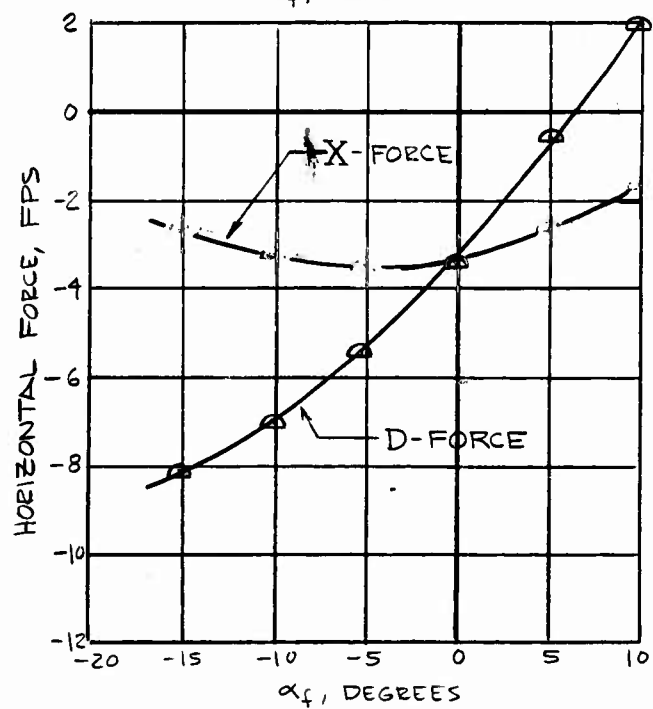
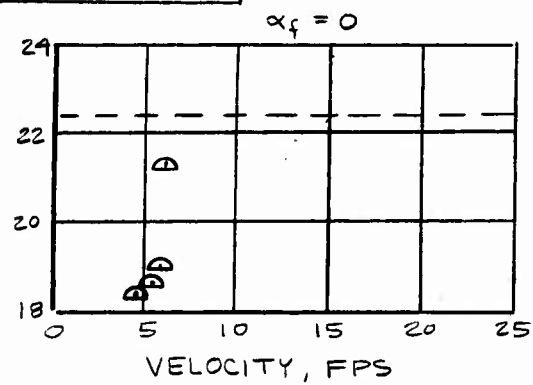
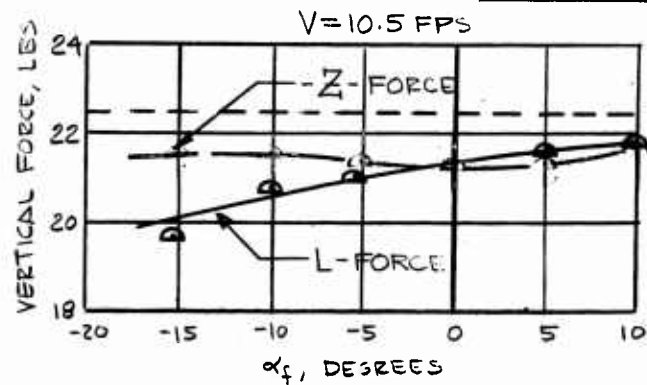
 $V = 10.5 \text{ fps}$ 

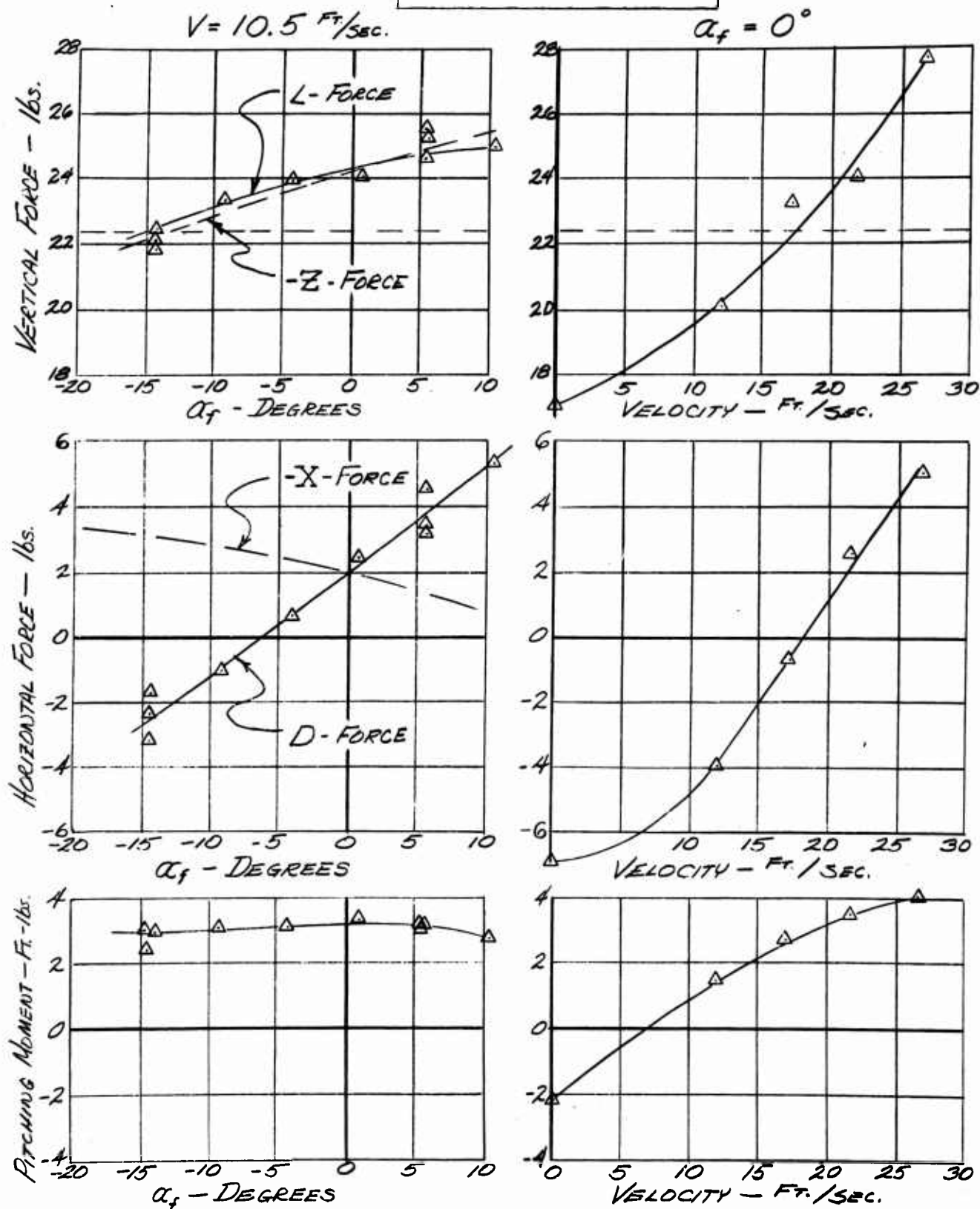
Fig. 22

$$i_w = 70^\circ \quad \theta_{0.75R} = 14.72^\circ$$



Static Test Data

$$\dot{i}_w = 57^\circ \quad \theta_{15R} = 11.97^\circ$$



Static Test Data

$$\lambda_w = 51^\circ \quad \Theta_{0.75R} = 12.22^\circ$$

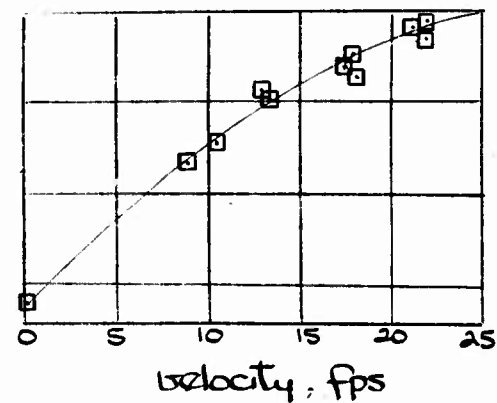
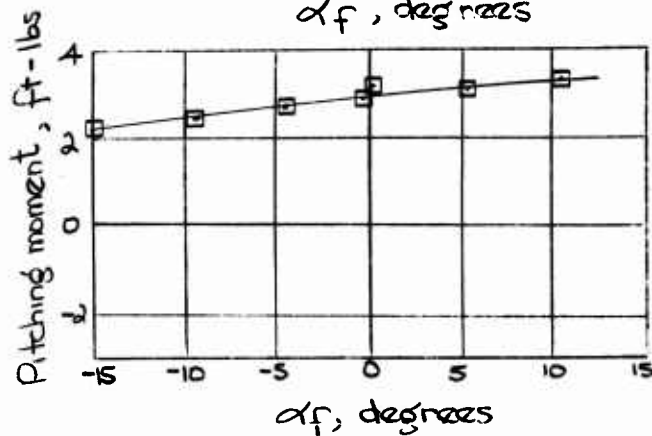
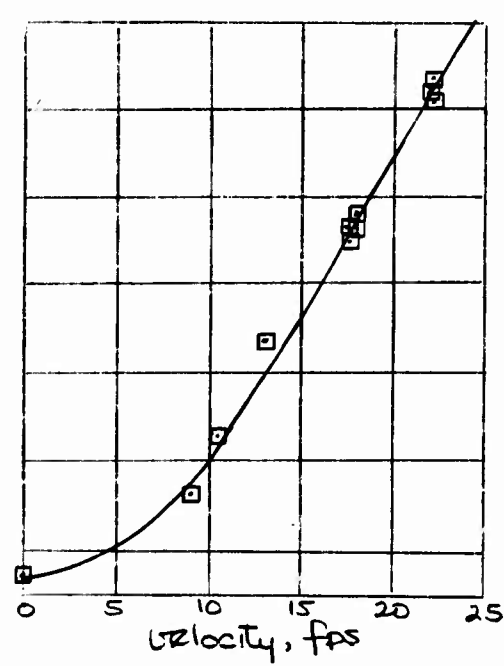
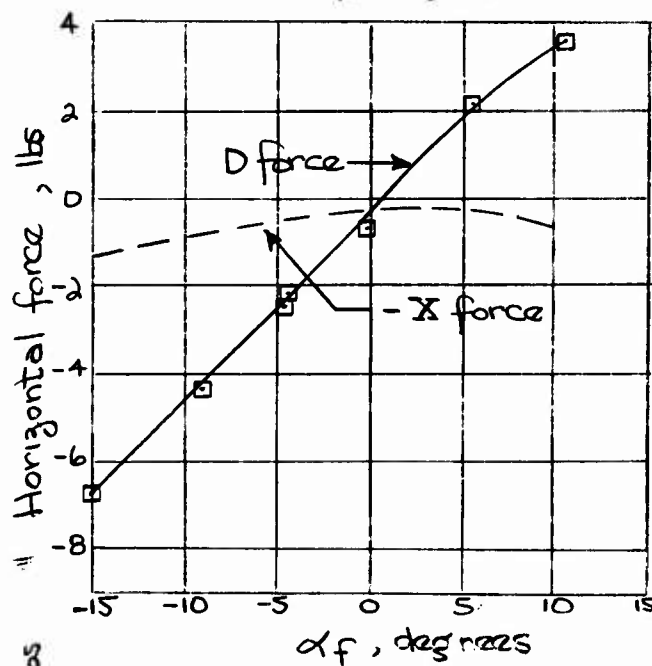
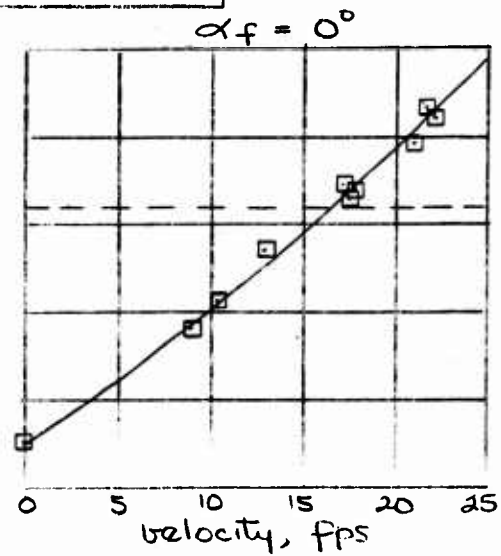
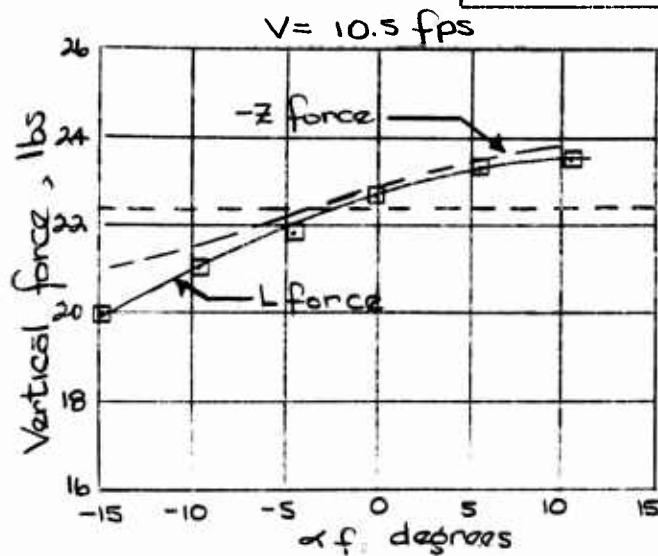
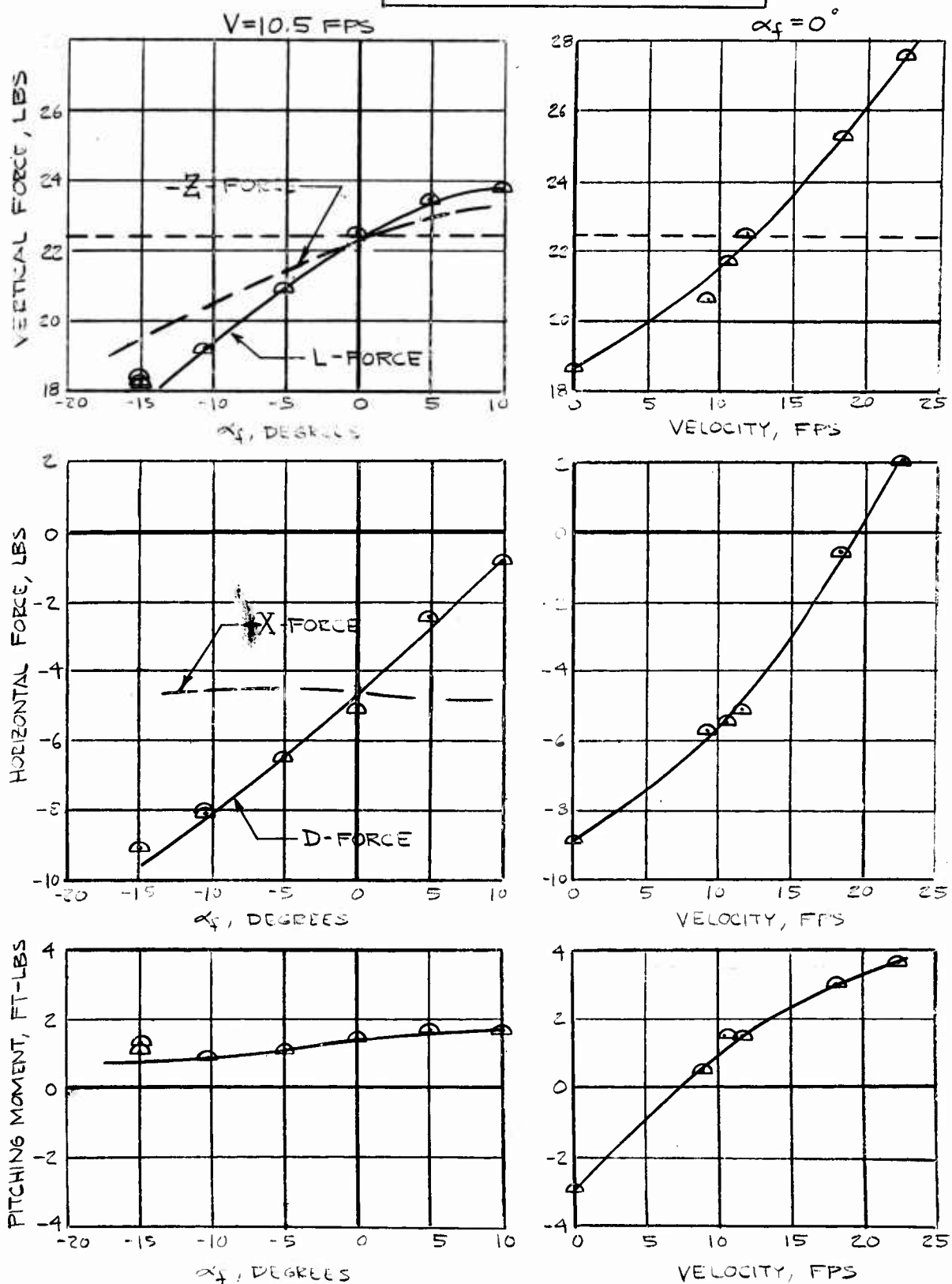


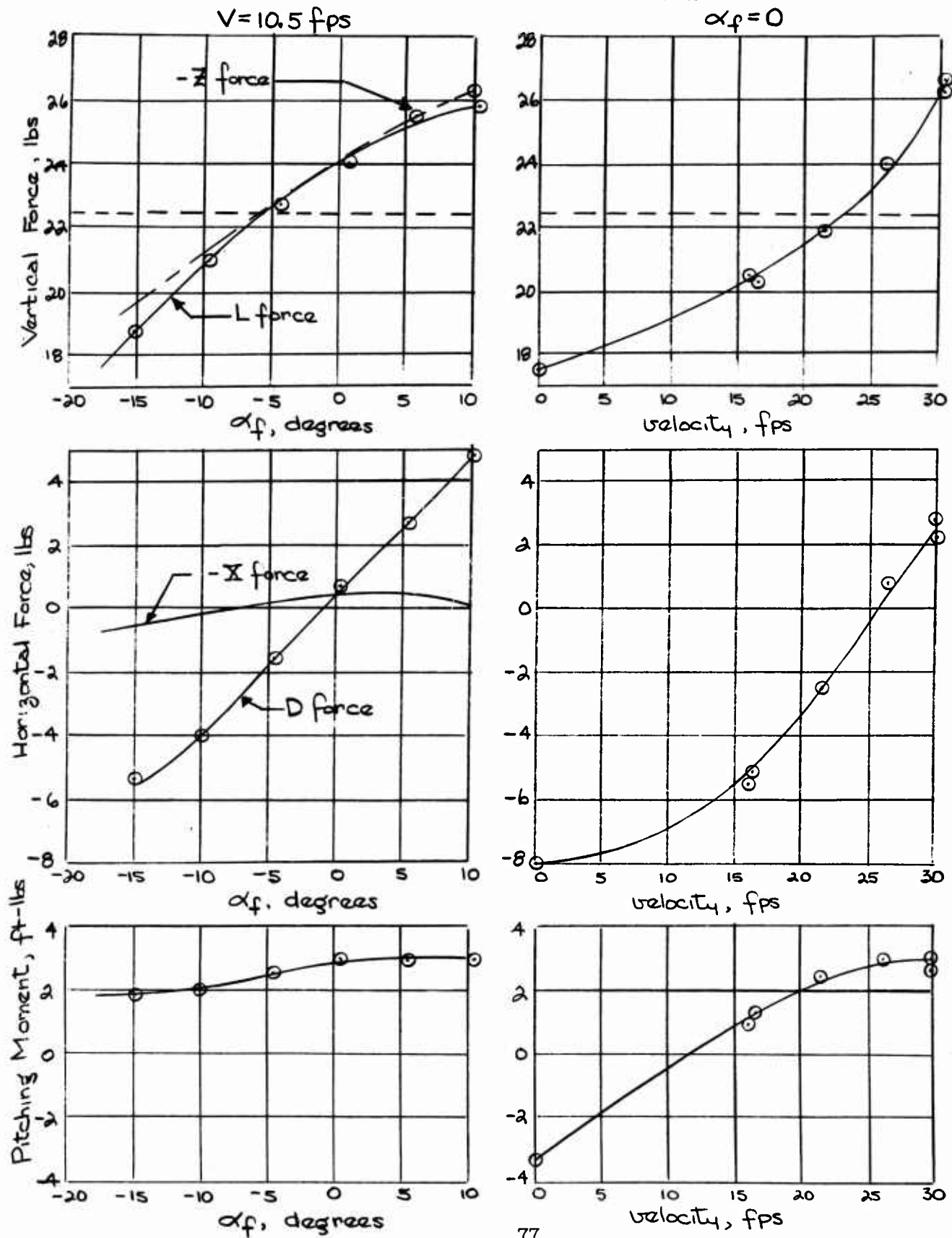
Fig. 25

$$\Lambda_w = 57^\circ \quad \theta_{0.75R} = 14.72^\circ$$

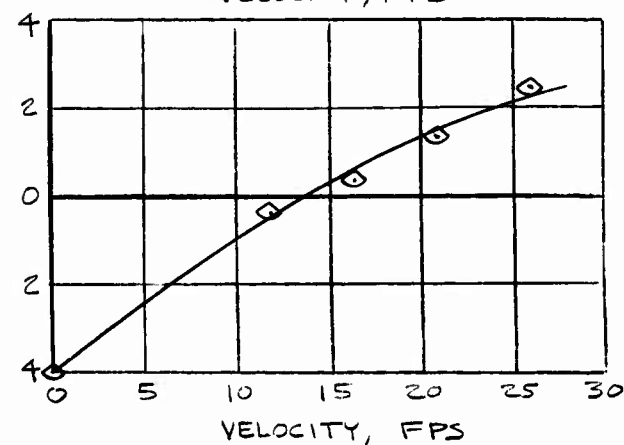
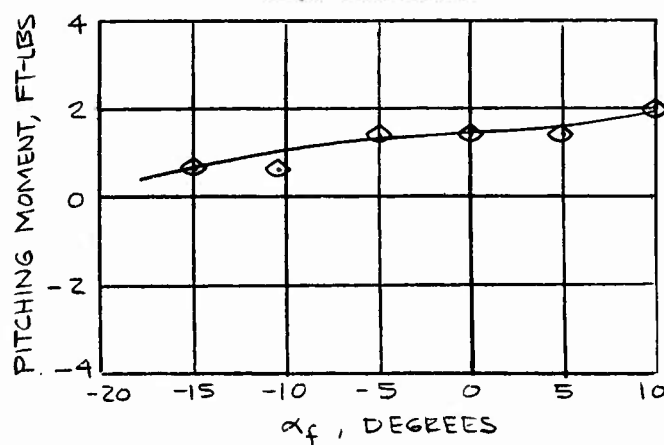
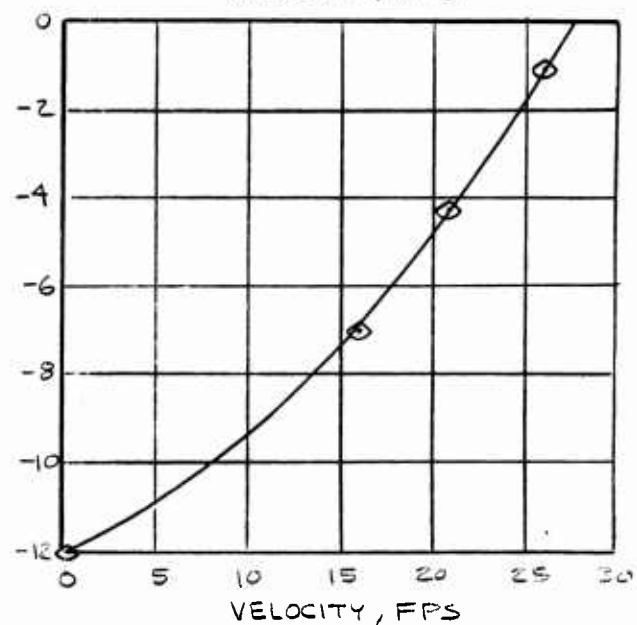
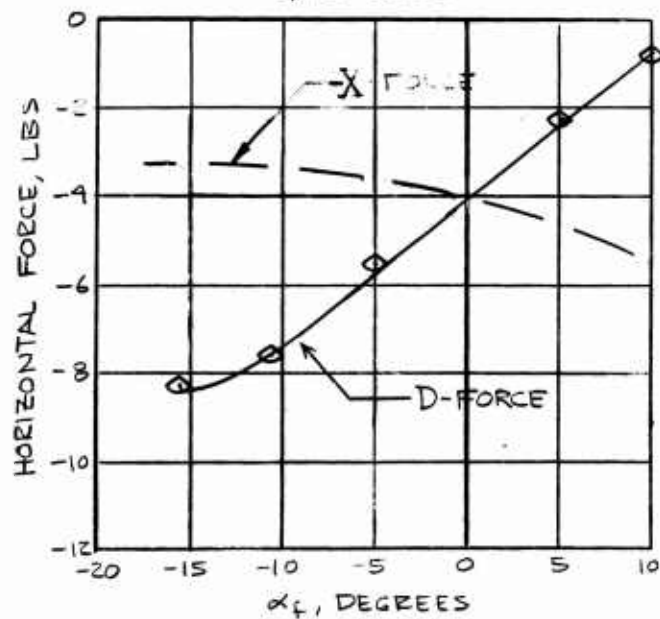
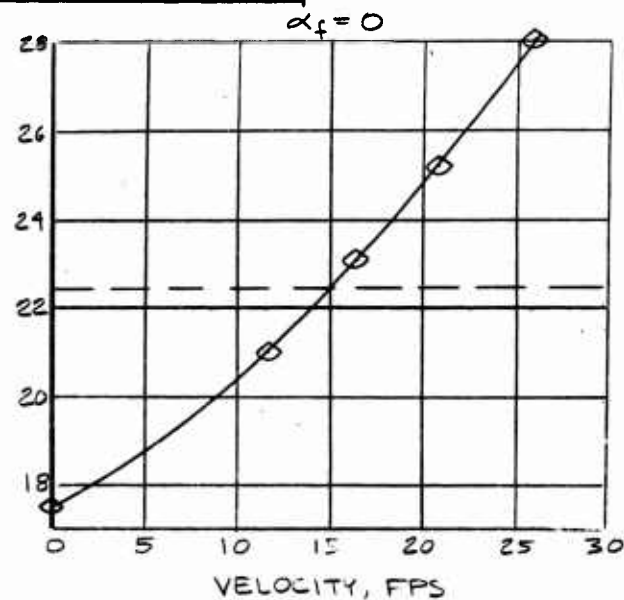
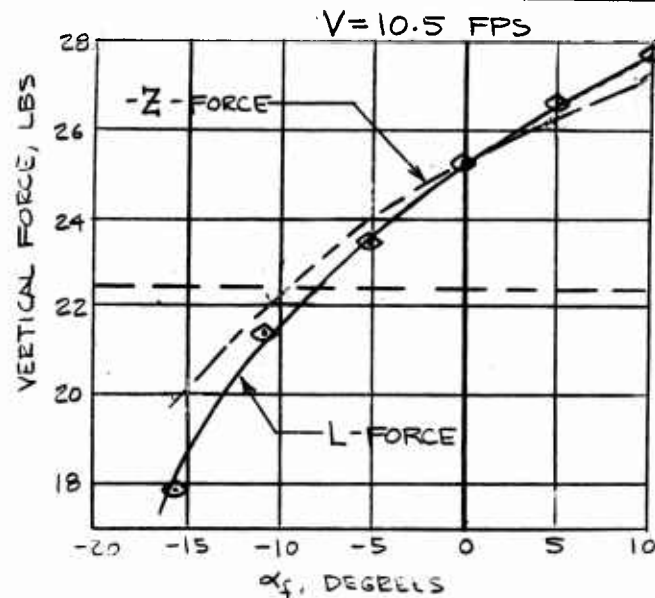


Static Test Data

$$i_w = 44^\circ \quad \Theta_{0KR} = 11.47^\circ$$



$$\dot{\alpha}_w = 44^\circ \quad \theta_{0.75R} = 15.22$$



Static Test Data

ONE DEGREE OF FREEDOM EXPERIMENTAL DATA

Run 22

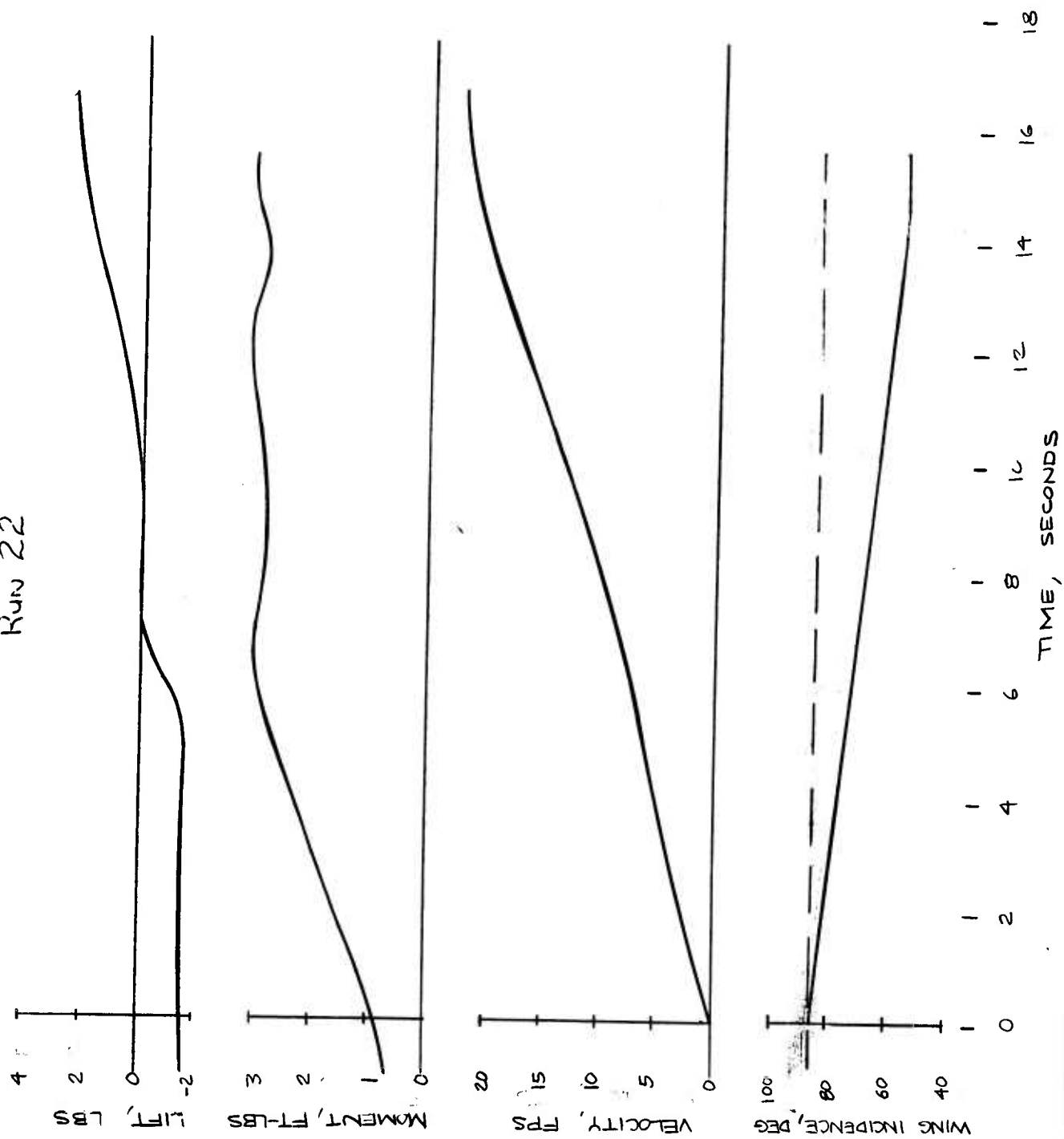


Fig. 28

ONE DEGREE OF FREEDOM EXPERIMENTAL DATA RUN 23

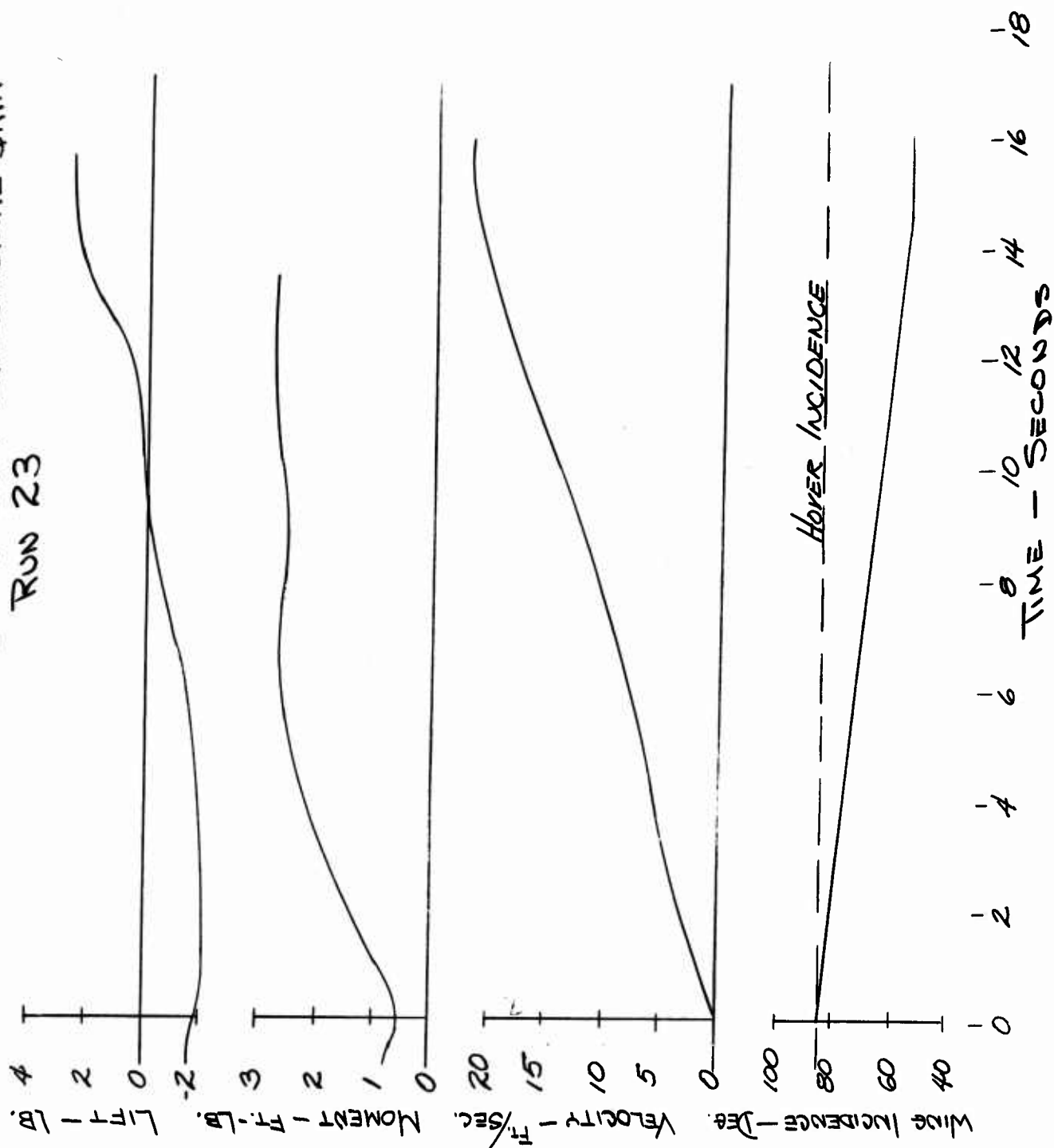
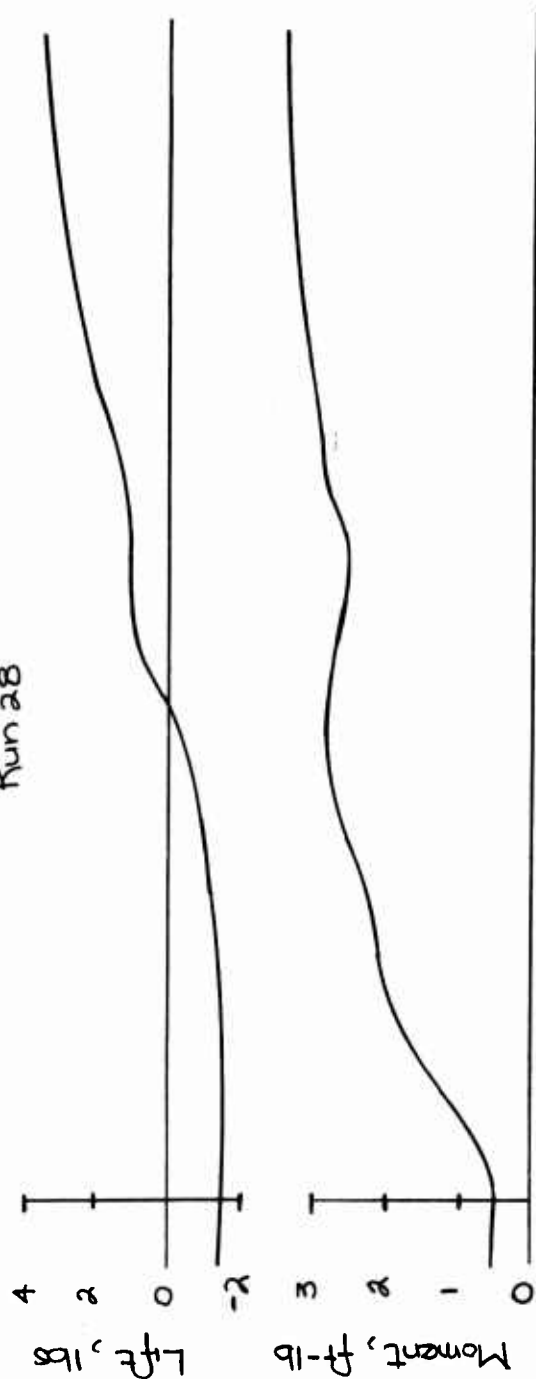


Fig. 29

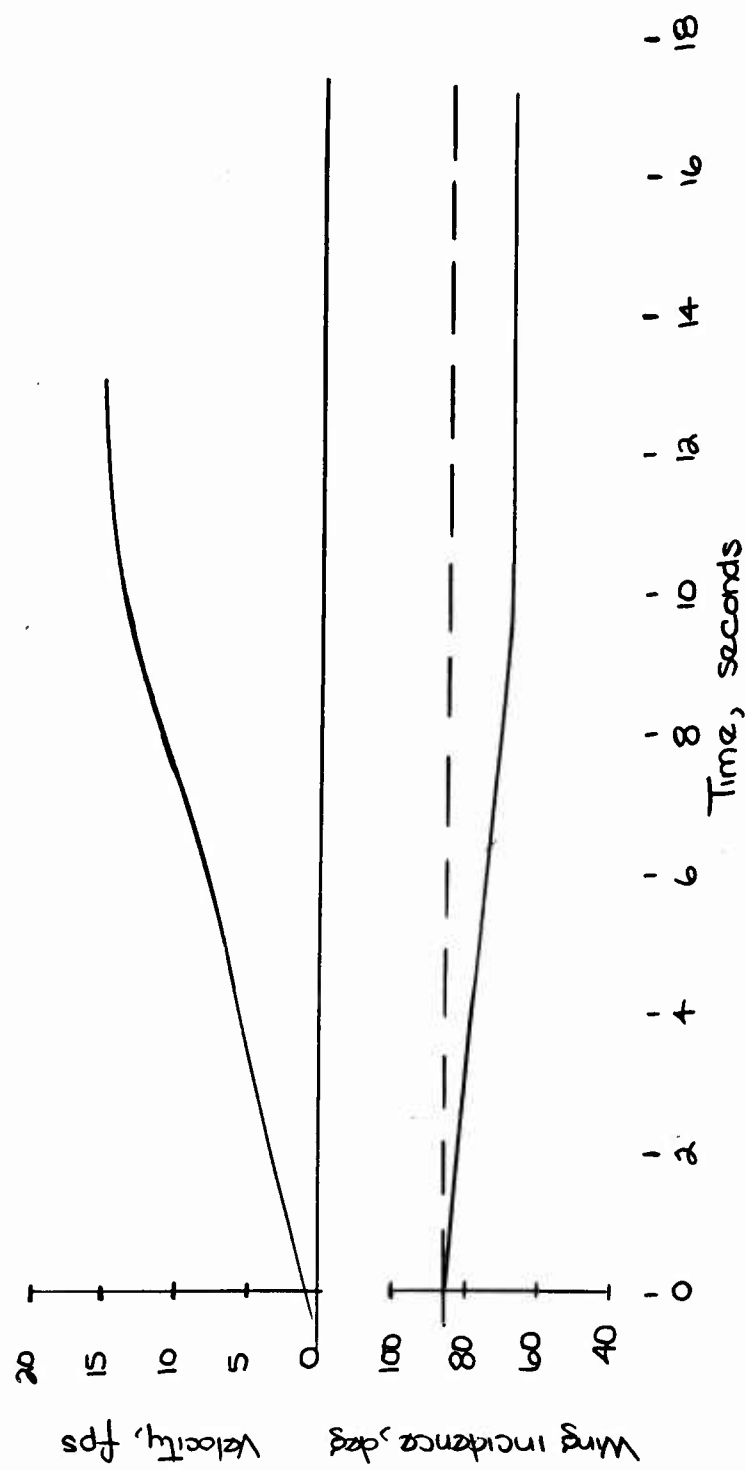
One Degree of Freedom Experimental Data

Run 28



81

Fig. 30



ONE DEGREE OF FREEDOM EXPERIMENTAL DATA Run 33

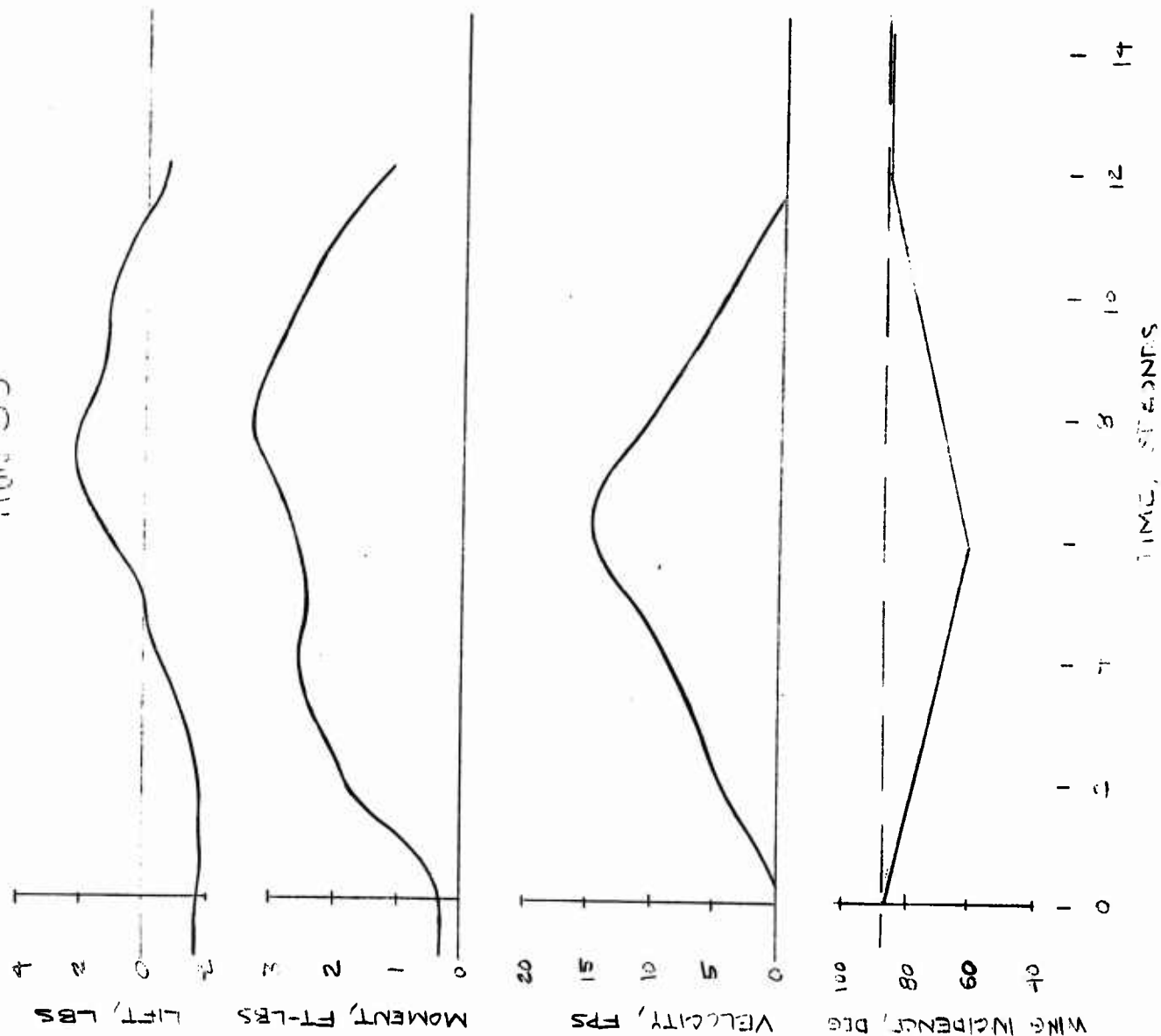


Fig. 31

ONE DEGREE OF FREEDOM EXPERIMENTAL DATA Run 34

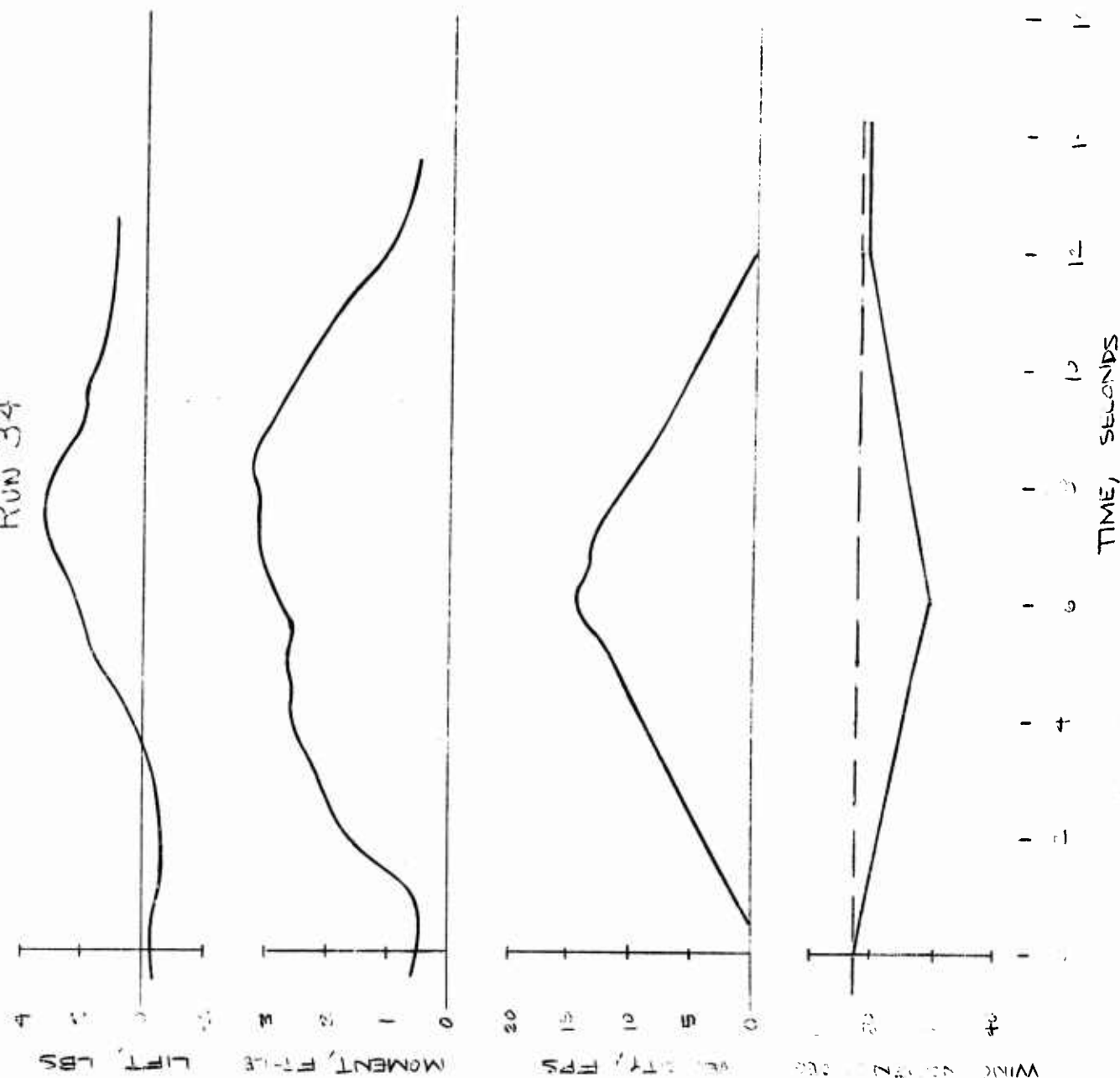


Fig. 32

ONE DEGREE OF FREEDOM EXPERIMENTAL DATA Run 35

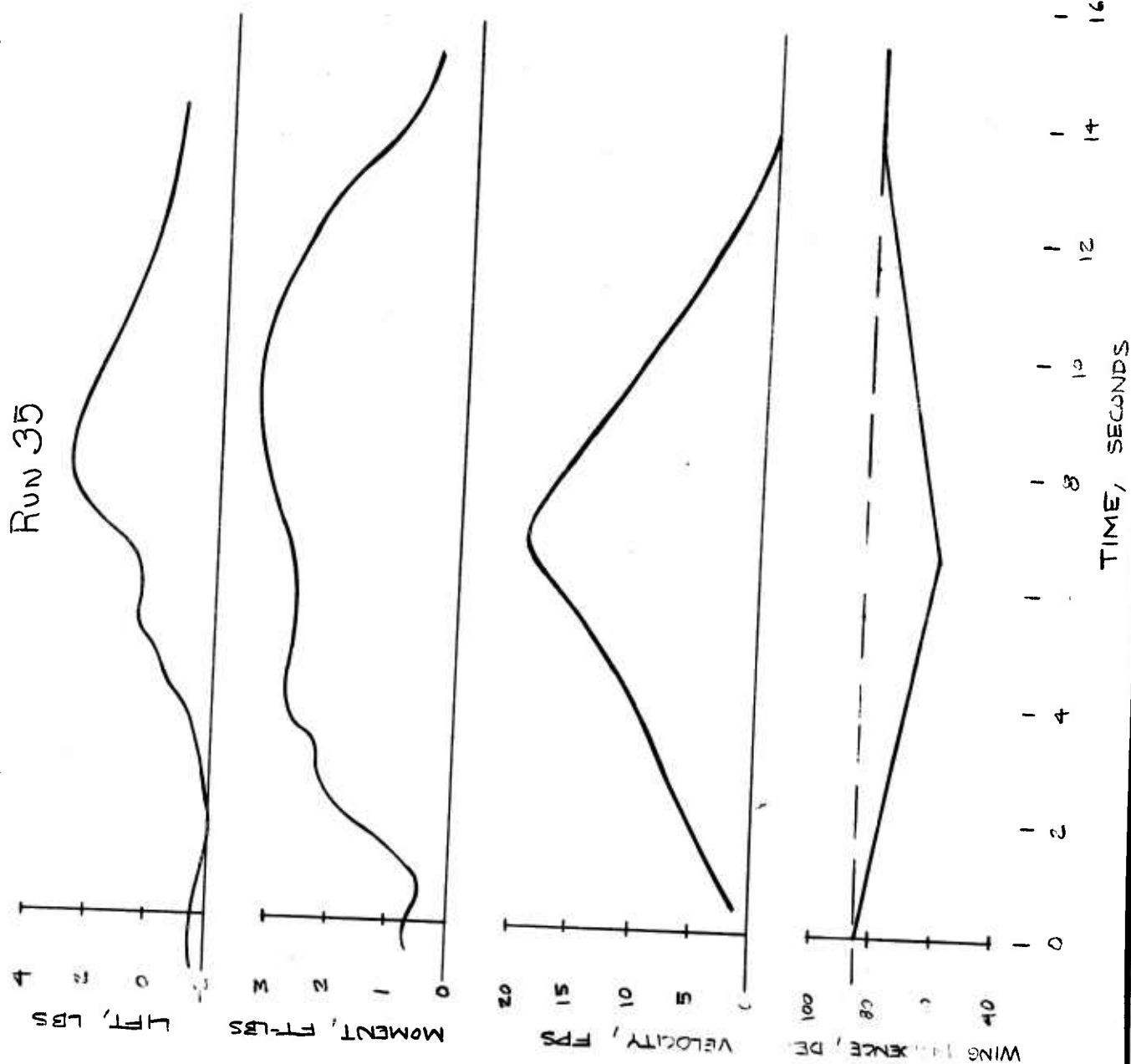


Fig. 33

Fig. 34

EXPERIMENTAL TRIM CROSS - PLOTS ACCELERATED FLIGHT — DRAG = -2 LBS

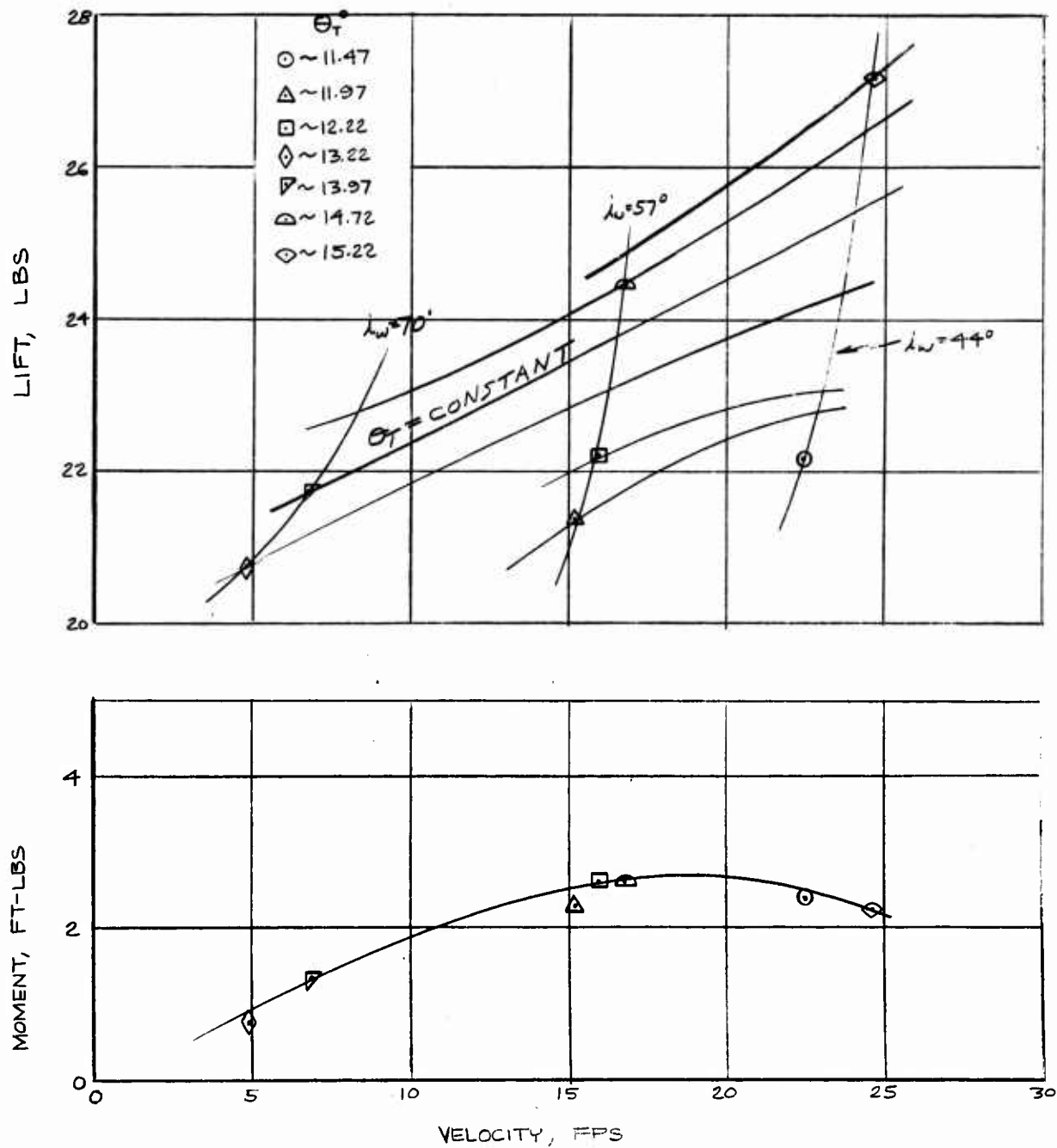


Fig. 35

EXPERIMENTAL TRIM CROSS- PLOTS
ACCELERATED FLIGHT — DRAG = -1 LB

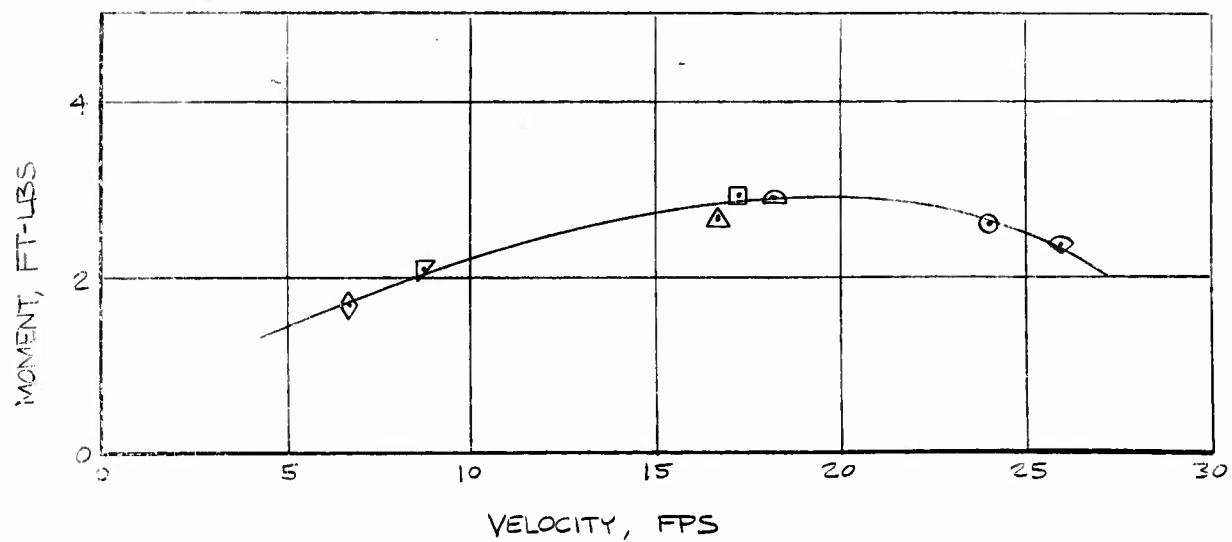
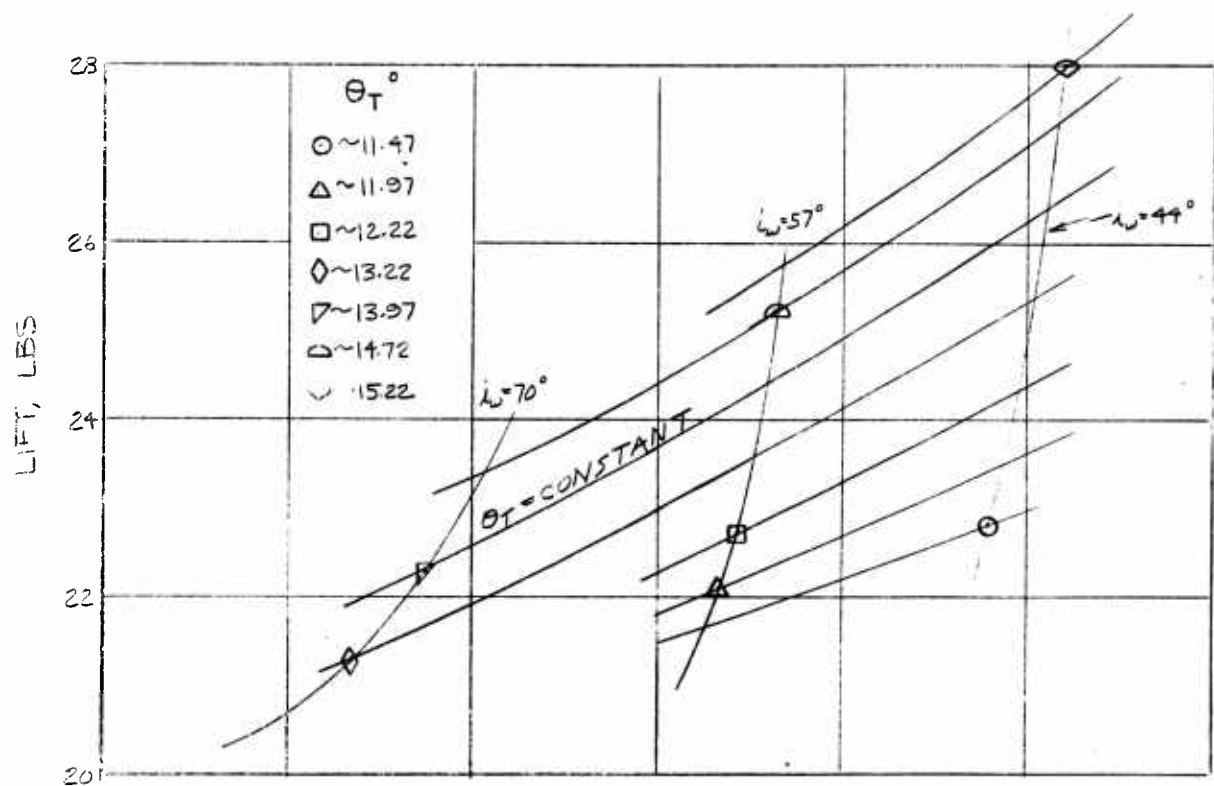
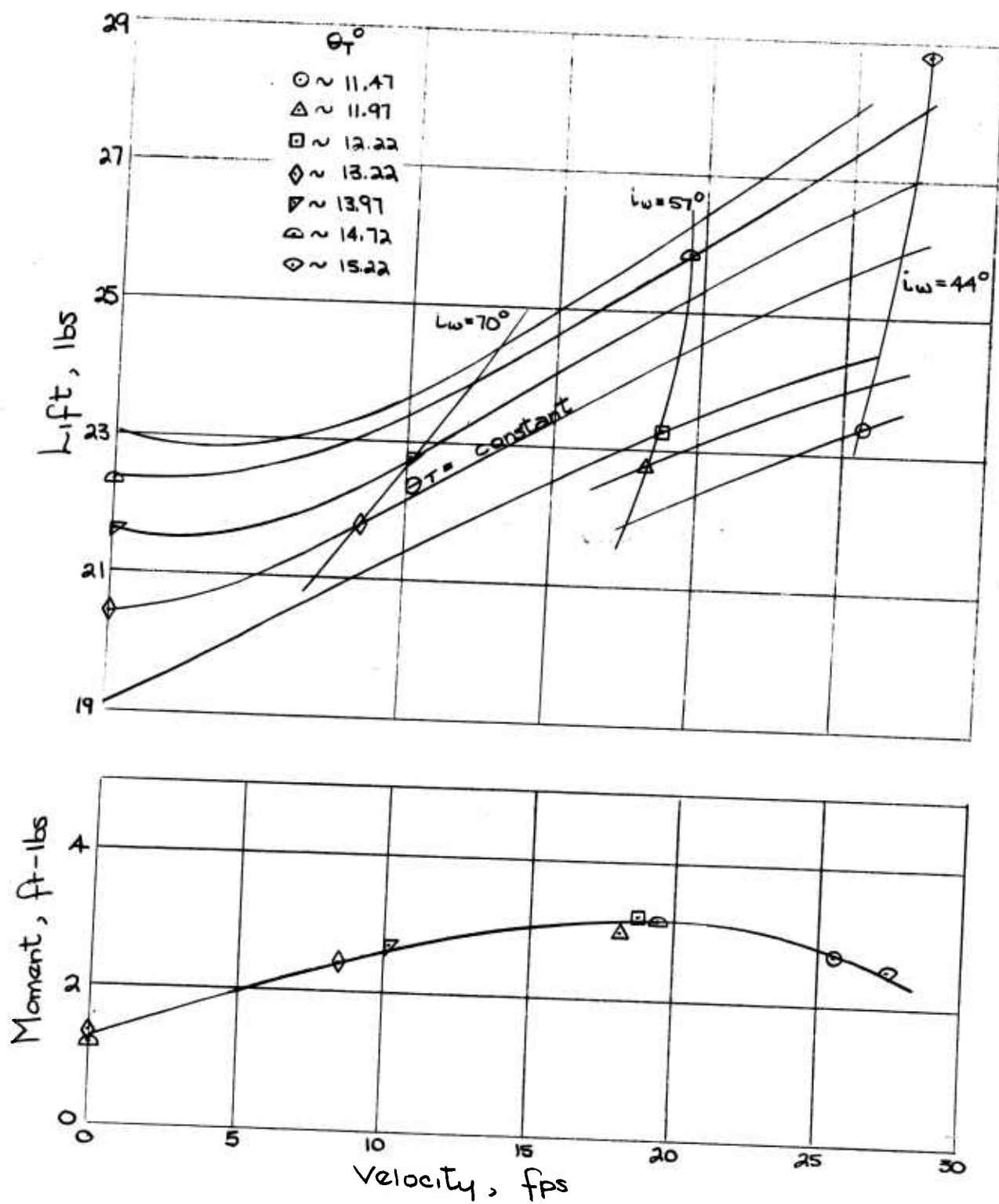


Fig. 36

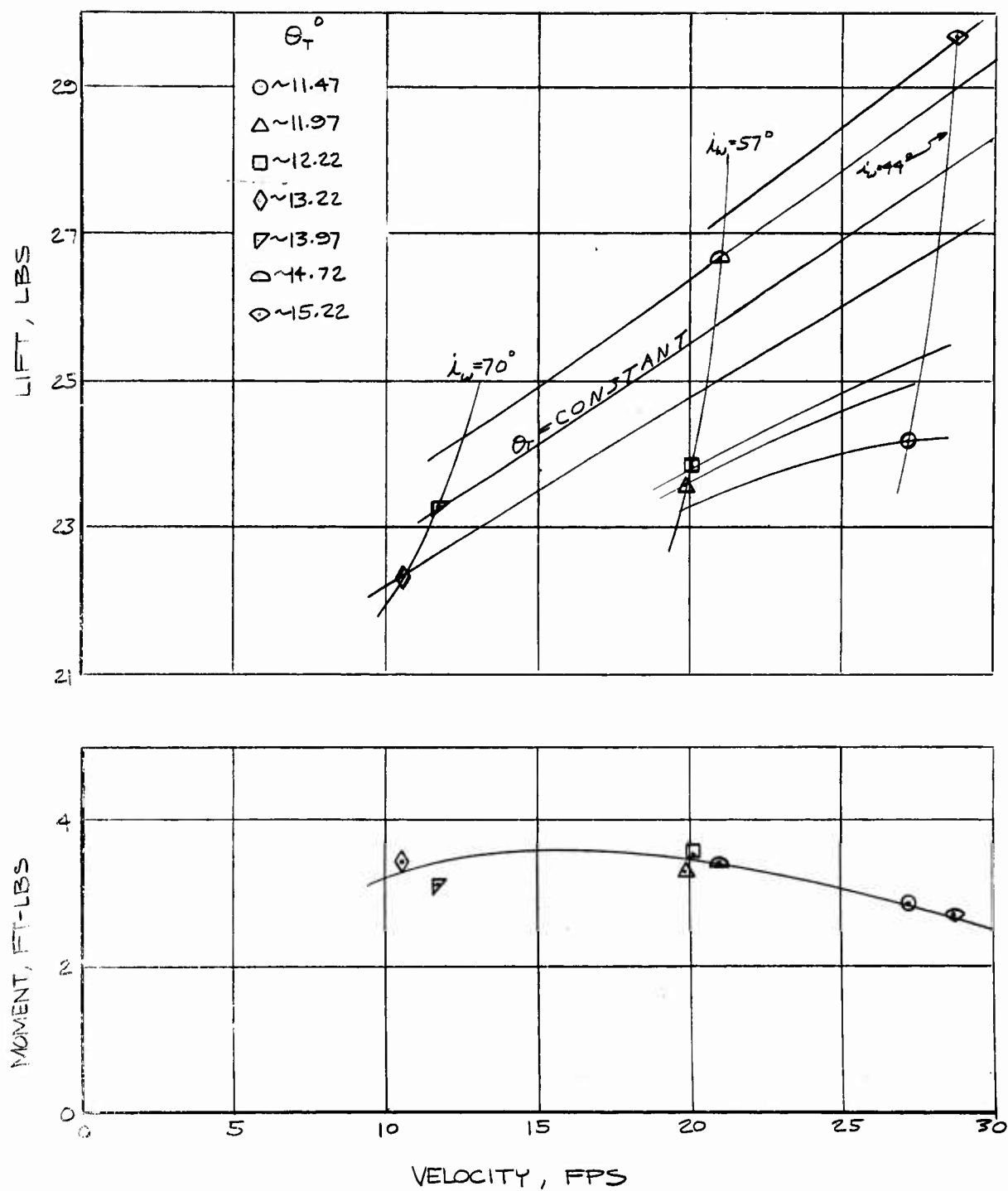
Experimental Trim Cross-Plots

Drag = 0



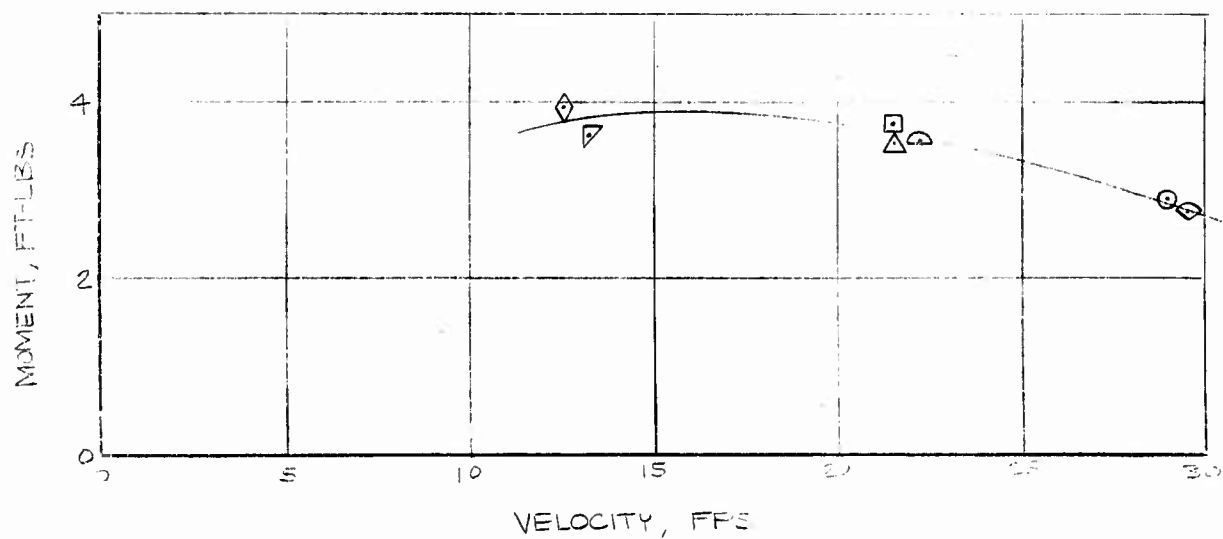
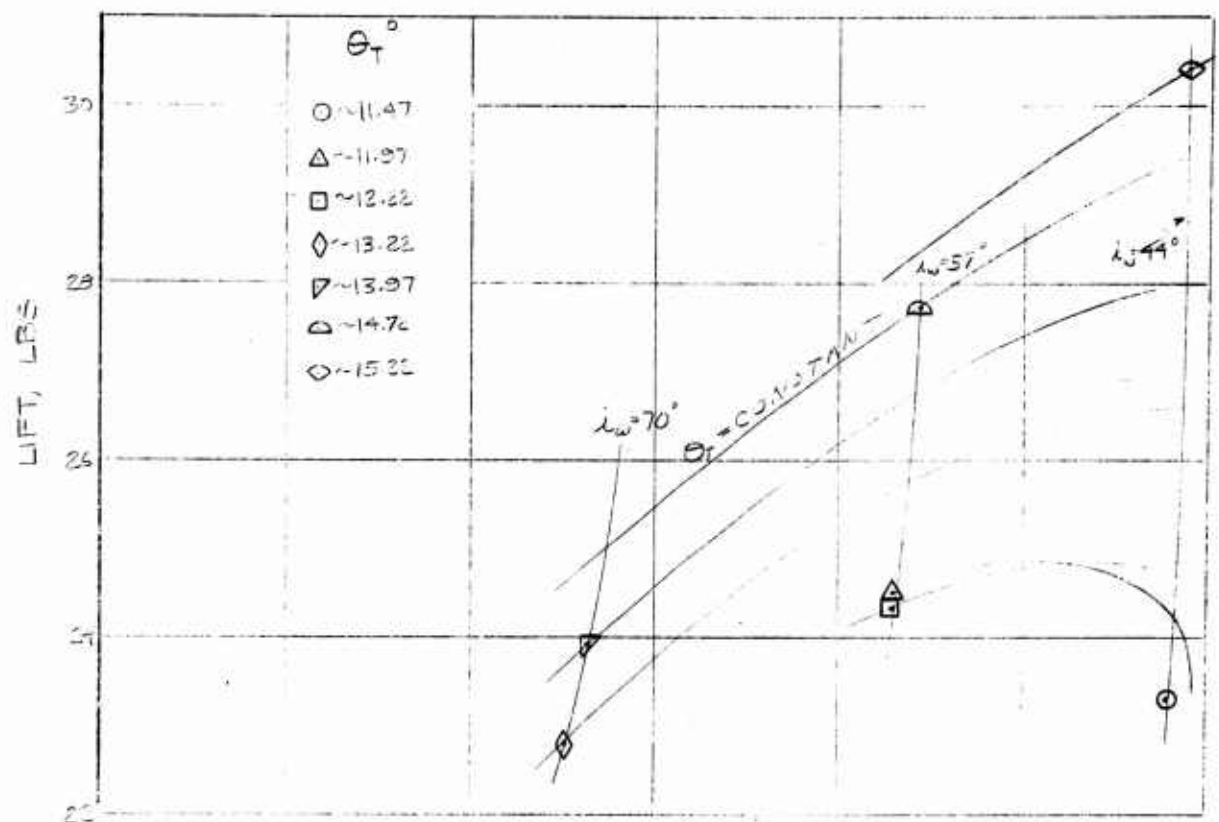
EXPERIMENTAL TRIM CROSS - PLOTS

DECELERATED FLIGHT - DRAG = 1 LB



EXPERIMENTAL TRIM CROSS-FLIGHT

DECELERATED FLIGHT - DRAG = 2 LBS



THEORETICAL STATIC STABILITY AND TRIM DEVELOPMENTS

ASSUMPTIONS AND LIMITATIONS

In Appendix A of this report it presented a theoretical development intended to enable one to predict in a straight-forward fashion the static stability derivatives and trim conditions of the aircraft under consideration or of any similar type. This development is not wholly unlike some others available, notably those of References 4 and 5, but unlike those noted, is directed towards an eventual comparison with experimental data with attempts being made to determine the validity and applicability of the developments. The theory is intended to describe a first-order approximation to the actual processes and as such should predict, with limitations, the sign, magnitude, and general trends of the stability derivatives. More important, it should demonstrate the significance and predictability of some of the major contributory effects in both trim conditions and stability derivatives, and give an initial evaluation of some of the simplifying assumptions generally made in a stability and control analysis.

In developing a theory to predict the forces and moments generated by a wing-rotor combination, three reasonable approaches may be considered:

- 1) The isolated wing and rotor may be analyzed separately and the results added for a combined affect.
- 2) An isolated rotor may be considered separately and the results used to determine the operating conditions of a wing immersed in the rotor slipstream.

3) A mutually interferring arrangement of wing and rotor may be considered and an analysis attempted on the combination.

The first of these is unrealistic in that for the relative size of wing and rotor considered here, virtually the entire wing is immersed in the rotor slipstream, and the actual flow at the wing is considerably different from freestream conditions. The second approach is a much better representation of the actual conditions in that the change in local flow direction and magnitude at the wing can be taken into consideration. The last method is certainly the most complete, however it has been demonstrated in Reference 14 that the influence of the wing on the rotor is of an order of magnitude less importance than the influence of the rotor on the wing. It was therefore not thought worthwhile to attempt to account for the wing on rotor effects in a first approach such as is considered here.

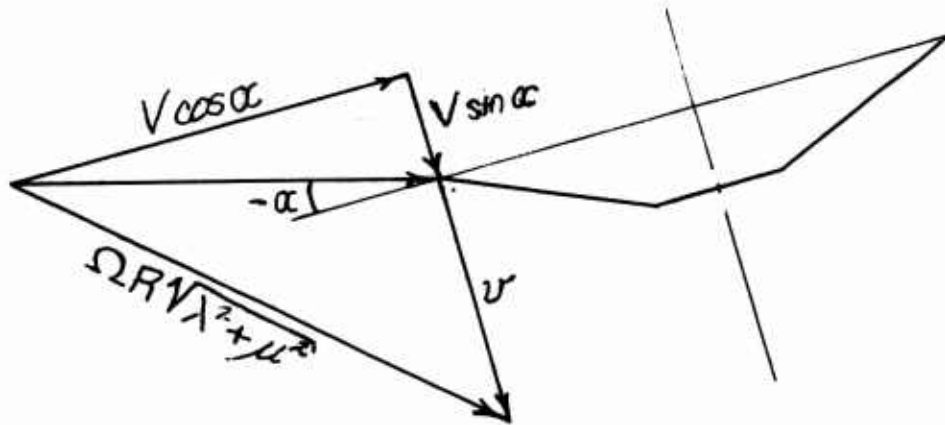
Analysis of an isolated rotor in low speed flight is a problem in itself whose solution at present leaves much to be desired. It is not possible to reasonably account for the effects of induced velocity variation across or around the disk of an articulated rotor without resorting to very complicated and still unprecise blade dynamic motion analysis. Such techniques are certainly beyond the scope of a stability and control analysis as is considered here. Constant axial induced velocity based on axial momentum considerations has therefore been assumed in all derivations of rotor forces and moments presented in this report.

Due to the limitations in the techniques of predicting isolated rotor characteristics it would be difficult to account for some of the

wing on rotor effects that might be present. Possibly the two most significant of such effects would be the increase in angle of attack at the rotor due to wing upwash and some distribution of induced velocity across the disk contributed by the wing circulation. The first of these may be accounted for in the constant induced velocity theory, and a more comprehensive study could include these effects once there is some reasonable assurance that the wing operating conditions are known. Accounting for the velocity distribution effects, however, would be difficult in view of the limitations of the present theory. In the particular case under consideration these effects would not be too severe since variations in velocity across the disk in the longitudinal plane are not as serious an effect on the longitudinal forces and moments of an articulated rotor as they are on a rigid rotor. Analysis of a flapping rotor as a rigid body reveals a 90° phase shift between force and displacement of the blade, since it is a heavily damped second order system being forced at its natural frequency. This means that longitudinal forcing, as would be produced by the velocity distribution under consideration, would result in lateral flapping and hence yawing and rolling moments and side - force. The higher harmonics of the blade motion contribute no steady-state components and therefore need not be considered for a stability analysis. In a rigid rotor, however, one would expect large contributions to pitching moments from longitudinal velocity distribution. In this case some account should be made for these effects regardless of their source.

MOMENTUM CONSIDERATIONS

Due to the articulated nature of the rotor and the regime of operation under consideration, helicopter notation and analysis techniques are used throughout to define and discuss the rotor parameters. In accordance with conventional helicopter theory the mass flow through the rotor is defined as that flow passing through an imaginary sphere of which the rotor disk is a great circle. Referring to the diagram below which depicts a rotor operating in its normal condition at a negative angle of attack, we can see that the total mass flow is $\rho A \Omega R \sqrt{\lambda^2 + \mu^2}$. Here λ and μ are as defined on page 10 and A is the area of the great circle of radius R perpendicular to the net velocity vector $\Omega R \sqrt{\lambda^2 + \mu^2}$ and is therefore equal to the rotor disk area.



Conservation of axial momentum states that the net thrust produced by the rotor is equal to the change in axial momentum of the flow induced by the rotor, which is simply the mass flow $\rho A \Omega R \sqrt{\lambda^2 + \mu^2}$ times the total change in velocity of the flow which is $2N$, the induced velocity when the slipstream static pressure reaches atmospheric downstream. Equating this product to the thrust we have

$$T = 2N \rho A \Omega R \sqrt{\lambda^2 + \mu^2},$$

which upon re-arrangement and substitution of the definition of C_T gives

$$\frac{N}{\Omega R} = \frac{C_T}{2 \sqrt{\mu^2 + \lambda^2}}$$

It is desirable in an analysis such as this to promote clarity by simplification whenever it is possible, without seriously compromising the results, and it is for this purpose that assumptions are frequently made at this point concerning the mass flow through the rotor. One such approach is to assume that only the flow normal to the disk contributes significantly to the total mass flow, in which case the mass flow is given by $\rho A (\sqrt{\mu^2 + \lambda^2} - \sigma)$ and the resultant induced velocity is $\frac{N}{\Omega R} = \frac{C_T}{2|\lambda|}$. In order to compare these two

methods and their results we can consider the blade element theory expression as given in Appendix A, Equation 13

$$\frac{2C_T}{2\sigma} = \frac{\lambda}{2} + \frac{\theta}{3} \left(1 + \frac{3\mu^2}{2} \right)$$

and note that for a given rotor operating at some $\sqrt{\lambda^2 + \mu^2}$, C_T can be

expressed in terms of the inflow parameter λ . Substituting the above expressions for induced velocity into the definition of λ we have

$$\lambda = \frac{V \mu \sin \alpha}{\Omega R} - \frac{C_T}{2 \sqrt{\lambda^2 + \mu^2}}$$

$$\xi \quad \lambda_{\text{NORMAL}} = \frac{V \mu \sin \alpha}{\Omega R} - \frac{C_{TN}}{2 \lambda_N}$$

Dividing both sides of these two expressions by $\lambda_o = -\sqrt{\frac{C_T}{2}}$ as in Appendix B enables one to make a comparison of these two methods on the basis of the λ they each would predict for a rotor operating at some given C_T . This comparison is presented in Figure 39 where significant departure from the complete mass flow prediction is apparent only at low negative α 's and the higher μ_x 's. This comparison, however, is not the complete picture since only the ratio of predicted $\frac{\lambda}{\sqrt{C_T/2}}$ is compared and the predicted C_T can vary somewhat more as indicated by the sample calculations shown below. Combining the blade element and normal mass flow equations, we can write a quadratic which can be solved for C_T explicitly.

$$\lambda_N = \frac{V \sin \alpha}{\Omega R} - \frac{v}{\Omega R} = \frac{V \mu \sin \alpha}{\Omega R} - \frac{C_T}{2 |\lambda_N|}$$

$$C_T = -2 \lambda_N |\lambda_N| + 2 |\lambda_N| \frac{V \mu \sin \alpha}{\Omega R}$$

Remembering that λ_N is negative for the normal flight condition we can write

$$C_{TN} = 2 \lambda_N^2 - 2 \lambda_N \frac{V \mu \sin \alpha}{\Omega R}$$

which, when combined with the blade element equation gives

$$2\left(\frac{4}{\partial\sigma}\right)^2 C_{T_N}^2 - \left[\frac{8}{\partial\sigma}(\mu_x \mu \sin\alpha + \frac{4\Theta}{3}) + 1\right] C_{T_N} + \frac{4\Theta}{3}(\mu_x \mu \sin\alpha + \frac{2\Theta}{3}) = 0$$

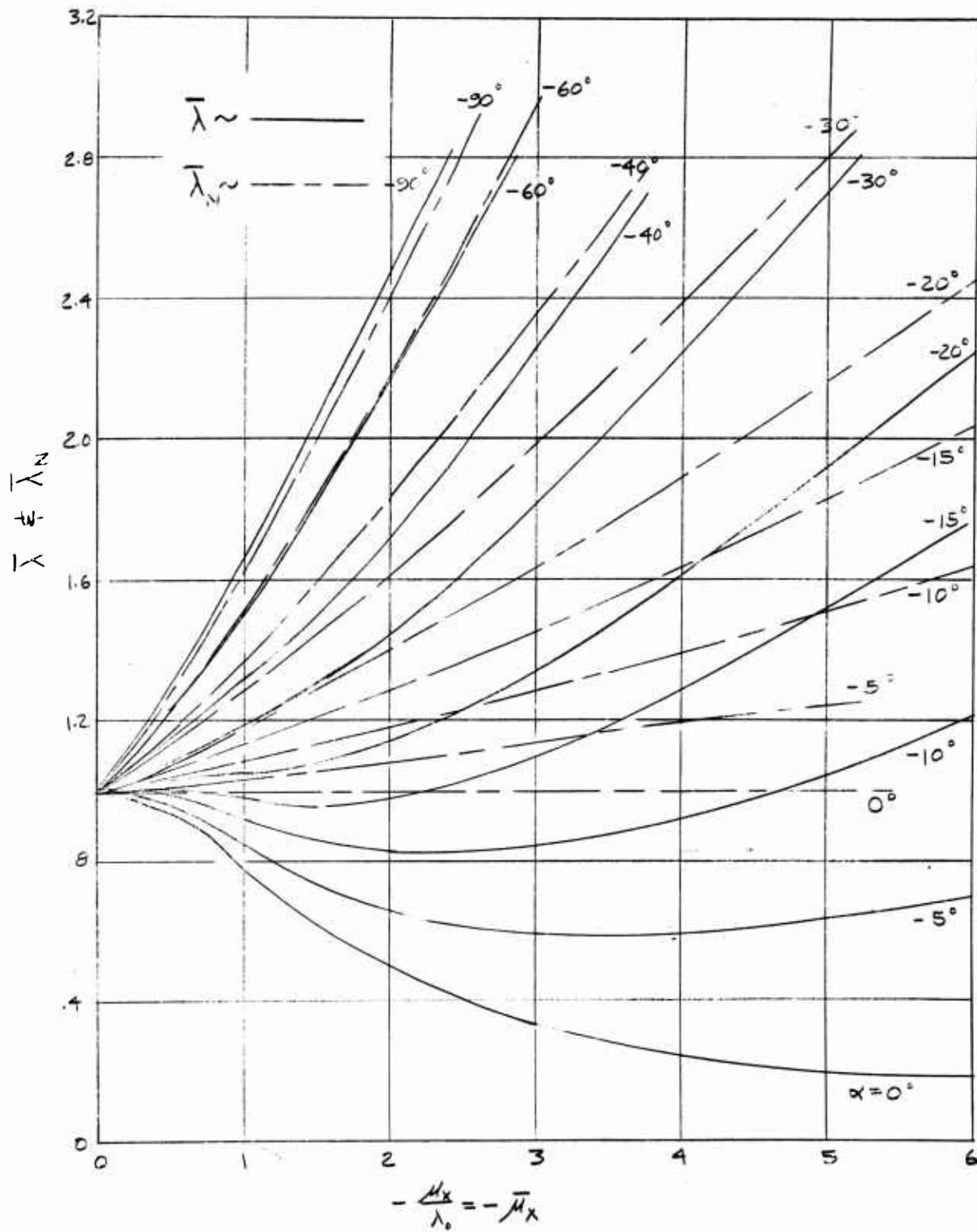
Upon substitution of the values of V , α , and Θ for the three trim conditions we can solve for C_{T_N} which is compared to the complete flow C_T below.

@ $i_w = 70^\circ$,	$C_{T_N} = .01447$,	$C_T = .01588$
@ $i_w = 57^\circ$,	$C_{T_N} = .01150$,	$C_T = .01217$
@ $i_w = 44^\circ$,	$C_{T_N} = .00825$,	$C_T = .00848$

The agreement indicated is remarkably good, however, as Figure 39 indicates the various thrust derivatives can be seriously in error near the hovering condition. However, the major error that the normal component assumption introduces is in the induced velocity magnitude and derivatives where the neglect of μ^2 with respect to λ^2 can have quite serious consequences. The importance of the induced velocity in its influence on the wing is the primary reason why this significant simplification was not exercised in this analysis. In particular the wing angle of attack α' and its derivatives are very strongly affected by the induced velocity and its derivatives, and reference to Figures 47 through 53 indicates that the wing α' derivatives, are frequently the strongest single contributions to the total airplane derivatives. This being the case, it was not considered

prudent to adopt the normal mass flow simplification only for the sake of easing the computations, particularly in view of the availability of the methods developed in Appendix B.

COMPARISON OF λ FOR COMPLETE AND NORMAL MASS FLOW ASSUMPTION



ROTOR OPERATING CONDITIONS

The results of a blade element analysis as developed in Reference 6 have been modified to a certain extent for application in this development. As noted on page 190 of Appendix A the blade tip-loss factor B has been assumed equal to unity, and another method has been substituted to account for this effect. This method takes advantage of experimental values of thrust measured at the trim values of collective pitch and zero velocity at the beginning of each static run and uses these values to compute effective collective pitches for the various conditions as shown in Appendix A. The small error introduced by wing zero- α drag is only 1-2 per cent at most and is neglected in this part of the analysis. Such a procedure as shown allows correction for velocity independent errors in the blade element theory such as blade tip loss and hub and nacelle interference effects, and eliminates the possible influence of errors in the measurement or setting of blade pitch. Use of the charts as developed in Appendix B is a great aid in determining the various rotor and slipstream parameters as well as their derivatives, and eliminates the necessity of having to solve fourth order equations, or making very compromising assumptions to simplify these equations. It should be noted that these charts are developed using only momentum considerations, and so are generally applicable to both rigid and articulated rotors throughout their ranges of operation. It is also possible of course, to develop these charts for the magnitudes and derivatives of induced velocity, resultant velocity, and effective angle of attack behind

the rotor so that both rotor and wing operating conditions can be determined very quickly if C_T and λ_x are known. If C_T is not known, an application of blade element theory, or some modification thereof, in combination with the charts is necessary as indicated in Appendix A.

ROTOR CONTRIBUTIONS

As mentioned in the discussion of the normal mass flow approximation, one of the strongest over-all effects exhibited by the rotor is the influence of induced velocity on the operating conditions and derivatives of the wing exercised through the determination of V_R as shown in the vector diagram of Figure 40. The important

derivatives to consider are $\frac{\partial \alpha'}{\partial \mu_x}$, $\frac{\partial \alpha'}{\partial \alpha}$, $\frac{\partial V_R}{\partial \mu_x}$ & $\frac{\partial V_R}{\partial \alpha}$ which,

for the conditions under consideration, are all positive. The α' derivatives, however, are strong functions of C_T and can conceivably reverse sign at high values of C_T and low μ_x and α , conditions realized near hover or in strongly accelerated flight. Consideration of the velocity vector diagram of Figure 40 shows that an increase in V reduces α' while increasing either μ_x or α produces an increase in α' . Therefore it can be deduced that a strong positive

$\frac{\partial V}{\partial \alpha}$ or $\frac{\partial V}{\partial \mu_x}$ can possibly produce negative $\frac{\partial \alpha'}{\partial \alpha}$ or $\frac{\partial \alpha'}{\partial \mu_x}$

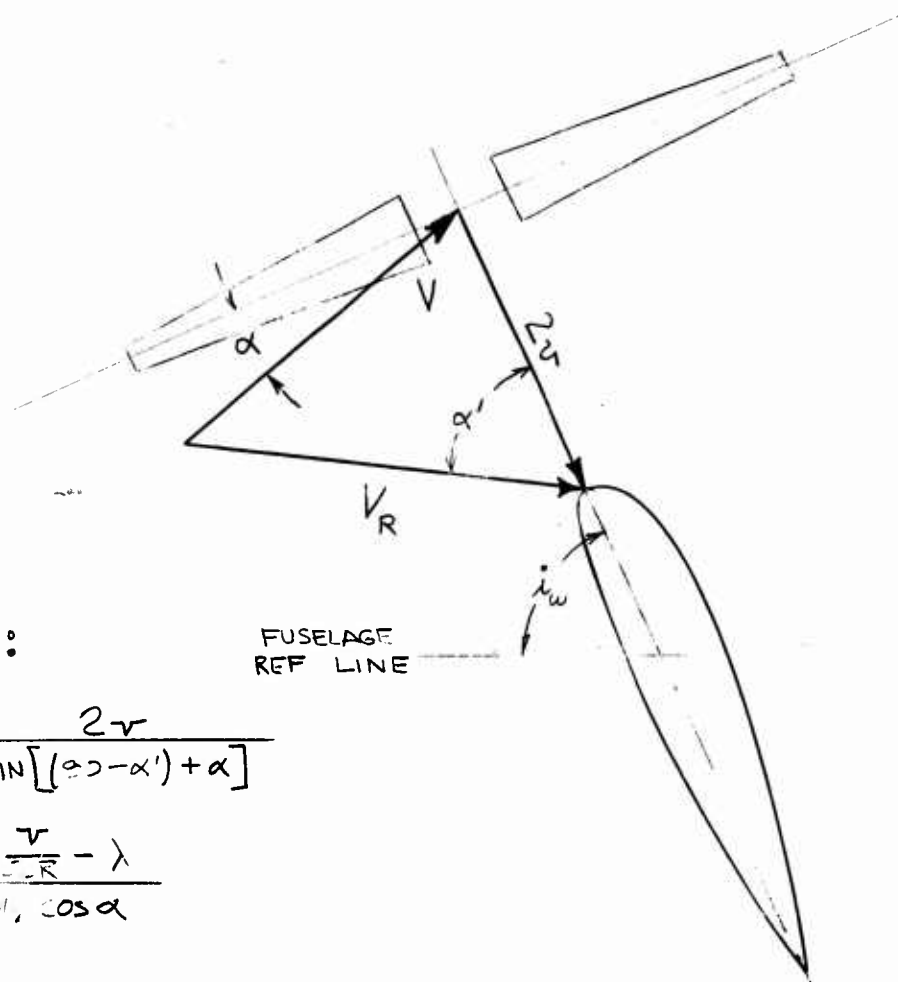
or at least considerably reduce the magnitude of these derivatives.

The induced velocity derivatives are essentially proportional to the sum of C_T and the absolute magnitude of the respective C_T derivative thereby producing a direct relationship between the rotor operating condition and the most important wing derivatives. With the possible exception of the direct rotor contributions to Z_α and X_α which are very straight-forward, this induced velocity effect is probably the most important contribution of the rotor to over-all aircraft static

derivatives. The rotor pitch-rate derivative due to the flapping hinge offset is a completely different situation, however, and will be considered in another section. Hinge offset effects are certainly present in the static moment derivatives, but the geometry of the rotor location with respect to the c.g. allows the moment derivatives generated by the rotor forces to effectively cancel the hinge offset contributions as can be seen in the rotor contribution breakdown figures. In short, it can be said that the rotor contribution to the moment derivatives is essentially reduced to an indirect influence on the wing derivatives.

WING DEPENDENT VARIABLES

$$\alpha' \neq V_R$$



LAW OF SINES:

$$\frac{V}{\sin \alpha'} = \frac{2r}{\sin[(90 - \alpha') + \alpha]}$$

$$\alpha' = \cot^{-1} \frac{\frac{V}{2r} - \lambda}{\mu \cos \alpha}$$

LAW OF COSINES:

$$V_R^2 = (2r)^2 + V^2 - 2V(2r) \cos(90 - \alpha)$$

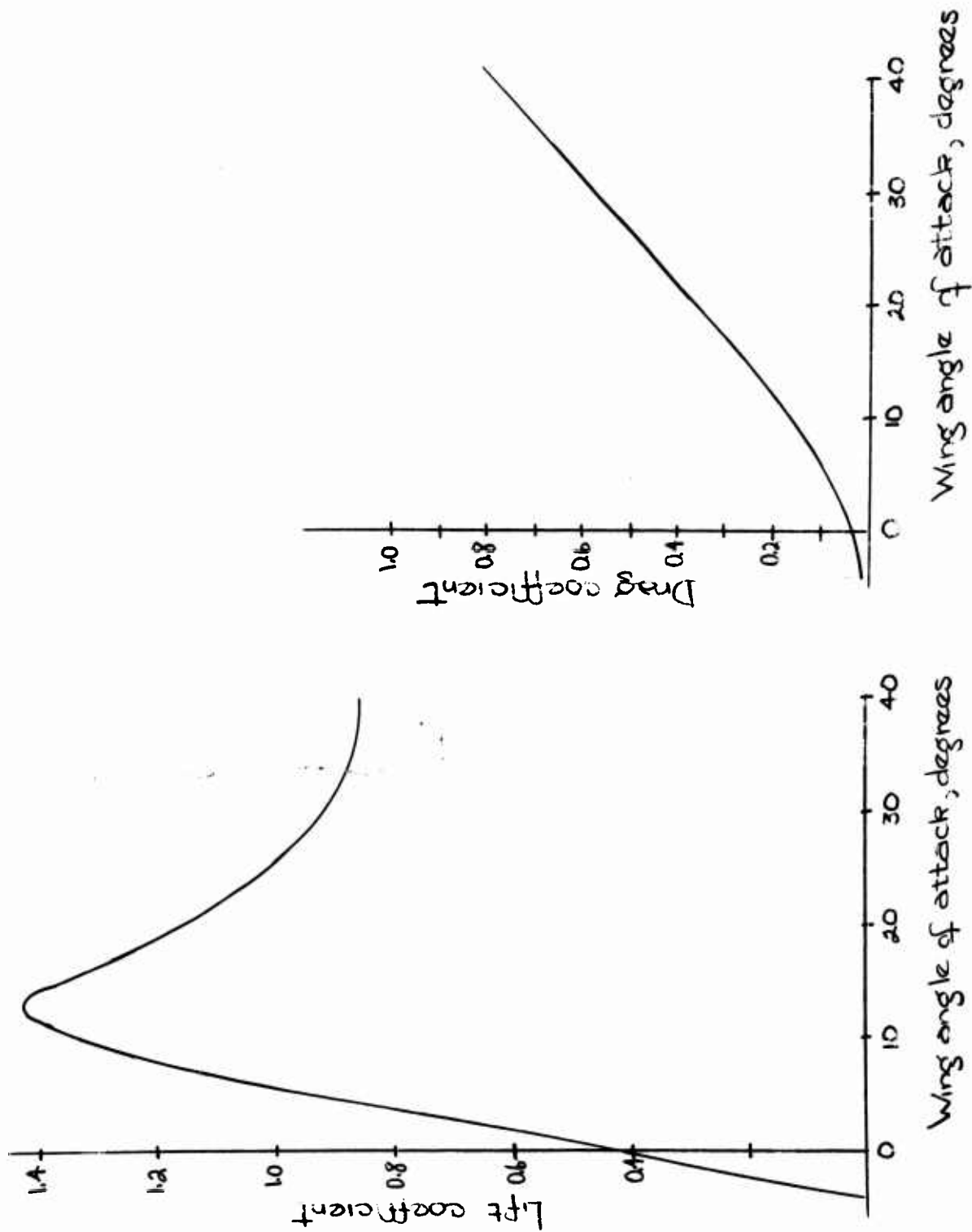
$$\left(\frac{V_R}{2r}\right)^2 = \mu^2 - 4 \frac{V}{2r} \lambda$$

WING OPERATING CONDITIONS

Several methods are presented in Appendix A for determining the operating conditions of the wing behind the rotor, the first of which is similar to the developments of Reference 4. This method consists quite simply of determining the rotor downwash as outlined above, and adding it vectorially to the free-stream velocity to give a resultant velocity and angle of attack. For this purpose it is assumed that the wing is completely immersed in the slipstream, and the slipstream is fully developed by the time it reaches the wing whose .25 chord is about 35 per cent diameter behind the disk. The authors of Reference 7 have determined experimentally that insignificant additional development occurs beyond 10-15 per cent D behind the rotor disk, and the airplane configuration is such that the rotor just spans the wing outboard of the fuselage cut-out so that both the above assumptions seem reasonably valid. In this method, it is assumed that the wing angle of attack and resultant velocity as determined above, together with the power-off lift and drag characteristics of the particular airfoil section under consideration completely determine the wing operating conditions. For simplicity the sectional lift and pitching moment coefficients, at the proper Reynold's Number, are assumed to apply for the entire wing, and induced drag is computed on the basis of the aspect ratio of the semi-span. The lift and drag curves used are presented in Figure 41 as functions of angle of attack. Ideally, these curves should be replaced with actual measured force data on the wing in the slipstream, and coefficients could be derived from

the particular slipstream velocity and wing area and plotted against angle of attack as derived from the rotor conditions. This is done, with minor variations, in Reference 7 for a different wing-rotor combination than that under consideration here. The pertinent curves given in this Reference are reproduced in this report in Figure 42. In attempting to adapt this data for application to the V-76 wing, correction was made for the cambered section by adding 0.4 to the C_L of the symmetrical section. As Figure 42 illustrates, the wing parameters are certainly functions of more than α' and V_R with the result that the total C_L and the character of stall are considerably altered, depending upon power condition.

Fig. 41



Reference 4 Wing Characteristics

WING LIFT & DRAG

REFERENCE 7 EXPERIMENTAL DATA

$$T_c'' = 0.914$$

α' INDICATED FOR $\lambda_w = 70^\circ$

TRIM CASE

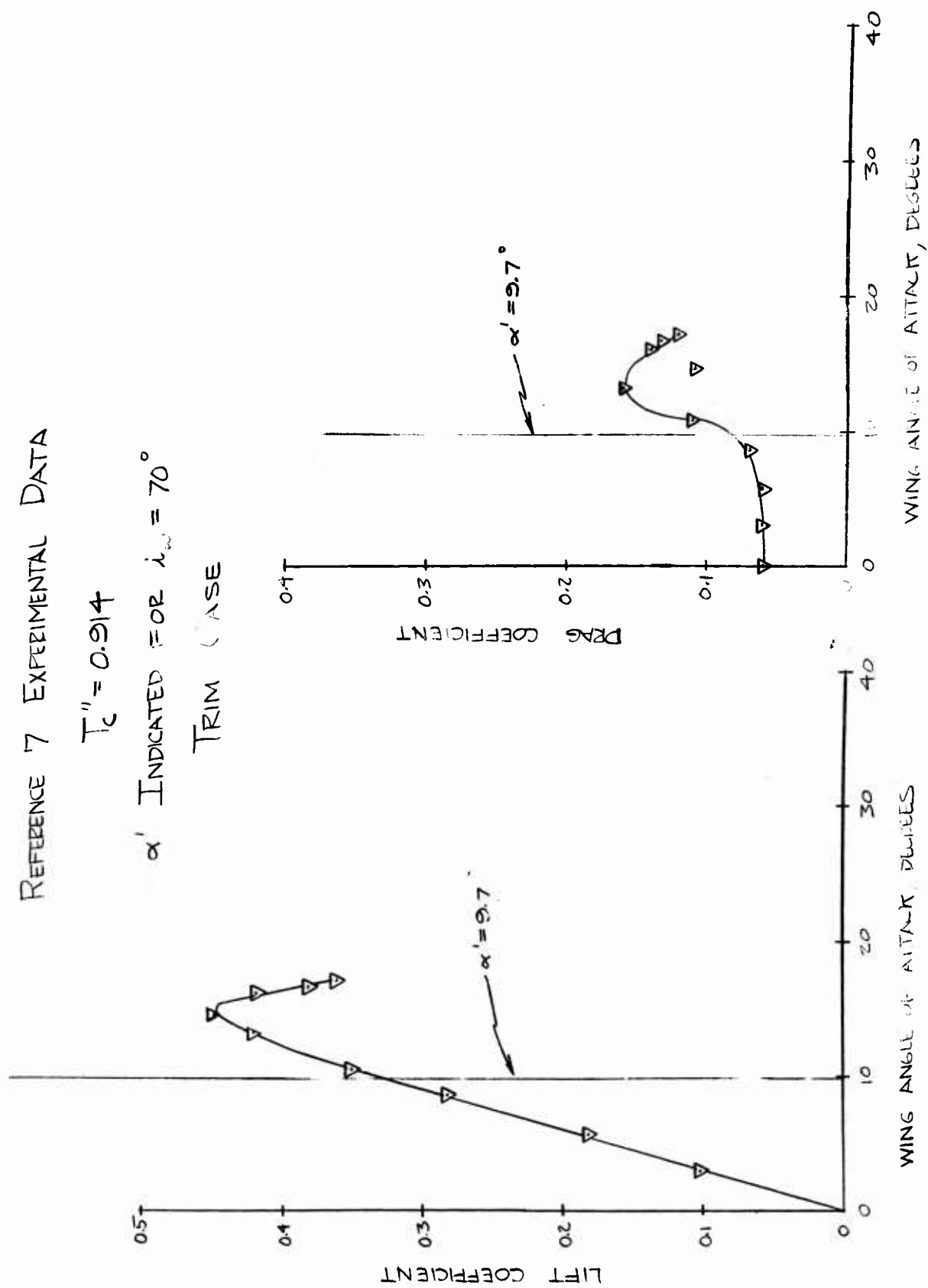


Fig. 42a

WING LIFT & DRAG

REFERENCE 7 EXPERIMENTAL DATA

$$T_c'' = 0.88$$

α' INDICATED FOR $i_w = 57^\circ$

TRIM CASE

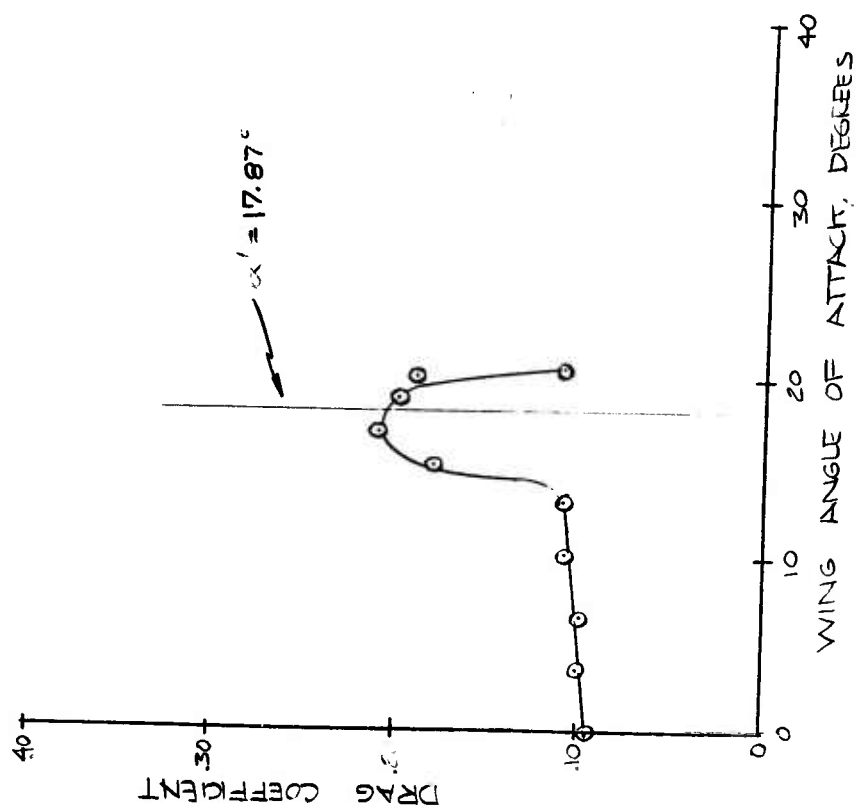
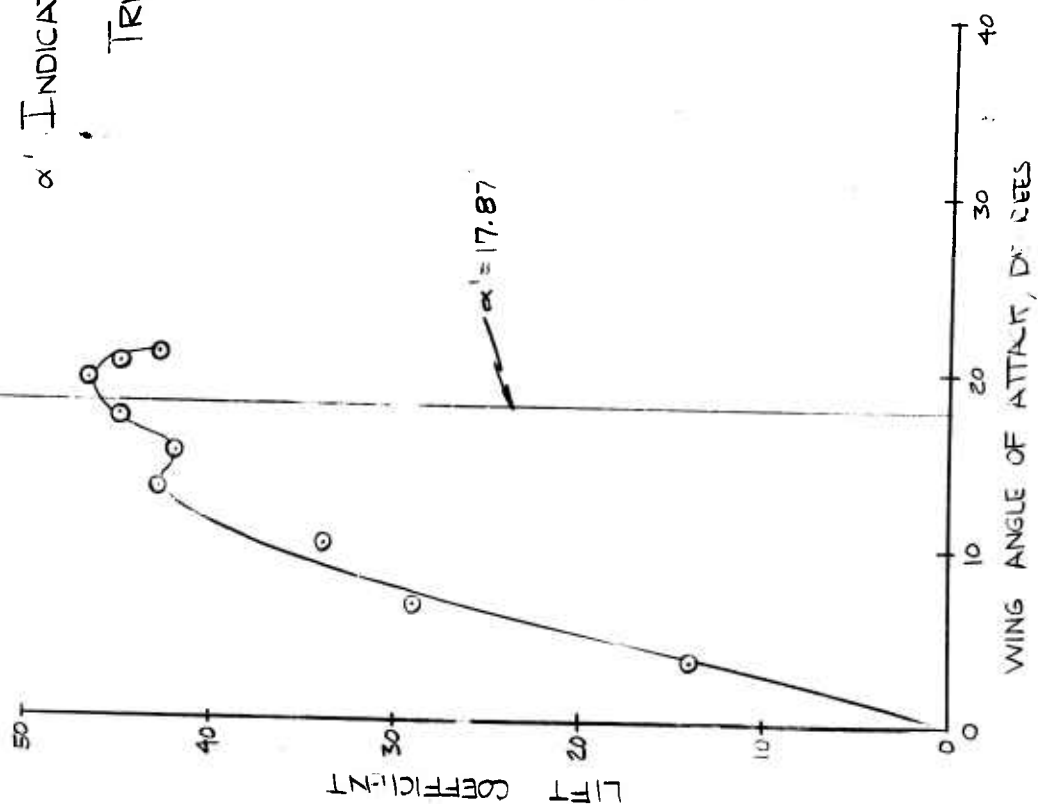


Fig. 42b

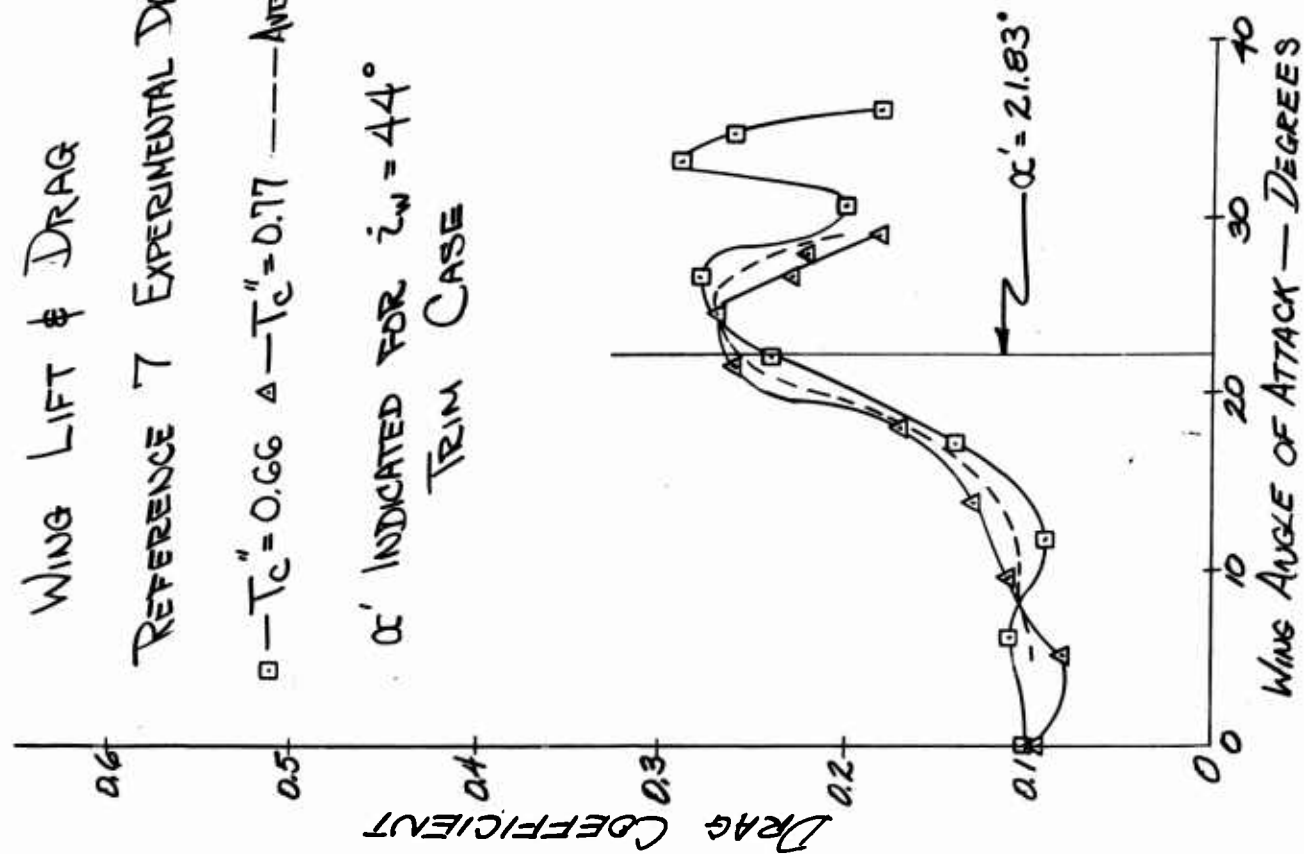
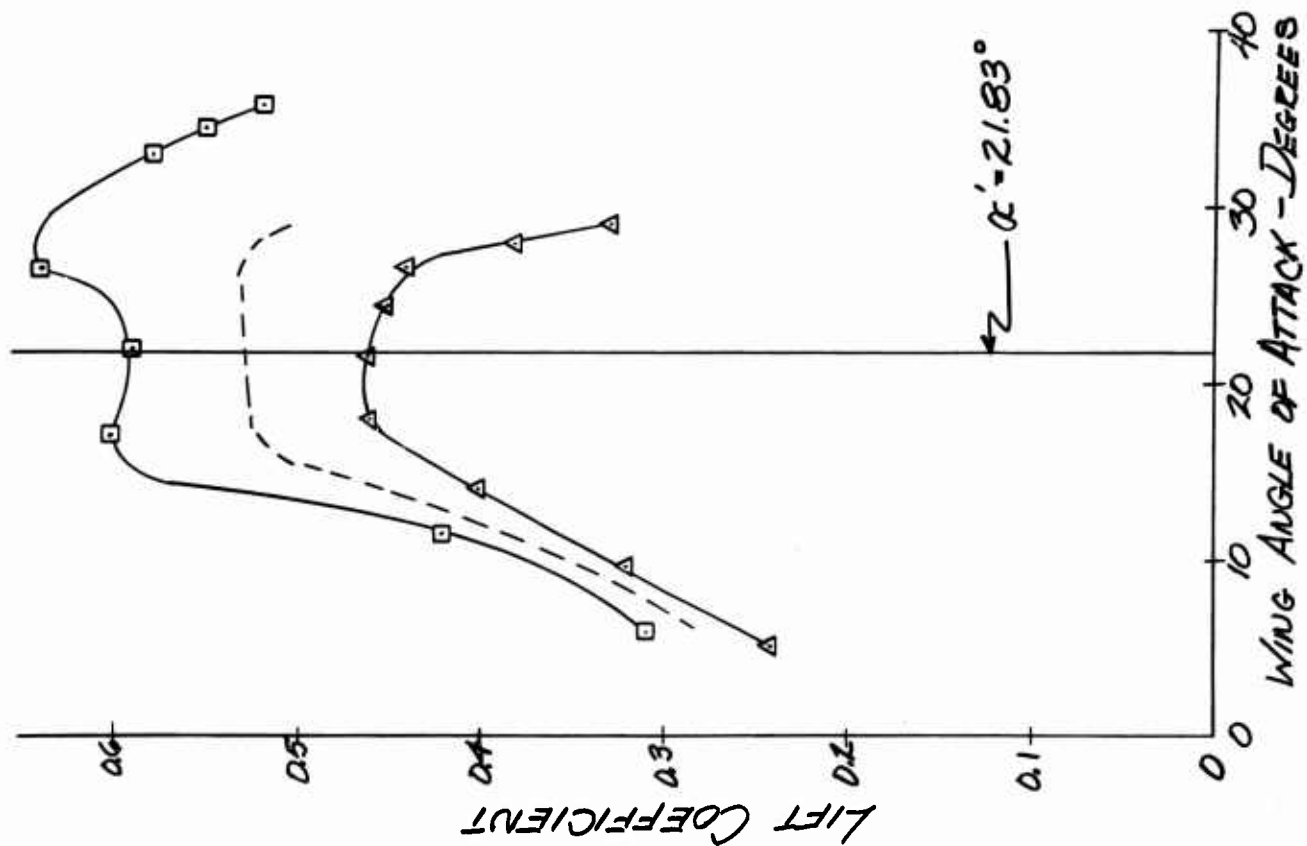


Fig. 42-c

WING CONTRIBUTIONS

The variations in wing operating conditions exert a very profound influence on the wing derivatives particularly where they involve changes in lift curve slope. Figures 47 through 53 present breakdowns of the various effects going to make up the static stability derivatives along with the summation of these component effects as compared to the experimentally measured derivatives. It can be seen that the effects due to α' are generally much stronger than those due to V_R with the result that the important wing characteristic is lift curve slope rather than over-all lift coefficient. This is unfortunate as far as the desire to predict these effects is concerned, since the character of wing stall is a major contribution to lift curve slope changes and being completely dependent on local flow conditions, is very difficult to predict. The third method of determining wing conditions by using the trim condition and theoretical rotor forces to solve for wing forces, gives results that allow a check on wing forces but not wing derivatives. Figure 43 presents a comparison of the information obtained by all three methods considered, and points out the general agreement in lift coefficient and the large variations in lift curve slope as determined by the two available methods. A similar presentation in Figure 44 of the wing drag shows somewhat large discrepancies due, in part, to the differences in magnitude of the various forces involved in the trim solution and, in part, to the effects of local stalling which cannot be predicted. In general, the wing drag terms are of an order of magnitude less importance than the lift terms, except

perhaps in the Z_{α} derivative at $i_w = 70^\circ$ where a strong positive $C_{D\alpha}$, might account for the positive experimental value of Z_{α} as shown in Figure 47. The overpowering influence of $C_{L\alpha}$ in all other cases makes it reasonable to compare the two wings and their resultant derivatives on the basis of this parameter alone. With this supposition, an examination of the comparison of theoretical to experimental total derivatives in Figures 47 and 48 indicates that, if the rotor derivatives are generally correct, the wing should have a positive lift curve slope in all conditions tested. The magnitude of this slope would seem to vary from a value somewhere between that given by the wings of References 4 and 7 at $i_w = 70^\circ$ to approximately zero in the $i_w = 44^\circ$ condition—a trend that is generally followed by the data of Reference 7 but certainly not by the results given by the power-off curves.

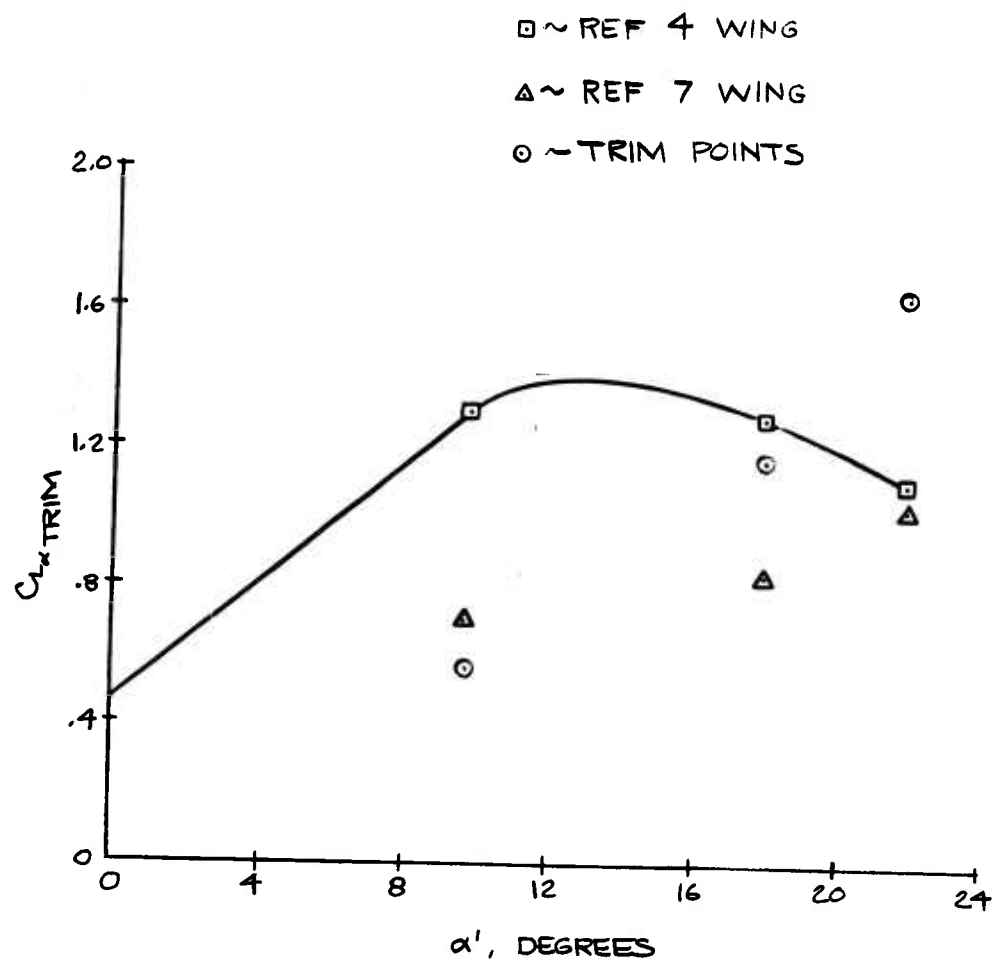
Several possibilities can be considered to account for the dependence of wing C_L and $C_{L\alpha}$ on thrust and velocity beyond the effects of V_R and α' . Perhaps the most obvious one is to suppose that rotor slipstream development along the wing chord produces a sufficient favorable pressure gradient as to provide a boundary layer control effect and thereby delay wing stall. If this were the case one would expect that $C_{L_{max}}$ of the power-on wing would be higher than that of the power-off condition, and this effect would increase in relation to the slipstream strength. This is definitely not the case presented by the data of Figure 42 and reason has already been given to support the validity of assuming little slipstream development beyond the wing leading edge.

The method presented in Reference 7 of accounting for the diminishing value of C_L with constant α' and increasing thrust by a mass flow correction for un-immersed wing sections is a reasonable approach, but cannot predict the existence of continued positive $C_{L\alpha'}$ beyond the α' —stall of the power-off wing. In any case, the wing center cut-out on the V-76 obviates the possibility of applying such a correction, since for all intents and purposes this wing probably behaves as though it were two separate completely immersed semi-spans. The trim points of Figure 43 show, however, that there still exists some strong effect producing a change in C_L with thrust and/or forward velocity that cannot be accounted for by V_R and α' alone, and, as has been pointed out previously, this effect evidently also influences the stall characteristics of the wing as a whole. The three-dimensional effects on lift curve slope are accounted for in the considerations of Reference 5, and will in general produce a decrease in $C_{L\alpha'}$ with increasing thrust. These approaches alone, however, offer no explanation for the wing behavior beyond the predicted stall condition.

A partial explanation for both of these phenomena is the next subject for discussion, and takes the form of a consideration of the possible effects of slipstream rotation on the over-all wing operating conditions and how these effects might be predicted. In advance of the development it can be said that the desire is to demonstrate that such a phenomenon as change in local angle of attack along the span due to rotational velocities can manifest itself in changes of averaged over-all wing parameters whose net effect is definitely non-zero.

Also one would hope to demonstrate that such net effects follow definite important trends that are to some degree predictable. First the local effects will be evaluated and then an explanation given of the over-all significance of these effects.

COMPARISON OF ASSUMED WING CHARACTERISTICS
TO REQUIREMENTS FOR HORIZONTAL & VERTICAL TRIM



Comparison of Assumed Wing Characteristics to Requirements for Horizontal & Vertical Trim

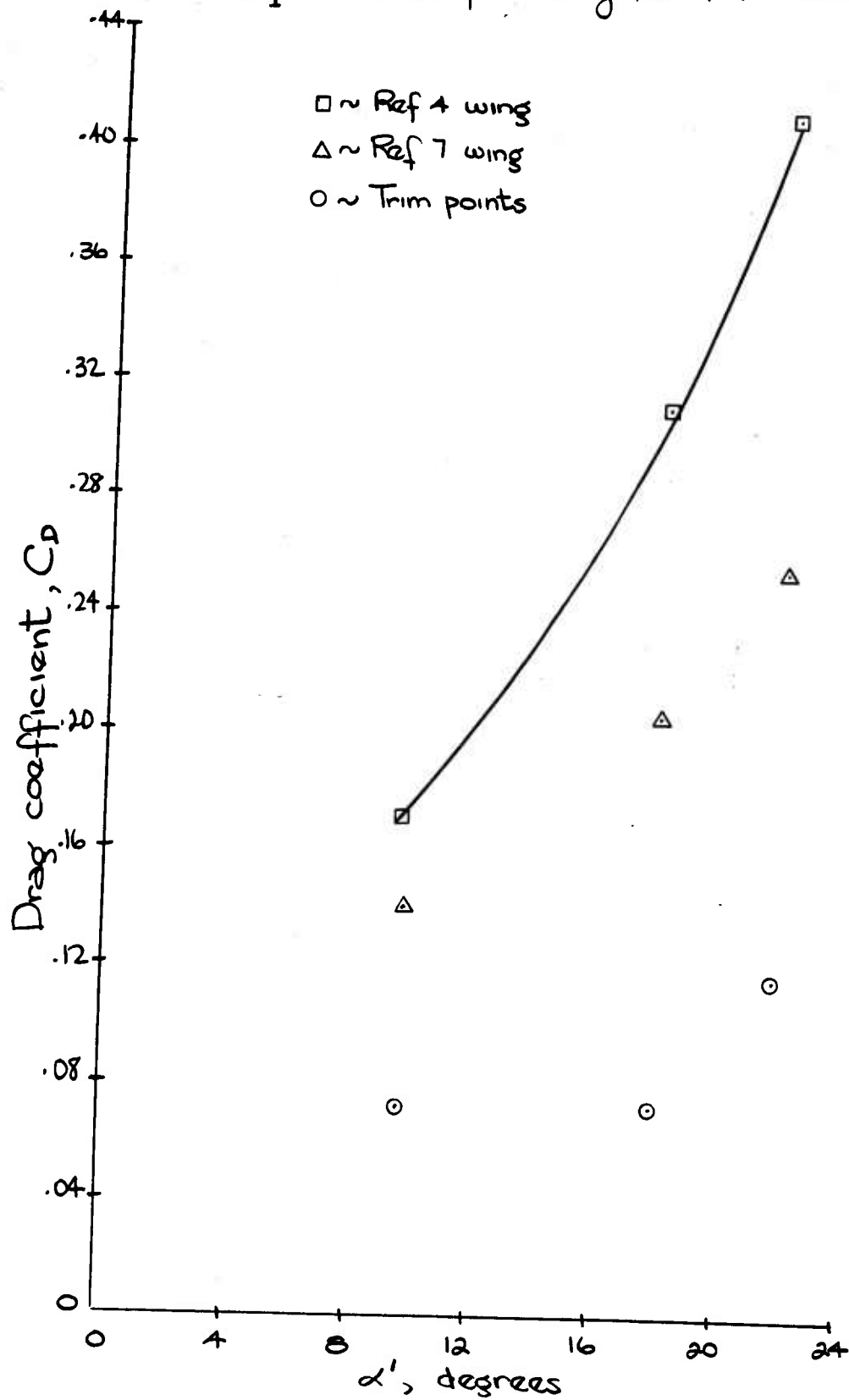


Fig. 45

EXPERIMENTAL STATIC DERIVATIVES ACCELERATION EFFECTS

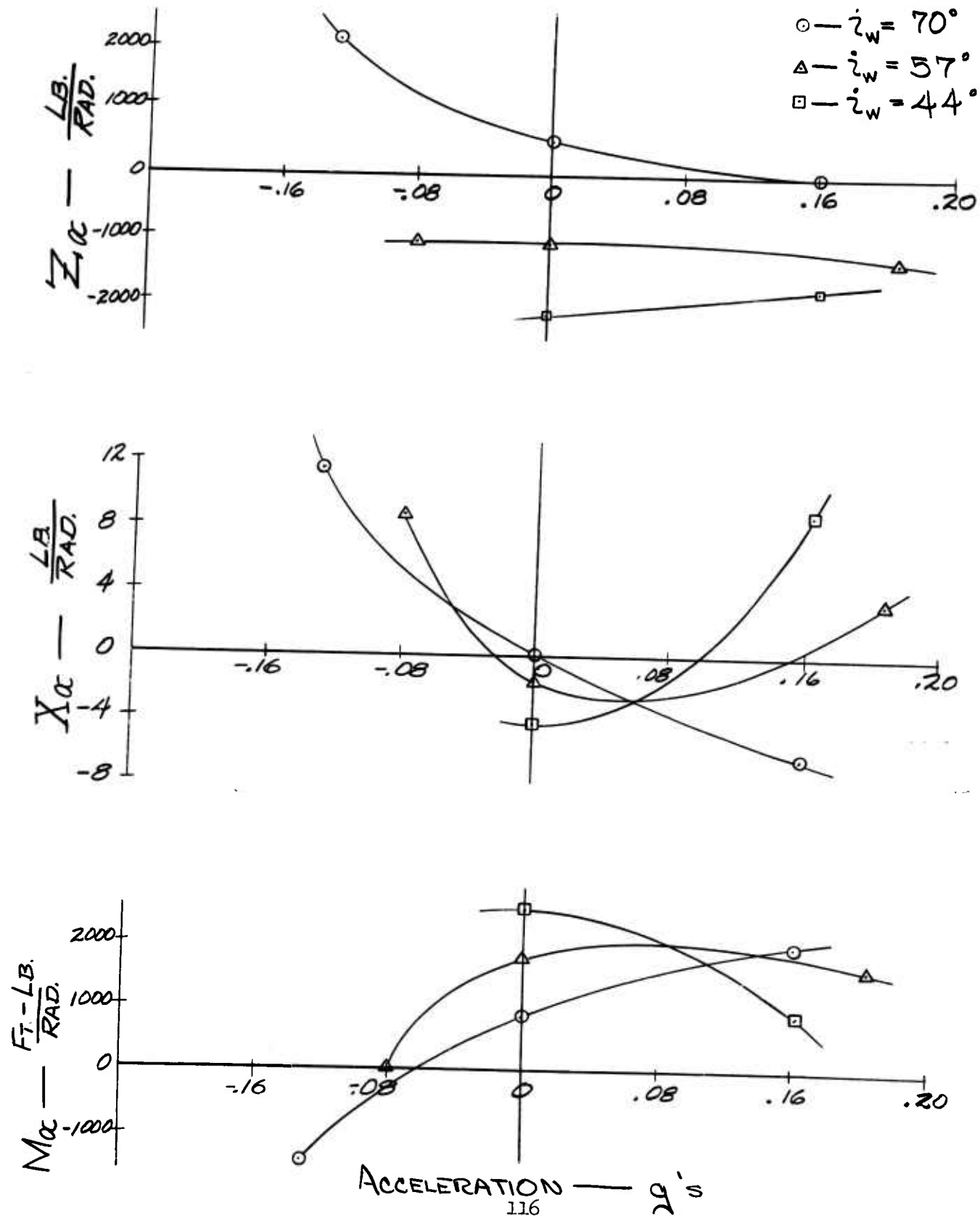
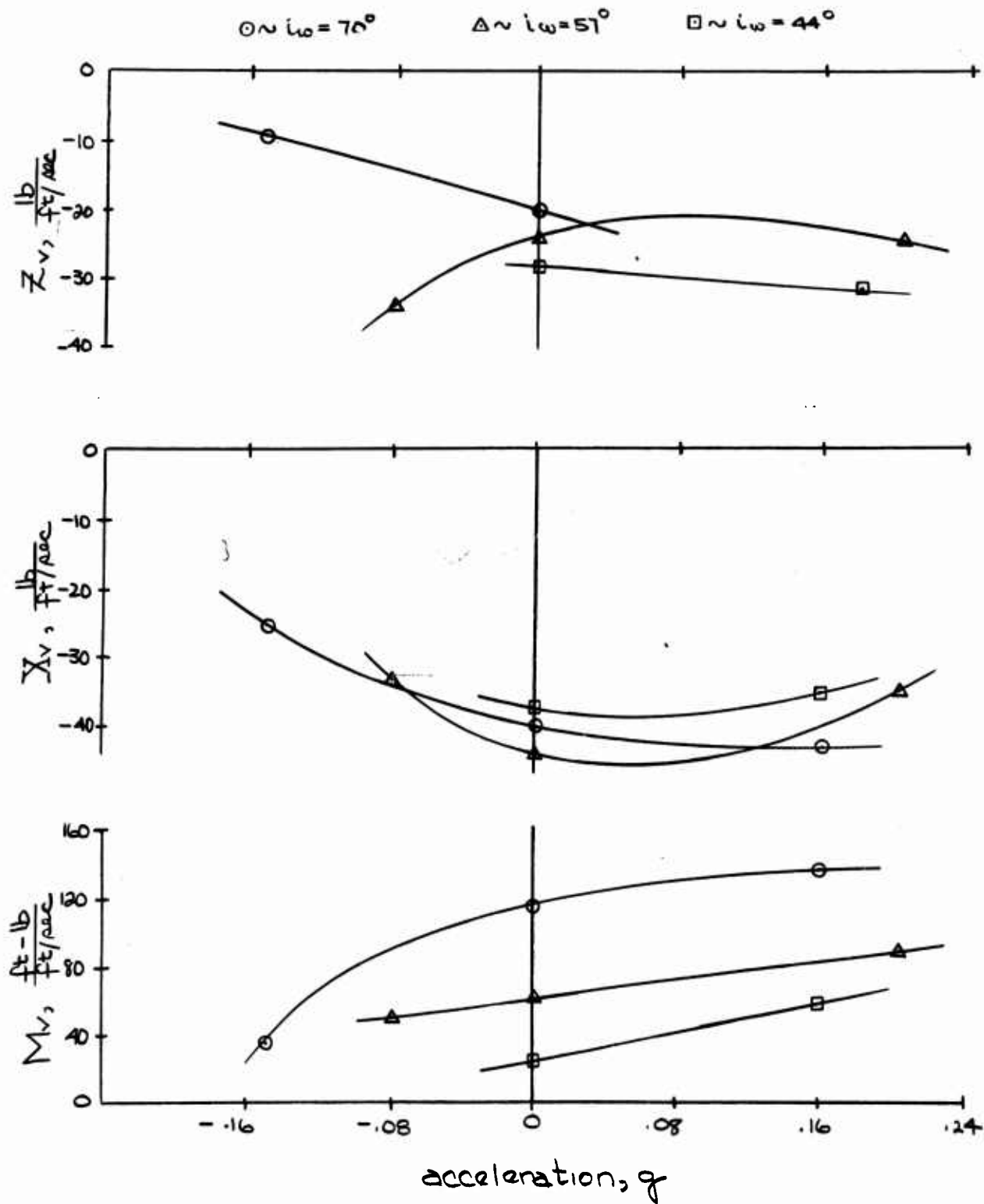
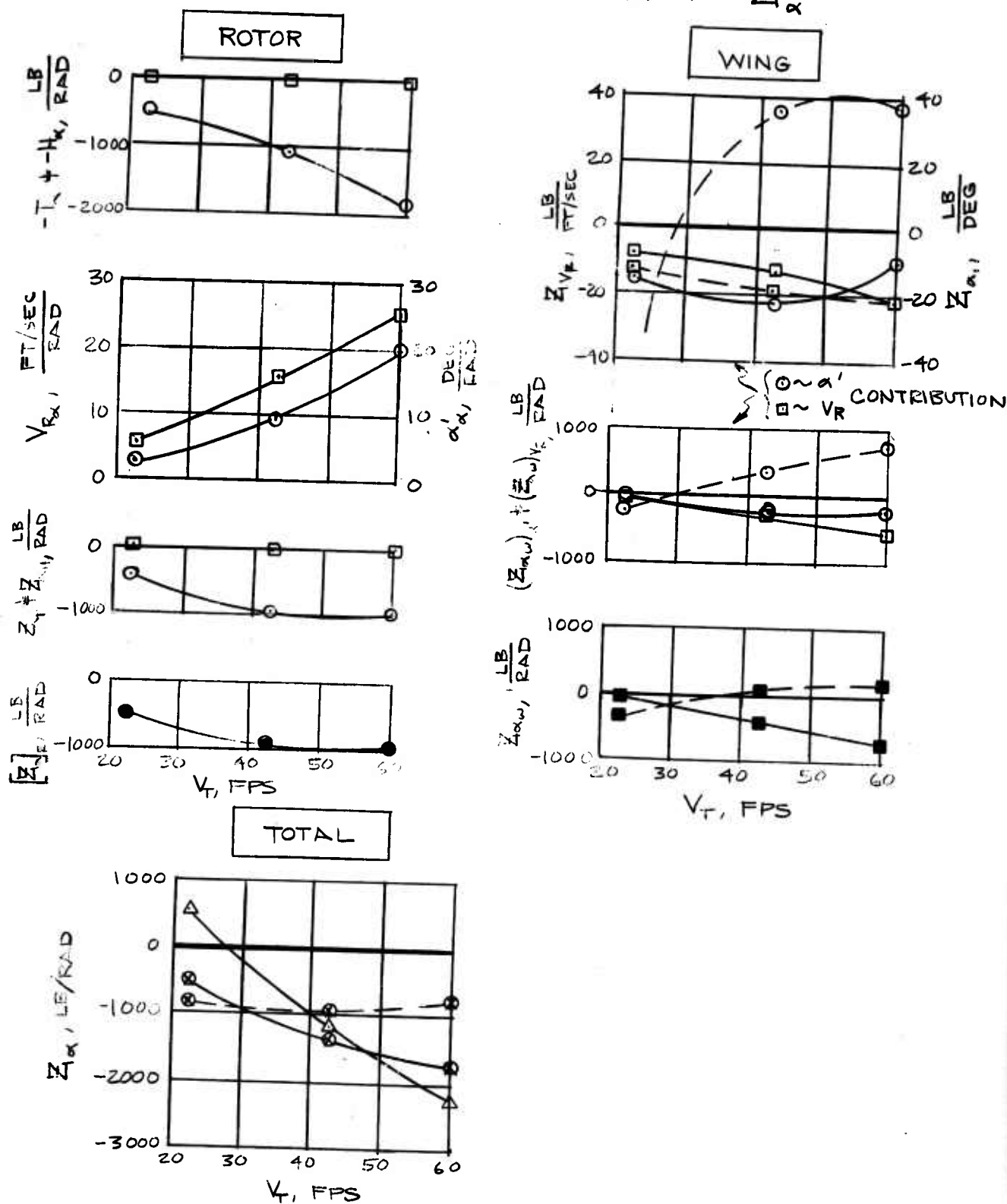
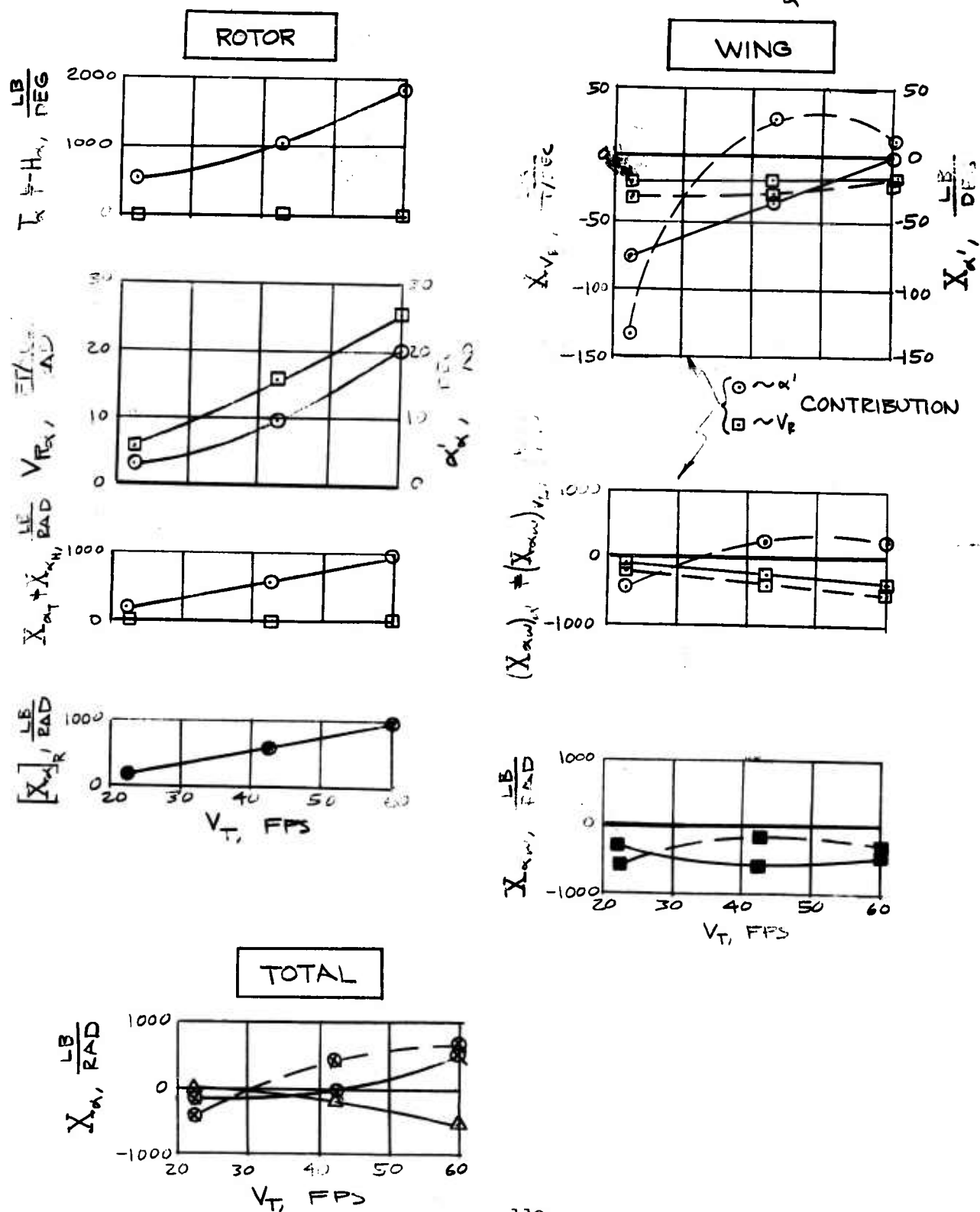


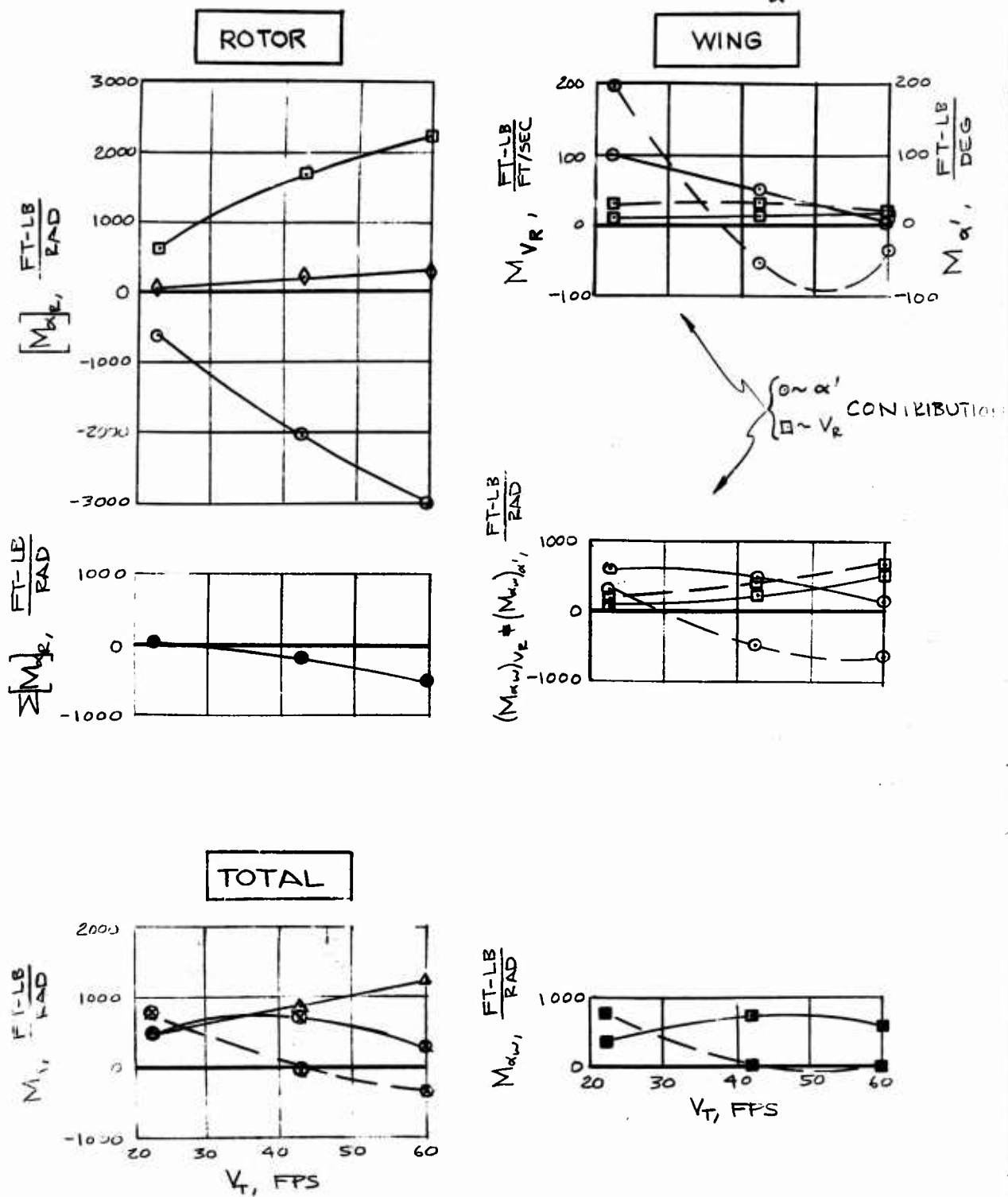
Fig. 46

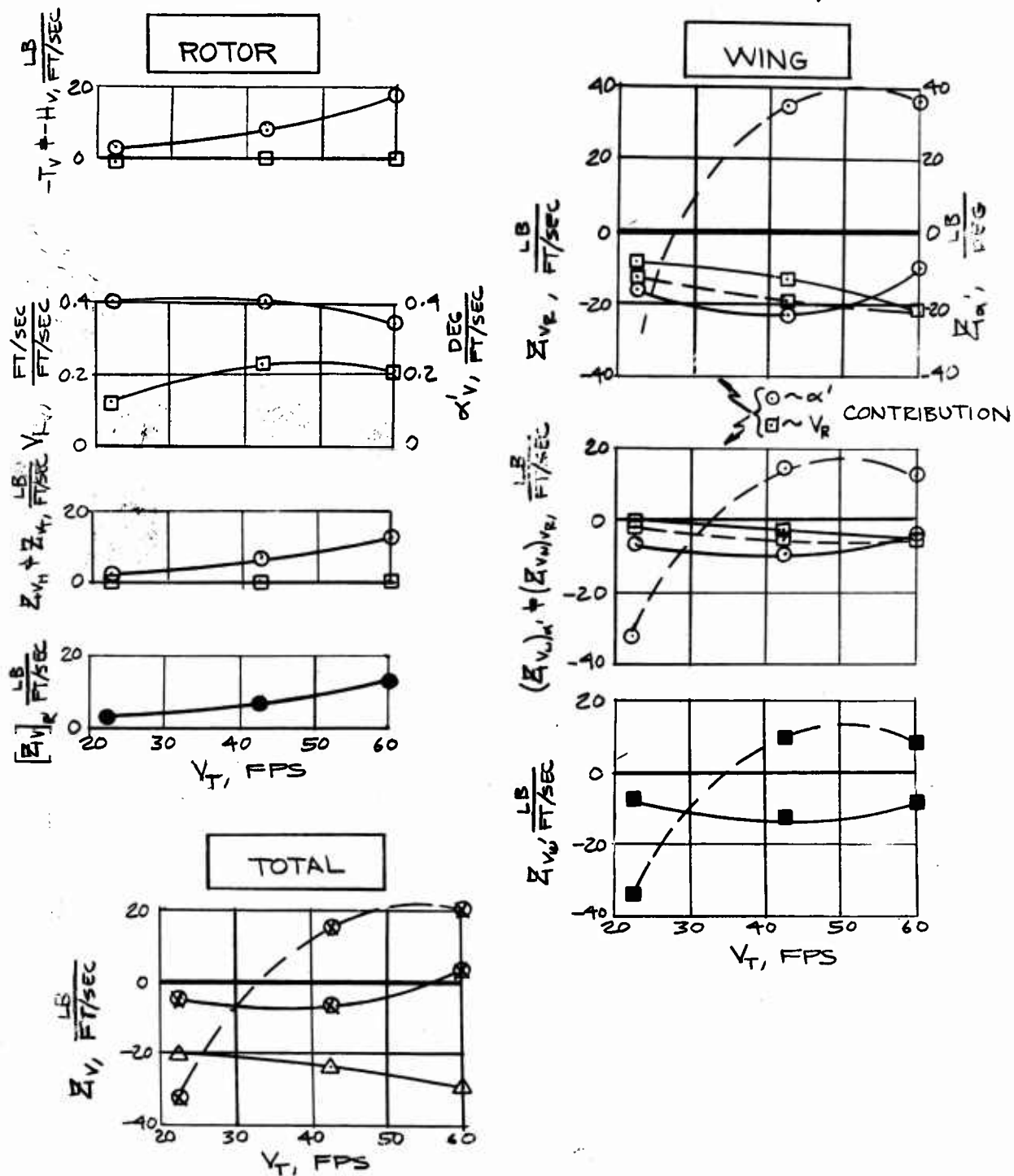
Experimental Static Derivatives Acceleration Effects

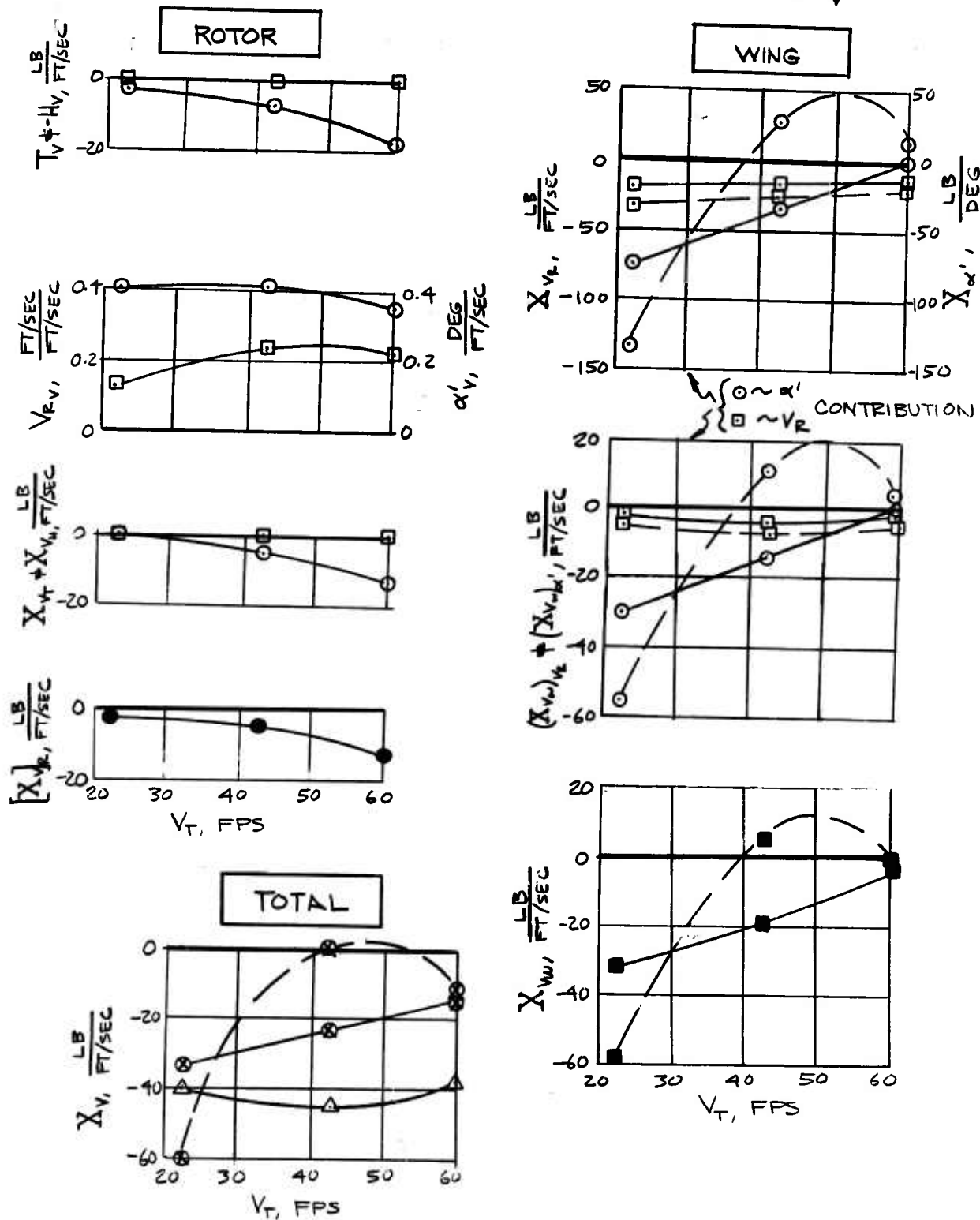


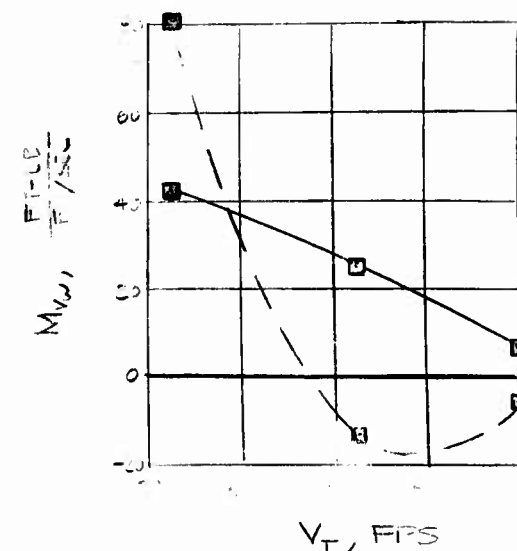
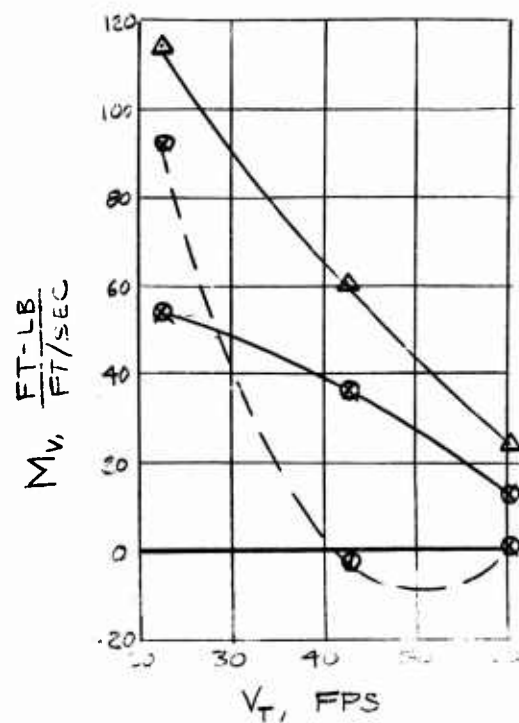
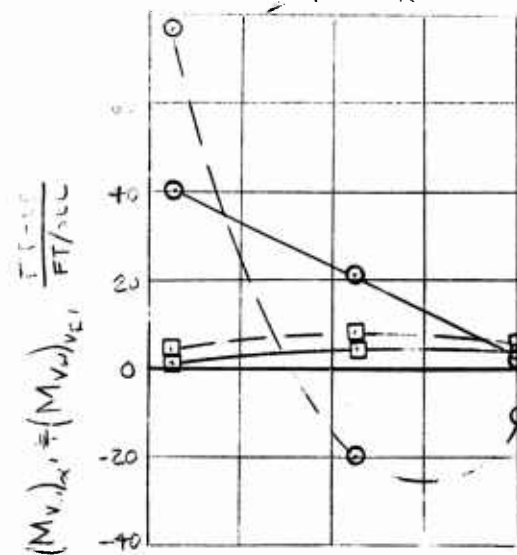
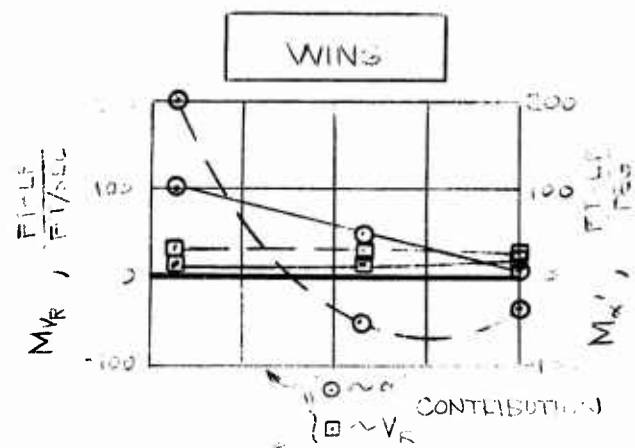
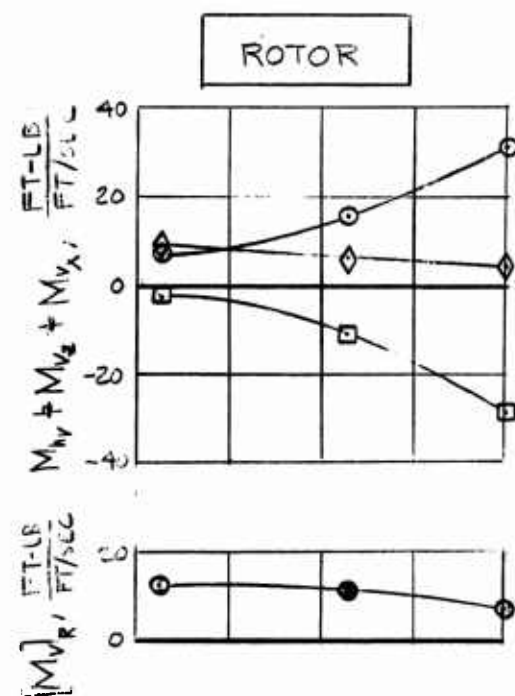
CONTRIBUTIONS OF WING & ROTOR TO Z_α 

CONTRIBUTIONS OF WING & ROTOR TO X_α 

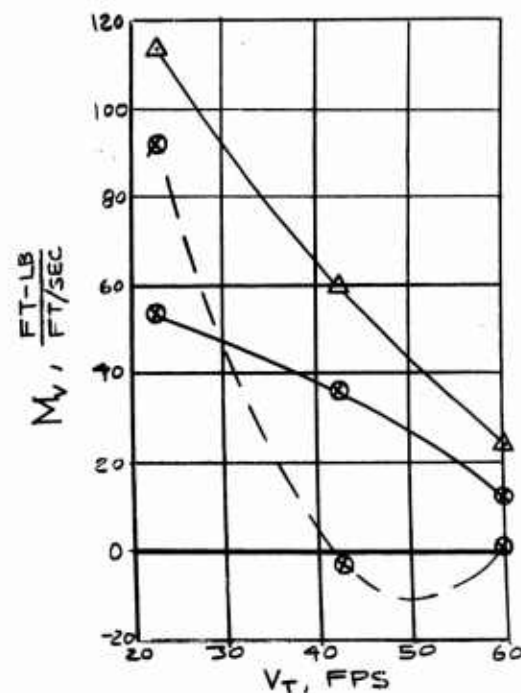
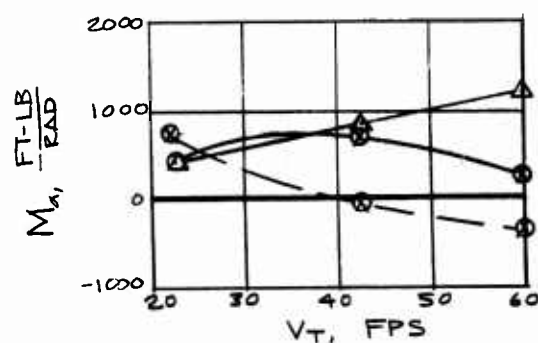
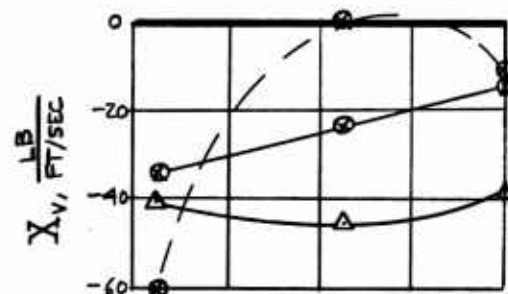
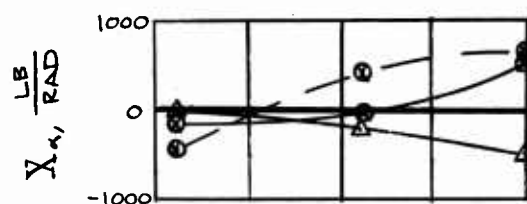
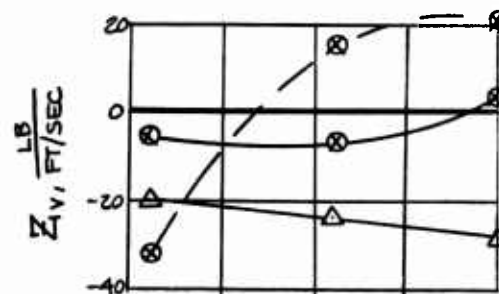
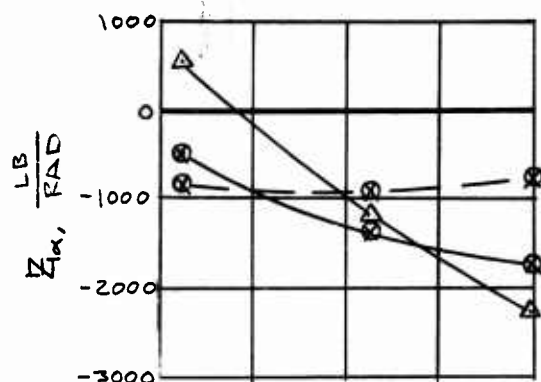
CONTRIBUTIONS OF WING + ROTOR TO M_{α} 

CONTRIBUTIONS OF WING & ROTOR TO Z_V 

CONTRIBUTIONS OF WING & ROTOR TO X_V 

BREAKDOWN OF THROUSTING CONTRIBUTIONS TO M_V 

COMPARISON OF EXPERIMENTAL AND THEORETICAL DERIVATIVES (WING + ROTOR)



Legend for Figures 47 through 53

$\text{---}\Delta\text{---}$	experimental
$\text{---}\text{---}$	ref 7 wing
$\text{---}\text{---}\text{---}$	ref 4 wing
\square	wing total
\bullet	rotor total
\otimes	wing + rotor total

Equations for Figures 47 through 52

ROTOR

WING

Fig 29: $[Z_\alpha]_R = Z_{\alpha_H} + Z_{\alpha_T}$

Fig 30: $[X_\alpha]_R = X_{\alpha_H} + X_{\alpha_T}$

Fig 31: $[M_\alpha]_R = M_{h\alpha} - X_R Z_{\alpha R} - Z_R X_{\alpha R}$

Fig 32: $[Z_v]_R = Z_{v_H} + Z_{v_T}$

Fig 33: $[X_v]_R = X_{v_H} + X_{v_T}$

Fig 34: $[M_v]_R = M_{h_v} - Z X_{v_R} - X Z_{v_R}$

$$Z_{\alpha w} = Z_{\alpha'} \alpha'_{\alpha} + Z_{v_R} v_{R\alpha}$$

$$= (Z_{\alpha w})_{\alpha'} + (Z_{\alpha w})_{v_R}$$

$$X_{\alpha w} = X_{\alpha'} \alpha'_{\alpha} + X_{v_R} v_{R\alpha}$$

$$= (X_{\alpha w})_{\alpha'} + (X_{\alpha w})_{v_R}$$

$$M_{\alpha w} = M_{\alpha'} \alpha'_{\alpha} + M_{v_R} v_{R\alpha}$$

$$= (M_{\alpha w})_{\alpha'} + (M_{\alpha w})_{v_R}$$

$$Z_{v w} = Z_{\alpha'} \alpha'_{v} + Z_{v_R} v_{Rv}$$

$$= (Z_{v w})_{\alpha'} + (Z_{v w})_{v_R}$$

$$X_{v w} = X_{\alpha'} \alpha'_{v} + X_{v_R} v_{Rv}$$

$$= (X_{v w})_{\alpha'} + (X_{v w})_{v_R}$$

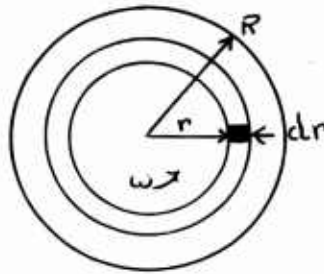
$$M_{v w} = M_{\alpha'} \alpha'_{v} + M_{v_R} v_{Rv}$$

$$= (M_{v w})_{\alpha'} + (M_{v w})_{v_R}$$

SLIPSTREAM ROTATION

In order to determine the magnitude of the rotational velocities to be expected, a very simple application of Conservation of Momentum may be made to the angular flow through the rotor similar to the analysis of axial flow. An application of Newton's Second Law to the axial flow yields the relation that net thrust equals net change in axial momentum through the disk. For rotational flow this can be modified to say that the net torque exerted by the rotor on the flow equals net change in angular momentum through the disk.

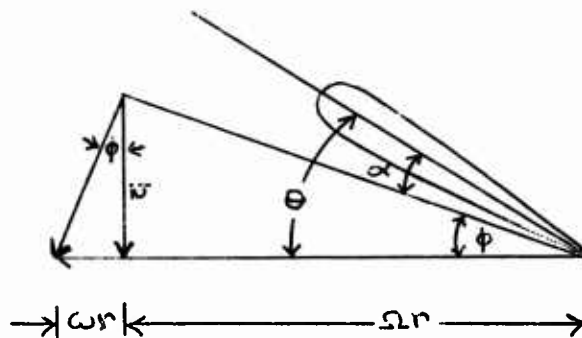
Assuming zero initial rotation and referring to the diagram below, we can write an expression for the net change in angular momentum of an annular ring of mass $2 \pi r m dr$ as



$$dQ = (2 \pi r m dr) r [2 r \omega(r)]$$

where $2r\omega(r)$ is the downstream tangential velocity at r . It is difficult to determine the exact distribution of rotational velocity in forward flight. However, a reasonable blade element analysis can be made in hover. Using the results of such an analysis, a general profile of induced velocity can be obtained and the magnitudes adjusted so that the average value of induced velocity corresponds to that obtained by the constant induced velocity analysis of Appendix A.

Referring to the diagram below, which represents a blade element in hovering flight



we see that

$$\tan \phi \cong \phi = \frac{v}{\Omega r}$$

$$\& \tan \phi \cong \phi = \frac{\omega r}{v}$$

or rearranging and substituting,

$$v = \phi \Omega r$$

$$\omega r = \phi^2 \Omega r$$

A hovering blade-element analysis as in Reference 6 yields for a rotor with linear twist

$$\phi = -\frac{\sigma a_0}{16x} + \sqrt{\left(\frac{\sigma a_0}{16}\right)^2 \frac{1}{x^2} + \frac{\sigma a_0}{8} \frac{1}{x} (\theta_0 - .419x)}$$

where $x = \frac{r}{R}$ and $(\theta_0 - .419x)$ represents the blade pitch as a function of r . A solution of this expression for the V-76 rotor is presented in Figure 55 as a plot of $\phi(\Omega R)$ vs. x and the necessary correction factors have been applied to the hovering results to bring the average $v = \phi(\Omega R)x$ up to the indicated value determined for the various trim

conditions. Also shown in this Figure are the values of $\Omega R^2 \phi^2$, ωr , and $x^2 \omega r$ obtained by the above analysis.

As a check on the above analysis we can refer back to the angular momentum developments and compute the power required using the rotational velocity distribution and magnitude determined. Rewriting the torque expression

$$dQ = 4\pi m r^2 (r\omega) dr = 4\pi R^3 x^2 (r\omega) dx$$

and noting that $\pi R^2 m = \text{total mass flow through the rotor} = \frac{T}{2N}$ we can integrate both sides, giving

$$Q = \frac{2TR}{N} \int_0^1 x^2 (r\omega) dx$$

Figure 55 gives a graphical evaluation of the integral in the $i_w = 70^\circ$ case as

$$\int_0^1 x^2 (r\omega) dx = 3.06 \text{ ft/sec}$$

Using the values of T and v obtained from the analysis of Appendix A the resulting power per rotor can be written.

$$HP_{\text{ROTOR}} = \frac{Q\Omega}{550} = 204 \text{ HP}$$

Assuming a maximum profile power of 25 per cent of induced power, the net total horsepower required in this condition is found to be 510 horsepower. Full scale flight test results indicate that this value is probably conservative, and correspondingly higher rotational

velocities than those predicted might be encountered. The values determined, however, are adequate to demonstrate the effect of rotational velocity on wing operating conditions. In Figures 56 through 58 are presented composite representations of the vector velocity diagrams at the rotor and the wing. The resulting wing angles of attack are determined by the vector summation of the fully developed rotor slipstream velocities and the forward flight velocity at the three trim speeds. Figure 59 shows the local wing angle of attack plotted along the semi-span along with C_L and $C_{L\alpha'}$ as determined from the power-off lift curve of Figure 41. Also shown in Figure 59 and 60 are the average values of α' , C_L , $C_{L\alpha'}$, C_D and $C_{D\alpha'}$ as compared to those values predicted by neglecting rotation and assuming constant induced velocity. The most interesting effects apparent are the decrease in C_L and the net effective positive $C_{L\alpha'}$ predicted by the rotation analysis for the $i_w = 70^\circ$ and $i_w = 57^\circ$ trim conditions. These values are in considerable disagreement with the non-rotating predictions, but seem to satisfy reasonably well the requirements of the wing as dictated by the measured static derivatives and trim conditions.

The $i_w = 44^\circ$ case indicates a completely stalled wing with all local $C_{L\alpha'}$'s negative, but an examination of the vector velocity diagram of Figure 53 reveals that a small increase in rotation could afford a significant change in local α' . The assumption of a hovering induced velocity distribution in this case is questionable and small changes in α' around the depicted values could quite conceivably alter the averaged $C_{L\alpha'}$ values appreciably. For these reasons

the conflict between the apparent $C_{L\alpha'} \cong 0$ requirement prescribed by the measured derivatives and the value given by the above analysis is not too disturbing. Such a conflict simply points out the sensitivity of the results to small changes in flow conditions and the difficulty in accounting for these effects.

It is possible however, to make some generalizations based upon the above developments concerning the net over-all effect of rotational considerations on the wing's operating conditions. Assuming some distribution of angle of attack along the immersed semi-span, an examination of Figure 61 (a) reveals that a general trend $C_{L\text{AVERAGE}} < C_{L\text{NON-ROT.}}$

will always be the result so long as one end of the α' spectrum is below the stall angle and the other end above. This means that an increase in the width of the α' spectrum — which would correspond to an increase in thrust coefficient at constant V , α , and Ω — would give a decrease in $C_{L\text{AVE.}}$ completely disassociated from any change in $\alpha'_{\text{NON-ROT.}}$ or V_R . However, if the lowest α' predicted is greater than the power-off stall angle than a similar increase in C_T would cause an increase in $C_{L\text{AVERAGE}}$ due to the negative lift curve slope beyond stall as shown in Figure 61 (b). Such an effect as this might account for the fact that in Figure 43 the power-off curve over predicts $C_{L\text{AVE.}}$ for high wing tilt angles and C_T under predicts it for lower i_w and C_T .

Another, and perhaps more important effect that can be noticed is the influence of rotation on the effective lift curve slope as demonstrated in Figure 61 (c). Here it can be seen that an increase

in α' NON-ROT. with the rotation constant results in an increase in $C_{L\text{AVERAGE}}$ as long as the lowest C_L' 's are below the stall angle and the absolute magnitude of the negative $C_{L\alpha'}$ slope on the power-off curve above stall is less than the positive value below stall.

Even when the lowest local α' is above stall, the real lift curve indicates partial recovery and positive values of $C_{L\alpha'}$ beyond stall which would contribute towards a lessening of the negative net $C_{L\alpha'}$ even at very large α' 's. This "softening" of stall effects on $C_{L\alpha'}$ is just the kind of effect required to account for the values indicated in the derivative breakdowns of Figures 47 through 52, and certainly the explanation is sufficiently plausible to warrant further consideration in a more detailed study of wing and rotor configurations.

HOVERING INDUCED VELOCITY DISTRIBUTION

Fig. 55

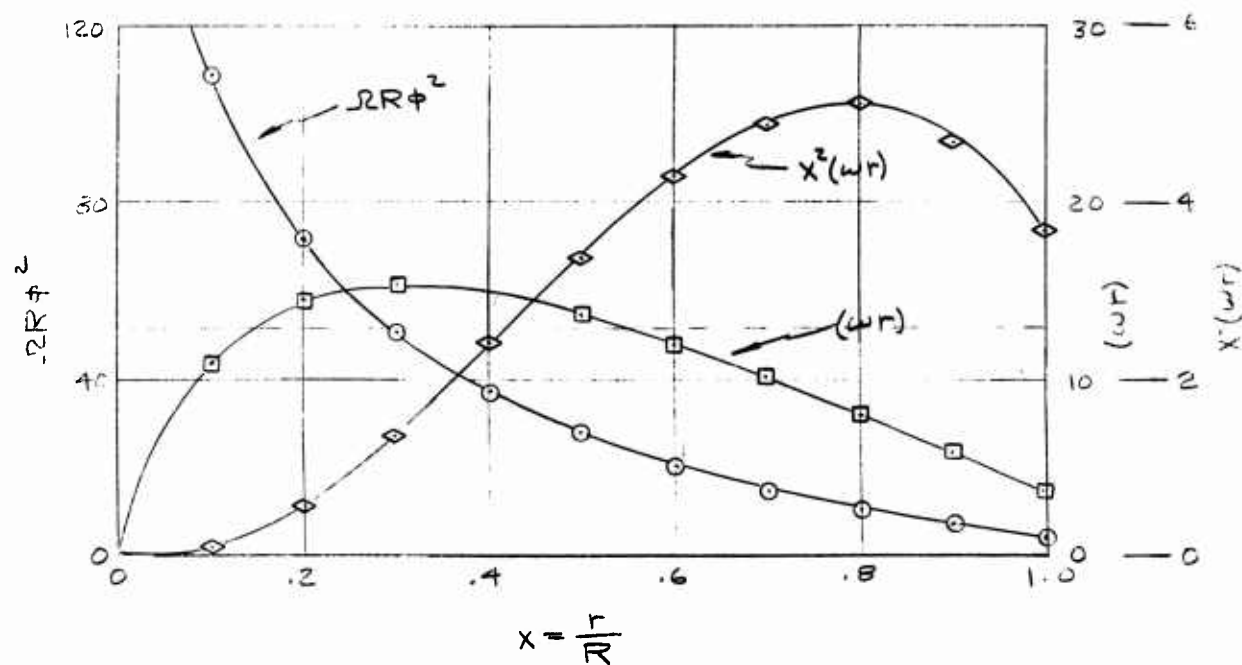
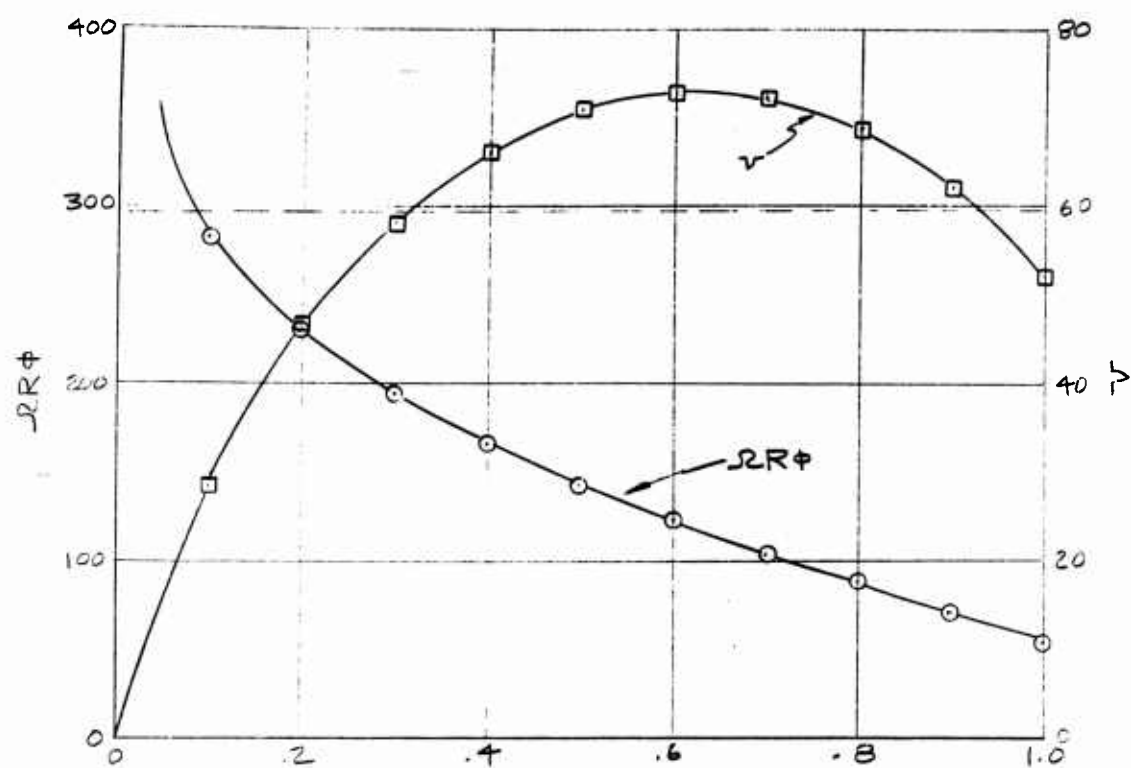
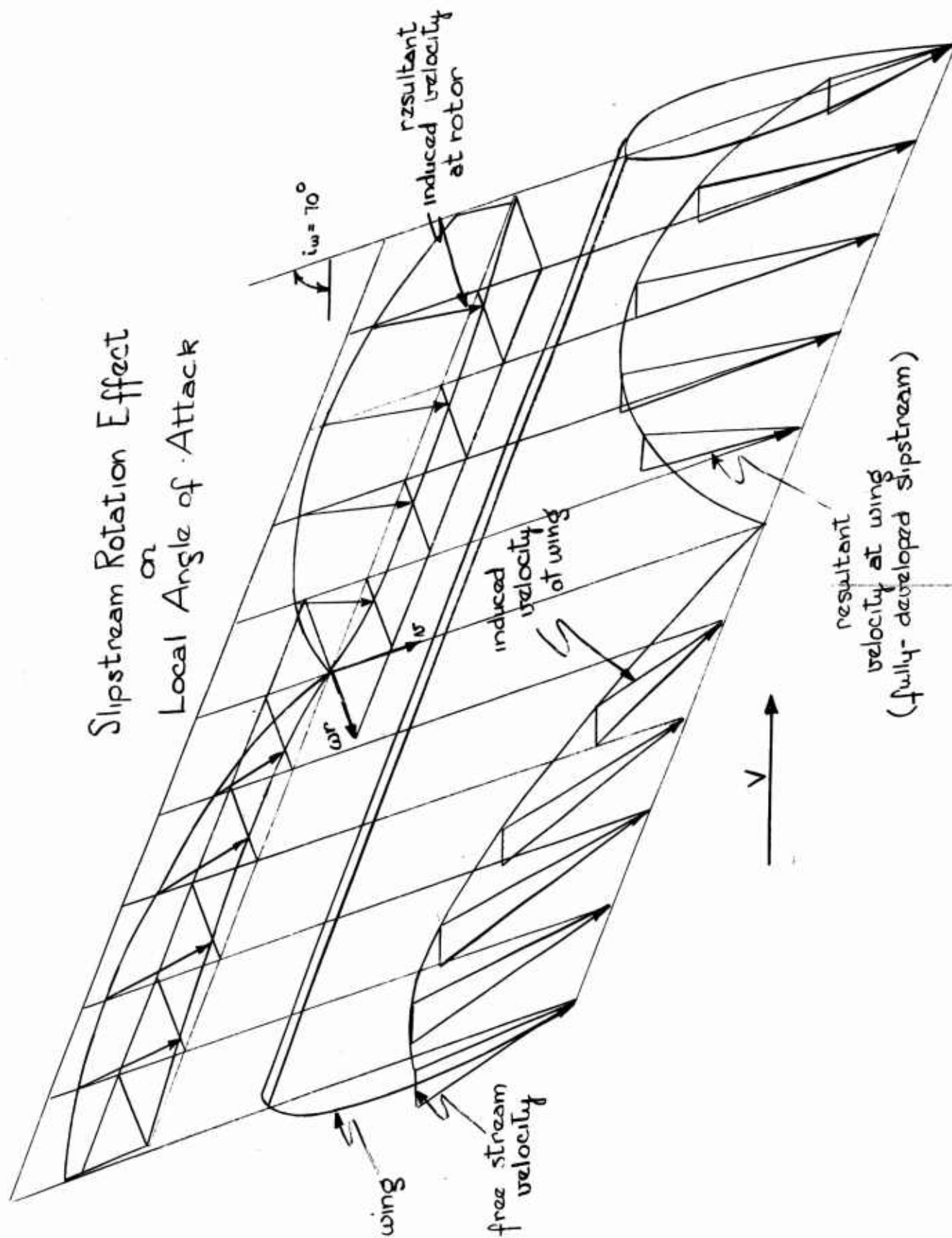
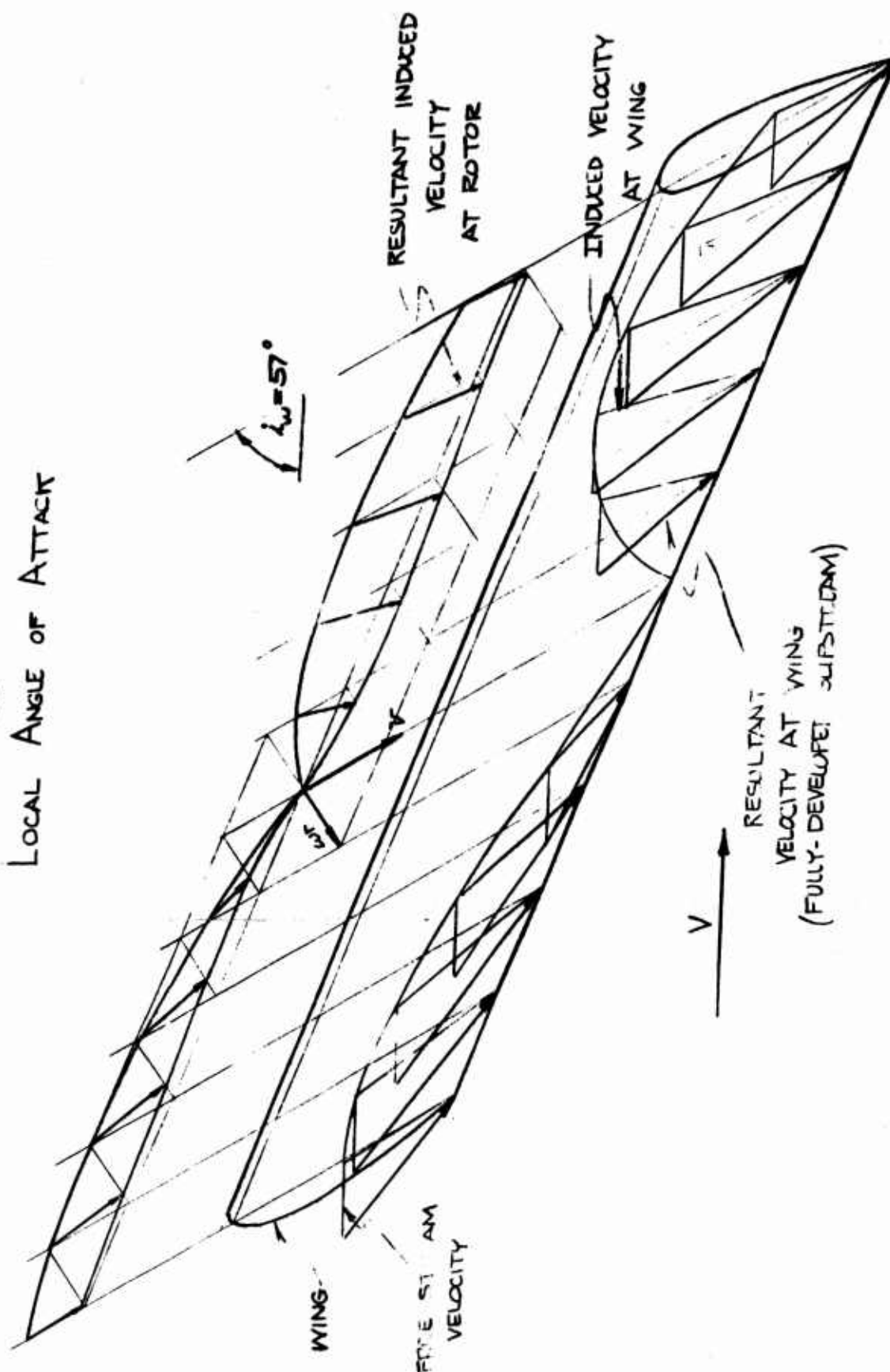


Fig. 56



STREAM ROTATION EFFECT
ON
LOCAL ANGLE OF ATTACK



SLIPSTREAM ROTATION EFFECT

ON

LOCAL ANGLE OF ATTACK

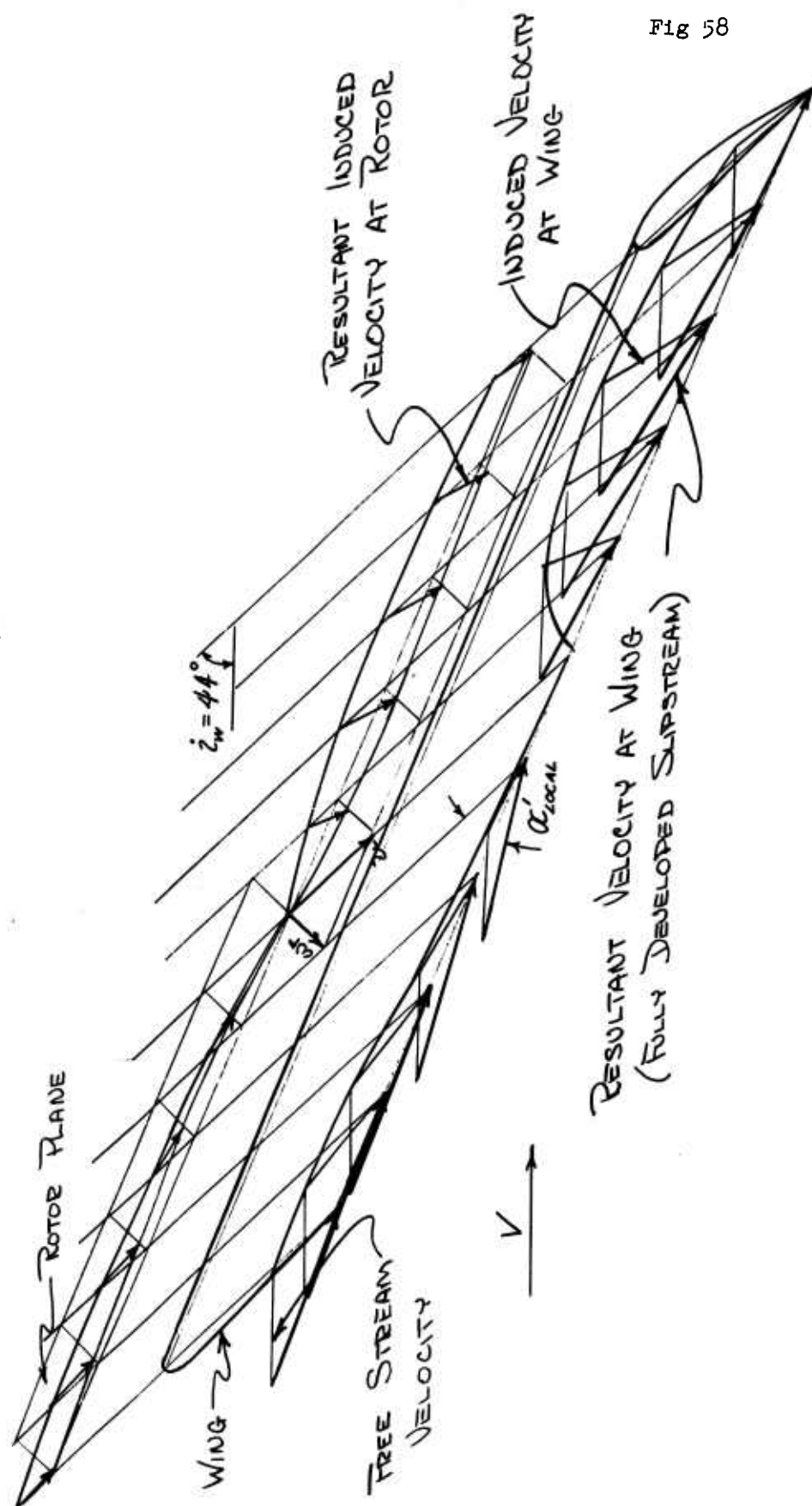
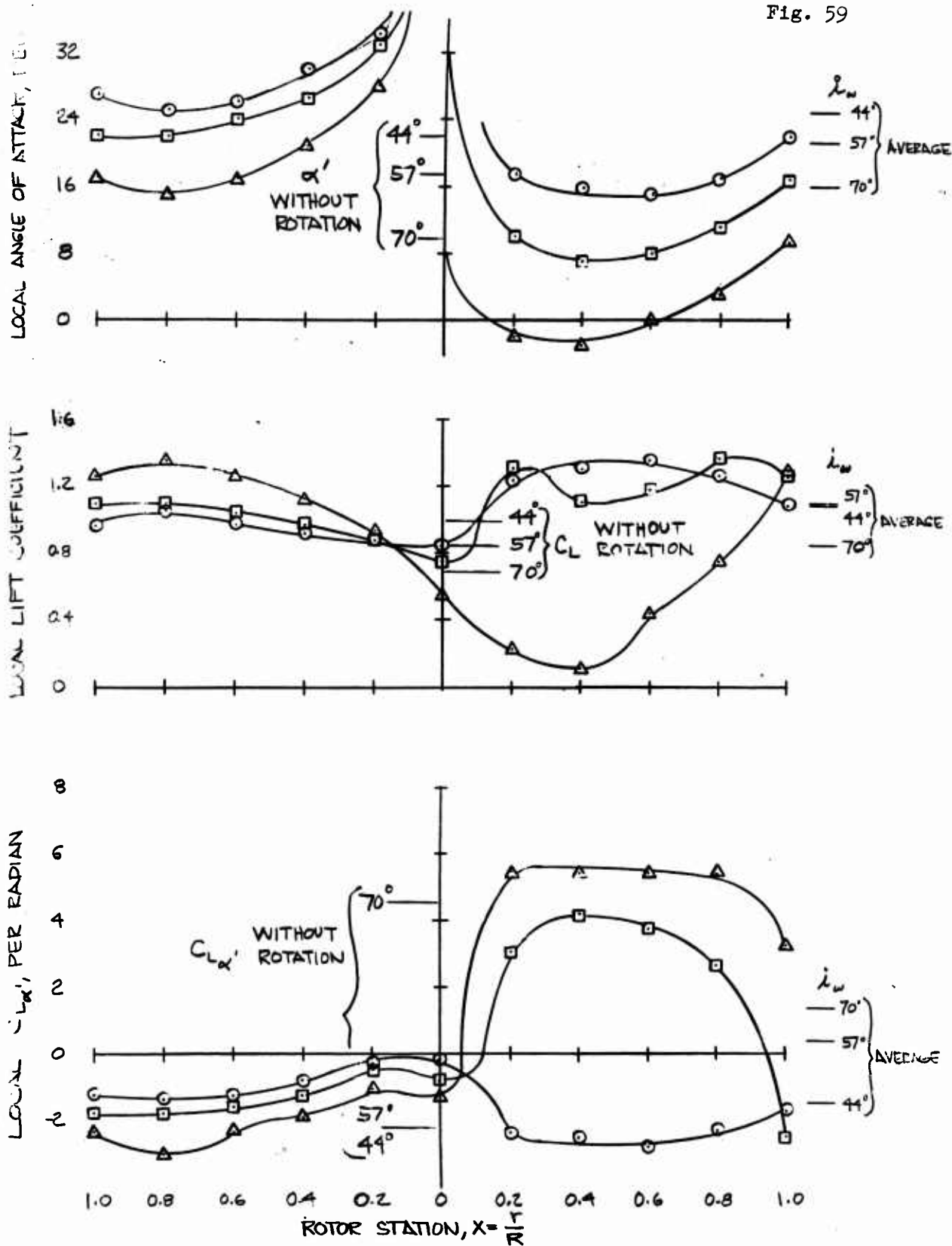


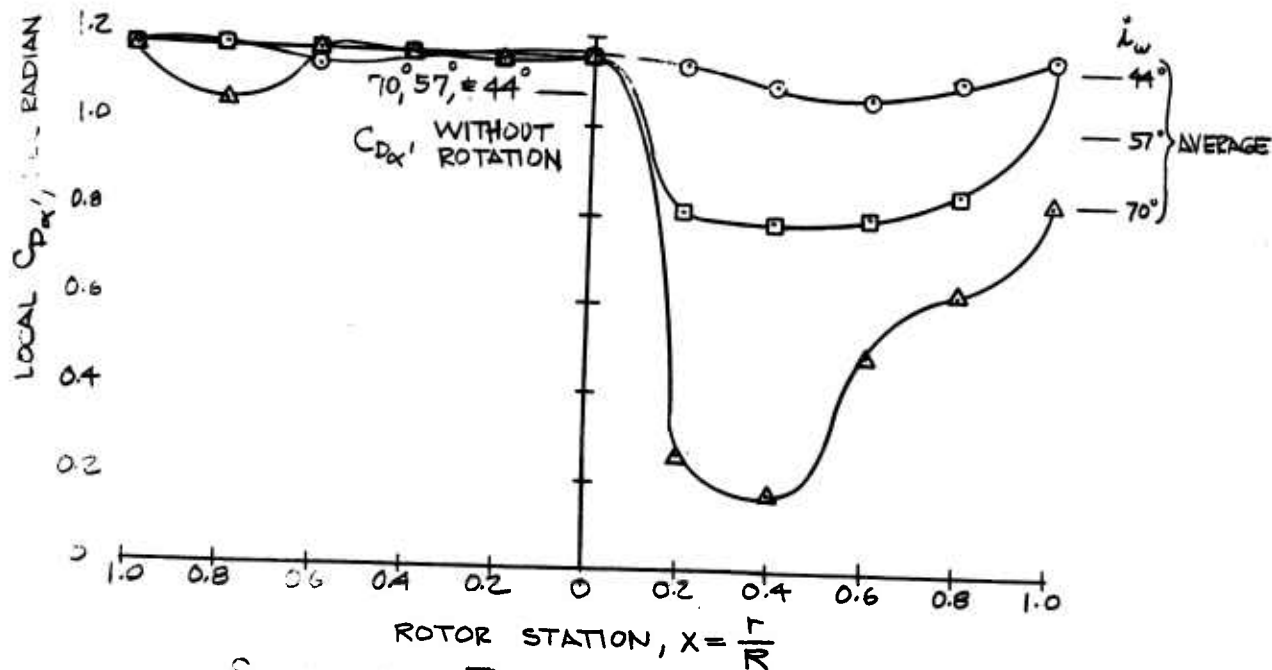
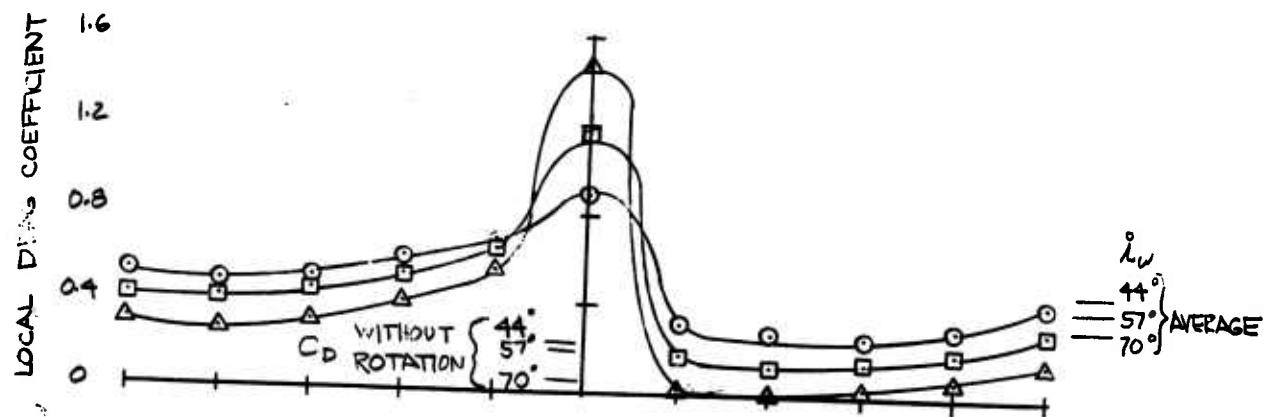
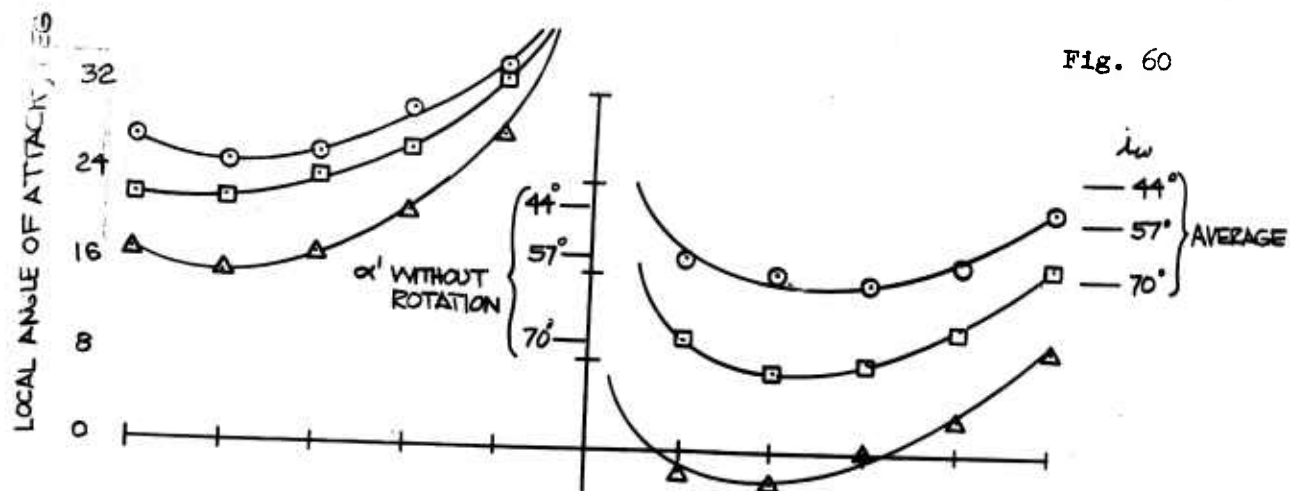
Fig 58

Fig. 59



SLIPSTREAM ROTATION EFFECT ON
 LOCAL LIFT CHARACTERISTICS

Fig. 60



SLIPSTREAM ROTATION EFFECT ON
LOCAL DRAG CHARACTERISTICS

NET TRENDS OF SLIPSTREAM ROTATION EFFECTS

$$\alpha'_{\text{NON-ROT}} < \alpha'_{\text{STALL}}$$

$$C_{L\text{AV}} < C_{L\text{NON-ROT}}$$

$$\alpha'_{\text{NON-ROT}} > \alpha'_{\text{STALL}}$$

$$C_{L\text{AV}} > C_{L\text{NON-ROT}}$$

$$\frac{\Delta C_{L\text{AV}}}{\Delta \alpha'} = - \text{ WITHOUT ROTATION}$$

$$\frac{\Delta C_{L\text{AV}}}{\Delta \alpha'} = + \text{ WITH ROTATION}$$

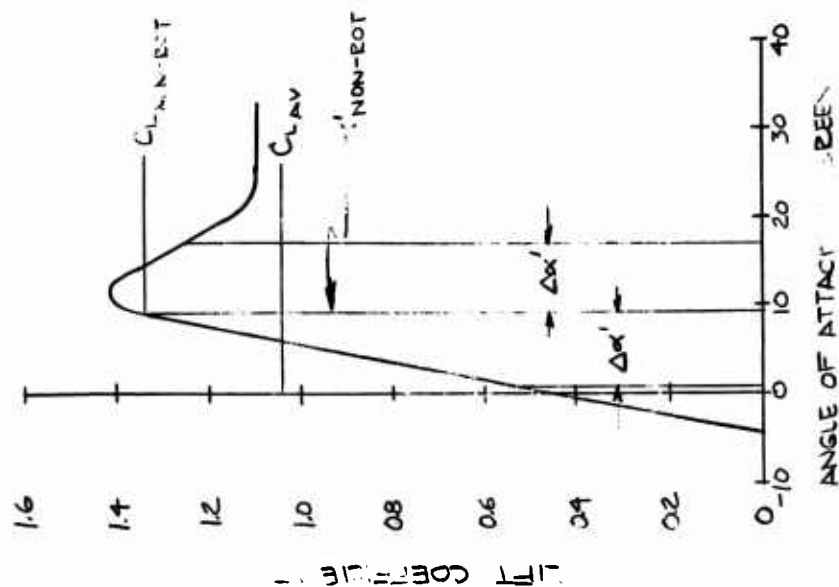


Fig 49(a)

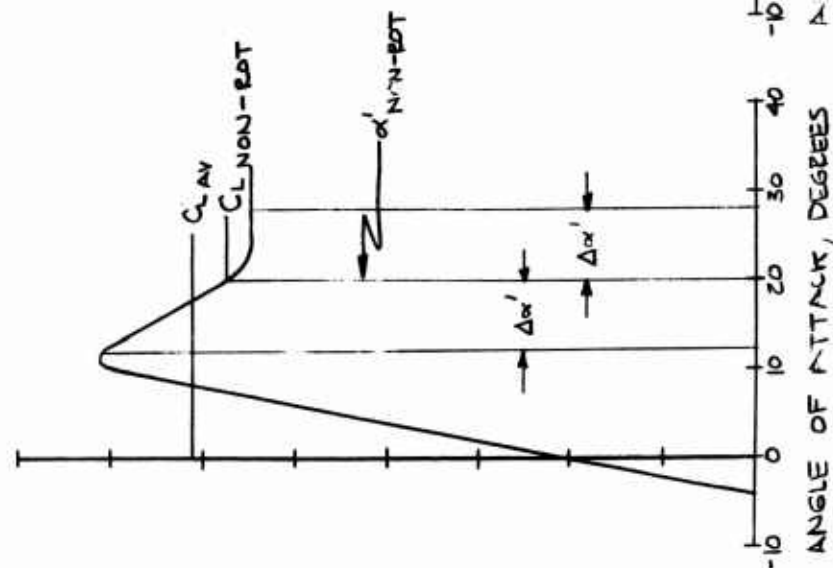


Fig 49(b)

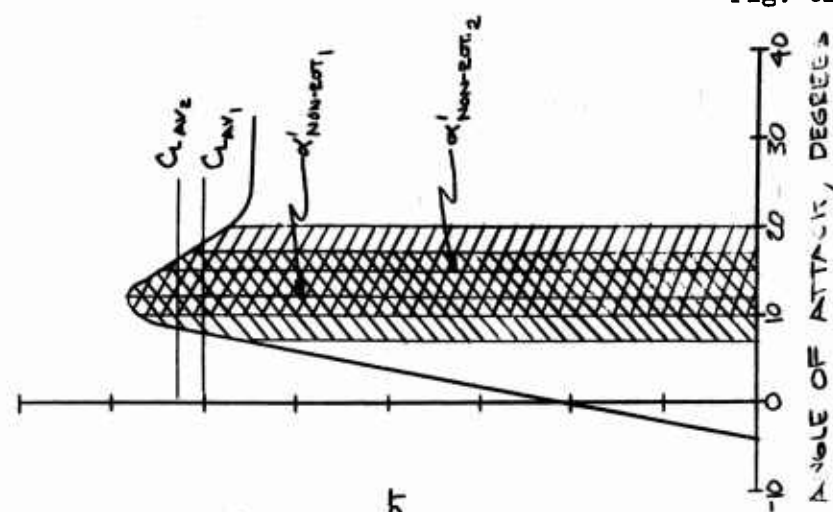


Fig 49(c)

Fig. 61

LONGITUDINAL DYNAMICS

On page 257 of Reference 8 is to be found a set of equations defining the motions of an aircraft in the three longitudinal degrees of freedom, within an axis system fixed in the airplane and initially aligned with the undisturbed flight path. The variables are horizontal velocity, u , vertical velocity, w , and airplane pitch attitude referenced to earth, Θ . Rewriting these equations in the angular notation of this report, they become

$$X_u u + X_w w + X_\Theta \dot{\Theta} - w \Theta \cos \gamma - \dot{u} \frac{w}{g} = 0 \quad (D-1)$$

$$Z_u u + Z_w w + Z_\Theta \dot{\Theta} - w \Theta \sin \gamma + u \Theta \frac{w}{g} - \dot{w} \frac{w}{g} = 0 \quad (D-2)$$

$$M_u u + M_w w + M_\Theta \ddot{\Theta} - I \ddot{\Theta} = 0 \quad (D-3)$$

where the variables u , w and Θ are actually the perturbations Δu , Δw and $\Delta \Theta$ and the trim conditions have already been subtracted out.

For the purposes of this report it is felt desirable to retain the body axis system as defined, but to use a different set of variables since the rotor characteristics are most easily expressed in terms of flight velocity, V , and rotor angle of attack, α . The transformation of variables may be accomplished by the following substitutions:

$$u = V \cos \alpha \quad (D-4)$$

$$w = V \sin \alpha \quad (D-5)$$

$$\dot{u} = \dot{V} \cos \alpha - V (\sin \alpha) \dot{\alpha} \quad (D-6)$$

$$\dot{w} = (\dot{V} \sin \alpha) + V \cos \alpha \dot{\alpha} \quad (D-7)$$

$$\Theta = \Theta \quad (D-8)$$

Equations (D-1) through (D-3) then become, for initially trimmed level flight ($\gamma = 0$),

$$X_v \dot{v} + X_\alpha \dot{\alpha} + X_{\dot{\theta}} \dot{\theta} - W\theta - \frac{W}{g} [\dot{v} \cos \alpha_0 - (v_0 \mu \sin \alpha_0) \dot{\alpha}] = 0 \quad (D-9)$$

$$Z_v \dot{v} + Z_\alpha \dot{\alpha} + Z_{\dot{\theta}} \dot{\theta} + v_0 \dot{\theta} \frac{W}{g} - \frac{W}{g} [(v_0 \cos \alpha_0) \dot{\alpha} + \dot{v} \mu \sin \alpha_0] = 0 \quad (D-10)$$

$$M_v \dot{v} + M_\alpha \dot{\alpha} + M_{\dot{\theta}} \dot{\theta} - I \ddot{\theta} = 0 \quad (D-11)$$

The solution of this set of homogeneous linear differential equations will be of the form

$$v = \sum v_0 e^{\lambda_n t} \quad (D-12)$$

$$\alpha = \sum \alpha_0 e^{\lambda_n t} \quad (D-13)$$

$$\theta = \sum \theta_0 e^{\lambda_n t} \quad (D-14)$$

and may be found by solving the algebraic equation

$$A\lambda^4 + B\lambda^3 + C\lambda^2 + D\lambda + E = 0 \quad (D-15)$$

obtained by equating the determinate of the coefficients of equations (D-9) through (D-11) to zero. The coefficients of the resulting quartic are as follows:

$$A = -m^2 v_0 I \quad (D-16)$$

$$B = m v_0 I X_v + m I Z_\alpha + m^2 v_0 M_{\dot{\theta}} \quad (D-17)$$

$$C = mV_0 \dot{X}_\theta M_v + m(\dot{Z}_\theta + mV_0) M_\alpha + (\dot{Z}_v X_\alpha - \dot{X}_v \dot{Z}_\alpha) I - m(\dot{X}_v V_0 + \dot{Z}_\alpha) M_\theta \quad (D-18)$$

$$D = [\dot{X}_\alpha (\dot{Z}_\theta + mV_0) - \dot{Z}_\alpha \dot{X}_\theta - W m V_0] M_v + [\dot{Z}_v \dot{X}_\theta - \dot{X}_v (\dot{Z}_\theta + mV_0)] M_\alpha + (\dot{X}_v \dot{Z}_\alpha - \dot{Z}_v \dot{X}_\alpha) M_\theta \quad (D-19)$$

$$E = (W \dot{Z}_\alpha) M_v - (W \dot{Z}_v) M_\alpha \quad (D-20)$$

A preliminary order of magnitude evaluation of the pitch-rate derivatives indicated that the only aerodynamic term of significance is the pitch damping term M_θ and considerable simplification in the analysis was affected by assuming the \dot{X}_θ and \dot{Z}_θ aerodynamic contributions are negligible compared to the other terms in the coefficients. Normalized quartic coefficients may be obtained if the initial equations of motion are divided through by various constants as follows:

Divide Z-Force equation by mV_0

Divide X-Force equation by m

Divide Moment equation by I

Performing these operations and making the above simplifications the coefficients of the resulting quartic become:

$$A = 1 \quad (D-21)$$

$$B = - \left[\frac{M_\theta}{I} + \left(\frac{\dot{X}_v}{m} + \frac{\dot{Z}_\alpha}{mV_0} \right) \right] \quad (D-22)$$

$$C = \left[\frac{M\ddot{\theta}}{I} \left(\frac{X_v}{m} + \frac{Z_\alpha}{mV_0} \right) + \left(\frac{X_v}{m} \frac{Z_\alpha}{mV_0} - \frac{Z_v}{mV_0} \frac{X_\alpha}{m} \right) - \frac{M_h}{I} \right] \quad (D-23)$$

$$D = \left[\frac{M_\alpha}{I} \frac{X_v}{m} - \frac{M_v}{I} \left(\frac{X_\alpha}{m} - g \right) - \frac{M\ddot{\theta}}{I} \left(\frac{X_v}{m} \frac{Z_\alpha}{mV_0} - \frac{Z_v}{mV_0} \frac{X_\alpha}{m} \right) \right] \quad (D-24)$$

$$E = \left[\frac{M_\alpha}{I} \frac{Z_v}{mV_0} - \frac{M_v}{I} \frac{Z_\alpha}{mV_0} \right] g \quad (D-25)$$

All of the above parameters have been evaluated both experimentally and theoretically as presented and discussed in the preceding section, with the exception of the pitch rate derivative $M\ddot{\theta}$. This particular derivative does not readily lend itself to experimental evaluation using conventional static testing procedures and a restrained model as in the tests under consideration. However, a theoretical determination may be made for a first order approximation to the derivative in Appendix A. This procedure consists of evaluating the contribution of the wing and rotor and adding them as is done with the static derivatives. The results given by the wing of Reference 7 were used for the $M\ddot{\theta}$ predictions presented herein.

The effect of $M\ddot{\theta}$ or any other particular term in the equations of motion, can be quite simply demonstrated by employing the root locus method as developed in Reference 9. For this purpose we wish to factor out of the characteristic equation all terms containing the variable under consideration, which for this particular example gives

$$A\ddot{\theta} p^4 + B\ddot{\theta} p^3 + C\ddot{\theta} p^2 + D\ddot{\theta} p + E\ddot{\theta} - \frac{M\ddot{\theta}}{I} z (b\ddot{\theta} z + c\ddot{\theta} z + d\ddot{\theta}) = 0 \quad (D-26)$$

where the coefficients are simply the coefficients of the complete characteristic equation as given above reduced by the coefficients of the terms containing $\frac{M\ddot{\theta}}{I}$. That is to say that

$$A_{\ddot{\theta}} = A = 1 \quad (D-27)$$

$$B_{\ddot{\theta}} + b_{\ddot{\theta}} \frac{M\ddot{\theta}}{I} = B \quad (D-28)$$

$$C_{\ddot{\theta}} + c_{\ddot{\theta}} \frac{M\ddot{\theta}}{I} = C \quad (D-29)$$

$$D_{\ddot{\theta}} + d_{\ddot{\theta}} \frac{M\ddot{\theta}}{I} = D \quad (D-30)$$

$$E_{\ddot{\theta}} = E \quad (D-31)$$

Rearranging equation (D-26) slightly we can write

$$\frac{-\frac{M\ddot{\theta}}{I} (b_{\ddot{\theta}} z^2 + c_{\ddot{\theta}} z + d_{\ddot{\theta}}) z}{A_{\ddot{\theta}} p^4 + B_{\ddot{\theta}} p^3 \dots + E_{\ddot{\theta}}} = -1 \quad (D-32)$$

which upon factoring becomes

$$\frac{-\frac{M\ddot{\theta}}{I} z_1 (z_2 - a)(z_3 - b)}{(p_1 - c)(p_2 - d)(p_3 - e)(p_4 - f)} = -1 = e^{i\pi} \quad (D-33)$$

This expression can be represented on the complex plane for all values of $\frac{M\ddot{\theta}}{I}$ from 0 to ∞ as the locus of all points for which the sum of the arguments of the poles minus the zeroes is π radians and for $-\infty < \frac{M\ddot{\theta}}{I} < 0$ as the locus for a similar phase condition of zero.

Similar procedures can be followed to give root locus diagrams for other variables, in particular the effects of $\frac{M_V}{I}$ and $\frac{M_\alpha}{I}$, along with the $\frac{M\ddot{\theta}}{I}$ effects for all conditions tested are demonstrated in Figures 62 through 64. The resulting numerator (zeroes) and denominator (poles) coefficients derived from factoring of the variables are given below.

For $\frac{M\ddot{\theta}}{I}$ varying:

Zeroes

$$-\frac{M\dot{\theta}}{I} \left[z^2 - \left(\frac{X_v}{m} + \frac{Z_\alpha}{mV_0} \right) z + \left(\frac{X_v}{m} \frac{Z_\alpha}{mV_0} - \frac{Z_v}{mV_0} \frac{X_\alpha}{m} \right) \right] z = 0 \quad (D-34)$$

Poles

$$A_{\dot{\theta}} = 1 \quad (D-35)$$

$$B_{\dot{\theta}} = -\left(\frac{X_v}{m} + \frac{Z_\alpha}{mV_0} \right) \quad (D-36)$$

$$C_{\dot{\theta}} = \left(\frac{X_v}{m} \frac{Z_\alpha}{mV_0} - \frac{Z_v}{mV_0} \frac{X_\alpha}{m} \right) - \frac{M_\alpha}{I} \quad (D-37)$$

$$D_{\dot{\theta}} = \frac{M_\alpha}{I} \frac{X_v}{m} - \frac{M_v}{I} \left(\frac{X_\alpha}{m} - g \right) \quad (D-38)$$

$$E_{\dot{\theta}} = E = \left[\frac{M_\alpha}{I} \frac{Z_v}{mV_0} - \frac{M_v}{I} \frac{Z_\alpha}{mV_0} \right] g \quad (D-39)$$

For $\frac{M_v}{I}$ varying:

Zeroes

$$-\frac{M_v}{I} \left[\left(\frac{X_\alpha}{m} - g \right) z + \frac{Z_\alpha}{mV_0} g \right] = 0 \quad (D-40)$$

Poles

$$A_v = 1 \quad (D-41)$$

$$B_v = -\left[\frac{M\dot{\theta}}{I} + \left(\frac{X_v}{m} + \frac{Z_\alpha}{mV_0} \right) \right] \quad (D-42)$$

$$C_v = \left[\frac{M\dot{\theta}}{I} \left(\frac{X_v}{m} + \frac{Z_\alpha}{mV_0} \right) + \left(\frac{X_v}{m} \frac{Z_\alpha}{mV_0} - \frac{Z_v}{mV_0} \frac{X_\alpha}{m} \right) - \frac{M_\alpha}{I} \right] \quad (D-43)$$

$$D_v = \left[\frac{M_\alpha}{I} \frac{X_v}{m} - \frac{M\dot{\theta}}{I} \left(\frac{X_v}{m} \frac{Z_\alpha}{mV_0} - \frac{Z_v}{mV_0} \frac{X_\alpha}{m} \right) \right] \quad (D-44)$$

$$E_v = \frac{M_\alpha}{I} \frac{Z_v}{mV_0} g \quad (D-45)$$

and for $\frac{M_\alpha}{I}$ varying:

Zeroes

$$- \frac{M_\alpha}{I} (z^2 - \frac{X_v}{m} z - \frac{Z_v}{mV_0} g) = 0 \quad (D-46)$$

Poles

$$A_\alpha = 1 \quad (D-47)$$

$$B_\alpha = - \left[\frac{M\dot{\theta}}{I} + \left(\frac{X_v}{m} + \frac{Z_\alpha}{mV_0} \right) \right] \quad (D-48)$$

$$C_\alpha = \left[\frac{M\dot{\theta}}{I} \left(\frac{X_v}{m} + \frac{Z_\alpha}{mV_0} \right) + \left(\frac{X_v}{m} \frac{Z_\alpha}{mV_0} - \frac{Z_v}{mV_0} \frac{X_\alpha}{m} \right) \right] \quad (D-49)$$

$$D_\alpha = - \left[\frac{M_v}{I} \left(\frac{X_\alpha}{m} - g \right) + \frac{M\dot{\theta}}{I} \left(\frac{X_v}{m} \frac{Z_\alpha}{mV_0} - \frac{Z_v}{mV_0} \frac{X_\alpha}{m} \right) \right] \quad (D-50)$$

$$E_\alpha = - \frac{M_v}{I} \frac{Z_\alpha}{mV_0} g \quad (D-51)$$

The zeroes of the $M_{\dot{\theta}}$ root locus are of particular interest, in that they are identical to the roots of the complete airplane characteristic equation when $M_{\dot{\theta}} = M_v = M_{\alpha} = 0$. The roots of this characteristic equation consist of two zero roots and two other roots which can be real or complex depending upon the relative magnitude and sign of the derivatives Z_{α} , Z_v , X_{α} and X_v . For conventional signs for the above derivatives, that is that lift and drag increase with angle of attack and airspeed, the roots will invariably have negative real parts and give either convergences or in rare cases a stable oscillation, but peculiar combinations of wing and rotor contributions give values to the derivatives that can produce divergences in the mode. In order for this mode to be oscillatory the condition $b^2 - 4ac < 0$ must be satisfied where $a=1$, $b = -\left(\frac{X_v}{m} + \frac{Z_{\alpha}}{mV_0}\right)$ and $c = -\left(\frac{Z_v}{mV_0} \frac{X_{\alpha}}{m} - \frac{X_v}{m} \frac{Z_{\alpha}}{mV_0}\right)$.

Such a condition is realized in the $i_w = 57^\circ$ accelerated and decelerated and the $i_w = 44^\circ$ accelerated cases due to the large positive value of X_{α} . The positive values of Z_{α} noted in the $i_w = 70^\circ$ conditions produce divergences as indicated in the zeroes of Figures 62 and 63, and can probably be attributed to a strong gradient in the wing drag with angle of attack possibly due to partial stalling. In any case, the variations in these real roots quickly disappear with the addition of even small amounts of M_{α} either positive (destabilizing) or negative (stabilizing) as demonstrated in Figures 62 and 63. General observations possible from these Figures are:

- 1) With $M_v = 0$, addition of statically destabilizing (+) M_{α} results in the appearance of a moderately long period, low damping, stable

oscillation - plus a pair of real roots, one of which is usually positive and the other negative.

2) Addition of statically stabilizing (+) M_v to the above motion will, in general, reduce the magnitude of the positive real root, and if a sufficient amount is added, both real roots will be convergent, indicating a stable static margin defined by the E coefficient of the characteristic equation. This amount of static stability, however, in the absence of sufficient $M_{\dot{\theta}}$ and negative M_{α} in the C coefficient causes the previously stable oscillatory roots to become unstable and of higher frequency.

3) Addition of stabilizing (+) M_{α} in the absence of M_v results again in an unstable oscillation but in this case the divergences are transformed into another oscillation very similar to the one encountered in the + M_{α} case above, but formed by a different pair of roots.

4) Additional static margin provided by + M_v results in increasing the frequency of the unstable oscillation and driving the stable oscillation back into two convergences.

It can thus be seen that, for either sign of M_{α} of the magnitude present in the aircraft, the end result in the presence of + M_v and absence of significant amounts of $M_{\dot{\theta}}$ is an unstable oscillation and a convergence plus one other real root that will be either positive or negative, depending on the sign of the E coefficient. The only exception to this situation is to be found in the $i_w = 44^0$ trim condition where M_v is small enough that it does not quite drive the oscillatory mode unstable, but by the same token, not enough static stability is present to eliminate the divergence caused by the destabilizing M_{α} .

At this point hope still exists for the salvation of the airplane's dynamics, since all the above considerations are presented for the tail-off airplane. The possibility exists that the tail can contribute desirable effects to the over-all airplane dynamics and such contributions will now be considered.

Accelerated flight

Insufficient data

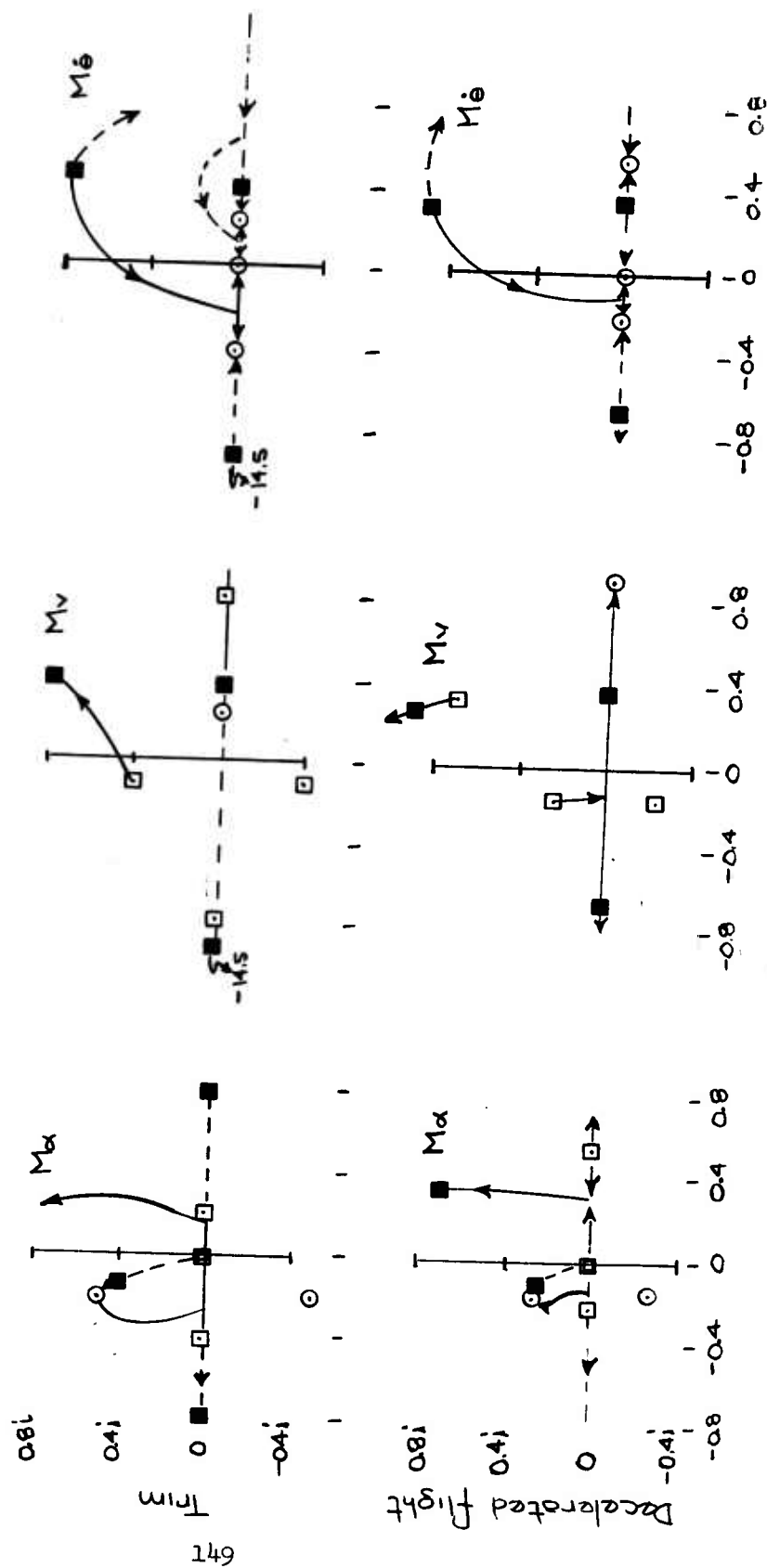
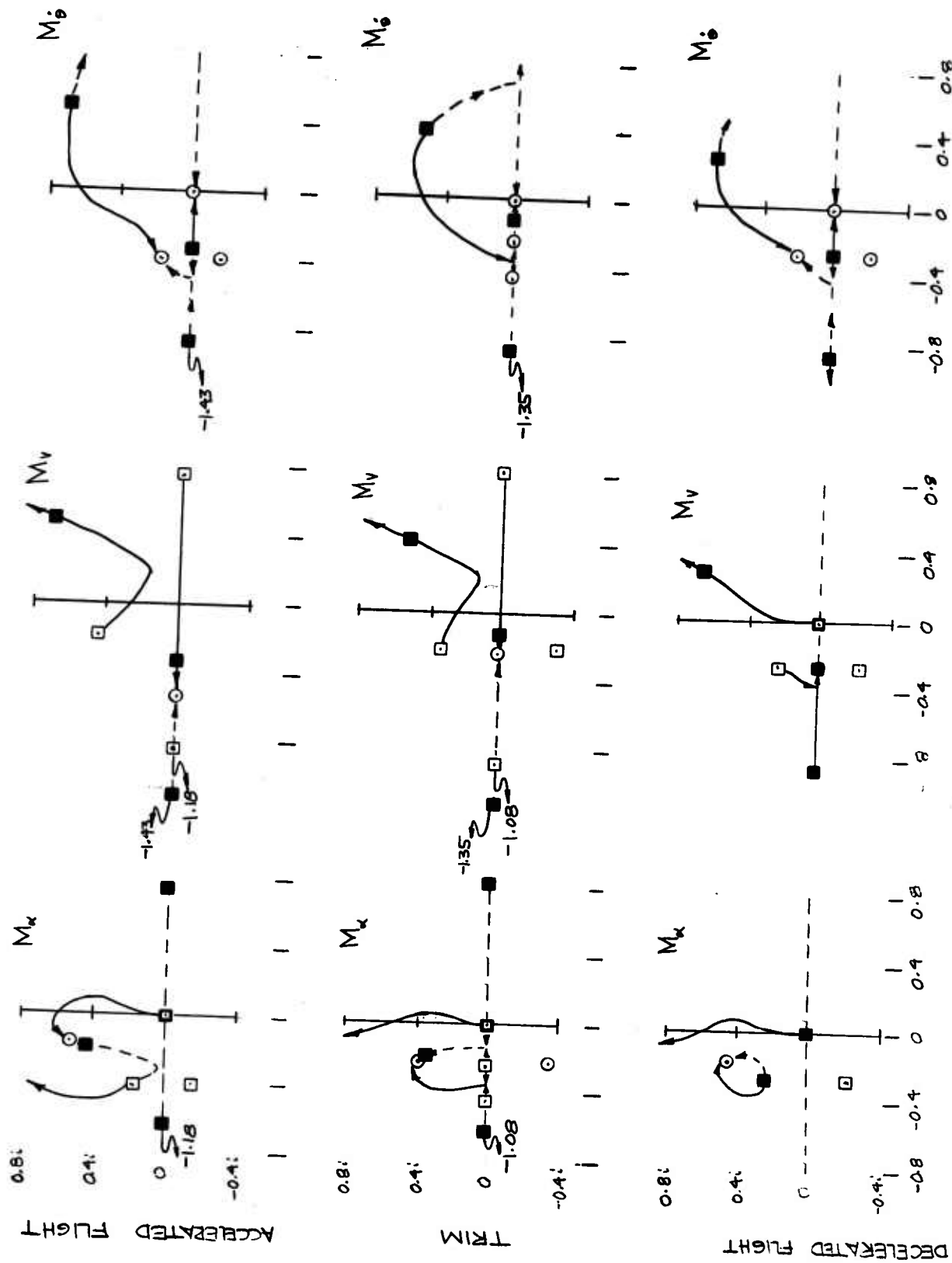


Fig. 62

Experimental Tail Off Root Loci

■ — solution for experimental values of the variable

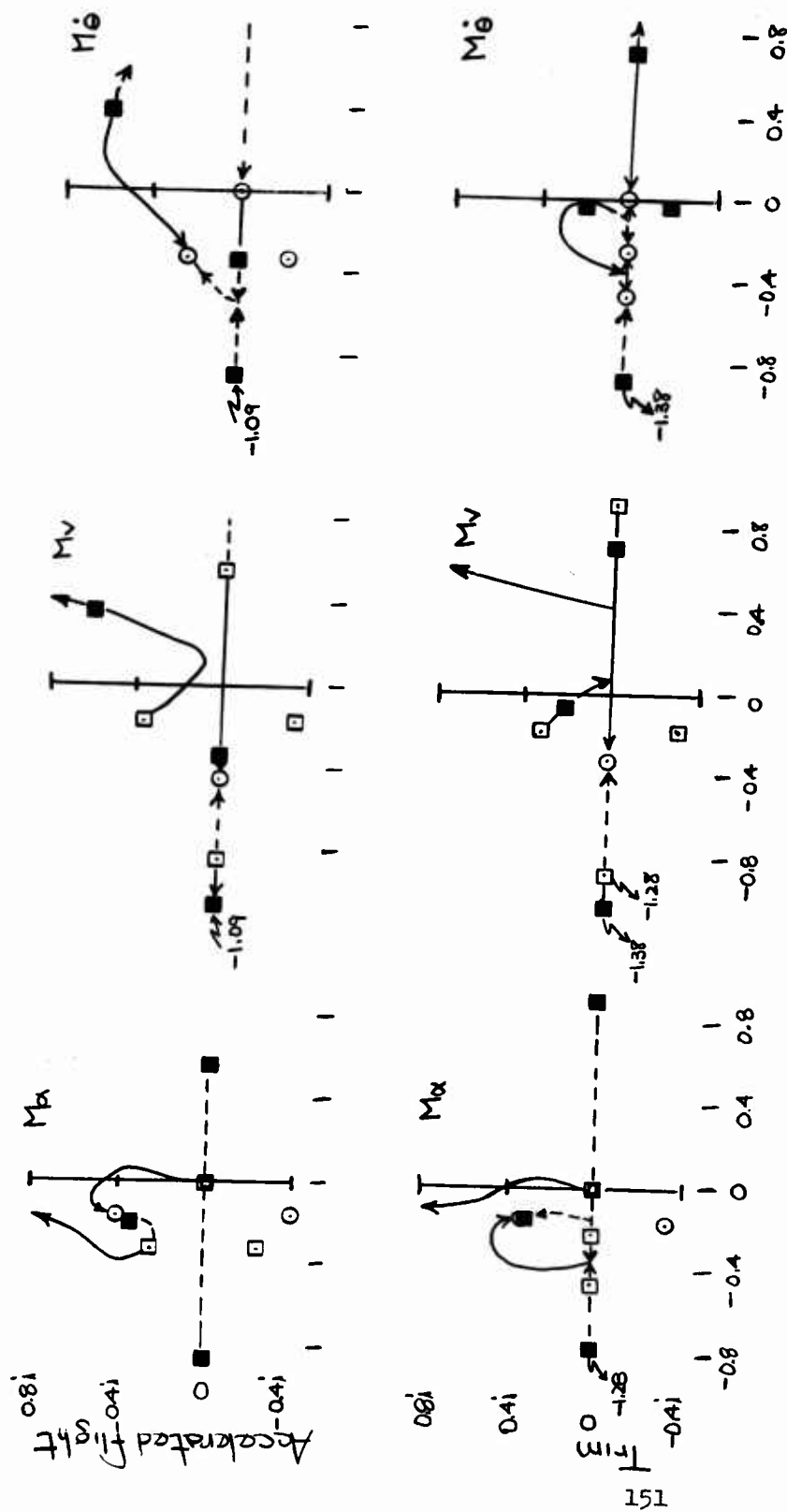
Fig. 63



EXPERIMENTAL TAIL OFF ROOT LOCI

■ ~ SOLUTION FOR EXPERIMENTAL VALUES OF THE VARIANCE

$\lambda_{ij} = 57^\circ$



Insufficient Data

Experimental Tail Off Root Loci

■ ~ solution for experimental values of the variable

TAIL EFFECTS

In order to evaluate the dynamics of the complete airplane it is necessary to develop a method of predicting the stability derivative contributions of the horizontal tail and pitch fan. Several simplifying assumptions can aid considerably the facility with which this is done. They are:

- 1) For the wing incidences under consideration, the high T - tail is assumed to be completely isolated from and unaffected by the wing or rotor.

- 2) The tail makes no significant contribution to the trimmed forces of the airplane.

- 3) The horizontal stabilizer and pitch fan exert no interference effects on one another.

- 4) The shrouding effects of the buried fan do not significantly effect its operation. The first assumption is probably the least valid of all as later experiments indicate considerable downwash can be present even at high wing incidences, and this effect should certainly be investigated experimentally and the results incorporated into a more rigorous analysis.

Proceeding with these assumptions in mind, we can determine the operating conditions of the tail either by predicting the forces on the stabilizer and assuming the fan generates the remainder necessary to trim the moment measured in the experiments or the reverse of this. Since the stabilizer is a relatively simple surface operating in undisturbed flow by assumption, the former approach is assumed to be the

better of the two and the tail fan assumptions will only have to apply to its derivatives and not to predicted forces. In order to allow some latitude in the predictions, two separate lift curve slopes for the horizontal tail were assumed and the resulting horizontal stabilizer loads were computed at various stabilizer incidences and using the various free-stream trim speeds. These loads were then substituted into the trim equation

$$M_{TOTAL} - l_s L_s - l_F L_F = 0 \quad (D52)$$

from which a solution for the tail fan thrust was obtained. Using these thrusts a procedure exactly like the one presented in Appendix A was followed to obtain values of $\frac{\partial C_{TF}}{\partial \alpha}$ and $\frac{\partial C_{TF}}{\partial \mu_x}$ from which the contributions to the moment derivatives were obtained by the formula

$$M_{\alpha_{FAN}} = -l_F (\pi \rho \Omega_F^2 R_F^4) \frac{\partial C_{TF}}{\partial \alpha} \quad (D53)$$

$$M_{V_F} = -l_F (\pi \rho \Omega_F^2 R_F^4) \frac{\partial C_{TF}}{\partial \mu_x} \frac{1}{\Omega_T R_T} \quad (D54)$$

where both derivatives are evaluated at $\alpha = 0$. The stabilizer contributions are similarly expressed

$$M_{\alpha_s} = -l_s \left(\frac{1}{2} \rho V^2 S_s \right) \frac{\partial C_{L_s}}{\partial \alpha} \quad (D55)$$

$$M_{V_s} = -l_s \rho V S_s C_{L_s} \quad (D56)$$

where the C_{L_s} is simply the product of the $C_{L_{\alpha_s}}$ assumed = 2 and 4 and the stabilizer incidence under consideration. The total tail contributions to the static moment derivatives are given by

$$M_{\alpha_t} = M_{\alpha_F} + M_{\alpha_s} \quad (D57)$$

$$M_{v_t} = M_{v_F} + M_{v_s} \quad (D58)$$

and the values obtained are to be found in Table III.

The remaining stability contribution of the tail—the pitch damping derivative $M_{\dot{\theta}}$ —can now be very easily evaluated using the relations developed above. For this purpose it is assumed that rotations of the fan and stabilizer about their own axes make no significant contribution to $M_{\dot{\theta}_t}$, assumptions which are quite valid for both the small diameter rigid rotor and for the stabilizer. The only remaining effects are the change in angle of attack and velocity at the tail due to angular rotation of the aircraft about its c.g. Denoting these changes due to rotation with the superscript *, we can write

$$\frac{\partial M_t}{\partial \dot{\theta}} = \frac{\partial M}{\partial \alpha_t^*} \frac{\partial \alpha_t^*}{\partial \dot{\theta}} + \frac{\partial M_t}{\partial v_t^*} \frac{\partial v_t^*}{\partial \dot{\theta}} \quad (D59)$$

and referring to Figure 65 we see that

$$\frac{\partial \alpha_t^*}{\partial \dot{\theta}} = \frac{l_t}{V} \quad (D60)$$

$$\frac{\partial v_t^*}{\partial \dot{\theta}} = 0 \quad (D61)$$

when evaluated at $\dot{\Theta} = 0$ initially, and as in Appendix A

$$\frac{\partial M_t}{\partial \alpha_t^*} \equiv \frac{\partial M_t}{\partial \alpha} \quad (D62)$$

$$\xi \quad \frac{\partial M_t}{\partial v_t^*} \equiv \frac{\partial M_t}{\partial v} \quad (D63)$$

These results are to be found presented in Figure 66 as functions of v along with a comparison to total wing and rotor contributions.

The net results of the addition of the tail can be seen in Figure 67 through 70 and briefly summarized as follows:

1) The horizontal stabilizer and pitch fan contribute stabilizing M_α independent of tail incidence, but completely dependent on horizontal stabilizer lift curve slope and trim speed.

2) Contribution to $M_{\dot{\Theta}}$ is always stabilizing and for the $C_{L\alpha_s} = 2$ case, of the same order of magnitude as that of the tail-off airplane at high i_w . However, the tail contribution to $M_{\dot{\Theta}}$ increases in magnitude with trim speed, whereas the airplane tail-off $M_{\dot{\Theta}}$ decreases rapidly with increasing trim speed. Both M_α and $M_{\dot{\Theta}}$ contributions of the horizontal stabilizer are doubled by a twofold increase in assumed $C_{L\alpha_s}$.

3. The pitch fan contributes negative M_v essentially independent of stabilizer incidence and increasing with trim speed, while the horizontal stabilizer gives negative M_v for i_s (+) and positive M_v for i_s (-), again increasing in magnitude with trim speed and in proportion to $C_{L\alpha_s}$ assumed.

The effects of the tail contributions as noted in Figures 67 through 70 in the high i_w conditions can be regarded as slight. It is interesting to note that the stabilizing M_α contribution of the $C_{L\alpha_s} = 2$ tail does not give an over-all stable M_α until the $i_w = 44^\circ$ case is reached where the increase in static margin results in the elimination of the pure divergence at the expense of reduced period of the unstable oscillation.

Similar trends in all cases considered are the general result of assuming the more effective horizontal stabilizer. It is difficult to estimate whether the mode damping improvements achieved by the addition of still-- small amounts of $-M_\alpha$ offset the disadvantages presented by the extremely short periods. One very important point regarding the effect of stabilizer effectiveness assumed is demonstrated in Figure 70. In this figure it is apparent that, depending on the $-M_\alpha$ contributed by the tail, the effect of varying i_s and therefore M_v is considerably altered. For small amounts of $-M_\alpha$ as contributed by the $C_{L\alpha_s} = 2$ tail, increasing $+i_s$ produces primarily an increase in oscillatory mode period, while in the $C_{L\alpha_s} = 4$ case similar variation manifests itself in decreasing the period and increasing damping. Also of interest in this particular case is the appearance of another oscillatory mode associated with the large value of $-M_\alpha$. The zeroes of the M_α root locus represent the roots of the characteristic equation as $M_\alpha \rightarrow \infty$, i.e. the phugoid mode in that no angle of attack change occurs. In this case, however, this mode is formed by the two negative real roots that usually form the conventional aircraft short period mode.

TABLE II.

EXPERIMENTAL AND THEORETICAL TRIM CONDITIONS

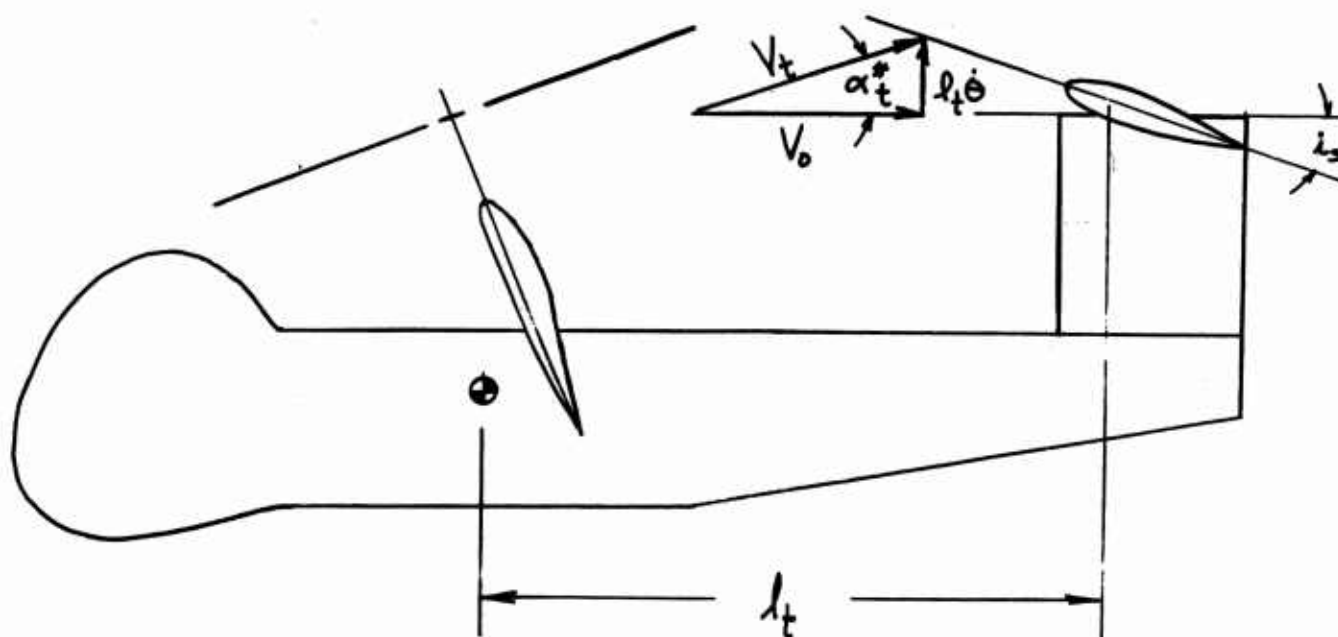
FULL SCALE VALUES

	$i_w = 70^\circ$	$i_w = 57^\circ$	$i_w = 44^\circ$
V_{-Ft}/Sec	23.5	42.6	59.8
α_f°	0	0	0
α	- 20°	- 33°	- 46°
$\theta_{\text{exp}}^\circ$	13.97	12.22	11.47
$\theta_{\text{eff}}^\circ$	12.25	11.18	10.70
G.W. Lb.	3200	3350	3360
μ_x	.0316	.0573	.0802
λ	- .0918	- .0905	- .0973
C_T	.01588	.01217	.00848
α'°	9.7	17.9	21.8
V_R^{Ft}/Sec	131.4	117.1	108.5

DERIVATIVE	$\lambda_w = 70^\circ$				$\lambda_w = 57^\circ$				$\lambda_w = 44^\circ$			
	DEC	TRIM	ACC		DEC	TRIM	ACC		TRIM	ACC		
$Z_{\alpha} - \frac{LB}{RAD}$	2125	543	0		- 1020	- 1088	- 1275		2220		- 1785	
$X_{\alpha} - \frac{LB}{RAD}$	1147.5	0	- 637.5		892.5	- 170	348.5		- 408		892.5	
$M_{\alpha} - \frac{FT-LB}{RAD}$	- 1463	877	1463		0	1760	1672		2520		919.6	
$Z_V - \frac{LB}{FT/SEC}$	- 9.89	- 20.2			- 33.99	- 24.2	- 24.72		- 28.4		- 31.52	
$X_V - \frac{LB}{FT/SEC}$	- 25.96	- 40.5	- 43.26		- 39.55	- 44.5	- 30.9		- 37.6		- 35.84	
$M_V - \frac{FT-LB}{FT/SEC}$	35.2	114.4	134.4		48	59.5	89.6		24.3		57.6	
TAIL CONTRIBUTIONS	$\lambda_s = 10^\circ$	$\lambda_s = 0^\circ$	$\lambda_s = 10^\circ$		$\lambda_s = 10^\circ$	$\lambda_s = 0^\circ$	$\lambda_s = 10^\circ$		$\lambda_s = 10^\circ$	$\lambda_s = 0^\circ$	$\lambda_s = 10^\circ$	
$M_{V_S} @ C_{W_S} = 2$	4.55	0	- 4.55		8.25	0	- 8.25		11.56	0	- 11.56	
$M_{V_S} @ C_{W_S} = 4$	9.10	0	- 9.10		16.50	0	- 16.50		23.02	0	- 23.02	
$M_{V_{TF}}$	- 3.01	- 3.02	- 3.03		- 4.66	- 4.58	- 4.52		- 5.83	- 5.82	- 5.73	
$M_{\alpha_{TF}}$	- 230	- 232	- 233		- 446	- 452	- 458		- 662	- 670	- 679	
M_{α_S}	-306.50	$C_{W_S} = 2$	$C_{W_S} = 4$		-1000.7	$C_{W_S} = 2$	$C_{W_S} = 4$		-1978	$C_{W_S} = 2$	$C_{W_S} = 4$	

TABLE III
EXPERIMENTAL TAIL OFF STATIC DERIVATIVES
AND
THEORETICAL TAIL CONTRIBUTIONS

PITCHING CONTRIBUTIONS TO TAIL VARIABLES



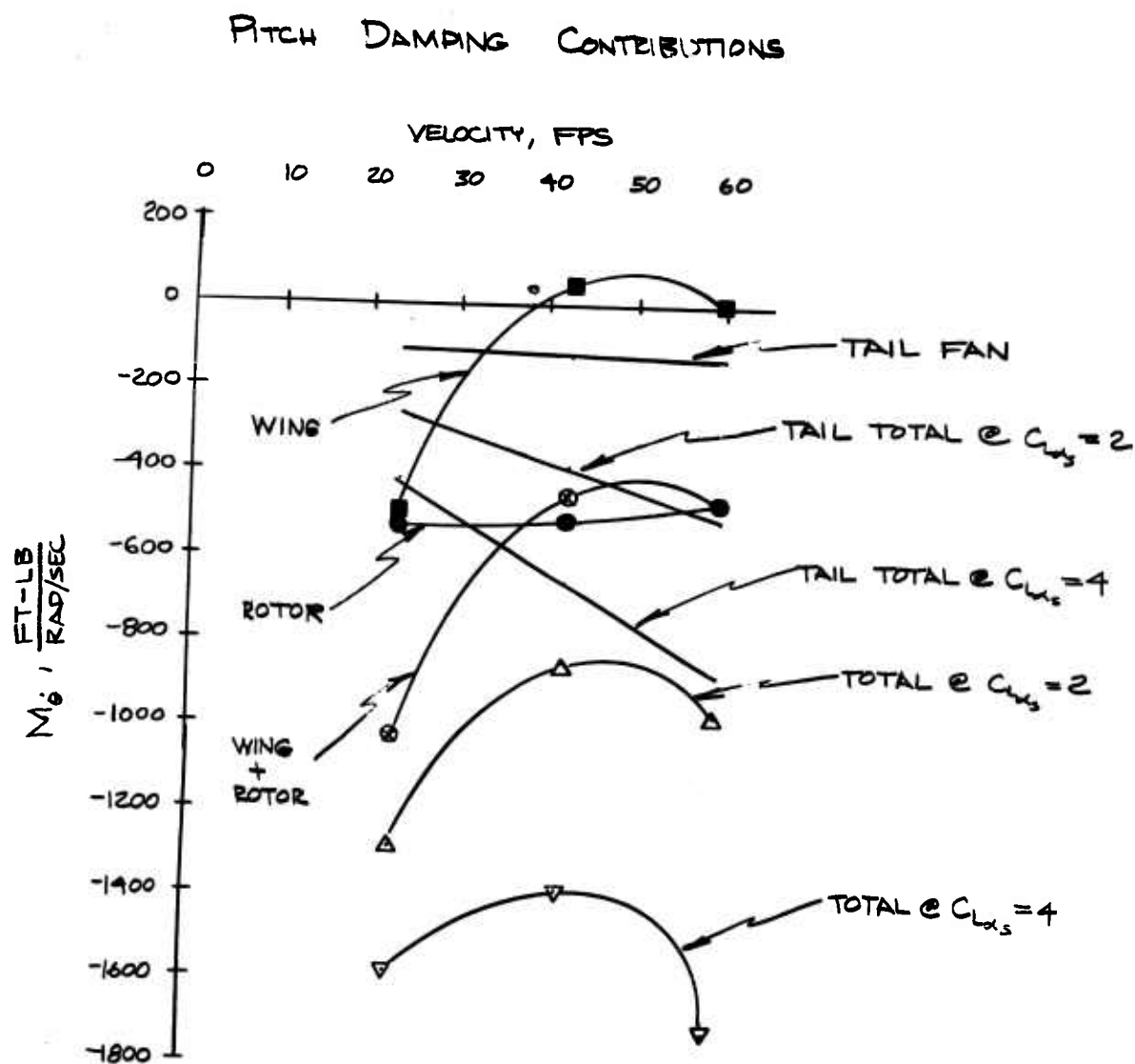
$$\tan \alpha_t^* \cong \alpha_t^* \cong \frac{l_t \dot{\theta}}{V_0}$$

$$V_t^2 = V_0^2 + (l_t \dot{\theta})^2$$

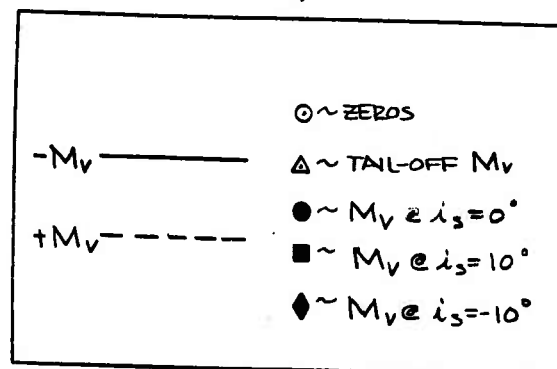
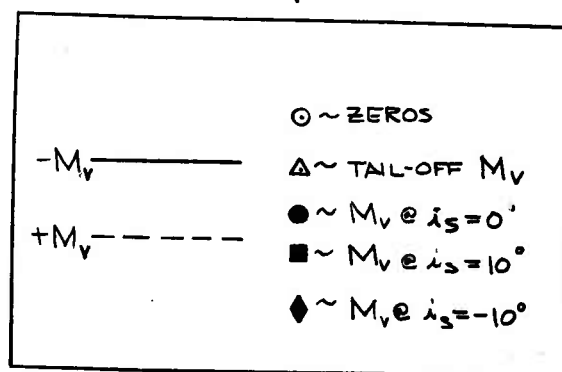
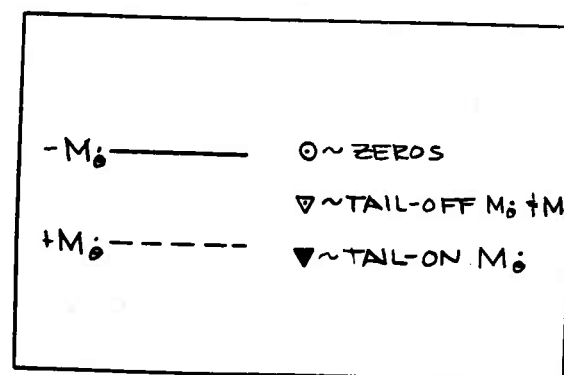
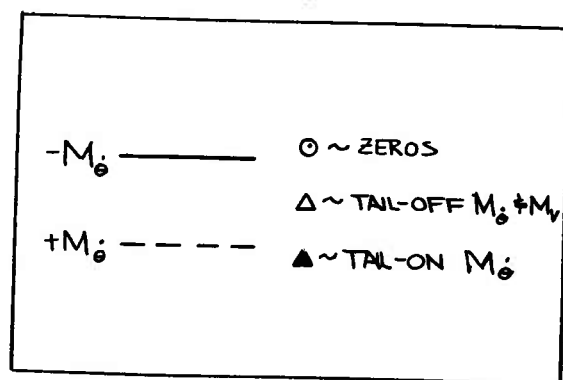
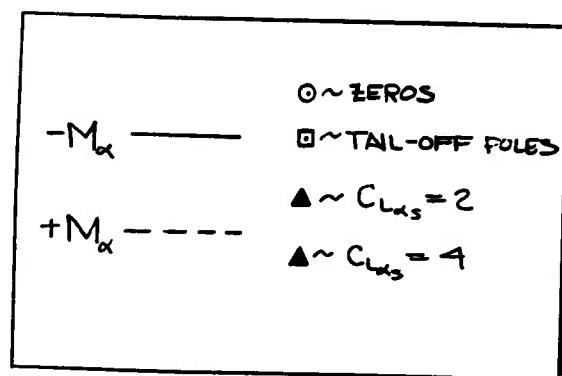
$$V_t^* = l_t \dot{\theta}$$

NOTE: PRESENTATION IS EXACT ONLY WITH C.G. AND HORIZONTAL STABILIZER IN SAME HORIZONTAL PLANE.

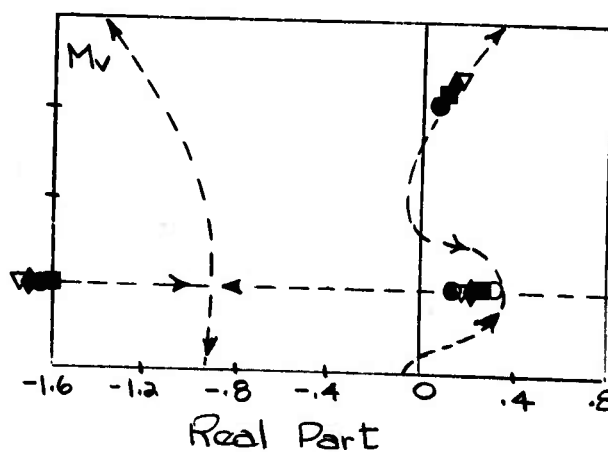
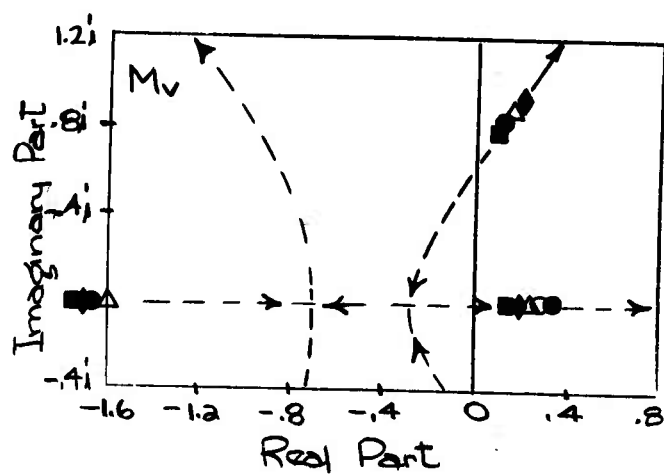
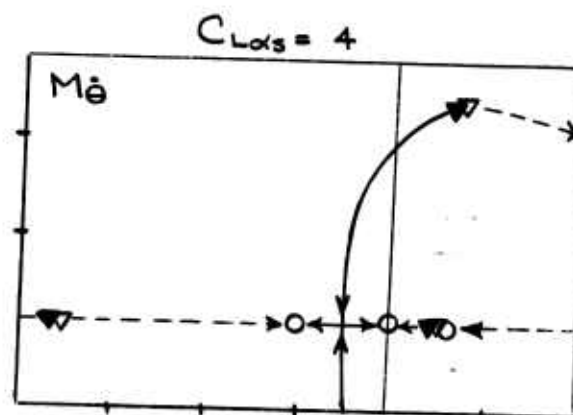
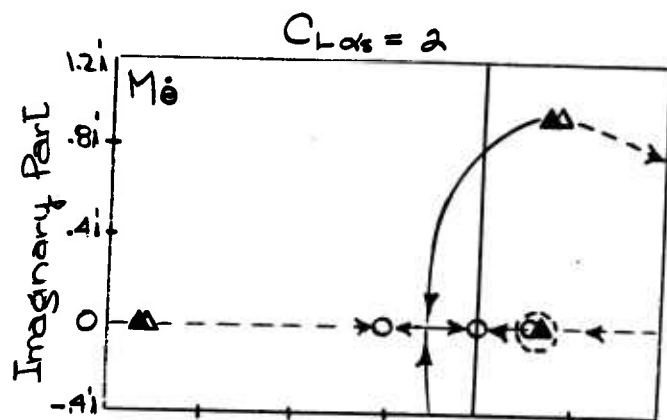
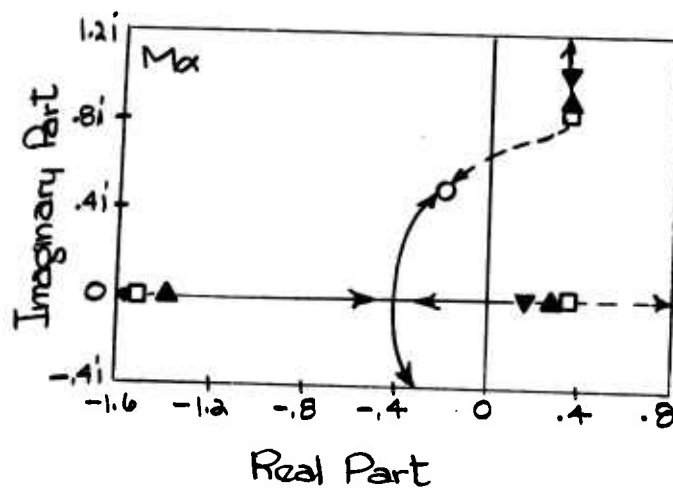
Fig. 66



SYMBOLS FOR FIGURES 68-70

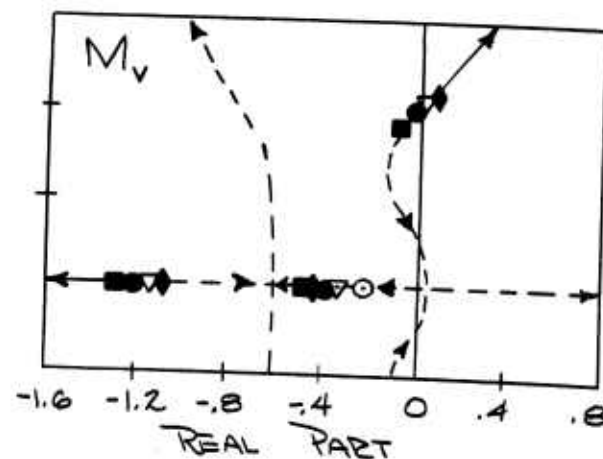
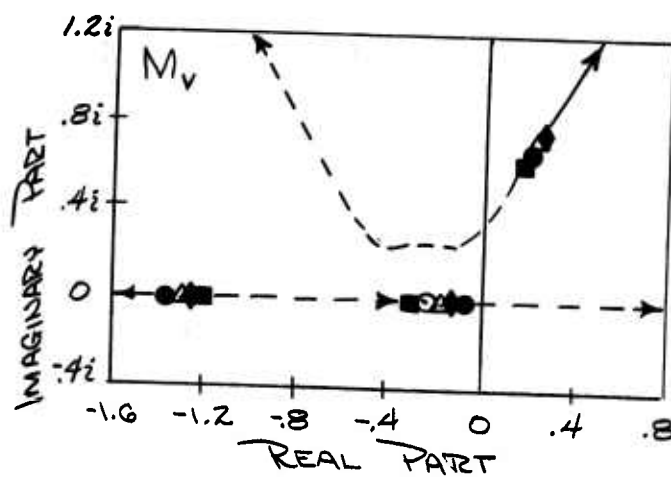
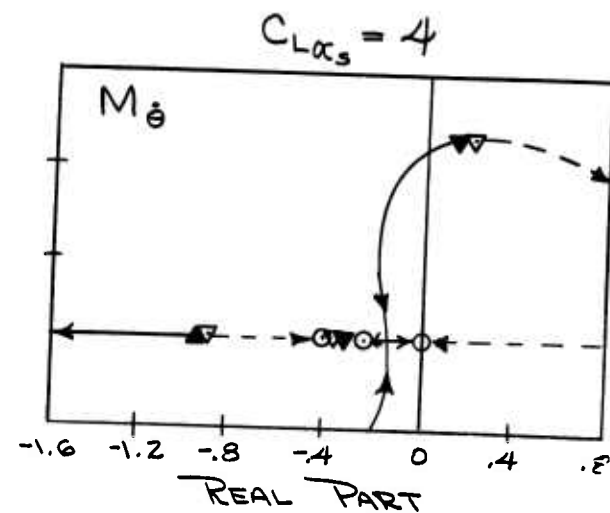
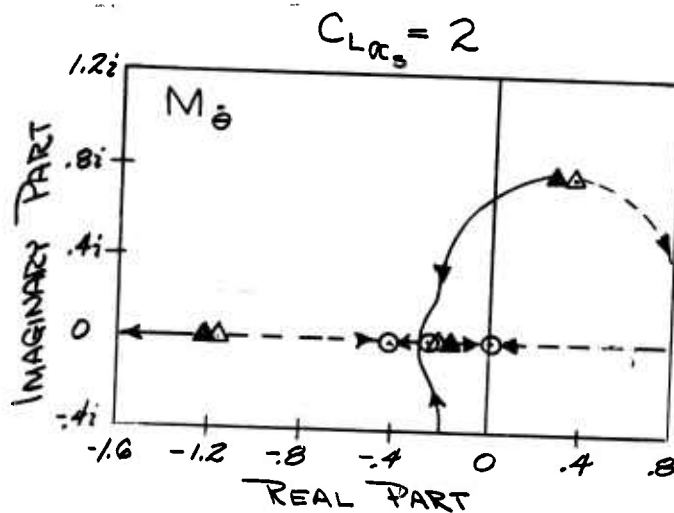
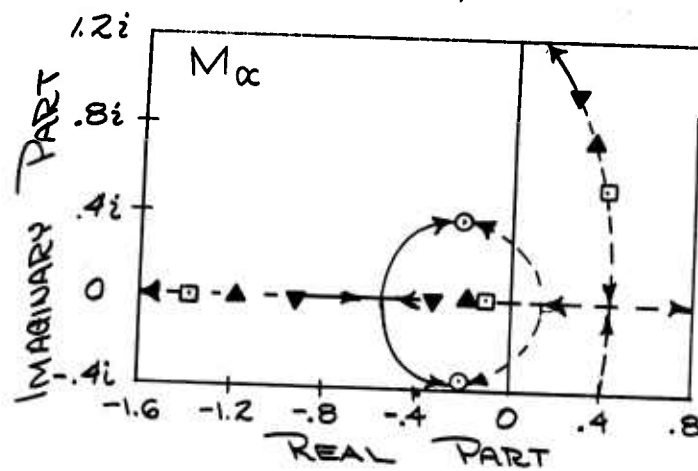


Loci of Roots of Tail-On Airplane

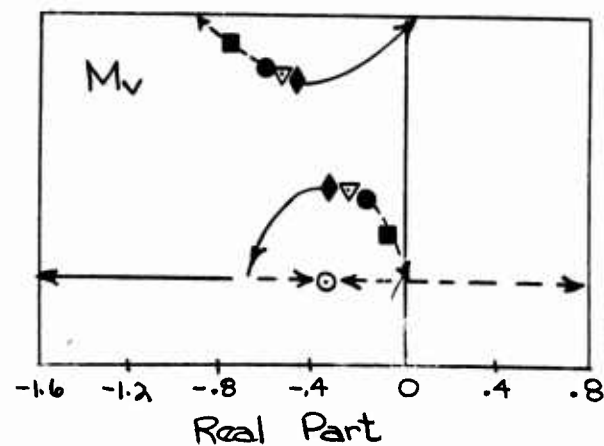
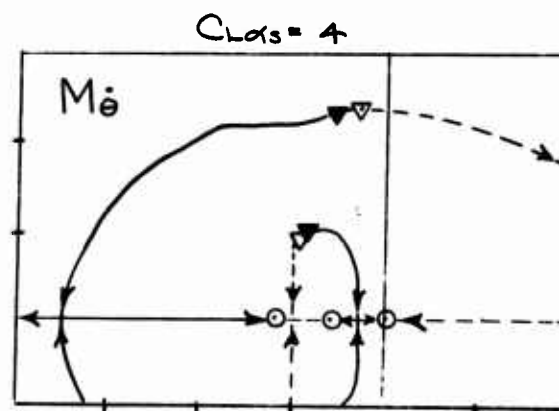
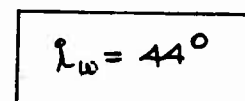


LOCI OF ROOTS OF TAIL-ON AIRPLANE

Fig. 69



Loc of Roots of Tail-On Airplane



RESULTS: THEORETICAL AND EXPERIMENTAL DATA

Possibly the best way to present an evaluation of the results of experiments such as those discussed herein, is to compare the experimental results to similar data from other sources. In general, this is only possible to the degree that the experiments in question are repetitions of preceding work, a situation that obviously can lead to great inefficiencies in the determination of new and significant information. In formulating a new test program, it is desirable to reach a compromise that will allow the accomplishment of both the test objectives concerned with increasing the knowledge of the subject of interest, as well as providing datums for evaluation of the validity of this information. Such a compromise is particularly important when the experiments are conducted on a new and novel Facility such as the Forward Flight Facility, since the inclination would be to favor a program closely duplicating existing work in order to provide the utmost in correlation possibilities. Correlation was not, however, the primary purpose of these experiments, but some comparisons are available between the data from tests conducted on the Forward Flight Facility and similar data from other sources. One group of these comparisons is presented in Figures 71 through 73 where three static test conditions are compared to results from a 1/4 scale model of the V-76 tested by the NACA in the Free Flight wind tunnel at Langley Field, Virginia. Since the actual 1/4 scale model forces were not available from the information in Reference 10, the comparison was affected by assuming that both models had scaled trim speeds equivalent to the

same full scale value. With the tunnel speed values given in Reference 10 the full scale force and moment values presented could then be reduced to the model values at the same scaling as the Princeton model according to the formulae given below.

$$L_{\text{model}} = L_{\text{F.S.}} \left(\frac{V_{\text{tunnel}}}{V_{\text{F.S.}}} \right)^2 \times \left(\frac{1}{5.2} \right)^2$$

$$D_{\text{model}} = D_{\text{F.S.}} \left(\frac{V_{\text{tunnel}}}{V_{\text{F.S.}}} \right)^2 \times \left(\frac{1}{5.2} \right)^2$$

$$M_{\text{model}} = M_{\text{F.S.}} \left(\frac{V_{\text{tunnel}}}{V_{\text{F.S.}}} \right)^2 \times \left(\frac{1}{5.2} \right)^3$$

It was necessary to plot these results versus i_w at constant α in order to determine interpolated values of the forces and moment at the wing tilt angles tested on the Princeton model. Operations of this sort as well as small discrepancies in the acceleration conditions compared tend to produce errors in the results, but general magnitude and trend agreement can still be detected in the comparisons presented. The most consistent inconsistency between the two sets of data is to be found in the moment values. This, however, is to be expected since neither Ω nor blade static moment about the flapping hinge were scaled on the 1/4 scale NACA model, and the hub moment due flapping hinge offset is a significant rotor contribution to moments about the c.g. of the aircraft. Another effect of not scaling Ω is the implication that torque scaling is neglected also. The developments concerning rotational effects

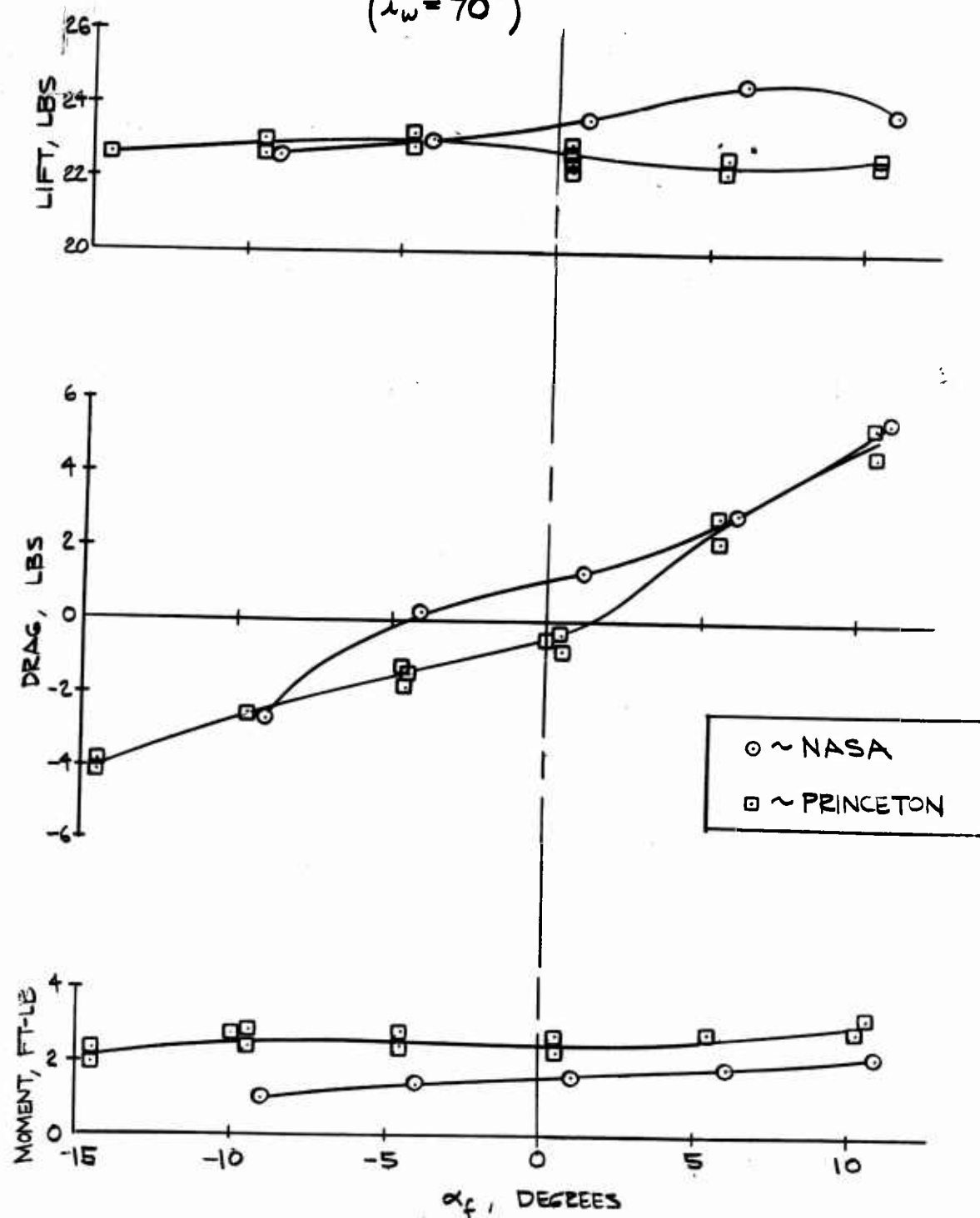
in a previous section indicate that this may have a profound influence on the data obtained, since the full scale wing operating conditions may not necessarily be duplicated.

Some evaluation of the assumption that the model trim speed is directly scalable from the full scale trim speed can be made by considering Figure 74 which presents a comparison between scaled-up $\frac{1}{5.2}$ scale model trim speeds and full scale as functions of wing tilt angle. The full scale values are those obtained from flight programs conducted by the NASA at Langley Field, Virginia, and by the Vertol Aircraft Corporation, and the model values are obtained from both the static and the 1-D/F tests. The general agreement is considered excellent since any discrepancies lie well within the probable inaccuracies of measurement of full scale velocity and fuselage angle of attack which is nominally zero.

Other qualitative remarks can be made in comparing the model results to full scale, including the general agreements in the tail force required to trim the pitching moment through a partial transition and the decrease in collective pitch necessary for constant altitude transition. These comparisons, however, cannot be made quantitatively due to lack of full scale information and so no attempt at a direct comparison has been made. Figure 75 taken from Reference 11 presents nearly all the full scale information available on these effects and can be compared qualitatively with the results of the 1-D/F tests in Figure 28 through 33. By way of explanation it should be noted that the full scale tests were made at constant altitude with a collective pitch decrease while the model tests were made at constant collective and indicate lift increasing.

From the trim and transition comparisons alone it is reasonable to expect that the model, scaling, and testing techniques employed provide reasonable representations of the full scale aircraft characteristics and behaviour.

COMPARISON OF EXPERIMENTAL DATA TO 1/4 SCALE WIND TUNNEL DATA ($i_w = 70^\circ$)



COMPARISON OF EXPERIMENTAL DATA TO 1/4 SCALE WIND TUNNEL DATA ($\lambda_w = 57^\circ$)

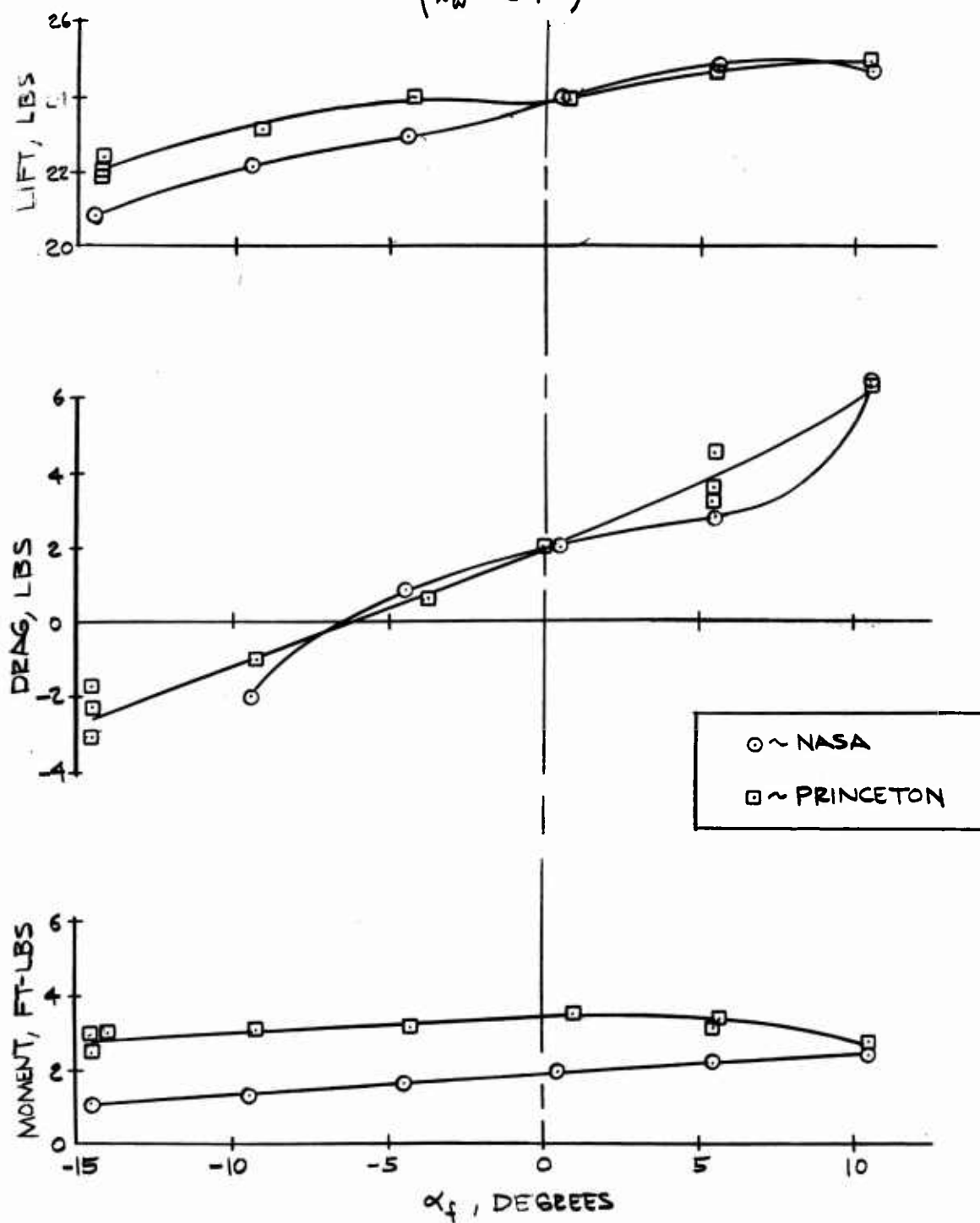
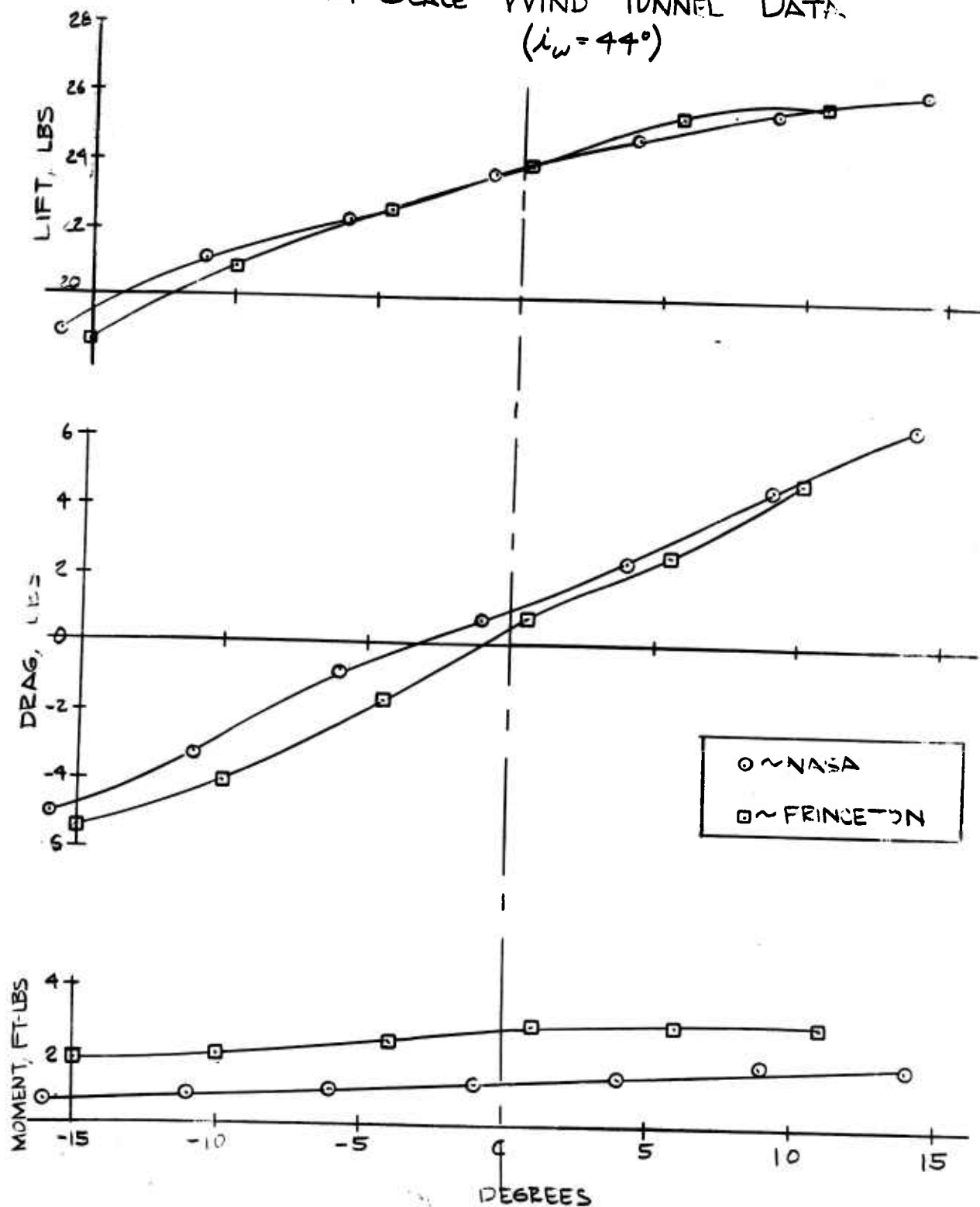


Fig. 73

COMPARISON OF EXPERIMENTAL DATA TO 1/4 SCALE WIND TUNNEL DATA ($\alpha_w = 44^\circ$)



V-76 TRIM SPEED COMPARISONS

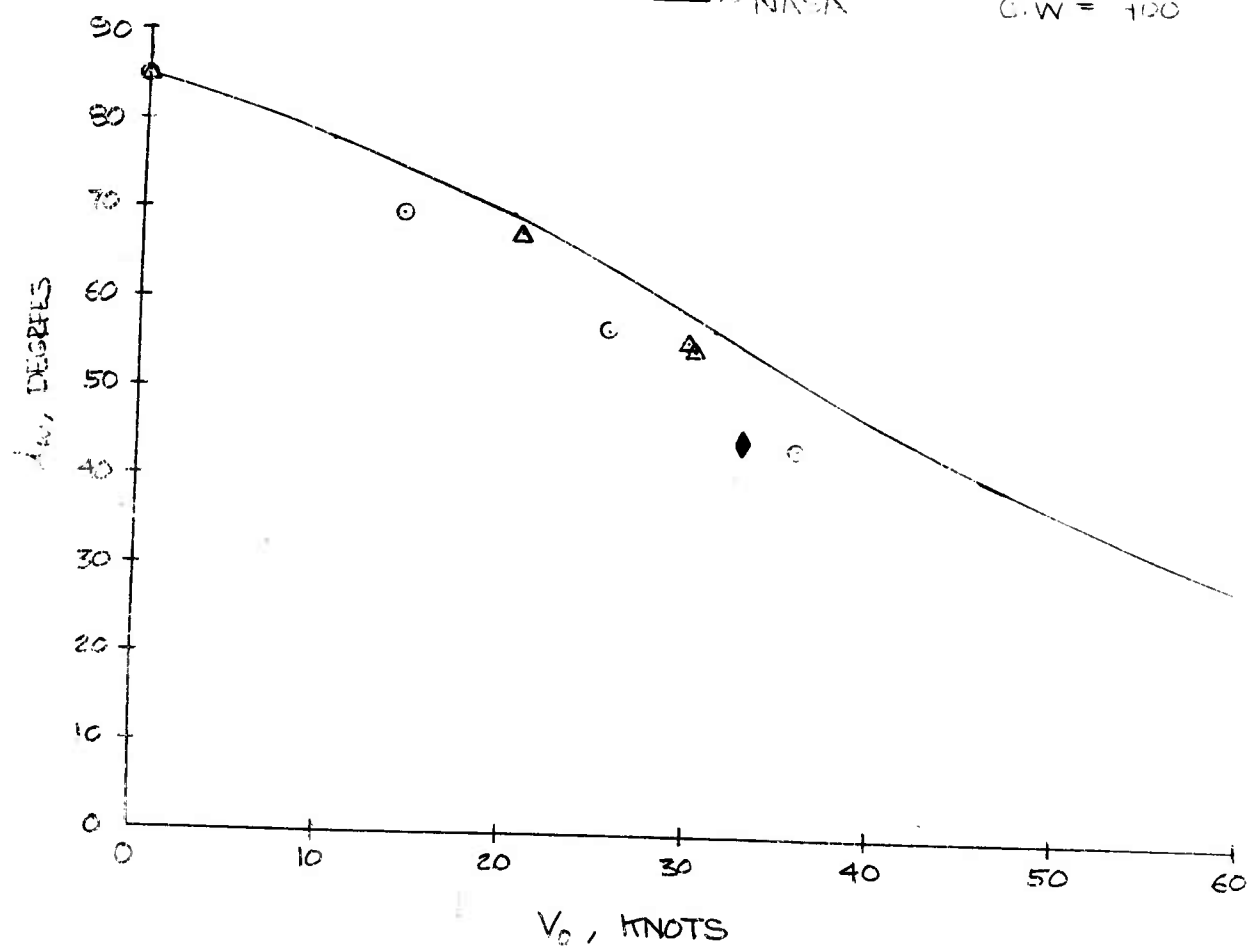
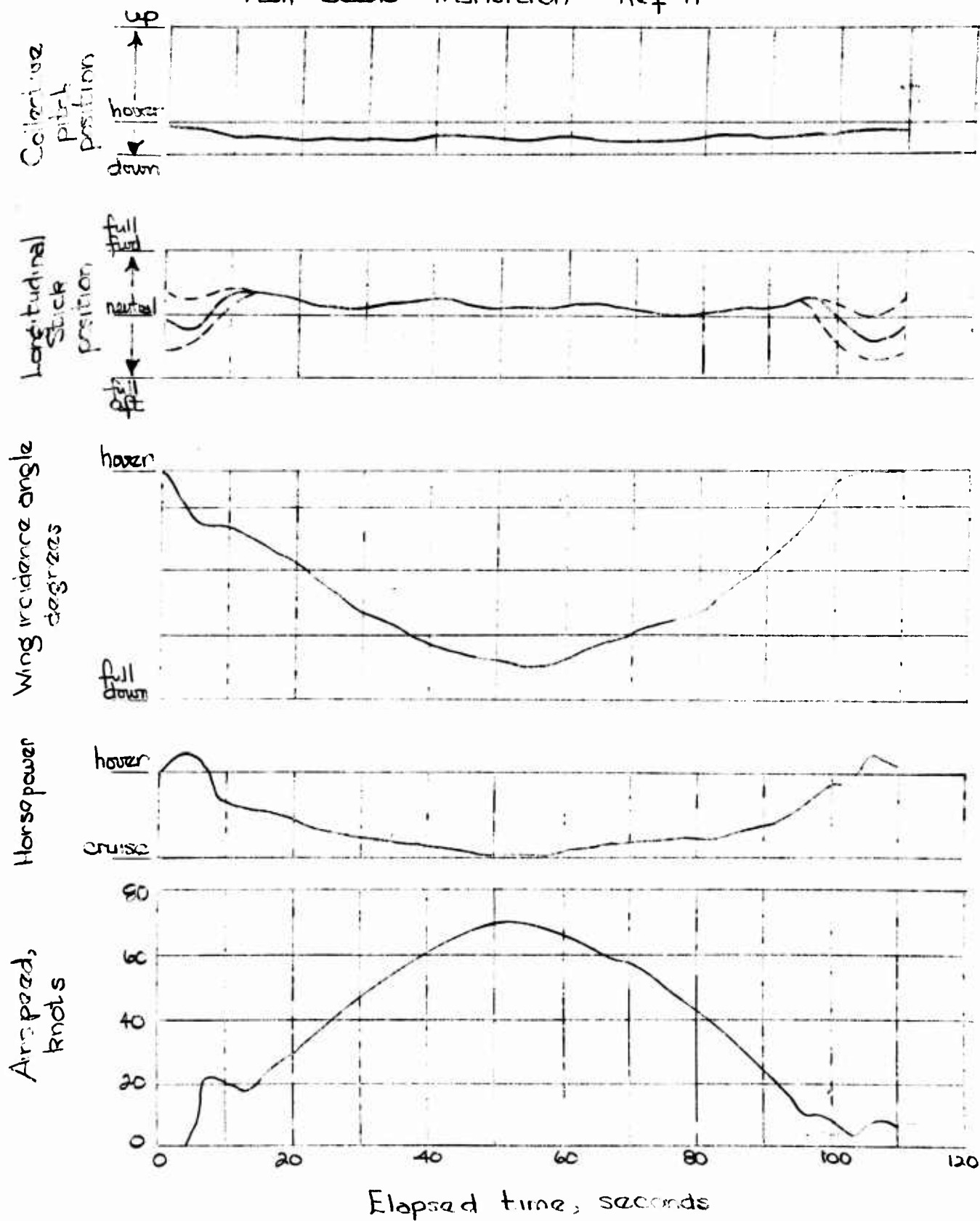
MODEL \neq FULL SCALE $\frac{1}{5.2}$ SCALE MODELO \sim PRINCETON G.W. = 3150 Δ \sim PRINCETON G.W. = 3400FULL SCALE \blacklozenge \sim VERTOL G.W. = 4000— \sim NASA G.W. = 4000

Fig. 75

Full Scale Transition - Ref 11



RESULTS: PREDICTED LONGITUDINAL TRIM

Figures 76 and 77 present the results of the theoretical predictions of the forces and moment contributions of the wing and rotor as compared to experimentally measured total trim values. Included are comparisons of the results obtained by assuming the wing characteristics of References 4 and 7 as well as those given by the average values of the rotational flow analysis. Some of the more interesting features to be observed in the comparisons are:

1) The predicted Z-Force values in the $i_w = 44^\circ$ case are approximately 30 per cent less than that required for vertical trim for all wings considered. From the X-Force considerations in the same condition, indications are that the deficiency in lifting force should be made up by nearly equal contributions of wing and rotor in order to maintain longitudinal trim.

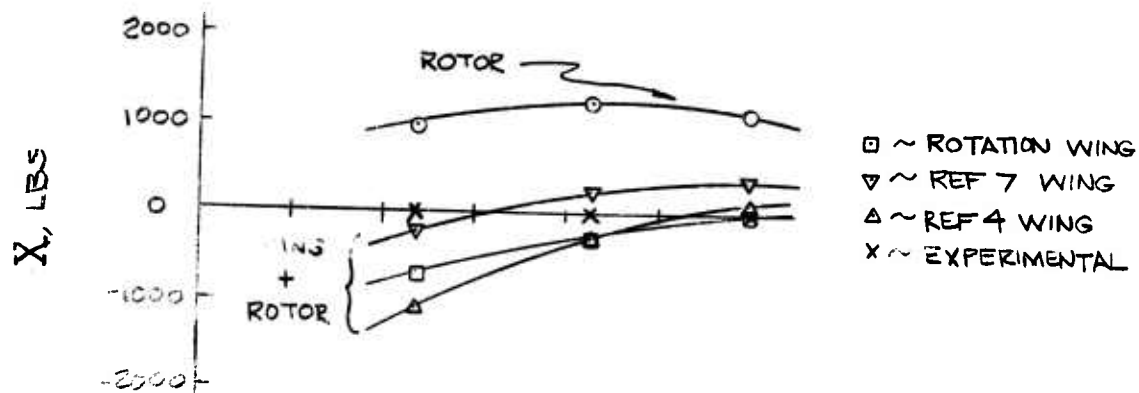
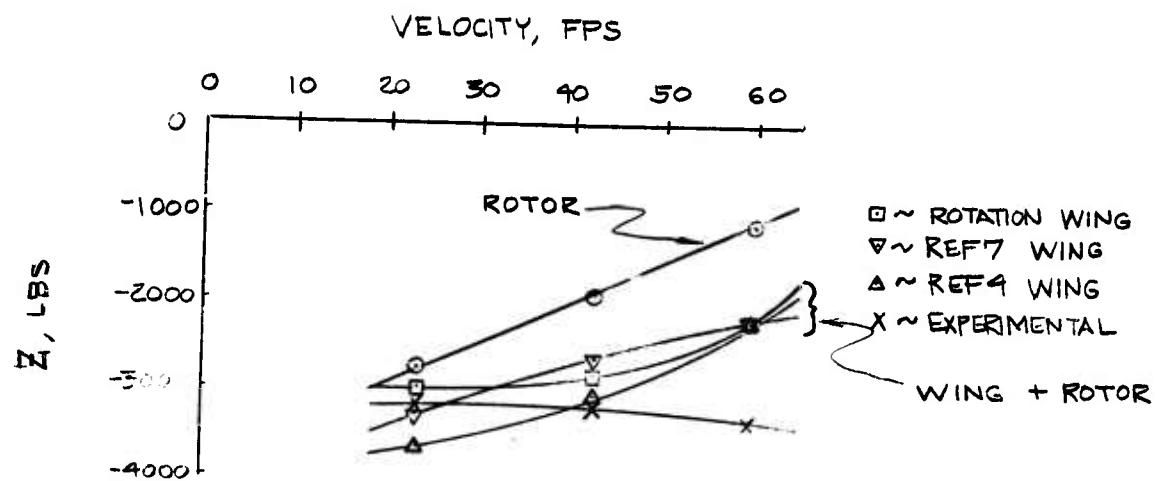
2) Discrepancies in X-Force comparisons can be attributed to several possible sources, not the least of which is the necessity of obtaining the difference of two large forces to ascertain longitudinal trim. One interesting possibility to be considered in attempting to resolve vagaries in the prediction of longitudinal trim conditions is the effect of rotation on the resolved directions of the wing lift and drag forces. These forces have been defined as acting respectively perpendicular to and along the resultant velocity vector as defined by α' . Changes in local α' due to rotation would therefore change the direction of action of the large lift force, thereby changing significantly the longitudinal trim solution. A strip analysis

has been performed to determine the magnitude of the corrections that might arise from local re-resolution of the wing lift and drag forces. The results of this analysis are presented in Figure 78 in a comparison to results obtained using the average of the rotational C_L and C_D but resolved on the basis of $\alpha'_{\text{NON-ROTATING}}$. The results presented are meaningful only to the extent that they indicate the magnitude of the corrections that could be required; attempts to infer anything beyond this are seriously questionable in view of the crude assumptions made in the induced velocity profile.

3) The theoretical moment predictions presented in Figure 77 show a general under-prediction of the positive moment encountered in the tail-off experiments. There exist numerous possible sources which could contribute to the inaccuracies apparent in the predicted values. Among the most significant of these are the inability to account for the influence of the wing on the flow at the rotor, the effect of fuselage aerodynamics, the questionable prediction of rotor H-Force and longitudinal flapping, and the possibility of chordwise center of pressure shifts in local wing flow conditions. The effect of rotation on wing forces has been considered in the moment contributions and the results are presented in Figure 77, and Figure 79 demonstrates the effect of rotation and re-resolution of the wing lift and drag forces. In general, both of these considerations appear to worsen the discrepancy between the predicted and measured moments, indicating that the inaccuracy lies elsewhere in the analysis.

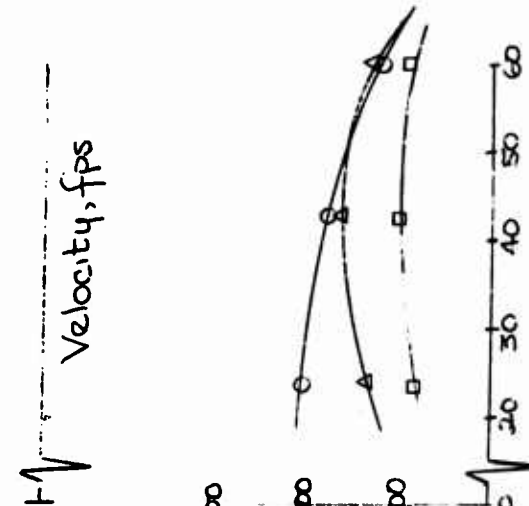
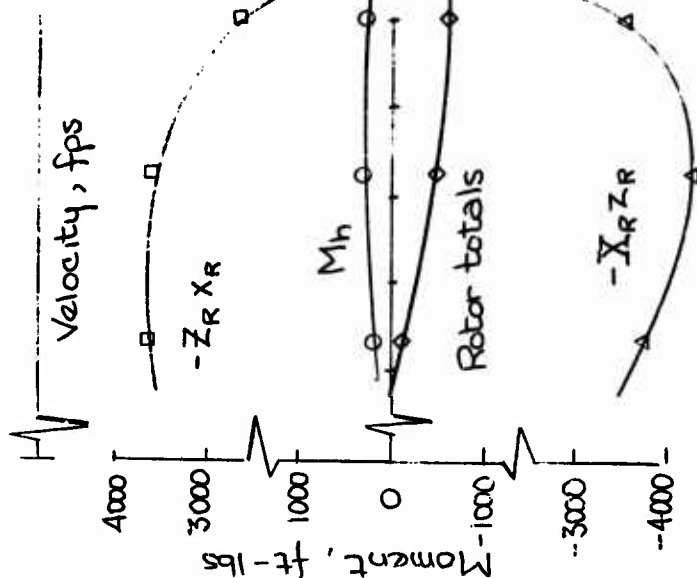
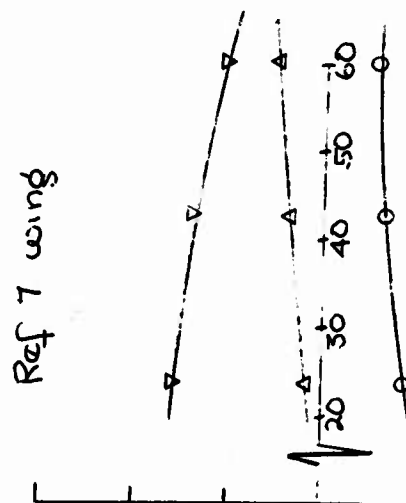
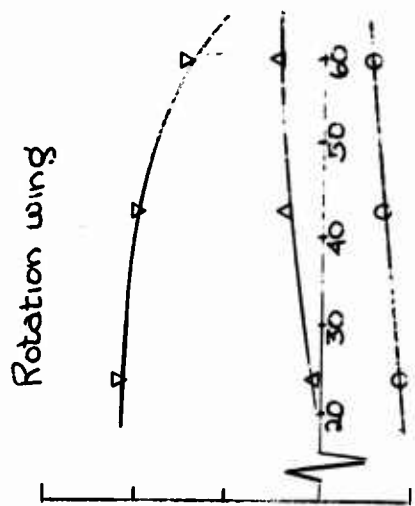
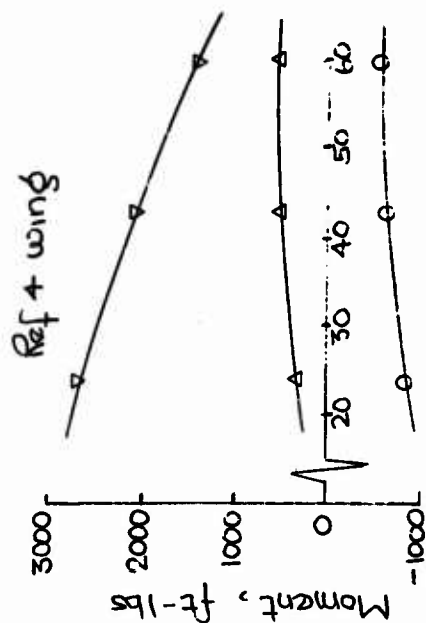
Fig. 76

LONGITUDINAL FORCE TRIM



Wing Contributions

$0 \sim M_{ac}$ $\Delta \sim \sum \omega x_{\omega}$ $\nabla \sim -\sum \omega z_{\omega}$



$0 \sim \text{Ref 4 wing}$
 $\Delta \sim \text{Rotation wing}$
 $\square \sim \text{Ref 7 wing}$

Rotor Contribution

Wing Totals

$0 \sim \text{Ref 4 wing}$
 $\Delta \sim \text{Rotation wing}$
 $\square \sim \text{Ref 7 wing}$
 $\times \sim \text{Experimental}$
 Rotor + Wing Totals

Fig. 78

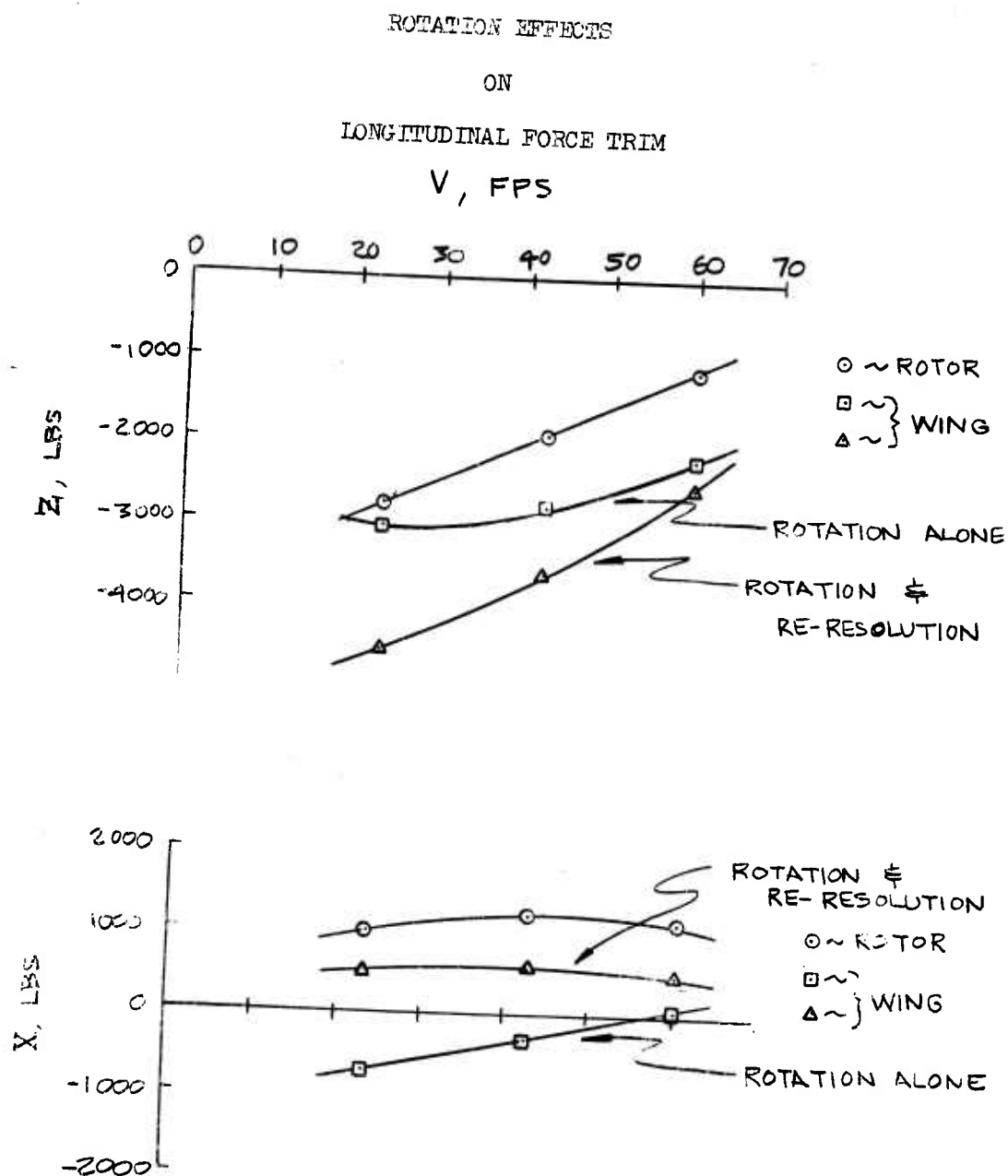
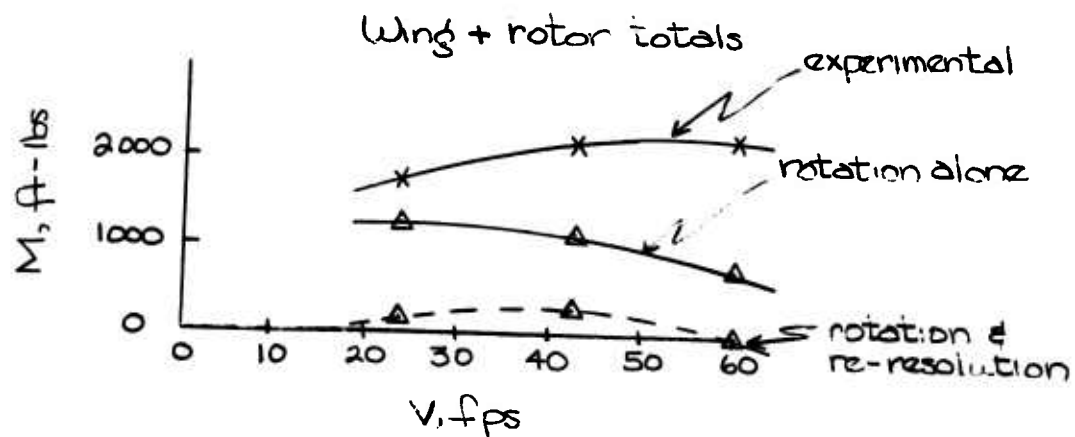
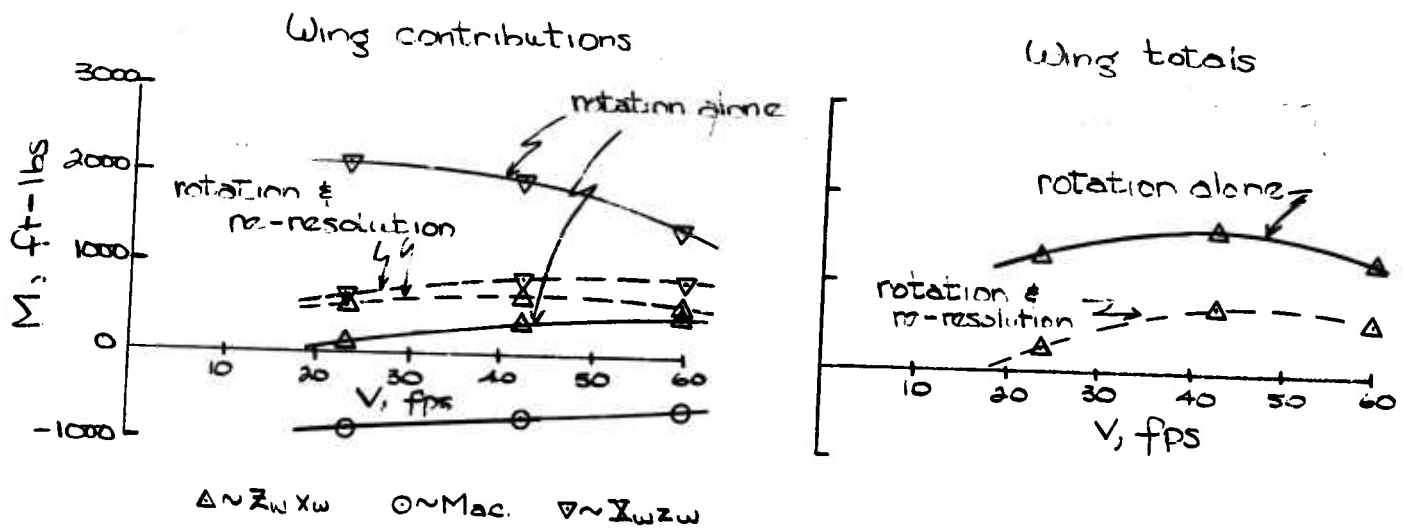


Fig. 79



ROTATIONAL EFFECTS
ON
LONGITUDINAL MOMENT TRIM

RESULTS: PREDICTED LONGITUDINAL DYNAMICS

The results concerned with the remaining test objectives -- determination of the static stability characteristics for use in formulation of expressions for the aircraft's dynamic behaviour -- are best presented in the Figures 47 through 54. However, some of the more salient features of these presentations are worth noting as being important results of the tests and analysis.

The most important single item to be noted in the static and dynamic stability characteristics is the overwhelming influence of the wing on virtually all parameters. The importance of wing effects dictates a shift in emphasis concerning the influence of the rotor from considerations of the forces and moments it develops to the operating conditions it produces at the wing. Thus such problems as induced velocity magnitude, distribution, direction and rotation assume a significance not generally attributed to them in conventional stability and control analyses of rotor aircraft. In particular, the slipstream rotation has a possible influence that would render the neglect of power scaling as a serious compromise on attempts to simulate the full scale aircraft by means of a model. Actually power scaling involves scaling both torque and RPM since the former determines the slipstream rotation while the latter determines the hub moment due to flapping hinge offset.

The importance of the rotor slipstream in its influence of the wing has another interesting corollary in the effects of accelerated flight conditions on the characteristics of the aircraft. A consideration of Figures 45, 46 and 62 through 64 shows that a trimmed aircraft

will exhibit distinctly different dynamic characteristics than one engaged in accelerated maneuvers such as transition or STOL maneuvers. These changes in behaviour generally transcend the expected variations due to change in flight speed or wing tilt angle alone.

The dynamics of the tail-off aircraft in the higher wing tilt angle conditions are generally characterized by excessive static stability with insufficient modal damping, both of which conditions can be attributed to large positive M_v derivatives and low and/or unstable M_α and M_δ derivatives. These effects manifest themselves in an unstable oscillatory mode with rather short period increasing with trim speed. Reference to Figures 49, 52 and 66, indicates that virtually all of the unfavorable contributions to M_v , M_α , and M_δ , come from the wing in its unstalled conditions and by far the greatest amounts of the wing contributions are due to the α' derivatives.

Theoretical horizontal tail and pitch fan contributions to the moment derivatives are generally small except in the highest velocity condition. Figure 70 indicates that both $M_{\dot{\alpha}}$ and $M_{\dot{\delta}}$ contributions of the tail are becoming significant in the oscillatory mode. In particular the more effective $C_{L_{\delta 5}} = 4$ horizontal stabilizer provides sufficient rate and attitude derivatives to stabilize this mode for all stabilizer incidences. An interesting result of a comparison of the two different horizontal tail effectivenesses assumed is the effect of varying tail incidence in each case. While both tails provide sufficient static stability for all incidences to eliminate the divergence noted in the tail-off case, the effect of varying incidence is to increase period with the less effective tail

and to decrease it with the more effective one. The appearance of a second oscillatory mode can be noted for the amount of M_{α} provided by the $C_{L\alpha_s} = 4$ tail.

In general the tail is very beneficial in eliminating divergences present in many of the tail-off conditions, but the mode damping improvements affected in the oscillatory mode are bought at the price of large decreases in the period of the oscillation.

One last point worthy of particular mention concerns the $i_w = 70^\circ$ divergence referred to above which comes as a direct result of a negative sign in the E coefficient of the characteristic equation. The static instability is caused by the positive value of the Z_{α} derivative which is multiplied by the large positive velocity stability derivative M_v . An examination of the static test data in Figures 20, 21, and 22 reveals that the total airplane forces are inflecting quite rapidly in the region of zero C_{α_f} , which, when coupled with the inability to establish any continuity or repeatability in the velocity varying runs, would lead one to suspect strongly the occurrence of discontinuous and hysteretic phenomena such as wing stall.

The non-rotating α' computed for this trim condition is only about 9° , however, so one must suspect local flow conditions such as rotational effects as being responsible for this behaviour. A more complete investigation of the airplane around these conditions utilizing some technique of flow visualization such as smoke or tufts might reveal some very interesting phenomena, but again the importance of careful power scaling must be emphasized.

and to decrease it with the more effective one. The appearance of a second oscillatory mode can be noted for the amount of M_{α} provided by the $C_{L\alpha_s} = 4$ tail.

In general the tail is very beneficial in eliminating divergences present in many of the tail-off conditions, but the mode damping improvements affected in the oscillatory mode are bought at the price of large decreases in the period of the oscillation.

One last point worthy of particular mention concerns the $i_w = 70^\circ$ divergence referred to above which comes as a direct result of a negative sign in the E coefficient of the characteristic equation. The static instability is caused by the positive value of the Z_{α} derivative which is multiplied by the large positive velocity stability derivative M_v . An examination of the static test data in Figures 20, 21, and 22 reveals that the total airplane forces are inflecting quite rapidly in the region of zero α_f , which, when coupled with the inability to establish any continuity or repeatability in the velocity varying runs, would lead one to suspect strongly the occurrence of discontinuous and hysteretic phenomena such as wing stall.

The non-rotating α' computed for this trim condition is only about 9° , however, so one must suspect local flow conditions such as rotational effects as being responsible for this behaviour. A more complete investigation of the airplane around these conditions utilizing some technique of flow visualization such as smoke or tufts might reveal some very interesting phenomena, but again the importance of careful power scaling must be emphasized.

Fig. 80

PERIOD OF SHORT-PERIOD OSCILLATORY MODE

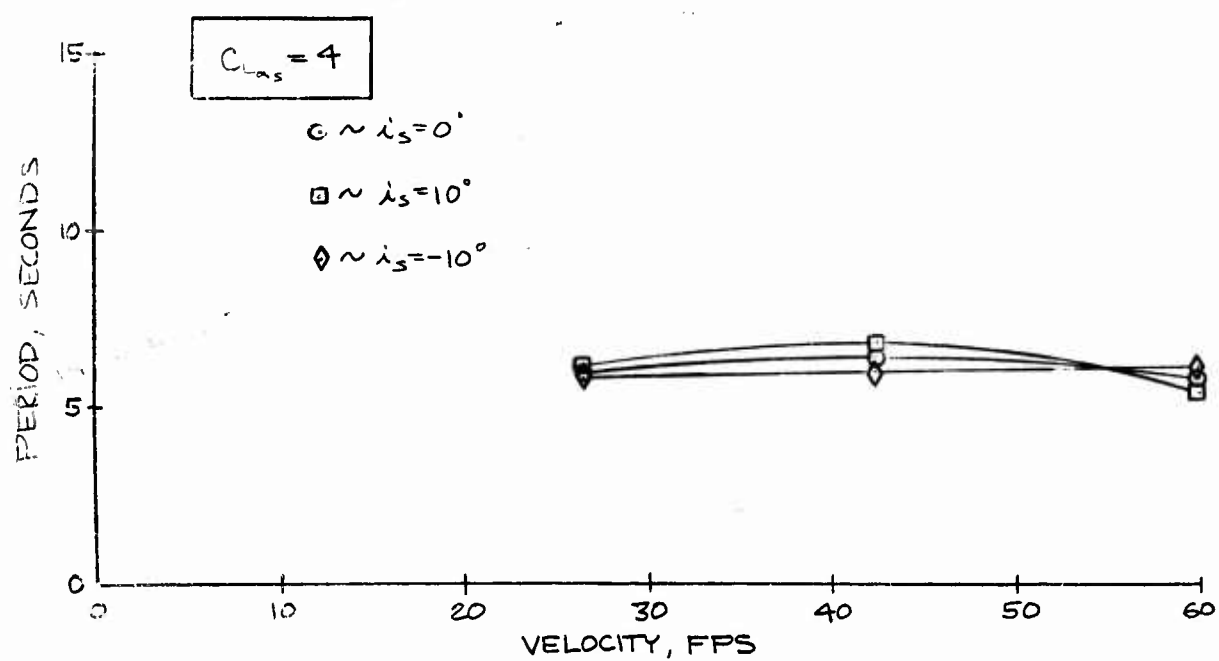
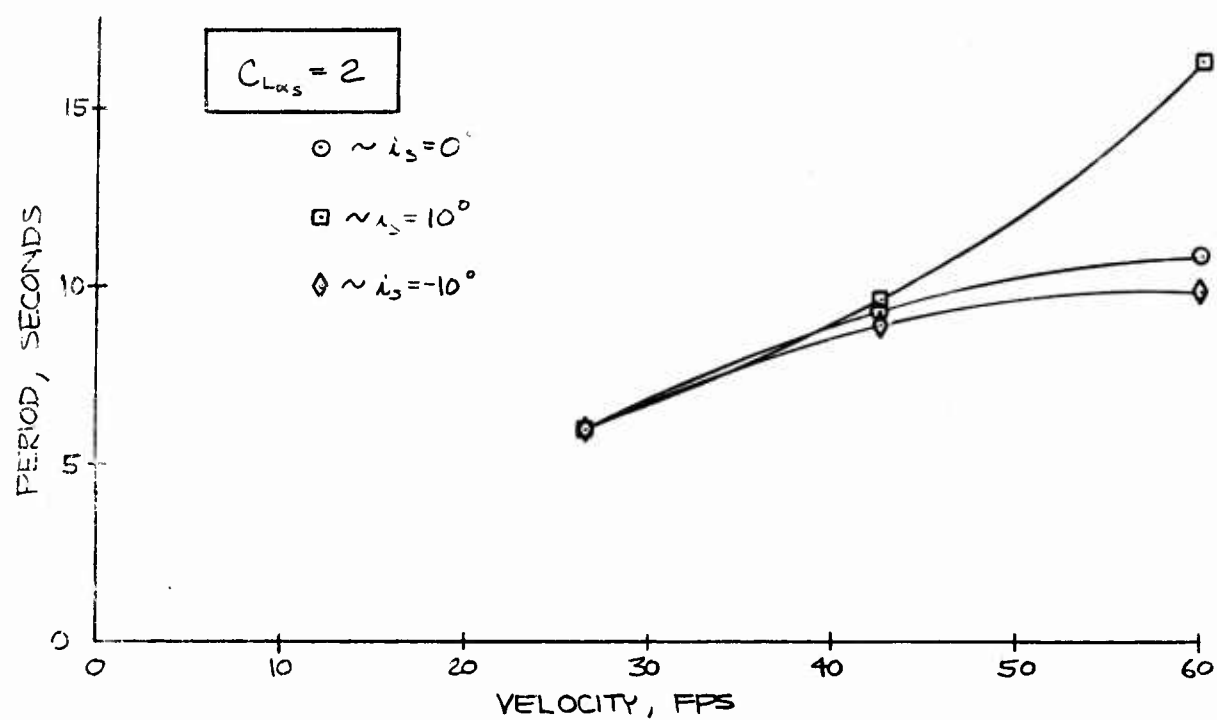
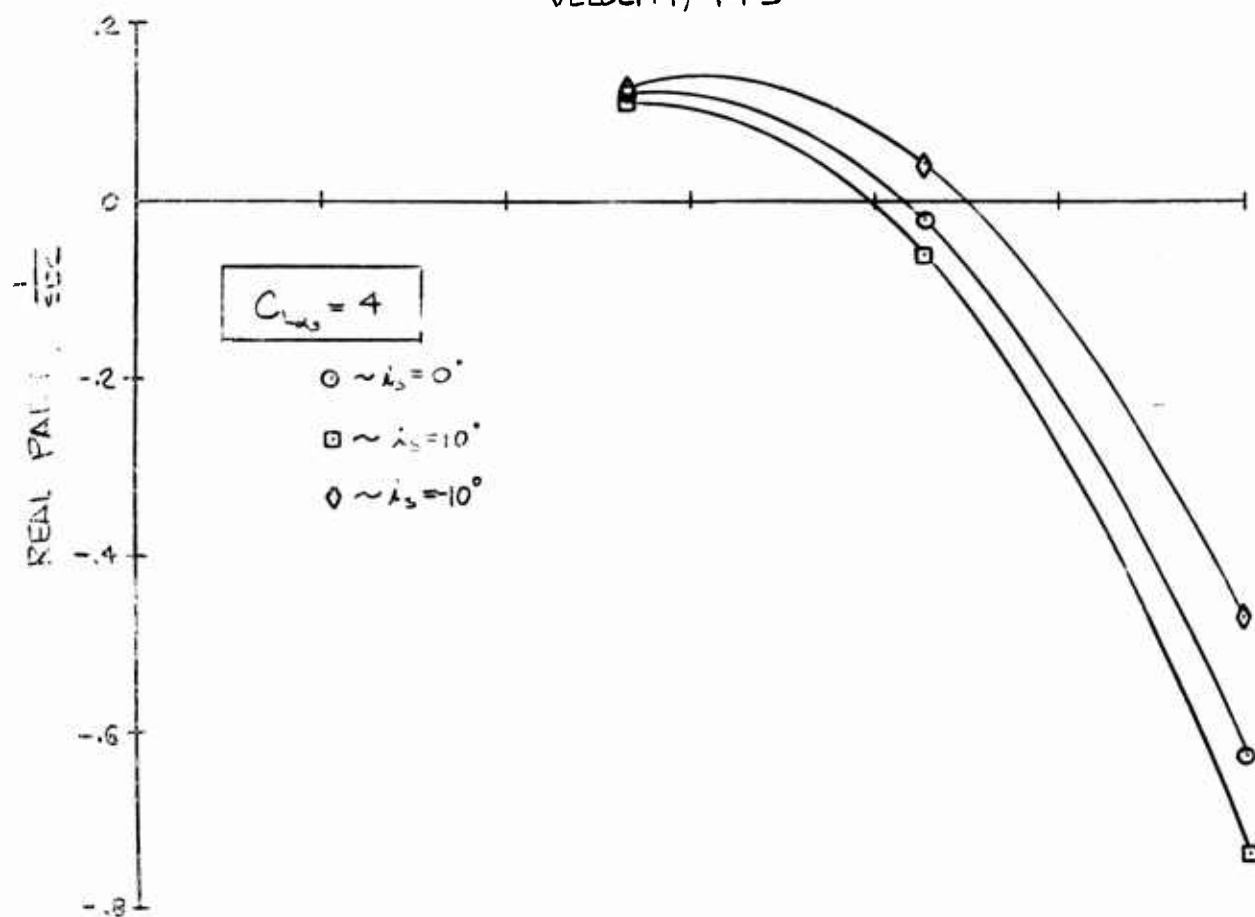
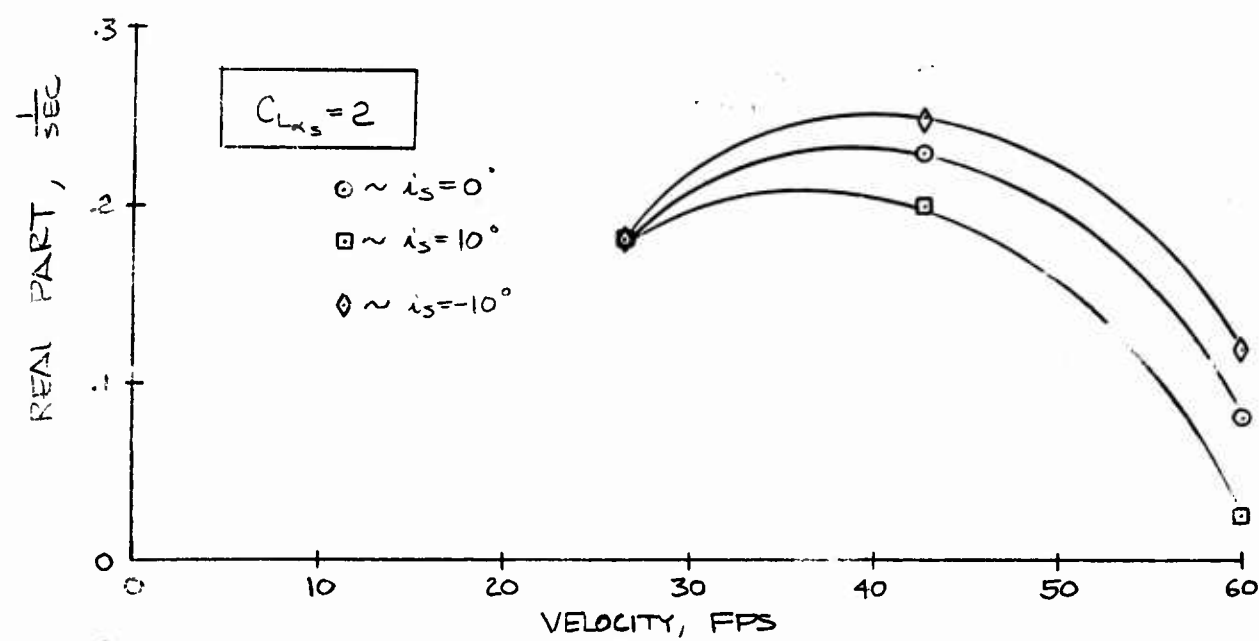


Fig. 81

REAL PART OF SHORT PERIOD OSCILLATORY ROOTS



CONCLUSIONS: THEORETICAL AND EXPERIMENTAL DATA

Several important conclusions can be drawn from the discussion and results of the tests and the associated analyses presented. Those deemed worthy of particular mention are listed below, not necessarily in order of importance.

1. (a) The Forward Flight Facility, although designed primarily for dynamic testing, can be satisfactorily and beneficially used as a static testing facility.
- (b) Information obtained from static tests of a $1/5$ scale model of the VERTOL V-76 compares favorably with the results of wind tunnel tests conducted on a $1/4$ scale model of the same aircraft. Neglect of proper torque and Ω scaling in the $1/4$ scale model tests eliminates the possibility of a comparison of the airplane pitching moments.
- (c) Trim speeds obtained from the static tests and the horizontal degree of freedom dynamic tests lie well within the probable scatter of trim speeds measured on the full scale aircraft.
- (d) General trends of collective pitch and tail load required to trim during model transition tests compare well with measurements made on the full scale aircraft in similar maneuvers.
2. (a) The importance of the wing and the influence of the rotor on the wing demand separate measurement of wing and rotor forces for adequate evaluation of their respective contributions to the trim forces and moments and the static stability derivatives.

2. (b) Use of power-off wing characteristics in conjunction with the vector summation of free stream and induced velocities is inadequate for prediction of wing characteristics.
- (c) The possibility exists of significant influence of rotational flow on the overall wing operating conditions and derivative contributions.
3. (a) Dynamic characteristics predicted by the use of the measured tail-off static stability derivatives exhibit a general symptomatic behavior of excessive static margin, contributed by M_v , and insufficient oscillatory mode damping.
- (b) Excess static margin as noted above in 3(a) manifests itself in a short period divergent oscillation. Addition of a theoretical tail is in itself inadequate to stabilize this oscillation except at high trim speeds.
- (c) Some alleviation of the problems associated with the oscillatory motion can be affected by the use of positive tail incidences which result in an overall reduction in the velocity stability of the aircraft. Such a procedure will effect both period and damping depending upon the tail effectiveness assumed.
4. (a) In view of the possible importance of the airplane power conditions it is recommended that future dynamic tests be conducted in the accelerated flight conditions encountered during transition.
- (b) In order to comply with the above recommendation, complete transitions of the model with trimmed vertical forces should be conducted to determine the exact acceleration profiles encountered in various scaled trim transitions.

REFERENCES

1. Gebhard, David F., An Economical Technique for the Construction and Hovering Flight Evaluation of Dynamically Similar Helicopter Models., Princeton University Aeronautical Engineering Department, Report No. 373, November 1956.
2. Bennett, Robert M. and Curtiss, Howard C. Jr., An Experimental Investigation of Helicopter Stability Characteristics Near Hovering Flight Using a Dynamically Similar Scale Model., Princeton University Aeronautical Engineering Department, Report No. 517, July 1960.
3. Martinez, Esteban, A New Facility For the Study of Aircraft Dynamics., Aeronautical Engineering Department, Princeton University, Report No. 532, December 1960.
4. Freck, P., A Preliminary Investigation of a Tilt-Wing Propeller Driven VTOL Aircraft, Princeton University Department of Aeronautical Engineering, Report No. 456, May 1959.
5. Hargraves, Charles R., An Analytical Study of the Longitudinal Dynamics of a Tilt-Wing VTOL., To be published.
6. Gessow, Alfred, and Myers, Garry C. Jr., Aerodynamics of the Helicopter., The MacMillan Company, 1952.
7. Cromwell, Charles H. III, and Payne, Henry E., III, A Stability Analysis of Tilt-Wing Aircraft, Princeton University Aeronautical Engineering Department, Report No. 477, May 1960
8. Shapiro, Jacob, Principles of Helicopter Engineering, McGraw Hill, 1955.
9. Nikolsky, A.A., "Notes From Princeton University Aeronautical Engineering Course A.E. 567, 568, 1957, Unpublished.
10. Fillicko, J.J. and Poore, P.L., NACA Wing Tunnel Test Results of the Vertol Model 76, Vertol Aircraft Corporation Report Aeronautical Inv. III - 133.
11. Stepniewski, W. Z., and Dancik, Paul J., Flight Testing Experiments with the Tilt-Wing Aircraft, Institute of Aeronautical Sciences Report No. 59 - 8, January 1959.

12. Nikolsky, A.A., Helicopter Analysis, John Wiley and Sons, Inc. 1951
13. Seckel, Edward, and Curtiss, Howard C. Jr., Aerodynamic Forces and Stability Derivatives, May 1957, Unpublished.
14. Kuhn, Richard E., and Draper, John W., "Investigation of the Aerodynamic Characteristics of a Model Wing Propeller Combination and of the Wing and Propeller Separately at Angles of Attack up to 90° ". NACA TR 1263, 1956.

APPENDIX A

For the purpose of developing theoretical expressions for the static stability derivatives of the Vertol 76, it is desirable to separate the effects of the rotor and those of the wing for analysis, combining them later for the total stability derivatives. It is assumed in this analysis that the presence of the wing behind the rotor has no effect on the rotor's operating characteristics, whereas the presence of the rotor ahead of the wing intimately affects the operating characteristics of the wing as discussed in the Part III page 101 and as presented in the following analysis.

Referring to Figure 13 page 69 we can write three equations of static equilibrium.

$$\sum F_z = 0 = \sum Z_{gravity} + \sum Z_{rotor} + \sum Z_{wing} + \sum Z_{fus.} \quad (1)$$

$$\sum F_x = 0 = \sum X_{gravity} + \sum X_{rotor} + \sum X_{wing} + \sum X_{fus.} \quad (2)$$

$$\sum M_{cg} = 0 = \sum M_{gravity} + \sum M_{rotor} + \sum M_{wing} + \sum M_{fus.} \quad (3)$$

Writing the rotor forces about an axis system coincident with the shaft with its origin in the plane of the flapping hinges and resolving the moment about the airplane c.g. gives:

$$Z_R = -H \cos i_w - T \sin i_w \quad (4)$$

$$X_R = -H \sin i_w + T \cos i_w \quad (5)$$

$$M_R = M_h - X_R Z_R - Z_R X_R \quad (6)$$

Similarly the wing forces and moment may be written

$$\bar{Z}_w = -L_w \cos(i_w - \alpha') + D_w \sin(i_w - \alpha') \quad (7)$$

$$\bar{X}_w = -L_w \sin(i_w - \alpha') - D_w \cos(i_w - \alpha') \quad (8)$$

$$M_w = M_{a.c.} + \bar{Z}_w x_w - \bar{X}_w z_w \quad (9)$$

and finally for the fuselage

$$\bar{Z}_f = -L_f \cos \alpha_f - D_f \sin \alpha_f \quad (10)$$

$$\bar{X}_f = -D_f \cos \alpha_f + L_f \sin \alpha_f \quad (11)$$

$$M_{fT} = M_f - \bar{Z}_f x_f + \bar{X}_f z_f \quad (12)$$

The choice of axis system for the rotor could be an unfortunate one were it not for the fact that this airplane has no cyclic control provided, and therefore no complication due to the appearance of control terms in the expressions for forces and derivatives. Using the developments of References 6 and 12 the expressions for the non-dimensionalized rotor characteristics are:

$$\frac{\partial C_T}{\partial \delta} = \frac{\theta}{3} + \frac{\lambda}{2} + \frac{\mu_x^2 \cos^2 \alpha}{2} \theta \quad (13)$$

where the tip-loss factor $B = 1$

$$\begin{aligned} \frac{\partial C_H}{\partial \delta} = & \mu_x \cos \alpha \left\{ \frac{\delta}{2a} + 8 \left[\left(\frac{\partial C_T}{\partial \delta} \right)^2 - \frac{3}{16} \lambda \right. \right. \\ & \left. \left(\frac{\partial C_T}{\partial \delta} \right) \left(\frac{2 \mu_x \cos \alpha}{3\pi} - \frac{7}{6} \mu_x^2 \cos^2 \alpha \right) \right. \\ & \left. \left. - \lambda^2 \frac{\mu_x \cos \alpha}{16\pi} \left(1 - \frac{5\pi}{8} \mu_x \right) \right] \right\} \quad (14) \end{aligned}$$

$$a_1 = \frac{8M_x \cos \alpha}{2 + M_x^2 \cos^2 \alpha} \left[\frac{\lambda}{2} - \frac{\lambda M_x^2 \cos^2 \alpha}{8} + \frac{2\theta}{3} \right] \quad (15)$$

$$M_h = \frac{eb a_1}{2} \text{ C.F.} \quad \text{in dimensional form} \quad (16)$$

The wing terms may be written in terms of the dependent variables

$$\alpha' = \alpha' (M_x, \alpha) \quad \text{and} \quad V_R = V_R (M_x, \alpha) \quad \text{as follows:}$$

$$L_w = \frac{1}{2} \rho V_R^2 S C_L \quad (17)$$

$$D_w = \frac{1}{2} \rho V_R^2 S C_D \quad (18)$$

$$M_{ac.} = \frac{1}{2} \rho V_R^2 S_w (C_{M_{ac.}}) \quad (19)$$

where C_L and C_D are functions of α' .

Again referring to Figure 2 and using the laws of sines and cosines respectively, and assuming fully developed slipstream at the wing, we can write the expressions for the dependent variables

$$\alpha' = \cot^{-1} \frac{V/\Omega R - \lambda}{M_x \cos \alpha} \quad (20)$$

$$V_R = \Omega R \sqrt{M_x^2 + 4\lambda V/\Omega R} \quad (21)$$

Using simple axial momentum theory and equating the thrust to the change in axial momentum through the disk, we find that

$$\frac{N}{\Omega R} = \frac{C_T}{2 \sqrt{\lambda^2 + \mu_x^2 \cos^2 \alpha}} \quad (22)$$

In order to determine the operating conditions of the wing and rotor it is necessary to evaluate the rotor parameters C_T and λ . With these quantities it is then possible to determine from equations (20) through (22) the wing angle of attack α' , the resultant velocity at the wing, V_R as well as C_H and a_1 , of the rotor. At this point two or more alternatives present themselves for estimating the wing parameters C_L and C_D . The most straight-forward one as presented in Reference 4, and with modifications in Reference 5, is to use power-off lift and drag curves with the α' determined above. Another is to use experimental plots of wing forces versus α' at various power conditions which are rarely obtainable, but available in Reference 7 for a rather different wing-rotor combination than that under consideration in this report. Still another method is to go through an inverse solution from the experimental trim conditions, using theoretically determined values of C_T , C_H and α' as above, and solving for the wing lift and drag forces. For this purpose it can be assumed that the fuselage is non-lifting, makes a negligible contribution to pitching moment, and, over small ranges of angle of attack, has constant drag contributed solely by the approximately spherical nose bubble. Since the trim conditions are at $\alpha_f = 0$ the two force trim equations may be written as

$$W = H \cos i_w + T \sin i_w + L_w \cos(i_w - \alpha') - D_w \sin(i_w - \alpha') \quad (23)$$

$$\text{and } D = 0 = T \cos i_w - H \sin i_w - L_w \sin(i_w - \alpha') - D_w \cos(i_w - \alpha') + X_f \quad (24)$$

λ could be arrived at, but only after much labor. A simpler method given values for α , θ and M_x an explicit solution for C_T and

$$\lambda = M_x \sin \alpha - \frac{C_T}{2 \sqrt{X^2 + M_x^2 \cos^2 \alpha}} \quad (29)$$

the other a fourth order in λ , two equations can be written in C_T and λ ; one is equation (10) and

$$\lambda = M_x \sin \alpha - \frac{C_T}{2R} \quad (28)$$

Using equations (13), (28) and the definition of

above developments.

termining the rotor parameters C_T and λ necessary for all of the Proceeding with this in view, we can now present a method of de-

the methods used.

of this report, it being the purpose of this section only to develop D_w . All of these methods were tried and are discussed in Part III equations (25) and (26) will yield another set of values for L_w and

Noting that $X_F = -D_F \approx -\frac{1}{2} P (M_x \Omega R)^2 A_{FRONTAL} C_{SPHERE}$

$$D_w = (-W + H \cos I_w + P \sin I_w) \sin (I_w - \alpha') - H \sin I_w - P \cos I_w - X_F \cos (I_w - \alpha') \quad (26)$$

and

$$L_w = (W - H \cos I_w - P \sin I_w) \cos (I_w - \alpha') + (X_F + P \cos I_w - H \sin I_w) \sin (I_w - \alpha') \quad (25)$$

Combining and solving for L_w and D_w gives

Combining and solving for L_w and D_w gives

$$L_w = (W - H \cos i_w - T \sin i_w) \cos (i_w - \alpha') + (X_f + T \cos i_w - H \sin i_w) \sin (i_w - \alpha') \quad (25)$$

and

$$D_w = (-W + H \cos i_w + T \sin i_w) \sin (i_w - \alpha') - H \sin i_w - T \cos i_w - X_f) \cos (i_w - \alpha') \quad (26)$$

Noting that $X_f = -D_f \cong -\frac{1}{2} \rho (\mu_x \Omega R)^2 A_{\text{FRONTAL}} C_{D_{\text{SPHERE}}}$

equations (25) and (26) will yield another set of values for L_w and D_w . All of these methods were tried and are discussed in Part III of this report, it being the purpose of this Section only to develop the methods used.

Proceeding with this in view, we can now present a method of determining the rotor parameters C_T and λ necessary for all of the above developments.

Using equations (13), (28) and the definition of

$$\lambda = \mu_x \sin \alpha - \frac{N}{\Omega R} \quad (28)$$

two equations can be written in C_T and λ ; one is equation (10) and the other a fourth order in λ ,

$$\lambda = \mu_x \sin \alpha - \frac{C_T}{2 \sqrt{\lambda^2 + \mu_x^2 \cos^2 \alpha}} \quad (29)$$

Given values for α , Θ and μ_x an explicit solution for C_T and λ could be arrived at, but only after much labor. A simpler method

is to use the charts developed in Appendix B for this purpose, and as explained below. On page 99 of Part III is discussed a method of determining a Θ_{eff} which may be used in turn to solve for C_T and λ in the following manner. We have in the experimental data three values of hovering thrust (neglecting wing profile and induced drag at $\alpha' = 0$) presented as Figure 20 page 71, corresponding to the collective pitch settings for the three unaccelerated forward flight conditions of Figures 22, 25 and 27 on pages 73, 76 and 78. Setting $\mu_x = 0$ in equation (28) gives

$$\lambda_h = - \frac{N}{\Omega R} \quad (30)$$

and again applying axial momentum theory

$$N = \sqrt{\frac{T_h}{2\rho\pi R^2}} = \Omega R \sqrt{\frac{C_{Th}}{2}} \quad (31)$$

Combining equations (30) and (31) gives

$$\lambda_h = - \sqrt{\frac{C_{Th}}{2}} \quad (32)$$

which can be substituted into equation (13) to obtain a solution for Θ_{eff}

With the value for Θ_{eff} we can now proceed to solve for C_T and λ in the following manner. Using the notation of Appendix B where

$$\lambda_o = - \sqrt{\frac{C_T}{2}} \quad (33)$$

$$\bar{\lambda} = \frac{\lambda}{\lambda_o} \quad (34)$$

$$\bar{\mu}_x = \frac{\mu_x}{\lambda_o} \quad (35)$$

we can re-arrange equation (13) to give

$$\sqrt{\frac{C_T}{2}} = \frac{-\frac{\bar{\lambda}}{2} \pm \sqrt{\frac{\bar{\lambda}^2}{4} + \frac{16}{\alpha \sigma} \frac{\Theta_{eff}}{3}}}{8/\alpha \sigma} \quad (36)$$

and combining expressions (33) and (32) with the definition of $\mu_x = \frac{V}{\Omega R}$ we have

$$V = -\Omega R \bar{\mu}_x \sqrt{\frac{C_T}{2}} \quad (37)$$

Figure 83 page 215 presents a plot of $\bar{\lambda}$ versus $\bar{\mu}_x$ for constant α which may be used to determine $\bar{\lambda}$ for any value of $\bar{\mu}_x$ chosen at the particular α . Using the values of $\bar{\lambda}$ so determined from Figure 83 in equation (36) and an arbitrarily chosen value of $\bar{\mu}_x$ in equation (37) enables us to make a plot of $\sqrt{\frac{C_T}{2}}$ versus V for $\alpha = \text{constant}$. From this curve we can then determine the values of C_T corresponding to the particular condition under consideration (V and α). The only quantity left, λ , can be found by substituting C_T into equation (33) to find λ_0 which may be used in equation (34) along with $\bar{\lambda}$ from above to find λ . Having determined the operating conditions of the wing and rotor we can now proceed to the development of expressions for the static stability derivatives.

Referring to equations (1) through (3) we can write

$$\frac{\partial Z}{\partial \alpha} \Big|_{\mu_x} = \frac{\partial Z_R}{\partial \alpha} \Big|_{\mu_x} + \frac{\partial Z_w}{\partial \alpha} \Big|_{\mu_x} + \frac{\partial Z_f}{\partial \alpha} \Big|_{\mu_x} \quad (38)$$

$$\frac{\partial X}{\partial \alpha} \Big|_{\mu_x} = \frac{\partial X_R}{\partial \alpha} \Big|_{\mu_x} + \frac{\partial X_w}{\partial \alpha} \Big|_{\mu_x} + \frac{\partial X_f}{\partial \alpha} \Big|_{\mu_x} \quad (39)$$

$$\frac{\partial M}{\partial \alpha} \Big|_{\mu_x} = \frac{\partial M_R}{\partial \alpha} \Big|_{\mu_x} + \frac{\partial M_w}{\partial \alpha} \Big|_{\mu_x} + \frac{\partial M_f}{\partial \alpha} \Big|_{\mu_x} \quad (40)$$

$$\Omega R \frac{\partial Z}{\partial V}|_{\alpha} = \frac{\partial Z_R}{\partial \mu_x}|_{\alpha} + \frac{\partial Z_w}{\partial \mu_x}|_{\alpha} + \frac{\partial Z_f}{\partial \mu_x}|_{\alpha} \quad (41)$$

$$\Omega R \frac{\partial X}{\partial V}|_{\alpha} = \frac{\partial X_R}{\partial \mu_x}|_{\alpha} + \frac{\partial X_w}{\partial \mu_x}|_{\alpha} + \frac{\partial X_f}{\partial \mu_x}|_{\alpha} \quad (42)$$

$$\Omega R \frac{\partial M}{\partial V}|_{\alpha} = \frac{\partial M_R}{\partial \mu_x}|_{\alpha} + \frac{\partial M_w}{\partial \mu_x}|_{\alpha} + \frac{\partial M_f}{\partial \mu_x}|_{\alpha} \quad (43)$$

where all derivatives are to be evaluated at the trim conditions previously determined. The contributions may then be written using equations (4) through (6) as

$$\frac{\partial Z_R}{\partial \alpha} = - \frac{\partial H}{\partial \alpha} \cos i_w - \frac{\partial T}{\partial \alpha} \sin i_w \quad (44)$$

$$\frac{\partial X_R}{\partial \alpha} = - \frac{\partial H}{\partial \alpha} \sin i_w + \frac{\partial T}{\partial \alpha} \cos i_w \quad (45)$$

$$\frac{\partial M_R}{\partial \alpha} = \frac{\partial M_h}{\partial \alpha} - Z_R \frac{\partial X_R}{\partial \alpha} - X_R \frac{\partial Z_R}{\partial \alpha} \quad (46)$$

$$\frac{\partial Z_R}{\partial \mu_x} = - \frac{\partial H}{\partial \mu_x} \cos i_w - \frac{\partial T}{\partial \mu_x} \sin i_w \quad (47)$$

$$\frac{\partial X_R}{\partial \mu_x} = - \frac{\partial H}{\partial \mu_x} \sin i_w + \frac{\partial T}{\partial \mu_x} \cos i_w \quad (48)$$

$$\frac{\partial M_R}{\partial \mu_x} = \frac{\partial M_h}{\partial \mu_x} - Z_R \frac{\partial X_R}{\partial \mu_x} - X_R \frac{\partial Z_R}{\partial \mu_x} \quad (49)$$

where

$$\frac{\partial T}{\partial \alpha} = \pi \rho \Omega^2 R^4 \frac{\partial C_I}{\partial \alpha} \quad (50)$$

$$\frac{\partial T}{\partial \mu_x} = \pi \rho \Omega^2 R^4 \frac{\partial C_T}{\partial \mu_x} \quad (51)$$

$$\frac{\partial H}{\partial \alpha} = \pi \rho \Omega^2 R^4 \frac{\partial C_H}{\partial \alpha} \quad (52)$$

$$\frac{\partial H}{\partial \mu_x} = \pi \rho \Omega^2 R^4 \frac{\partial C_H}{\partial \mu_x} \quad (53)$$

and the constant α and μ_x notation is implicit. Differentiating equation (13) with respect to α and μ_x respectively

$$\frac{\partial}{\partial \sigma} \frac{\partial C_T}{\partial \alpha} \Big|_{\mu_x} = \frac{1}{2} \frac{\partial \lambda}{\partial \alpha} \Big|_{\mu} - \mu_x^2 \sin \alpha \cos \alpha \quad (54)$$

$$\frac{\partial}{\partial \sigma} \frac{\partial C_T}{\partial \mu_x} \Big|_{\alpha} = \frac{1}{2} \frac{\partial \lambda}{\partial \mu_x} \Big|_{\alpha} + 2 \mu_x \cos^2 \alpha \quad (55)$$

and operating similarly on equations (14) and (15) we have

$$\begin{aligned} \frac{\partial}{\partial \sigma} \frac{\partial C_H}{\partial \alpha} \Big|_{\mu_x} = & -\mu_x \sin \alpha \{A\} + 8 \mu_x \cos \alpha \left\{ \left(\frac{\partial}{\partial \sigma} \right)^2 2 C_T \frac{\partial C_T}{\partial \alpha} \Big|_{\mu_x} \right. \\ & - \frac{3}{16} \left[\left(\frac{\partial C_T}{\partial \sigma} \right) B \frac{\partial \lambda}{\partial \alpha} \Big|_{\mu_x} + B \lambda \left(\frac{\partial}{\partial \sigma} \right) \frac{\partial C_T}{\partial \alpha} \Big|_{\mu_x} \right. \\ & + \left. \left(\frac{\partial C_T}{\partial \sigma} \right) \lambda \left(-\frac{2 \mu_x \sin \alpha}{3 \pi} + \frac{7}{3} \mu_x^2 \cos \alpha \sin \alpha \right) \right] \\ & \left. - \frac{\mu_x}{16 \pi} \left[2 \lambda C \cos \alpha \frac{\partial \lambda}{\partial \alpha} \Big|_{\mu_x} - \lambda^2 C \sin \alpha \right] \right\} \quad (56) \end{aligned}$$

$$\begin{aligned} \frac{\partial}{\partial \sigma} \frac{\partial C_H}{\partial \mu_x} \Big|_{\alpha} = & A \cos \alpha + 8 \mu_x \cos \alpha \left\{ \left(\frac{\partial}{\partial \sigma} \right)^2 2 C_T \frac{\partial C_T}{\partial \mu_x} \Big|_{\alpha} \right. \\ & - \frac{3}{16} \left[\left(\frac{\partial C_T}{\partial \sigma} \right) B \frac{\partial \lambda}{\partial \mu_x} \Big|_{\alpha} + \frac{\partial}{\partial \sigma} \lambda B \frac{\partial C_T}{\partial \mu_x} \Big|_{\alpha} \right. \\ & + \left. \left(\frac{\partial C_T}{\partial \sigma} \right) \lambda \left(\frac{2 \cos \alpha}{3 \pi} - \frac{7}{3} \mu_x \cos^2 \alpha \right) \right] \\ & \left. - \frac{\cos \alpha}{16 \pi} \left[2 \lambda \mu_x C \frac{\partial \lambda}{\partial \mu_x} \Big|_{\alpha} + \lambda^2 C + \lambda^2 \mu_x \frac{5 \pi}{8} \right] \right\} \quad (57) \end{aligned}$$

where

$$A = \left\{ \frac{\delta}{2\alpha} + 8 \left[\left(\frac{2C_T}{\alpha\delta} \right)^2 - \frac{3}{16} \lambda \left(\frac{2C_T}{\alpha\delta} \right) \left(\frac{2\mu_x \cos \alpha}{3\pi} - \frac{1}{6} \mu_x^2 \cos^2 \alpha \right) - \frac{\lambda^2 \mu_x \cos \alpha}{16\pi} \left(1 - \frac{5\pi \mu_x}{8} \right) \right] \right\} \quad (58)$$

$$B = \left(\frac{2\mu_x \cos \alpha}{3\pi} - \frac{1}{6} \mu_x^2 \cos^2 \alpha \right) \quad (59)$$

$$C = \left(1 - \frac{5\pi \mu_x}{8} \right) \quad (60)$$

$$\begin{aligned} \frac{\partial \alpha}{\partial \mu_x} \Big|_{\mu_x} = & -8\mu_x \sin \alpha \frac{(\mu_x^2 \cos^2 \alpha - 2)}{(\mu_x^2 \cos^2 \alpha + 2)^2} \left[\frac{\lambda}{2} \left(1 - \frac{\mu_x^2 \cos^2 \alpha}{4} \right) + \frac{2\theta}{3} \right] \\ & + \frac{8\mu_x \cos \alpha}{2 + \mu_x^2 \cos^2 \alpha} \left[\frac{1}{2} \left(1 - \frac{\mu_x^2 \cos^2 \alpha}{4} \right) \frac{\partial \lambda}{\partial \alpha} \Big|_{\mu_x} \right. \\ & \left. + \frac{\lambda}{4} \mu_x^2 \cos \alpha \sin \alpha \right] \quad (61) \end{aligned}$$

$$\begin{aligned} \frac{\partial \alpha}{\partial \mu_x} \Big|_{\alpha} = & 8 \cos \alpha \frac{(2 - \mu_x^2 \cos^2 \alpha)}{(2 + \mu_x^2 \cos^2 \alpha)^2} \left[\frac{\lambda}{2} \left(1 - \frac{\mu_x^2 \cos^2 \alpha}{4} \right) + \frac{2\theta}{3} \right] \\ & + \frac{8\mu_x \cos \alpha}{2 + \mu_x^2 \cos^2 \alpha} \left[\frac{1}{2} \left(1 - \frac{\mu_x^2 \cos^2 \alpha}{4} \right) \frac{\partial \lambda}{\partial \mu_x} \Big|_{\alpha} \right. \\ & \left. + \frac{\lambda \mu_x \cos^2 \alpha}{4} \right] \quad (62) \end{aligned}$$

* Referring to Table II page 157 which presents a table of the calculated values of the trim variables, we find that considerable simplification is possible if some of the higher order terms are neglected in the derivatives. It follows that equations (54), (55), (61) and (62) may be simplified to

$$\frac{2}{\alpha \sigma} \frac{\partial C_T}{\partial \alpha} \Big|_{\mu_x} \approx \frac{1}{2} \frac{\partial \lambda}{\partial \alpha} \Big|_{\mu_x} \quad (63)$$

$$\frac{2}{\alpha \sigma} \frac{\partial C_T}{\partial \mu_x} \Big|_{\alpha} \approx \frac{1}{2} \frac{\partial \lambda}{\partial \mu_x} \Big|_{\alpha} \quad (64)$$

$$\frac{\partial a_1}{\partial \alpha} \Big|_{\mu_x} \approx -4\mu_x \sin \alpha \left(\frac{\lambda}{2} + \frac{\theta}{3} \right) + 2\mu_x \cos \alpha \frac{\partial \lambda}{\partial \alpha} \Big|_{\mu_x} \quad (65)$$

$$\frac{\partial a_1}{\partial \mu_x} \Big|_{\alpha} \approx 4 \cos \alpha \left(\frac{\lambda}{2} + \frac{2\theta}{3} \right) + 2\mu_x \cos \alpha \frac{\partial \lambda}{\partial \mu_x} \Big|_{\alpha} \quad (66)$$

neglecting only terms whose contribution would be on the order of 5 per cent or less. Unfortunately, however, the rather lengthy expressions (56) through (60) for the H-force derivatives cannot be handily simplified without neglecting terms of greater than 10 per cent contribution and therefore the calculations were carried out using all terms of equations (56) and (57).

Differentiating equation (16) with respect to α and μ_x respectively, gives for the flapping-hinge offset contribution to moment derivatives

$$\frac{\partial M_h}{\partial \alpha} \Big|_{\mu_x} = \frac{e b c.f.}{2} \frac{\partial a_1}{\partial \alpha} \Big|_{\mu_x} \quad (67)$$

$$\frac{\partial M_h}{\partial \mu_x} \Big|_{\alpha} = \frac{e b c.f.}{2} \frac{\partial a_1}{\partial \mu_x} \Big|_{\alpha} \quad (68)$$

using the expressions (65) and (66) for $\frac{\partial a_1}{\partial \alpha} \Big|_{\mu_x}$ and $\frac{\partial a_1}{\partial \mu_x} \Big|_{\alpha}$ respectively.

The C_T and λ derivatives may be evaluated by means of the charts presented on page 216 Appendix B, by the following method.

Applying the chain rule of differentiation to the λ derivatives gives:

$$\frac{\partial \lambda}{\partial \alpha} \bigg|_{\mu_x} = \frac{\partial \lambda}{\partial \alpha} \bigg|_{\mu_x, C_T} + \frac{\partial \lambda}{\partial C_T} \bigg|_{\alpha, \mu_x} \frac{\partial C_T}{\partial \alpha} \bigg|_{\mu_x} \quad (69)$$

$$\frac{\partial \lambda}{\partial \mu_x} \bigg|_{\alpha} = \frac{\partial \lambda}{\partial \mu_x} \bigg|_{\alpha, C_T} + \frac{\partial \lambda}{\partial C_T} \bigg|_{\alpha, \mu_x} \frac{\partial C_T}{\partial \mu_x} \bigg|_{\alpha} \quad (70)$$

which, when solved simultaneously with equations (63) and (64) respectively, gives

$$\frac{\partial C_T}{\partial \alpha} \bigg|_{\mu_x} = \frac{\frac{\partial \lambda}{\partial \alpha} \bigg|_{\mu_x, C_T}}{\frac{4}{\alpha \sigma} - \frac{\partial \lambda}{\partial C_T} \bigg|_{\mu_x, \alpha}} \quad (71)$$

$$\frac{\partial \lambda}{\partial \alpha} \bigg|_{\mu_x} = \frac{4}{\alpha \sigma} \frac{\partial C_T}{\partial \alpha} \bigg|_{\mu_x} \quad (72)$$

$$\frac{\partial C_T}{\partial \mu_x} \bigg|_{\alpha} = \frac{\frac{\partial \lambda}{\partial \mu_x} \bigg|_{\alpha, C_T}}{\frac{4}{\alpha \sigma} - \frac{\partial \lambda}{\partial C_T} \bigg|_{\mu_x, \alpha}} \quad (73)$$

$$\frac{\partial \lambda}{\partial \mu_x} \bigg|_{\alpha} = \frac{4}{\alpha \sigma} \frac{\partial C_T}{\partial \mu_x} \bigg|_{\alpha} \quad (74)$$

The derivatives $\frac{\partial \lambda}{\partial \alpha} \bigg|_{\mu_x, C_T}$, $\frac{\partial \lambda}{\partial \mu_x} \bigg|_{\alpha, C_T}$ & $\frac{\partial \lambda}{\partial C_T} \bigg|_{\mu_x, \alpha}$

may be evaluated by using the charts on pages 216 through 218 of Appendix B, noting that

$$\frac{\partial \lambda}{\partial \alpha} \bigg|_{\mu_x, C_T} = \lambda_0 \frac{\partial \bar{\lambda}}{\partial \alpha} \bigg|_{\mu_x, C_T} \quad (75)$$

$$\frac{\partial C_T}{\partial \lambda} \bigg|_{\mu_x, \alpha} = \frac{1}{\lambda_0} \left(\lambda_0 \frac{\partial \lambda}{\partial C_T} \bigg|_{\mu_x, \alpha} \right) \quad (76)$$

and using the definitions of equations (33) through (35) and the values obtained in the previous analysis.

Proceeding now to the wing force and moment derivatives and using the dependent variables

$$\alpha' = \alpha'(\mu_x, \alpha)$$

$$V_R = V_R(\mu_x, \alpha)$$

we have

$$\frac{\partial Z_w}{\partial \alpha}|_{\mu_x} = \frac{\partial Z_w}{\partial \alpha'}|_{\mu_x, \alpha} \frac{\partial \alpha'}{\partial \alpha}|_{\mu_x} + \frac{\partial Z_w}{\partial V_R}|_{\mu_x, \alpha} \frac{\partial V_R}{\partial \alpha}|_{\mu_x} \quad (77)$$

$$\frac{\partial Z_w}{\partial \mu_x}|_{\alpha} = \frac{\partial Z_w}{\partial \alpha'}|_{\mu_x, \alpha} \frac{\partial \alpha'}{\partial \mu_x}|_{\alpha} + \frac{\partial Z_w}{\partial V_R}|_{\mu_x, \alpha} \frac{\partial V_R}{\partial \mu_x}|_{\alpha} \quad (78)$$

$$\frac{\partial X_w}{\partial \alpha}|_{\mu_x} = \frac{\partial X_w}{\partial \alpha'}|_{\mu_x, \alpha} \frac{\partial \alpha'}{\partial \alpha}|_{\mu_x} + \frac{\partial X_w}{\partial V_R}|_{\mu_x, \alpha} \frac{\partial V_R}{\partial \alpha}|_{\mu_x} \quad (79)$$

$$\frac{\partial X_w}{\partial \mu_x}|_{\alpha} = \frac{\partial X_w}{\partial \alpha'}|_{\mu_x, \alpha} \frac{\partial \alpha'}{\partial \mu_x}|_{\alpha} + \frac{\partial X_w}{\partial V_R}|_{\mu_x, \alpha} \frac{\partial V_R}{\partial \mu_x}|_{\alpha} \quad (80)$$

$$\frac{\partial M_w}{\partial \alpha}|_{\mu_x} = \frac{\partial M_w}{\partial \alpha'}|_{\mu_x, \alpha} \frac{\partial \alpha'}{\partial \alpha}|_{\mu_x} + \frac{\partial M_w}{\partial V_R}|_{\mu_x, \alpha} \frac{\partial V_R}{\partial \alpha}|_{\mu_x} \quad (81)$$

$$\frac{\partial M_w}{\partial \mu_x}|_{\alpha} = \frac{\partial M_w}{\partial \alpha'}|_{\mu_x, \alpha} \frac{\partial \alpha'}{\partial \mu_x}|_{\alpha} + \frac{\partial M_w}{\partial V_R}|_{\mu_x, \alpha} \frac{\partial V_R}{\partial \mu_x}|_{\alpha} \quad (82)$$

Noting that the expressions (20) and (21) for α' and V_R respectively are in terms of another dependent variable $\frac{N}{\Omega R} = \frac{N}{\Omega R}(\mu_x, \alpha)$

we have

$$\frac{\partial \alpha'}{\partial \alpha} \Big|_{\mu_x} = \frac{\frac{\partial \lambda}{\partial \alpha} \Big|_{\mu_x} + (\lambda - \frac{N}{\Omega R}) \tan \alpha - \frac{\partial (\frac{N}{\Omega R})}{\partial \alpha} \Big|_{\mu_x}}{\mu_x \cos \alpha (1 + \cot^2 \alpha')} \quad (83)$$

$$\frac{\partial \alpha'}{\partial \mu_x} \Big|_{\alpha} = \frac{\frac{\partial \lambda}{\partial \mu_x} \Big|_{\alpha} - (\lambda - \frac{N}{\Omega R}) \frac{1}{\mu_x} - \frac{\partial (\frac{N}{\Omega R})}{\partial \mu_x} \Big|_{\alpha}}{\mu_x \cos \alpha (1 + \cot^2 \alpha')} \quad (84)$$

$$\frac{\partial V_R}{\partial \alpha} \Big|_{\mu_x} = -\frac{(\Omega R)^2}{V_R} \lambda \left[\frac{N}{\Omega R} \frac{\partial \lambda}{\partial \alpha} \Big|_{\mu_x} + \lambda \frac{\partial (\frac{N}{\Omega R})}{\partial \alpha} \Big|_{\mu_x} \right] \quad (85)$$

$$\frac{\partial V_R}{\partial \mu_x} \Big|_{\alpha} = \frac{(\Omega R)^2}{V_R} \lambda \left[\mu_x - \left(\frac{N}{\Omega R} \right) \frac{\partial \lambda}{\partial \mu_x} \Big|_{\alpha} - \lambda \frac{\partial (\frac{N}{\Omega R})}{\partial \mu_x} \Big|_{\alpha} \right] \quad (86)$$

and differentiating expression (22) gives

$$\lambda \frac{\partial (\frac{N}{\Omega R})}{\partial \alpha} \Big|_{\mu_x} = \frac{\frac{\partial C_T}{\partial \alpha} \Big|_{\mu_x} \sqrt{\lambda^2 + \mu_x^2 \cos^2 \alpha} - C_T (\lambda \frac{\partial \lambda}{\partial \alpha} \Big|_{\mu_x} + \mu_x^2 \cos \alpha \sin \alpha)}{2 (\lambda^2 + \mu_x^2 \cos^2 \alpha)} \quad (87)$$

$$\frac{\partial (\frac{N}{\Omega R})}{\partial \mu_x} \Big|_{\alpha} = \frac{\frac{\partial C_T}{\partial \mu_x} \Big|_{\alpha} \sqrt{\lambda^2 + \mu_x^2 \cos^2 \alpha} - C_T (\lambda \frac{\partial \lambda}{\partial \mu_x} \Big|_{\alpha} + \mu_x \cos^2 \alpha)}{2 (\lambda^2 + \mu_x^2 \cos^2 \alpha)} \quad (88)$$

Referring to equations (7) through (9) and making the simplifying assumptions that $\cos \alpha' \cong 1$, $\mu \sin \alpha' \cong \alpha'$ after differentiation,

we have

$$\frac{\partial Z_w}{\partial \alpha'} \Big|_{\mu_x, \alpha} = -\frac{1}{2} \rho V_R^2 S \left\{ [(C_{L\alpha'} + C_D) - (C_L - C_{D\alpha'}) \alpha'] \cos i_w + [(C_L - C_{D\alpha'}) + (C_{L\alpha'} + C_D) \alpha'] \mu \sin i_w \right\} \quad (89)$$

$$\frac{\partial Z_w}{\partial V_R} \Big|_{\mu_x, \alpha} = -\rho V_R S [(C_L - \alpha' C_D) \cos i_w + (\alpha' C_L - C_D) \mu \sin i_w] \quad (90)$$

$$\begin{aligned} \frac{\partial X_w}{\partial \alpha'} \Big|_{\mu_x, \alpha} = & -\frac{1}{2} \rho V_R^2 S \left\{ [(C_{D\alpha'} - C_L) - (C_D + C_{L\alpha'})\alpha'] \cos i_w \right. \\ & \left. + [(C_D + C_{L\alpha'}) + (C_{D\alpha'} - C_L)\alpha'] \sin i_w \right\} \end{aligned} \quad (91)$$

$$\frac{\partial X_w}{\partial V_R} \Big|_{\mu_x, \alpha} = -\rho V_R S [(C_D - \alpha' C_L) \cos i_w + (\alpha' C_D + C_L) \sin i_w] \quad (92)$$

$$\frac{\partial M_w}{\partial \alpha'} \Big|_{\mu_x, \alpha} = \frac{\partial M_{ac}}{\partial \alpha'} \Big|_{\mu_x, \alpha} + X_w \frac{\partial Z_w}{\partial \alpha'} \Big|_{\mu_x, \alpha} - Z_w \frac{\partial X_w}{\partial \alpha'} \Big|_{\mu_x, \alpha} \quad (93)$$

$$\frac{\partial M_w}{\partial V_R} \Big|_{\mu_x, \alpha} = \frac{\partial M_{ac}}{\partial V_R} \Big|_{\mu_x, \alpha} + X_w \frac{\partial Z_w}{\partial V_R} \Big|_{\mu_x, \alpha} - Z_w \frac{\partial X_w}{\partial V_R} \Big|_{\mu_x, \alpha} \quad (94)$$

where by definition of a.c.

$$\frac{\partial M_{ac}}{\partial \alpha'} \Big|_{\mu_x, \alpha} = 0 \quad (95)$$

and from equation (19)

$$\frac{\partial M_{ac}}{\partial V_R} \Big|_{\mu_x, \alpha} = \rho V_R S c C_{mac} \quad (96)$$

The fuselage derivatives may be evaluated by differentiating equations (10) through (12) with respect to V and α , remembering the previous assumptions concerning fuselage contributions and noting that $\alpha_f = 90 - i_w - \alpha$ giving finally

$$\frac{\partial Z_f}{\partial \alpha} \Big|_{\mu_x} = -\frac{1}{2} \rho V^2 A_s C_{Ds} (\sin i_w \cos \alpha - \cos i_w \sin \alpha) \quad (97)$$

$$\frac{\partial Z_f}{\partial V}|_{\alpha} = \rho V A_s C_{D_s} \cos(i\omega - \alpha) \cong 0 \quad (98)$$

$$\frac{\partial X_f}{\partial \alpha}|_{u_x} = \frac{1}{2} \rho V^2 A_s C_{D_s} (\sin i\omega \sin \alpha + \cos i\omega \cos \alpha) \quad (99)$$

$$\frac{\partial X_f}{\partial V}|_{\alpha} = -\rho V A_s C_{D_s} \sin(i\omega - \alpha) \quad (100)$$

$$\frac{\partial M_f}{\partial \alpha}|_{u_x} = -x_f \frac{\partial Z_f}{\partial \alpha}|_{u_x} + z_f \frac{\partial X_f}{\partial \alpha}|_{u_x} \quad (101)$$

$$\frac{\partial M_f}{\partial V}|_{\alpha} = -x_f \frac{\partial Z_f}{\partial V}|_{\alpha} + z_f \frac{\partial X_f}{\partial V}|_{\alpha} \quad (102)$$

where C_{D_s} is as defined above.

Using the values of C_L , $C_{L\alpha'}$, C_D and $C_{D\alpha'}$ derived by one of the various methods discussed and presented in Figures 41 and 42, along with the rotor derivatives, the wing derivatives may be evaluated at the various trim conditions by progressive substitution. The resulting values for wing, rotor and combined derivatives as well as the trim conditions are to be found tabulated in Table III on page 158.

Evaluation of the tail-off pitch-rate derivative $M_{\dot{\theta}}$ is for the most part an accomplished fact once the earlier developments of this section have been dealt with. The moments generated from a rotational velocity of the aircraft about its c.g. arise from three distinct sources

- 1) The contributions due to the wing and rotor rotating about

their own axis,

2) Contributions due to change in local angle of attack at the wing and rotor,

3) Contributions due to change in local velocity at the wing and rotor.

The latter two effects arise from the displacement of the wing and rotor from the c.g. and the resultant linear velocity produced by rotation about the c.g. If we denote the change in angle of attack due to rotation about the c.g. by α^* at the rotor and the change in velocity at the rotor by V^* then from Figure 82 we can write:

$$\frac{\partial \alpha^*}{\partial \dot{\theta}} \Big|_{V, \alpha} = \frac{h_R \sin(\alpha + \eta)}{(1 + \tan^2 \alpha)} \frac{V}{[V - h_R \dot{\theta} \cos(\alpha + \eta)]^2} \quad (103)$$

$$\frac{\partial V^*}{\partial \dot{\theta}} \Big|_{V, \alpha} = -h_R \quad (104)$$

which, when evaluated at $\dot{\theta} = 0$ initially, give

$$\frac{\partial \alpha^*}{\partial \dot{\theta}} \Big|_{V, \alpha} = \frac{h_R \sin(\alpha + \eta)}{1 + \tan^2 \alpha} \quad (103a)$$

$$\frac{\partial V^*}{\partial \dot{\theta}} \Big|_{V, \alpha} = -h_R \quad (104a)$$

Similarly for the wing we can refer to Figure 82 and, remembering that α' and V_R are both dependent functions of α and V , write

$$\frac{\partial \alpha'^*}{\partial \dot{\theta}} \Big|_{V, \alpha} = \frac{\partial \alpha'^*}{\partial \dot{\theta}} \Big|_{V^*, \alpha^*} + \frac{\partial \alpha'}{\partial \alpha^*} \frac{\partial \alpha^*}{\partial \dot{\theta}} + \frac{\partial \alpha'}{\partial V^*} \frac{\partial V^*}{\partial \dot{\theta}} \quad (105)$$

$$\left. \frac{\partial V_R^*}{\partial \dot{\theta}} \right|_{v, \alpha} = \left. \frac{\partial V_R^*}{\partial \dot{\theta}} \right|_{v^*, \alpha^*} + \frac{\partial V_R}{\partial V_R^*} \frac{\partial V_R^*}{\partial \dot{\theta}} + \frac{\partial V_R}{\partial \alpha^*} \frac{\partial \alpha^*}{\partial \dot{\theta}} \quad (106)$$

where

$$\left. \frac{\partial \alpha'^*}{\partial \dot{\theta}} \right|_{v^*, \alpha^*} = - \frac{h\omega \sin(\xi - \alpha')}{1 + \tan^2 \alpha'} \quad (107)$$

$$\left. \frac{\partial V_R^*}{\partial \dot{\theta}} \right|_{v^*, \alpha^*} = - h\omega \quad (108)$$

which have been evaluated at $\dot{\theta} = 0$ initially. It can be noted at this point that, since the definition of the partial derivative places no qualifications on the source of the change in the variable, then the following identities are true

$$\frac{\partial \alpha'}{\partial \alpha^*} \equiv \frac{\partial \alpha'}{\partial \alpha} \quad (109)$$

$$\frac{\partial \alpha'}{\partial V^*} \equiv \frac{\partial \alpha'}{\partial V} \quad (110)$$

$$\frac{\partial V_R}{\partial \alpha^*} \equiv \frac{\partial V_R}{\partial \alpha} \quad (111)$$

$$\frac{\partial V_R}{\partial V^*} \equiv \frac{\partial V_R}{\partial V} \quad (112)$$

where the quantities on the right hand side are the ones developed previously. Each of the above three sources of moment about the aircraft c.g. can, in turn, produce this moment in two ways, which are in general:

1) Pure moments about the hub of the rotor and the wing a.c.,
and

2) A force applied at some moment arm from the c.g.

Equations A(6) and A(9) state this more particularly by breaking the forces and moment arms up into two rectilinear components, giving:

$$M_R = M_h - X_R Z_R - Z_R X_R \quad (A6)$$

$$M_w = M_{a.c.} + Z_w X_w - X_w Z_w \quad (A9)$$

which, when differentiated with respect to $\dot{\theta}$ give

$$\frac{\partial M_R}{\partial \dot{\theta}} = \frac{\partial M_h}{\partial \dot{\theta}} - Z_R \frac{\partial X_R}{\partial \dot{\theta}} - X_R \frac{\partial Z_R}{\partial \dot{\theta}} \quad (113)$$

$$\frac{\partial M_w}{\partial \dot{\theta}} = \frac{\partial M_{a.c.}}{\partial \dot{\theta}} - Z_w \frac{\partial X_w}{\partial \dot{\theta}} + X_w \frac{\partial Z_w}{\partial \dot{\theta}} \quad (114)$$

The rotor forces are best handled by resolving about the thrust and H-force axes by equations A-4 and 5:

$$\frac{\partial Z_R}{\partial \dot{\theta}} = - \frac{\partial T}{\partial \dot{\theta}} \mu \sin i_w - \frac{\partial H}{\partial \dot{\theta}} \cos i_w \quad (115)$$

$$\frac{\partial X_R}{\partial \dot{\theta}} = - \frac{\partial H}{\partial \dot{\theta}} \mu \sin i_w + \frac{\partial T}{\partial \dot{\theta}} \cos i_w \quad (116)$$

and the hub moment is best determined in terms of the dependent variable a_1 , and the simple expansion

$$\frac{\partial M_h}{\partial \theta} = \frac{\partial M_h}{\partial a_1} \frac{\partial a_1}{\partial \theta} \quad (117)$$

Proceeding now with the determination of the various parts, we can expand by chain rule giving

$$\frac{\partial T}{\partial \theta} \Big|_{v, \alpha} = \frac{\partial T}{\partial \theta} \Big|_{v^*, \alpha^*} + \frac{\partial T}{\partial \alpha^*} \frac{\partial \alpha^*}{\partial \theta} + \frac{\partial T}{\partial v^*} \frac{\partial v^*}{\partial \theta} \quad (118)$$

$$\frac{\partial H}{\partial \theta} \Big|_{v, \alpha} = \frac{\partial H}{\partial \theta} \Big|_{v^*, \alpha^*} + \frac{\partial H}{\partial \alpha^*} \frac{\partial \alpha^*}{\partial \theta} + \frac{\partial H}{\partial v^*} \frac{\partial v^*}{\partial \theta} \quad (119)$$

$$\begin{aligned} \frac{\partial M_h}{\partial \theta} \Big|_{v, \alpha} = \frac{\partial M_h}{\partial a_1} \left[\frac{\partial a_1}{\partial \theta} \Big|_{v^*, \alpha^*} + \frac{\partial a_1}{\partial \alpha^*} \frac{\partial \alpha^*}{\partial \theta} \right. \\ \left. + \frac{\partial a_1}{\partial v^*} \frac{\partial v^*}{\partial \theta} \right] \end{aligned} \quad (120)$$

where

$$\frac{\partial T}{\partial \alpha^*} \equiv \frac{\partial T}{\partial \alpha} \quad (121)$$

$$\frac{\partial H}{\partial \alpha^*} \equiv \frac{\partial H}{\partial \alpha} \quad (122)$$

$$\frac{\partial T}{\partial v^*} \equiv \frac{\partial T}{\partial v} \quad (123)$$

$$\frac{\partial H}{\partial v^*} \equiv \frac{\partial H}{\partial v} \quad (124)$$

$$\frac{\partial a_1}{\partial \alpha^*} \equiv \frac{\partial a_1}{\partial \alpha} \quad (125)$$

$$\frac{\partial a_1}{\partial v^*} \equiv \frac{\partial a_1}{\partial v} \quad (126)$$

$$\frac{\partial M_h}{\partial a_1} = \frac{c b \text{ C.F.}}{z} \quad (127)$$

all of which have already been evaluated. The remaining terms to be determined for the rotor are the pure moment and forces due to the rotation of the hub about its own axis, all of which are due to rotor plane lagging behind the pitching shaft given by the derivative

$\frac{\partial a_1}{\partial \theta} |_{\alpha^*, v^*}$. In order to determine the forces produced by such a condition we must express the H and T forces in terms of the flapping angle a_1 , since this parameter has been eliminated from the expressions for H and T previously expressed. Reference 12 gives an expression for C_H in terms of the blade flapping on page 192 which when differentiated gives

$$\frac{\partial C_H}{\partial a_1} = \frac{\alpha \sigma}{2} \left[\frac{\theta}{3} + \frac{3}{4} \lambda \right] \quad (128)$$

where a higher order product of $a_1 M_x \cos \alpha$ has been neglected. Dependence of T on a_1 is very small for a high Ω rotor such as is under consideration here, and can safely be neglected. The two force terms can now be expressed as follows:

$$\frac{\partial H}{\partial \theta} |_{\alpha^*, v^*} = \rho \pi \Omega^2 R^4 \left[\frac{\partial C_H}{\partial a_1} \frac{\partial a_1}{\partial \theta} \right] \quad (129)$$

$$\frac{\partial T}{\partial \theta} |_{\alpha^*, v^*} \approx 0 \quad (130)$$

The one remaining term $\frac{\partial a_1}{\partial \theta} |_{\alpha^*, v^*}$ is given in

Reference 6 on page 275 as

$$\frac{\partial a_1}{\partial \dot{\theta}} \Big|_{\alpha^*, v^*} = - \frac{16}{\gamma \Omega} \quad (131)$$

Similarly the wing contributions may be expressed:

$$\begin{aligned} \frac{\partial M_{a.c.}}{\partial \dot{\theta}} \Big|_{v, \alpha} &= \frac{\partial M_{a.c.}}{\partial \dot{\theta}} \Big|_{v_R^*, \alpha'^*} + \frac{\partial M_{a.c.}}{\partial \alpha'^*} \frac{\partial \alpha'^*}{\partial \dot{\theta}} \Big|_{v, \alpha} \\ &\quad + \frac{\partial M_{a.c.}}{\partial v_R^*} \frac{\partial v_R^*}{\partial \dot{\theta}} \Big|_{v, \alpha} \end{aligned} \quad (132)$$

$$\begin{aligned} \frac{\partial Z_w}{\partial \dot{\theta}} \Big|_{v, \alpha} &= \frac{\partial Z_w}{\partial \dot{\theta}} \Big|_{v_R^*, \alpha'^*} + \frac{\partial Z_w}{\partial \alpha'^*} \frac{\partial \alpha'^*}{\partial \dot{\theta}} \Big|_{v, \alpha} \\ &\quad + \frac{\partial Z_w}{\partial v_R^*} \frac{\partial v_R^*}{\partial \dot{\theta}} \Big|_{v, \alpha} \end{aligned} \quad (133)$$

$$\begin{aligned} \frac{\partial X_w}{\partial \dot{\theta}} \Big|_{v, \alpha} &= \frac{\partial X_w}{\partial \dot{\theta}} \Big|_{v_R^*, \alpha'^*} + \frac{\partial X_w}{\partial \alpha'^*} \frac{\partial \alpha'^*}{\partial \dot{\theta}} \Big|_{v, \alpha} \\ &\quad + \frac{\partial X_w}{\partial v_R^*} \frac{\partial v_R^*}{\partial \dot{\theta}} \Big|_{v, \alpha} \end{aligned} \quad (134)$$

where, as before,

$$\frac{\partial M_{a.c.}}{\partial \alpha'^*} \equiv \frac{\partial M_{a.c.}}{\partial \alpha'} = 0 \quad (135)$$

$$\frac{\partial M_{a.c.}}{\partial v_R^*} \equiv \frac{\partial M_{a.c.}}{\partial v_R} \quad (136)$$

$$\frac{\partial Z_w}{\partial \alpha'^*} \equiv \frac{\partial Z_w}{\partial \alpha'} \quad (137)$$

$$\frac{\partial Z_w}{\partial v_R^*} \equiv \frac{\partial Z_w}{\partial v_R} \quad (138)$$

$$\frac{\partial X_w}{\partial \alpha'^*} \equiv \frac{\partial X_w}{\partial \alpha'} \quad (139)$$

$$\frac{\partial X_w}{\partial v_R^*} \equiv \frac{\partial X_w}{\partial v_R} \quad (140)$$

For the pitch rates to be encountered, it is safe to assume that pitching of the wing about its own a.c. produces little change in the wing force and moment at constant α' and V_R and the approximation

$$\frac{\partial M_{ac}}{\partial \dot{\theta}} \Big|_{V_R^*, \alpha'^*} \approx \frac{\partial Z_w}{\partial \dot{\theta}} \Big|_{V_R^*, \alpha'^*} \approx \frac{\partial X_w}{\partial \dot{\theta}} \Big|_{V_R^*, \alpha'^*} \approx 0 \quad (141)$$

is quite reasonable.

Progressive evaluation and substitution will eventually lead to the values of $M_{\dot{\theta}}^{\text{ROTOR}}$ and $M_{\dot{\theta}}^{\text{WING}}$ which are to be found presented in Figure 66 along with a breakdown of the major contributory terms.

The only remaining contribution to $M_{\dot{\theta}}$ on the tail-off airplane is due to the fuselage, and initial evaluations indicate that this effect is negligible compared to the other contributions considered above.

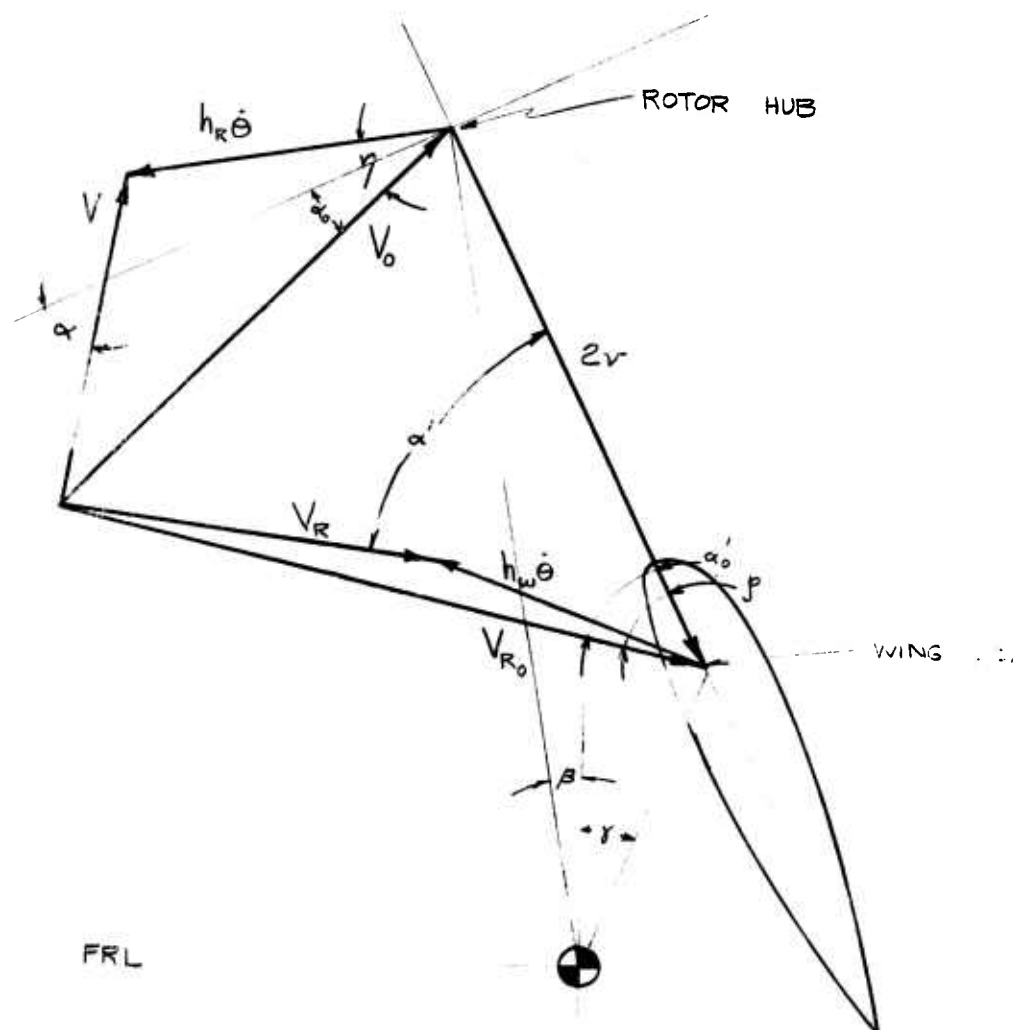
For the pitch rates to be encountered, it is safe to assume that pitching of the wing about its own a.c. produces little change in the wing force and moment at constant α' and V_R and the approximation

$$\left. \frac{\partial M_{ac}}{\partial \dot{\theta}} \right|_{V_R^*, \alpha'^*} \approx \left. \frac{\partial Z_w}{\partial \dot{\theta}} \right|_{V_R^*, \alpha'^*} \approx \left. \frac{\partial X_w}{\partial \dot{\theta}} \right|_{V_R^*, \alpha'^*} \approx 0 \quad (141)$$

is quite reasonable.

Progressive evaluation and substitution will eventually lead to the values of $M_{\dot{\theta} \text{ rotor}}$ and $M_{\dot{\theta} \text{ wing}}$ which are to be found presented in Figure 66 along with a breakdown of the major contributory terms.

The only remaining contribution to $M_{\dot{\theta}}$ on the tail-off airplane is due to the fuselage, and initial evaluations indicate that this effect is negligible compared to the other contributions considered above.

VECTOR DIAGRAM OF $\dot{\theta}$ INFLUENCE

$$V^* = -|V - V_0| = -h_R \dot{\theta}$$

$$\alpha^* = \alpha - \alpha_0$$

$$V_R^* = -|V_R - V_{R_0}| = -h_W \dot{\theta}$$

$$\alpha'^* = \alpha' - \alpha'_0$$

APPENDIX B

The authors of Reference 13 have developed a simple approach to the problem of determining the in-flow derivatives of a rotor in forward flight. With some slight modifications this method is presented here in part in terms of the advance ratio defined as

$$\mu_x = \frac{V}{\Omega R} \text{ in order to maintain its usefulness as } \alpha \rightarrow \frac{\pi}{2}.$$

Commencing with the definition of the in-flow parameter

$$\lambda = \frac{V \sin \alpha - v}{\Omega R} \quad (\text{B-1})$$

it was demonstrated in Part III that using momentum considerations only this can be expressed as:

$$\lambda = \mu_x \sin \alpha - \frac{c_T}{2} \frac{1}{\sqrt{\lambda^2 + \mu_x^2 \cos^2 \alpha}} \quad (\text{B-2})$$

Defining three new variables

$$\lambda_o = -\sqrt{c_T/2} \quad (\text{B-3})$$

$$\bar{\mu}_x = \frac{\mu_x}{\mu_o} \quad (\text{B-4})$$

and

$$\bar{\lambda} = \frac{\lambda}{\lambda_o} \quad (\text{B-5})$$

expression (B-2) may be rewritten as

$$\bar{\lambda} = \bar{\mu}_x \sin \alpha - \frac{1}{\sqrt{\bar{\lambda}^2 + \bar{\mu}_x^2 \cos^2 \alpha}} \quad (\text{B-6})$$

This expression is presented as a plot of $\bar{\lambda}$ vs. $\bar{\mu}_x$ for constant α 's in Figure 83. Knowing C_T and μ_x (ordinarily available from performance analysis) one can then readily determine λ from this plot without solving the quartic in λ of equation (B-2).

The necessary in-flow derivatives used in equations (A-71) through (A-74) in the analysis of Appendix A may be easily obtained by differentiating equation (B-6) and plotting the resulting functions at constant α . The expressions resulting from such operations and the figure numbers of the respective plots are presented below:

$$\lambda_0 \frac{2\lambda}{2\alpha} \Big|_{C_T, \mu_x} = \bar{\mu}_x \cos \alpha + \frac{\bar{\lambda} - \bar{\mu}_x \cos \alpha \sin \alpha}{(\bar{\lambda}^2 + \bar{\mu}_x^2 \cos^2 \alpha)^{3/2}} \quad (B-7)$$

Figure 84 plot of

$$\frac{1}{\mu_x \cos \alpha} \frac{2\lambda}{2\alpha} \Big|_{\mu_x, C_T} \text{ vs } \bar{\mu}_x$$

$$\frac{2\lambda}{2\mu_x} \Big|_{C_T, \alpha} = \sin \alpha + \frac{\bar{\lambda}^2 + 2\bar{\mu}_x \cos^2 \alpha}{2(\bar{\lambda}^2 + \bar{\mu}_x^2 \cos^2 \alpha)^{3/2}} \quad (B-8)$$

Figure 85 plot of

$$\frac{2\lambda}{2\mu_x} \Big|_{C_T, \alpha} \text{ vs } \bar{\mu}_x$$

and

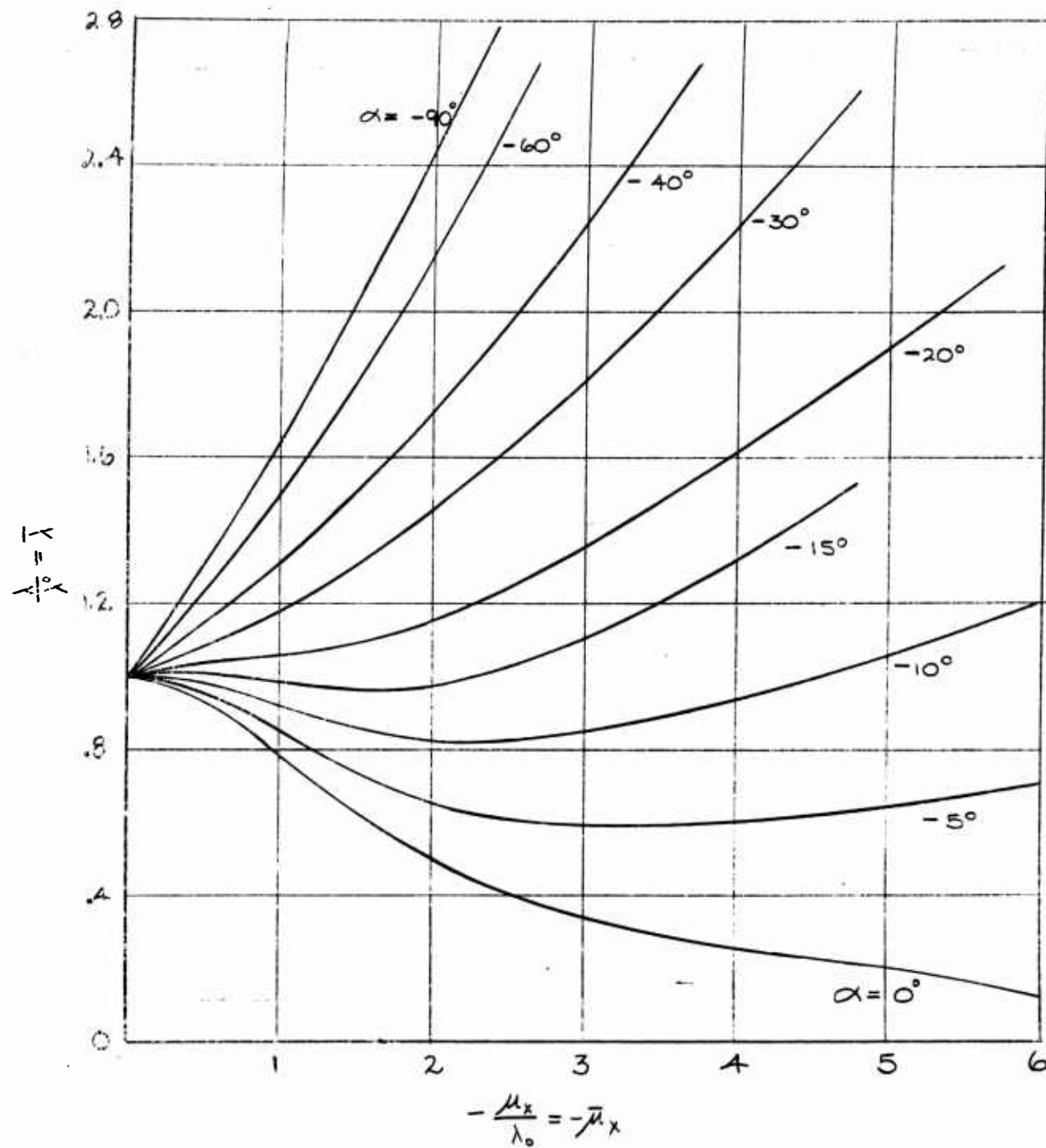
$$\lambda_0 \frac{2\lambda}{2C_T} \Big|_{\mu_x, \alpha} = - \frac{\bar{\lambda}}{2(\bar{\lambda}^2 + \bar{\mu}_x^2 \cos^2 \alpha)^{1/2} [\bar{\lambda} - (\bar{\lambda}^2 + \bar{\mu}_x^2 \cos^2 \alpha)^{3/2}]} \quad (B-9)$$

Figure 86 plot of

$$\lambda_0 \frac{2\lambda}{2C_T} \Big|_{\mu_x, \alpha} \text{ vs } \bar{\mu}_x$$

also included is a presentation of induced velocity at the rotor normalized by λ_0 in Figure 87.

Fig. 83

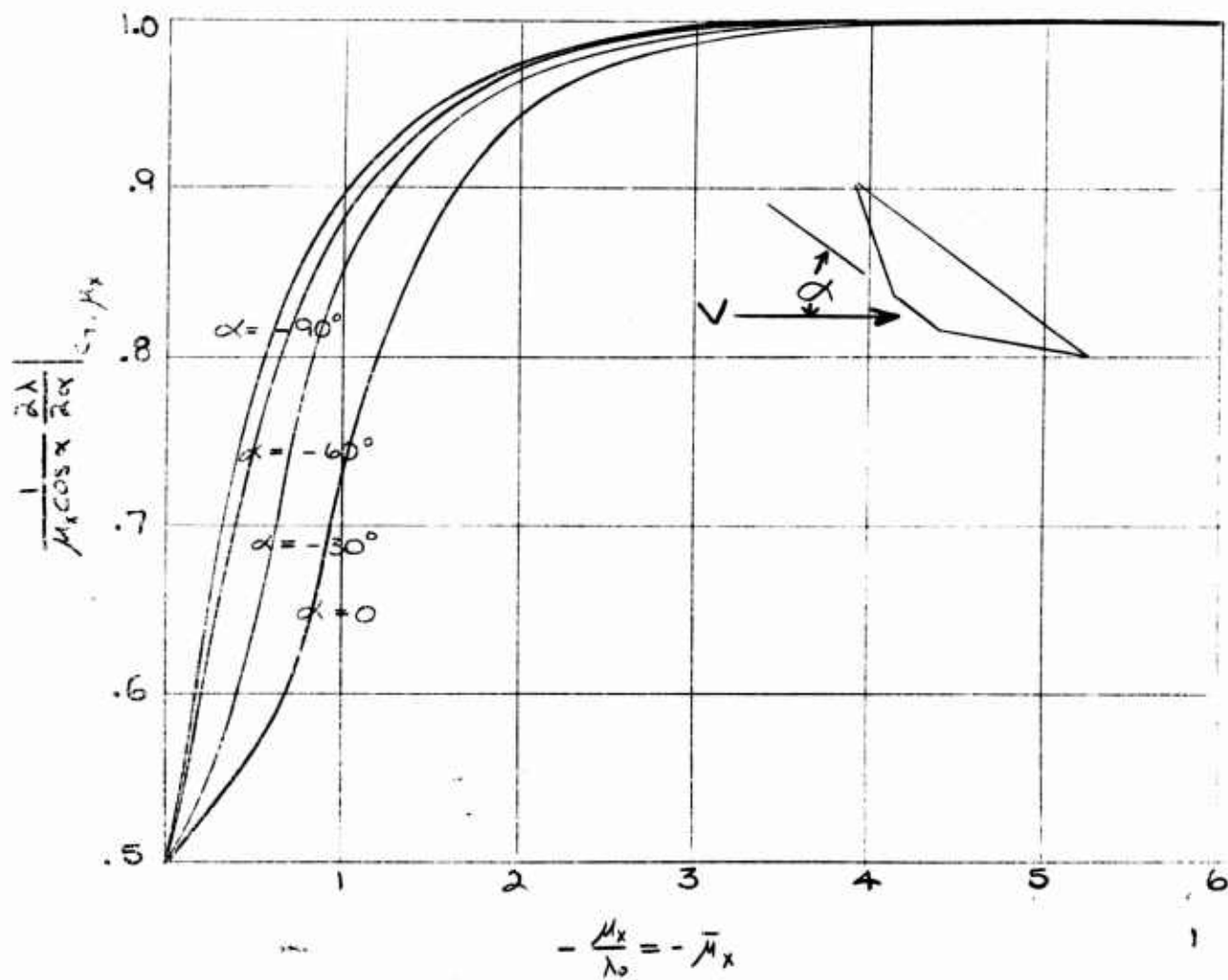


INFLOW PARAMETERS

$\bar{\lambda}$ vs $-\bar{\mu}_x$

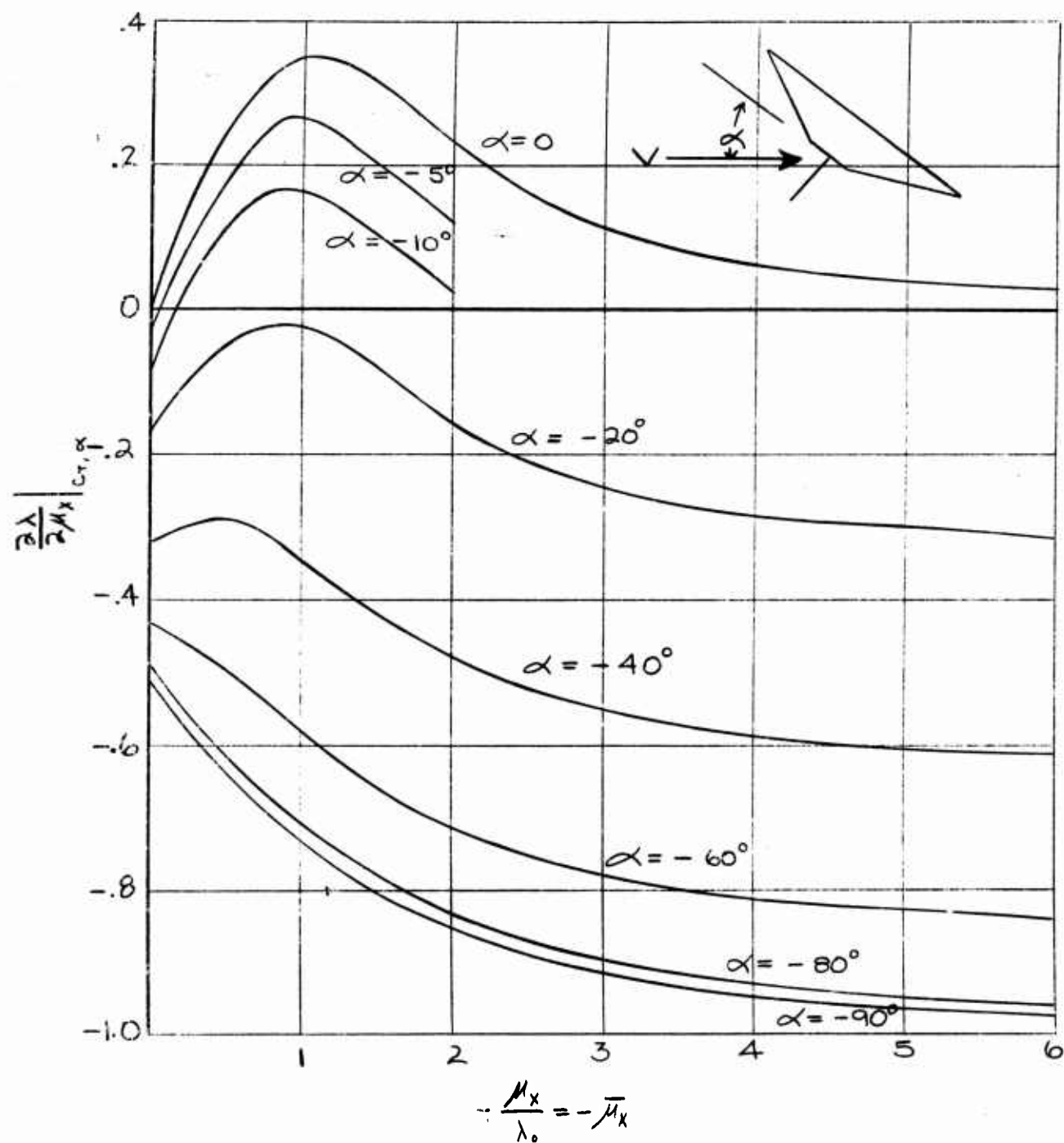
INFLOW DERIVATIVES

$$\frac{1}{N_x \cos \alpha} \frac{\partial \lambda}{\partial \alpha} \text{ VS } -\bar{\mu}_x$$



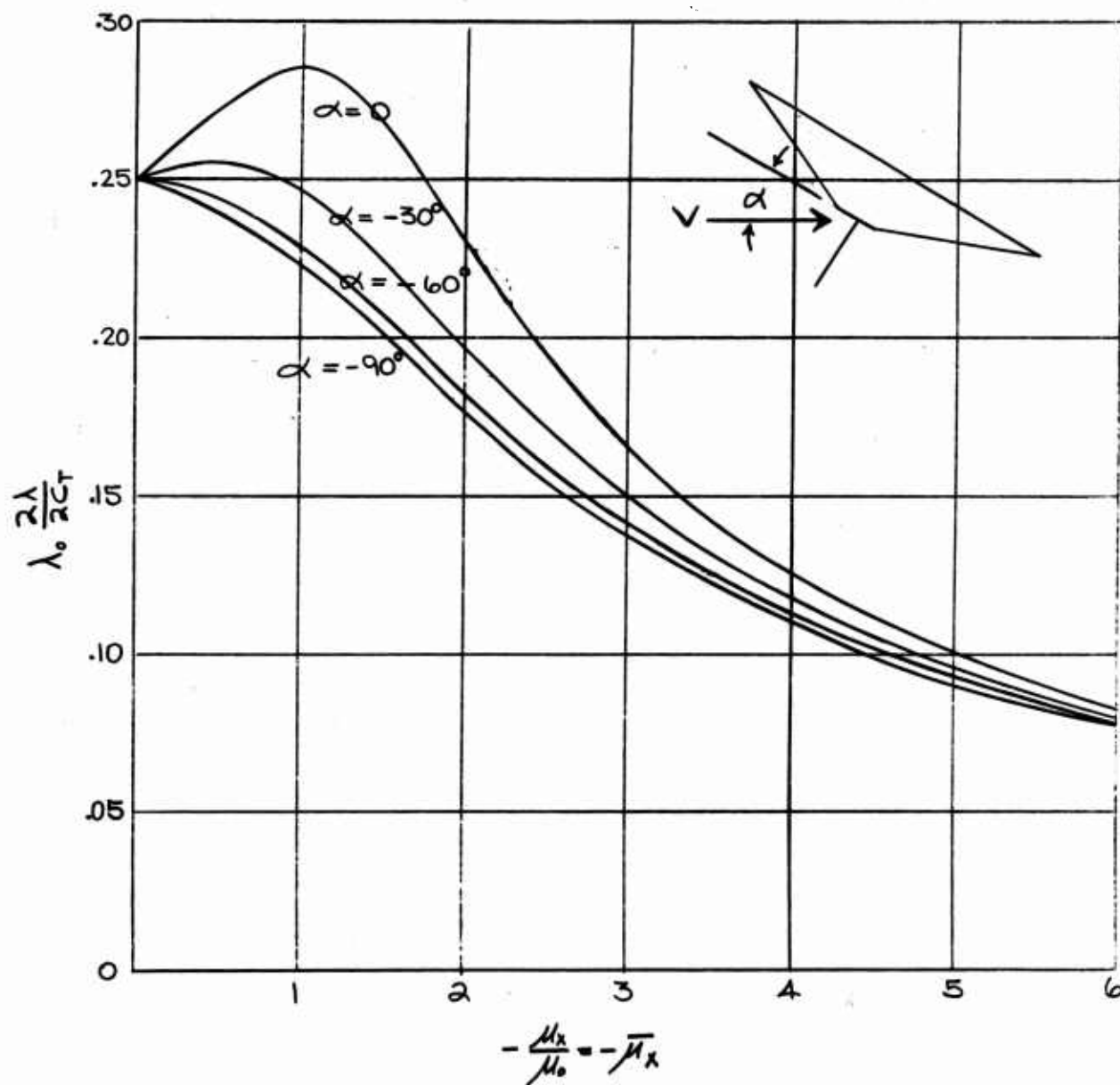
INFLOW DERIVATIVES

$$\frac{\partial \lambda}{\partial \mu_x} \text{ vs } -\bar{\mu}_x$$



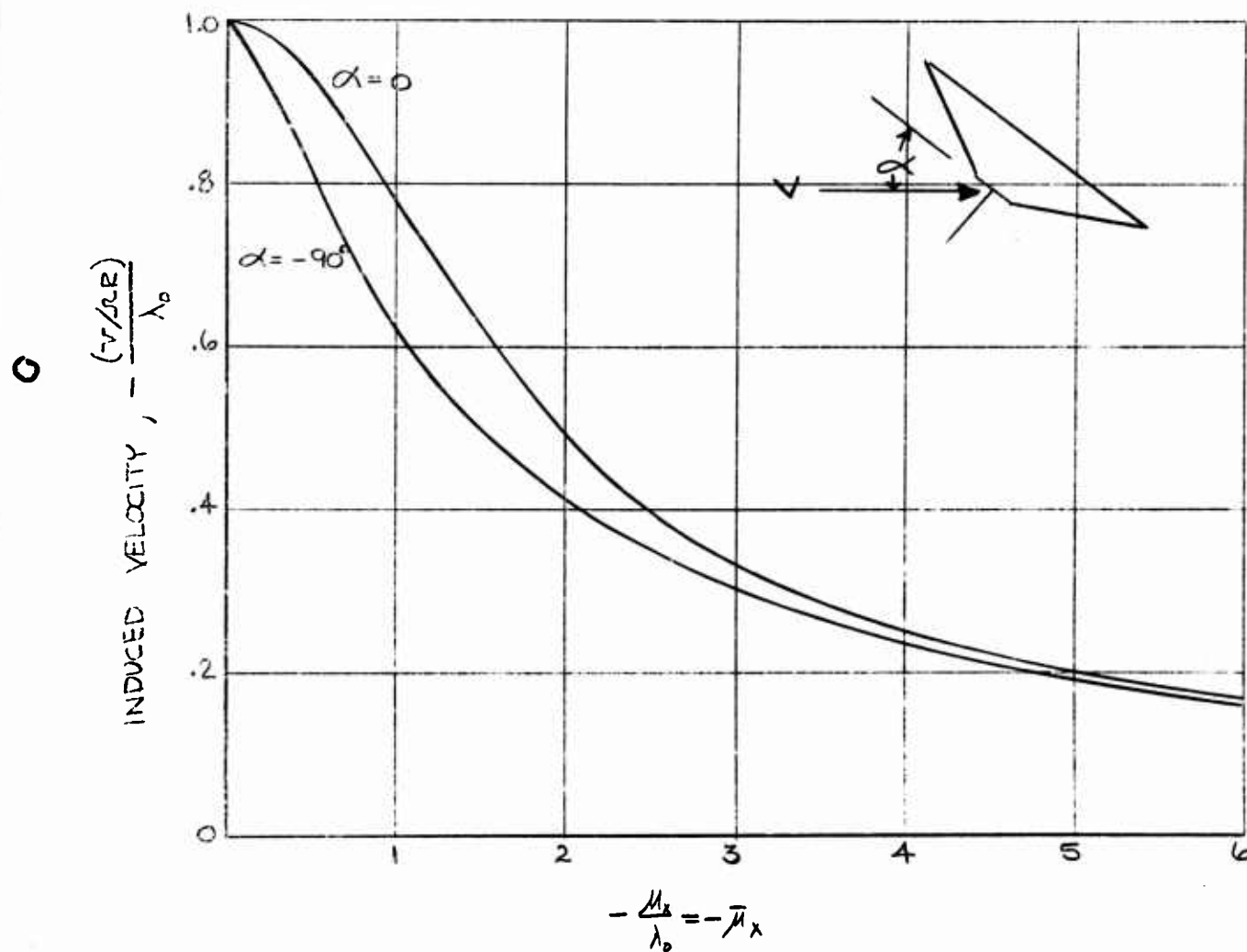
INFLOW DERIVATIVES

$$\lambda_0 \frac{\partial \lambda}{\partial C_T} \text{ vs } -\bar{\mu}_x$$



INDUCED VELOCITY AT ROTOR

$$-\frac{(v/rR)}{\lambda_0} \text{ VS } -\bar{\mu}_x$$



APPENDIX C

In order to simulate the dynamic characteristics of a full size aircraft by means of a scale model certain physical relationships must be satisfied. These are commonly called the conditions of "dynamical similitude" and imply that the ratio of all pertinent full scale forces to the corresponding model forces can be expressed by a single constant number. Physically it can be reasoned that the forces of interest in the rigid body motion—aerodynamic, gravitational, and inertial—must form similar closed polygons for the model and full scale in order for them to exhibit similar dynamic behavior. Such similarity can be preserved by holding constant on both machines the ratios of any $(n-1)$ pairs of forces, where n is the total number of types of forces acting, in this case 3. Therefore, if the ratios of aerodynamic to gravity forces and of gravity to inertia forces are the same for model and full scale, the similitude requirements will be satisfied. Figure 8C illustrates this condition and points out that the resulting dimensionless quantities are in fact thrust coefficient and Froude Number.

These two conditions, together with the obvious necessity of specifying a scale size in order to have a model, completely specify the model to full scale relationships of the three basic variables in a problem in mechanics—mass, length and time. Dimensional expressions may be set up equating model and full scale thrust coefficient and Froude Number in terms of the selected linear scale factor, λ , and solutions obtained for the mass and time scaling.

The results of such an operation, together with some other convenient parameters, are presented in Table IV.

Unfortunately, since the tests considered herein are conducted in the same gravity field and atmosphere as the full scale operates in, certain aerodynamic considerations cannot be completely satisfied. The result is that neither Mach Number nor Reynold's Number are simulated on the scale models, and the error is a function of scale factor as presented in Table IV. Although Mach Number effects are of little significance in stability studies in the low speed flight regime, Reynold's Number can play some part as in wind tunnel testing. As discussed in References 1 and 2 these effects can sometimes be compensated for and are frequently diminished due to the increased effective Reynold's Number in the highly turbulent flow in the wake of a rotor. This problem does, however, deserve close consideration in investigations of aircraft performance with scale models.

RELATIONSHIP OF ACTIVATED FORCES

Three classes of forces acting

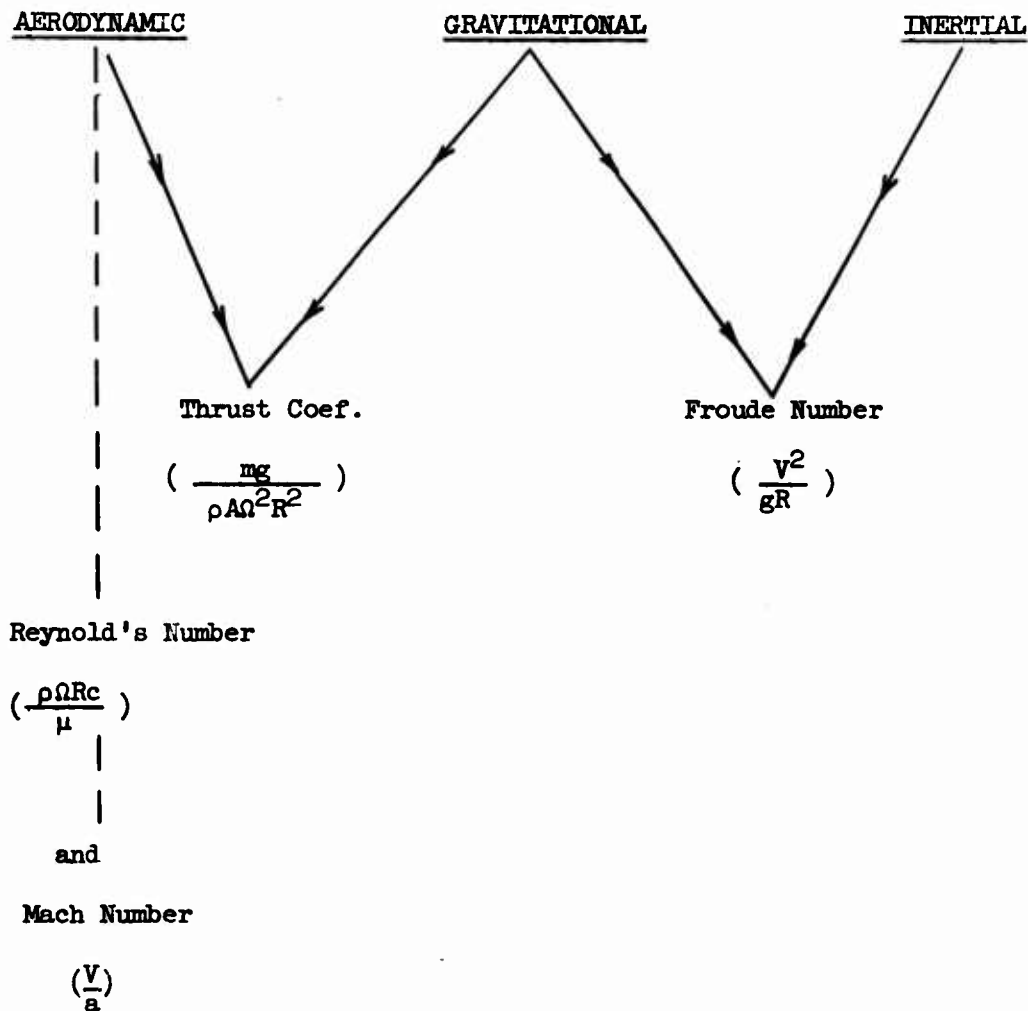


Figure 88

The relationship between the three classes of forces activated in
 stability and control maneuvers

TABLE IV

SCALE FACTORS

$$(\text{MODEL VALUE}) = (\text{FULL SCALE VALUE}) (\lambda)^n$$

<u>PARAMETER</u>	<u>FACTOR</u>
Linear Dimensions	λ^{-1}
Area	λ^{-2}
Volume, Mass, Force	λ^{-3}
Moment	λ^{-4}
Moment of Inertia	λ^{-5}
Linear Velocity	$\lambda^{-1/2}$
Linear Acceleration	λ^0
Angular Velocity	$\lambda^{1/2}$
Angular Acceleration	λ^1
Time	$\lambda^{-1/2}$
R.P.M.	$\lambda^{1/2}$
Disc Loading (T/A)	λ^{-1}
Power Loading	$\lambda^{1/2}$
Power	$\lambda^{-3.5}$
R. N.	$\lambda^{-1.5}$
Mach No.	$\lambda^{-1/2}$

ERRATA

Page 5, line 17	Change date "11-10-58" to "11-10-59"
Page 90, line 1	Change "it" to "is"
Page 90, line 20	Change "affect" to "effect"
Page 92, line 11	Change "to" to "too"
Page 130, line 21	Should read "...tilt angles and C_T and under ..."

ALART PROGRAM
Technical Report
Distribution List

ADDRESS	NO. OF COPIES
1. Chief of Transportation Department of the Army Washington 25, D.C. ATTN: TCACR	2
2. Commander Wright Air Development Division Wright-Patterson Air Force Base, Ohio ATTN: WCLJA	2
3. Commanding Officer U.S. Army Transportation Research Command Fort Eustis, Virginia ATTN: Research Reference Center ATTN: Aviation Directorate	4 3
4. U.S. Army Representative HQ AFSC (SCR-LA) Andrews Air Force Base Washington 25, D.C.	1
5. Director Air University Library ATTN: AUL-8680 Maxwell Air Force Base, Alabama	1
6. Commanding Officer David Taylor Model Basin Aerodynamics Laboratory Washington 7, D.C.	1
7. Chief Bureau of Naval Weapons Department of the Navy Washington 25, D.C. ATTN: Airframe Design Division ATTN: Aircraft Division ATTN: Research Division	1 1 1
8. Chief of Naval Research Code 461 Washington 25, D.C. ATTN: ALO	1

	ADDRESS	NO. OF COPIES
9.	Director of Defense Research and Development Room 3E - 1065, The Pentagon Washington 25, D.C. ATTN: Technical Library	1
10.	U.S. Army Standardization Group, U.K. Box 65, U.S. Navy 100 FPO New York, New York	1
11.	National Aeronautics and Space Administration 1520 H Street, N.W. Washington 25, D.C. ATTN: Bertram A. Mulcahy Director of Technical Information	5
12.	Librarian Langley Research Center National Aeronautics & Space Administration Langley Field, Virginia	1
13.	Ames Research Center National Aeronautics and Space Agency Moffett Field, California ATTN: Library	1
14.	Armed Services Technical Information Agency Arlington Hall Station Arlington 12, Virginia	10
15.	Office of Chief of Research and Development Department of the Army Washington 25, D.C. ATTN: Mobility Division	1
16.	Senior Standardization Representative U.S. Army Standardization Group, Canada c/o Director of Weapons and Development Army Headquarters Ottawa, Canada	1
17.	Canadian Liaison Officer U.S. Army Transportation School Fort Eustis, Virginia	3

	ADDRESS	NO. OF COPIES
18.	British Joint Services Mission (Army Staff) DAQMG (Mov & Tn) 1800 K Street, N.W. Washington 6, D.C. ATTN: Lt. Col. R.J. Wade, R.E.	3
19.	Office of Technical Services Acquisition Section Department of Commerce Washington 25, D.C.	2
20.	Librarian Institute of the Aeronautical Sciences 2 East 64th Street New York 21, New York	2
21.	U.S. Army Research & Development Liaison Group APO 79 New York, New York ATTN: Mr. Robert R. Piper	1

This report presents the results of a series of experiments conducted on a 1/5.2 scale dynamically similar model of a tilt-wing VTOL aircraft. The static longitudinal forces and moment and the character of horizontally-free partial transitions were examined through the use of the Princeton University Forward Flight Facility.

Included are discussions of the equipment and testing techniques employed in these tests as well as a development and evaluation of various analytical approaches to the prediction of the static and dynamic stability characteristics of a wing-rotor system.

Results demonstrate that additional experimental information is necessary in order to predict accurately the forces and moments developed by the wing and rotor.

A preliminary analysis indicates significant contributions to stability and control from the effects of slipstream rotation on wing local flow conditions.

This report presents the results of a series of experiments conducted on a 1/5.2 scale dynamically similar model of a tilt-wing VTOL aircraft. The static longitudinal forces and moment and the character of horizontally-free partial transitions were examined through the use of the Princeton University Forward Flight Facility.

Included are discussions of the equipment and testing techniques employed in these tests as well as a development and evaluation of various analytical approaches to the prediction of the static and dynamic stability characteristics of a wing-rotor system.

Results demonstrate that additional experimental information is necessary in order to predict accurately the forces and moments developed by the wing and rotor.

A preliminary analysis indicates significant contributions to stability and control from the effects of slipstream rotation on wing local flow conditions.

This report presents the results of a series of experiments conducted on a 1/5.2 scale dynamically similar model of a tilt-wing VTOL aircraft. The static longitudinal forces and moment and the character of horizontally-free partial transitions were examined through the use of the Princeton University Forward Flight Facility.

Included are discussions of the equipment and testing techniques employed in these tests as well as a development and evaluation of various analytical approaches to the prediction of the static and dynamic stability characteristics of a wing-rotor system.

Results demonstrate that additional experimental information is necessary in order to predict accurately the forces and moments developed by the wing and rotor.

A preliminary analysis indicates significant contributions to stability and control from the effects of slipstream rotation on wing local flow conditions.

This report presents the results of a series of experiments conducted on a 1/5.2 scale dynamically similar model of a tilt-wing VTOL aircraft. The static longitudinal forces and moment and the character of horizontally-free partial transitions were examined through the use of the Princeton University Forward Flight Facility.

Included are discussions of the equipment and testing techniques employed in these tests as well as a development and evaluation of various analytical approaches to the prediction of the static and dynamic stability characteristics of a wing-rotor system.

Results demonstrate that additional experimental information is necessary in order to predict accurately the forces and moments developed by the wing and rotor.

A preliminary analysis indicates significant contributions to stability and control from the effects of slipstream rotation on wing local flow conditions.

AD _____ Accession No. _____ UNCLASSIFIED

Princeton University Aero. Eng. Dept., Princeton, N.J.

1. Helicopters, test facilities

RESULTS OF EXPERIMENTS ON A TILT-WING VTOL AIRCRAFT USING THE PRINCETON UNIVERSITY FORWARD FLIGHT FACILITY - William F. Putman

2. VTOL model test results

3. VTOL stability (longitudinal)

4. VTOL test methods

Report No. 542, May 1961
223 pp.-illus.

Contract No. DA44-177-TC-524
Project No. 9-38-01-000, TK902
Unclassified Report

AD _____ Accession No. _____ UNCLASSIFIED

Princeton University Aero. Eng. Dept., Princeton, N.J.

1. Helicopters, test facilities

RESULTS OF EXPERIMENTS ON A TILT-WING VTOL AIRCRAFT USING THE PRINCETON UNIVERSITY FORWARD FLIGHT FACILITY - William F. Putman

2. VTOL model test results

3. VTOL stability (longitudinal)

4. VTOL test methods

Report No. 542, May 1961
223 pp.-illus.

Contract No. DA44-177-TC-524
Project No. 9-38-01-000, TK902
Unclassified Report

AD _____ Accession No. _____ UNCLASSIFIED

Princeton University Aero. Eng. Dept., Princeton, N.J.

1. Helicopters, test facilities

RESULTS OF EXPERIMENTS ON A TILT-WING VTOL AIRCRAFT USING THE PRINCETON UNIVERSITY FORWARD FLIGHT FACILITY - William F. Putman

2. VTOL model test results

3. VTOL stability (longitudinal)

4. VTOL test methods

Report No. 542, May 1961
223 pp.-illus.

Contract No. DA44-177-TC-524
Project No. 9-38-01-000, TK902
Unclassified Report

AD _____ Accession No. _____ UNCLASSIFIED

Princeton University Aero. Eng. Dept., Princeton, N.J.

1. Helicopters, test facilities

RESULTS OF EXPERIMENTS ON A TILT-WING VTOL AIRCRAFT USING THE PRINCETON UNIVERSITY FORWARD FLIGHT FACILITY - William F. Putman

2. VTOL model test results

3. VTOL stability (longitudinal)

4. VTOL test methods

Report No. 542, May 1961
223 pp.-illus.

Contract No. DA44-177-TC-524
Project No. 9-38-01-000, TK902
Unclassified Report

UNCLASSIFIED

UNCLASSIFIED